

**Award Number:** Contract: W81XWH-11-1-0121

**TITLE:** Noninvasive Spatially Offset and Transmission Raman Mapping of Breast Tissue: A Multimodal Approach Towards the *In Vivo* assessment of Tissue Pathology

**PRINCIPAL INVESTIGATOR:** Matthew Schulmerich

**CONTRACTING ORGANIZATION:** University of Illinois  
Urbana, IL 61801

**REPORT DATE:** June 2013

**TYPE OF REPORT:** Annual Summary

**PREPARED FOR:** U.S. Army Medical Research and Materiel Command  
Fort Detrick, Maryland 21702-5012

**DISTRIBUTION STATEMENT:** Approved for Public Release;  
Distribution Unlimited

The views, opinions and/or findings contained in this report are those of the author(s) and should not be construed as an official Department of the Army position, policy or decision unless so designated by other documentation.

REPORT DOCUMENTATION PAGE				Form Approved OMB No. 0704-0188	
Public reporting burden for this collection of information is estimated to average 1 hour per response, including the time for reviewing instructions, searching existing data sources, gathering and maintaining the data needed, and completing and reviewing this collection of information. Send comments regarding this burden estimate or any other aspect of this collection of information, including suggestions for reducing this burden to Department of Defense, Washington Headquarters Services, Directorate for Information Operations and Reports (0704-0188), 1215 Jefferson Davis Highway, Suite 1204, Arlington, VA 22202-4302. Respondents should be aware that notwithstanding any other provision of law, no person shall be subject to any penalty for failing to comply with a collection of information if it does not display a currently valid OMB control number. PLEASE DO NOT RETURN YOUR FORM TO THE ABOVE ADDRESS.					
1. REPORT DATE June 2013		2. REPORT TYPE Annual Summary		3. DATES COVERED 1 April 2011 – 25 June 2013	
4. TITLE AND SUBTITLE Noninvasive Spatially Offset and Transmission Raman Mapping of Breast Tissue: A Multimodal Approach Towards the <i>In Vivo</i> assessment of Tissue Pathology				5a. CONTRACT NUMBER W81XWH-11-1-0121	
				5b. GRANT NUMBER W81XWH-11-1-0121	
				5c. PROGRAM ELEMENT NUMBER	
6. AUTHOR(S) Matthew Schulmerich  E-Mail: schulmer@illinois.edu				5d. PROJECT NUMBER	
				5e. TASK NUMBER	
				5f. WORK UNIT NUMBER	
7. PERFORMING ORGANIZATION NAME(S) AND ADDRESS(ES) University of Illinois Urbana, IL 61801				8. PERFORMING ORGANIZATION REPORT NUMBER	
9. SPONSORING / MONITORING AGENCY NAME(S) AND ADDRESS(ES) U.S. Army Medical Research and Materiel Command Fort Detrick, Maryland 21702-5012				10. SPONSOR/MONITOR'S ACRONYM(S)	
				11. SPONSOR/MONITOR'S REPORT NUMBER(S)	
12. DISTRIBUTION / AVAILABILITY STATEMENT Approved for Public Release; Distribution Unlimited					
13. SUPPLEMENTARY NOTES					
14. ABSTRACT The purpose of this research project is to develop new approaches that can impact early diagnosis of breast cancer, post-biopsy analysis, lymph node examinations, and drug delivery studies. The scope of this training involves optimizing Raman instrumentation and methods for efficient illumination and collection of Raman scattered light originating from deep within breast tissue. Experiments encompass designing tissue phantoms using Intralipid®, dyes/pigments, inclusions, and agarose gel to quantitatively characterize the instruments' capabilities and performance. Additionally, we conduct spectroscopy on tissue biopsies to correlate spectral bands with healthy and diseased breast tissue. Observed spectral changes are compared to infrared images and H&E/HIS-stained images to relate observed biochemical changes to histology. The Raman data will be used to generate and train classification algorithms for automated histopathology as a starting point for in vivo work at the culmination of this training program. This report outlines progress for year 1 of the 3 year training program. In the approved statement of work 5 tasks were stated. All 5 tasks were successfully completed. We now have a working relationship with local clinicians. We have built-up a comprehensive database consisting of micrographs and IR spectral images for identify breast tissue histology and tissue chemistry. We have acquired Raman measurements on biopsied tissue. We have identified Raman spectral bands that can be used for distinguishing between different tissue types and have applied those Raman spectral bands to achieve cell-level contrast in Raman spectral images. Additionally, we have used clinical observations and interaction with clinicians to develop a conceptual design for a Raman Tomography instrument aimed at breast cancer screening. Finally for Raman tomographic reconstruction, we have evaluated existing diffuse optical tomography algorithms specifically for Raman measurements and have adapted a Monte Carlo framework for our Raman tomographic reconstruction. Through modeling and experimentation we characterized different instrument configurations and have implemented the transmission fan style configuration into our prototype instrument design which uses fiber-optics in-contact with tissue to give the maximum collection efficiency.					
15. SUBJECT TERMS Raman Spectroscopy, Breast Cancer, SORS, Transmission spectroscopy, Raman Tomography, Raman Imaging, Infrared Imaging					
16. SECURITY CLASSIFICATION OF: UNCLASSIFIED			17. LIMITATION OF ABSTRACT  UU	18. NUMBER OF PAGES  71	19a. NAME OF RESPONSIBLE PERSON
a. REPORT U	b. ABSTRACT U	c. THIS PAGE U			19b. TELEPHONE NUMBER (include area code)

## Table of Contents

	<u>Page</u>
Introduction.....	4
Body.....	5
Key Research Accomplishments.....	35
Reportable Outcomes.....	36
Conclusion.....	37
References.....	39
Appendices.....	42

**INTRODUCTION:** The **subject** of this research is to develop non-invasive optical instrumentation and methods for obtaining chemical contrast from deep within breast tissue. The overarching goal of this training program is to become steeped in breast cancer clinical practice and research to independently develop a new technology from a concept. My learning objectives include the following: first, fill in the gaps in my basic knowledge of breast cancer and pathology. Second, build a knowledge base as to the chemical changes that are occurring within breast tissue and how those changes are reflected in the vibrational spectra. Third, to understand the optics of breast tissue to gain most efficient illumination and collection schemes for instrumental design. The **purpose** of this research project is to develop new approaches that can impact early diagnosis of breast cancer, post-biopsy analysis, lymph node examinations, and drug delivery studies. Additionally, this technology could be used to study animal models for tissue engineering, 3D tissue scaffolds and has a variety of other basic research as well as clinical applications. The **scope** of this training involves optimizing Raman instrumentation and methods for efficient illumination and collection of Raman scattered light originating from deep within breast tissue. Experiments encompass designing tissue phantoms using Intralipid®, dyes/pigments, inclusions, and agarose gel to quantitatively characterize the instruments' capabilities and performance. Additionally, we conduct spectroscopy on tissue biopsies to correlate spectral bands with healthy and diseased breast tissue. Observed spectral changes are compared to infrared images and H&E/HIS-stained images to relate observed biochemical changes to histology. The Raman data will be used to generate and train classification algorithms for automated histopathology as a starting point for *in vivo* work at the culmination of this training program.

*Personnel receiving pay from this research effort: Matthew Schulmerich*



**BODY:** The approved statement of work is illustrated in figure 1. The work conducted for this fellowship ended after year 2 (an early termination of the fellowship was requested as a result of the PI accepting a new position of employment). For year one, five tasks were outlined and for year two, four tasks were outlined. Details of the work conducted in year one and two as well as future directions are presented on the following pages.



Figure 1) Summary figure and timeline for approved statement of work

**Task 1.1 Obtain tissue biopsy slides and put together a measurement plan (month 1-2):** This task was successfully completed. Tissue samples were obtained from Provena covenant medical center and US Biomax, Inc (IRB approved sources). 101 breast tissue biopsies cores (1mm) were obtained. Diagnosis were hyperplasia (n=20), Dysplasia (n=20), Malignant Tumor (n=40), Normal (n=11). Serial sections of these biopsies were stained and imaged to establish a database of micrographs that could be used to identify cell types and regions of interest in the tissue. The stains used for identifying tissue histology were carefully chosen upon consultation with two pathologists. The histological stains used were as follows:

**No Stain** For Raman –Serial Section 261  
**P53**–Serial Section 262  
**Ki67**–Serial Section 263  
**CD31**–Serial Section 264  
**P63**–Serial Section 265  
**No Stain** For IR–Serial Section 266

**Masson's Trichrome**–Serial Section 269  
**Vimentin**–Serial Section 270  
**Smooth Muscle Actin**–Serial Section 271  
**HMW Cytokeratin**–Serial Section 272  
**No Stain** For IR–Serial Section 273  
**Her2/neu**–Serial Section 274

**H&E**–Serial Section 267  
**Calponin** –Serial Section 268

**Estrogen Receptor**–Serial Section 275  
**Progesterone Receptor**–Serial Section 276

For each biopsy we built a database of micrographs that can be zoomed to a 20x magnification. A set low magnification serial sections are depicted in figure2 showing the different staining results.

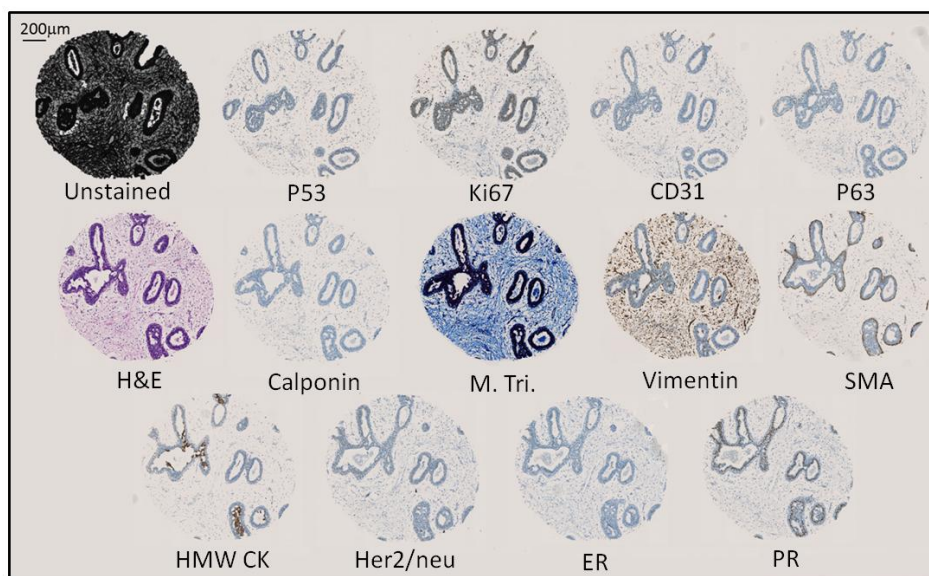


Figure 2) Serial sections and staining obtained for each breast tissue biopsy

In addition to stained serial sections we also acquired mid-infrared images from each of these biopsies. Some of our mid infrared results is reported in the publication ‘High Definition Spectroscopic Imaging’ attached in the appendix of this report. An example of an infrared spectral image is depicted in figure 3. These images are useful in working with pathologists in order to evaluate histology and pathology. We used this electronic database of infrared and white light micrographs to identified regions of interest for Raman measurements. Regions of interest were selected by correlating the tissues chemistry with the observed tissue staining to select different tissue types i.e.) distinguishing epithelial cells from myoepithelial cells.

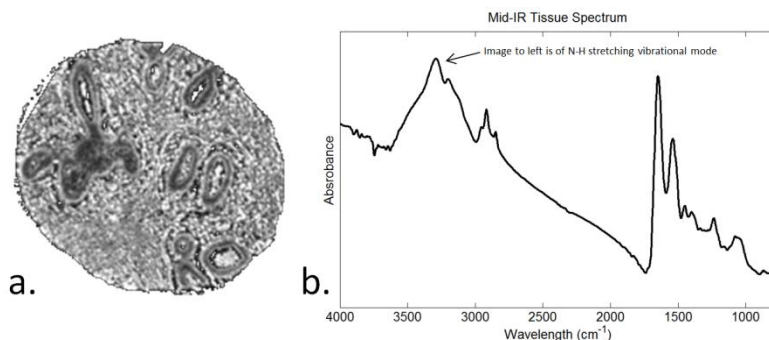


Figure 3) a) Infrared image of using the Amide A band for contrast b) representative mid IR spectrum illustrating the information available for contrast at each pixel in this image.

**Task 1.2 Raman measurements (month 3-10):** We have successfully completed this task. Raman spectra were acquired on a Horiba LabRam microscope using a video reference to mark the position of each measurement. Spectra were obtained using 785nm excitation with a 100x 0.90NA microscope objective. Acquisitions range from 15 to 60 seconds per measurement point depending on signal to noise. Spectra were acquired at a spectral resolution between 5 and 10  $\text{cm}^{-1}$ .

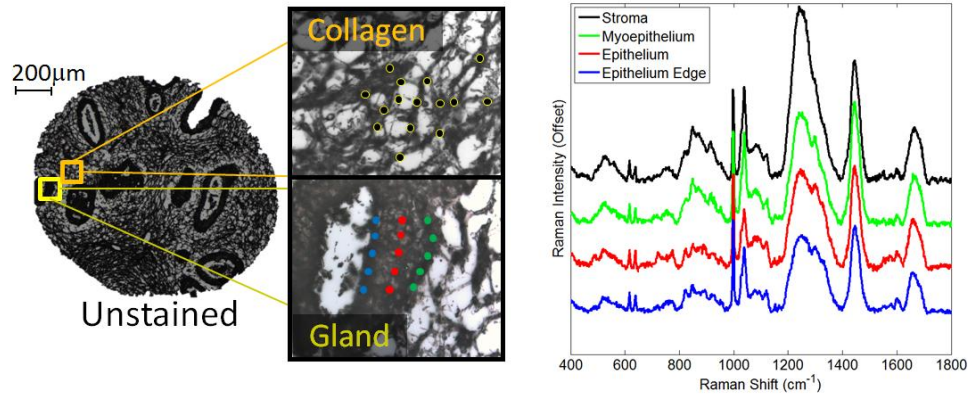


Figure 4) Raman spectra were collected from select regions within each biopsy core and compared based on tissue type.

Raman Band ( $\text{cm}^{-1}$ )	Major Assignments	Weighted towards
622	C-C twisting mode phenylalanine	Epithelium
643	C-C twisting mode tyrosine	Epithelium
781	Cytosine/Uracil ring breathing	Epithelium
828	Ring breathing tyrosine/O-P-O stretch	Epithelium
854	Tyrosine ring breathing	Stroma
936	C-C stretch Proline, Valine, and protein backbone ( $\alpha$ -helix)	Epithelium
1003	Symmetric ring breathing mode phenylalanine	Epithelium
1032	C-H in plane bending mode phenylalanine	Epithelium
1085	C-N stretch	Stroma
1126	C-N stretch	Epithelium
1156	C-C & C-N stretching	Epithelium
1205	Tryptophan & Phenylalanine $n(\text{C}-\text{C}_6\text{H}_5)$	Epithelium
1240-1265	Amide III	Stroma
1310	$\text{CH}_3\text{CH}_2$ twisting mode	Epithelium
1333	$\text{CH}_3\text{CH}_2$ wagging mode	Epithelium
1450	$\text{CH}_2$ bending mode	Stroma

We acquired Raman spectra from strategic locations on all biopsy cores that were available on serial section 261 (see page 5). We also acquired Raman measurements from surgical resections that were provided through Provena medical center. The primary focus of our measurements was in distinguishing different tissue types in anticipation of developing an algorithm classifier. Figure 4 illustrates an example of point measurements collected on regions of interest within a biopsy section. A representative example of the

data collected for each biopsy core is depicted in figure 4. All spectra in figure 4 were baselined and normalized to the phenylalanine band at  $1003 \text{ cm}^{-1}$ .

Figure 4 illustrates very clearly that different tissue types can be identified by observing the differences in Raman bands. For example, the black spectrum, collected over stromal tissue, has a much larger amide III Raman band ( $1244 \text{ cm}^{-1}$  and  $1274 \text{ cm}^{-1}$ ) than epithelial or myoepithelial tissue. This band is correlated with a C-N and N-H vibrational modes and can be used for contrast to distinguish epithelial tissue from stromal tissue. Additionally the band at  $1045 \text{ cm}^{-1}$  also has a

larger relative contribution in the stromal and myoepithelium tissue over epithelium. Some specific spectral band weightings are listed in the table below figure 4. Validating the exact position of a measurement was difficult as the tissue structure changed slightly in sequential serial sections and as a result this contrast is some-what difficult to visualize by point measurements.

To overcome this difficulty, we acquired Raman spectral images that allow us to more reliably identify where a Raman spectrum originates from relative to the surrounding tissue. Using the Raman spectrum for contrast and having the positional correspondence of many Raman spectra, we are able to visualize the tissue structure and pull out average differences in tissue types.

An example of a Raman spectral image is illustrated in figure 5. The top right image illustrates a Raman spectral image over-laid on an unstained biopsy micrograph. The primary contrast in this image is achieved using the band at  $1045\text{ cm}^{-1}$ . By correlating the position of the image with stained biopsy serial sections in our database, it is clear that we can distinguish epithelium, stroma, and myoepithelial cells without dyes or label. This is a significant finding because myoepithelial cells makeup the basal layer of normal mammary epithelial tissue. Their identification has particular diagnostic value as they are lost in malignancy but retained in most benign lesions. Quantification of these cells *in vivo* could play a key role in identifying invasive carcinomas.

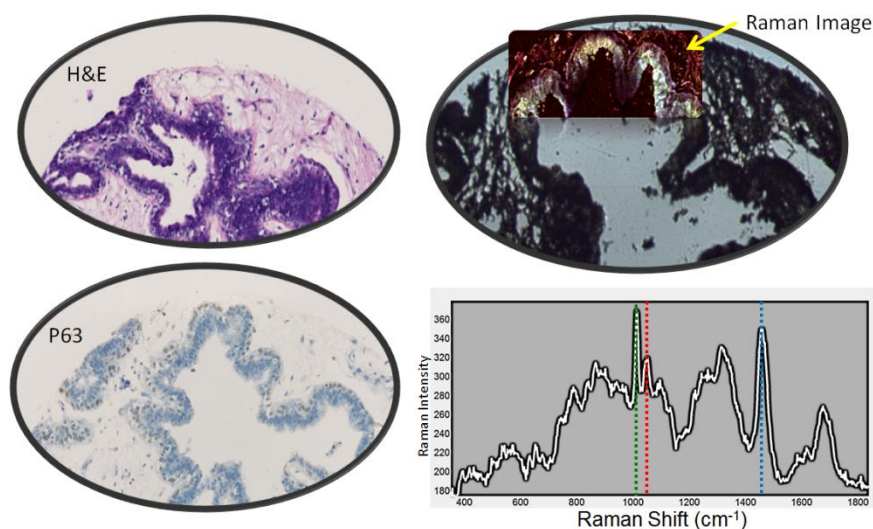


Figure 5) Raman spectral image compared to stained biopsy sections

**Task 1.3 Raman data processing (month 11-12):** Spectral processing involved calibrating the wavelength axis against a neon atomic emission lamp and using a NIST traceable white light source to correct for the instruments wavelength response. The Raman spectra were then imported into Matlab® and examined for cosmic rays (spikes). If spikes were found they were removed by using a median filter on adjacent points to determine an interpolating reference. The spike were then deleted and replaced by interpolating data points from both sides of the spike to fill in the gap. Baseline points on the data were identified and used for all spectra analyzed. Using these same baseline points a multi-linear baseline was then fit to the data and subtracted to provide baselined Raman spectra. The spectra were then normalized either by overall area or to specific band areas. Several algorithms and visualization approaches were developed for this work and have been



reported in the publication ‘Real-time interactive data mining for chemical imaging information: application to automated histopathology’ which is attached in the appendix of this report.

### **Task 2.1 Instrument conceptual design based on clinical observation (month 1-2):**

Dr. Krishna Tangella M.D. who is Teaching Faculty at the University of Illinois at Urbana-Champaign College of Medicine has spent the first year of this fellowship with me in a one-on-one course in Breast Cancer pathology. Over this year I have built-up my fundamental understanding of breast cancer. I’ve worked closely with the pathology team at Provena Covenant medical Center in Urbana, IL. In working with this team I’ve been fortunate to observe many aspects of clinical practice associated with breast cancer. I’ve observed screening with MRI and mammography as well as ultrasound guided biopsies. I’ve seen the processing that occurs when a biopsy is section and prepared for histological staining. Additionally, I’ve observed grossing procedure conducted on tissue from mastectomies. I was also fortunate to attend a week long intensive Breast Imaging course covering clinical breast imaging that was provided by the International Institute of Continuing Medical education (iiCME). This course was extremely useful in understanding current radiology practices and was very motivating as spectroscopy was brought-up as a future technology of interest!

Based on these observations and experiences, we developed conceptual design for a Raman based screening instrument as depicted in figure 6.

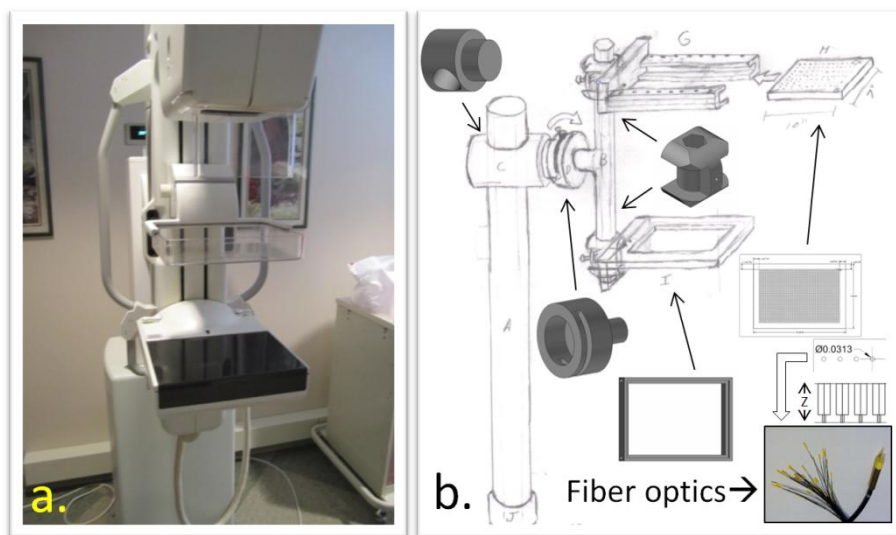


Figure 6) a) Photo taken at Provena Covenant Medical Center of a mammogram instrument b) Conceptual Design and AutoCAD files for a Breast Cancer Screening Raman Instrument

The instrument design is comprised of a stand that couples two breast paddles to an optical table. The stand has vertical and rotational motion to adjust to patient height and allow for multiple projections through the breast tissue. Both breast paddles are removable and can be made compatible with existing mammogram instruments. The bottom breast paddle has a transparent glass plate that is used to compress the breast tissue and will allow the Raman excitation source to

illuminate the bottom of the breast. The light transmitted through the breast is collected by fiber optics on the top paddle and is then relayed to an imaging Raman spectrometer. This data is then used to reconstruct the size, shape, and position of features using the innate chemical contrast in the breast tissue. Details on the construction of the instrument follow in the task outline for year 2 work.

### **Task 2.2 Instrument optical design (month 3-12):**

A transmission approach to illumination and collection has proven to be the most robust approach to diffuse optical tomography where as other methods, a back scattered configuration for example, are known to have reconstruction artifacts like higher surface weightings of reconstructed targets<sup>1</sup>. To explore and understand the use of transmission Raman measurements in tomographic reconstructions we conducted a series of experiments and modeling to aid in instrument design. We compared two forward-modeling methods, radiative transport calculation (via Nirfast, an open-source diffuse optical tomography modeling package) and Monte Carlo simulation (written in-house), for the modeling of light fluence in the phantom. Reconstruction of the size and position of buried targets was attempted via an iterative modified-Tikhonov minimization algorithm without the use of spatial priors. The results are validated against computed tomography (CT) images of the same samples.

#### ***Phantom Specimens and Fabrication***

Tissue phantoms were fabricated by dissolving 1 gram of agar (Sigma-Aldrich) in 50 ml of water at 95°C. Different volumes of 20% Intralipid (Sigma), an oil emulsion that is commonly used to mimic the scattering properties of fatty tissue,<sup>2-4</sup> were added to increase the scattering potential. 0.25ml or 1.25ml per 50ml of water were added to produce phantoms of total Intralipid concentration 0.1% or 0.5% by volume. A 0.1% concentration of Intralipid represents the lower limit of what is opaque to the naked eye, while a 0.5% solution close to the scattering level exhibited by epithelial tissue.<sup>5,6</sup> The solution was poured into the wells of a cell culture plate. One PTFE sphere of 1/8" diameter or two spheres of 1/16" diameter were suspended in each well by thin histology needles, and the plate was allowed to cool in a refrigerator for approximately one hour. The resulting phantoms were cylindrical, 1 cm in diameter and approximately 2 cm tall. Each sphere was positioned such that its middle sat approximately 1.2 cm above the base of the phantom. The radial position of the spheres, as well as the distance between two spheres embedded in the same phantom, were experiment-dependent.

#### ***Raman Instrumentation***

The instrument comprised of a 785 nm excitation laser (barrowed for these experiments) and CCD-coupled spectrometer with a pre-stage notch filter, a fiber-optic bundle detector and a motorized rotation stage, as shown in Figure 7. In all cases, the laser and detector were held at a constant height at the level of the PTFE target while the cylindrical phantom was rotated about its vertical (symmetrical) axis. This allowed for a single source/detector combination to sample the phantom from multiple angles, a requirement of optical tomography.<sup>7</sup>

The 400mW CW laser at 785nm (Invictus, Kaiser) was fiber-launched and passed through a collimator to produce a 1.25 mm diameter beam. In all cases, this beam was centered on the waist of the phantom at the height of the target. Collection was performed via two achromatic doublets which focused the photons exiting from the phantom onto a 50-fiber bundle (100 um diameter

each, in an approximately 5x10 array) (Fibertech Optica, Kitchener, Ontario, Canada). The focal lengths of these achromats were 60mm (focusing) and either 75mm or 200mm (collection) depending on the experiment. The output of the fiber bundle was imaged onto a spectral CCD (iDUS, Andor Technology, Belfast, Northern Ireland). The motorized rotation stage (NR360S, ThorLabs, Newton, New Jersey), controlled by LabView (National Instruments, Austin, Texas), was stepped clockwise in 4.5 degree increments in all experiments for a total of 80 discrete sampling angles.

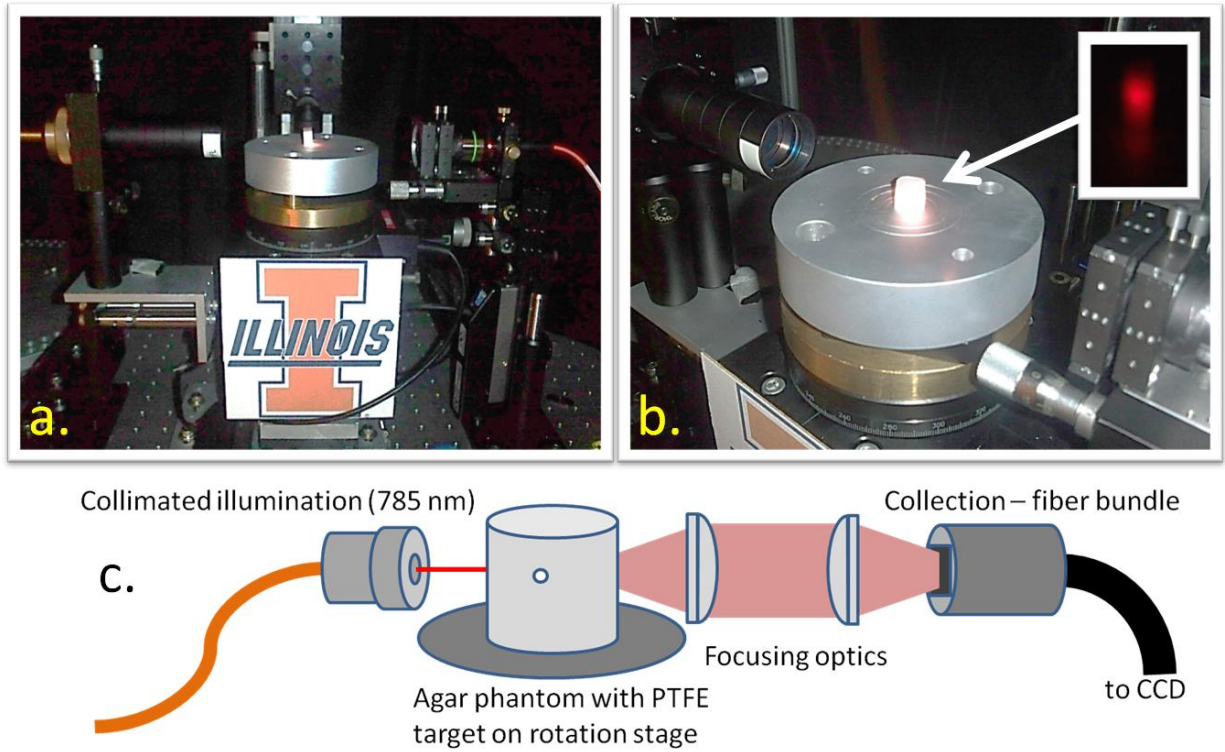


Figure 7) a.) and b.) Photos and c.) schematic of Raman tomography instrumentation. Both the illumination and collection fibers are centered on the phantom at the height of the PTFE sphere target.

### Experiments

For phantoms containing a single target, three separate instrumentation configurations (as shown in Figure 7) were considered. In the first, shown in Figure 8a, the source and detector were kept at a 180° angle while the phantom was rotated through 80 positions to demonstrate the insufficiency of using a single source-detector angle. Acquisition time was three minutes per step (two frames of 90 seconds each to aid in data processing). The second experiment involved varying the angle between the source and detector, shown in Figure 8b. In addition to 180 degrees, the source was moved relative to the detector to form angles of 135, 90, and 45 degrees. This setup mimics the “circular fan-beam” geometry which is commonly used in diffuse optical tomography experiments.<sup>1</sup> For each source position, the stage was rotated through the full 80 steps and two spectra of 30 seconds each (as opposed to 90 seconds) were acquired at each step. In the final configuration, the source/detector angle was returned to 180 degrees, but the achromatic collection lens nearest to the phantom was replaced with one of focal length 200mm as shown in Figure 8c. The entire

detector setup was moved an appropriate distance away from the phantom to keep the fibers in focus. This expanded the collection region from an area of approximately 0.97 mm x 1.3 mm to 2.9 mm x 3.8 mm with the intent of being able to collect spatial information from each individual fiber. This fan-like geometry was chosen to mimic the cone-beam transmission computed tomography (CT) source-detector configuration.<sup>8</sup>

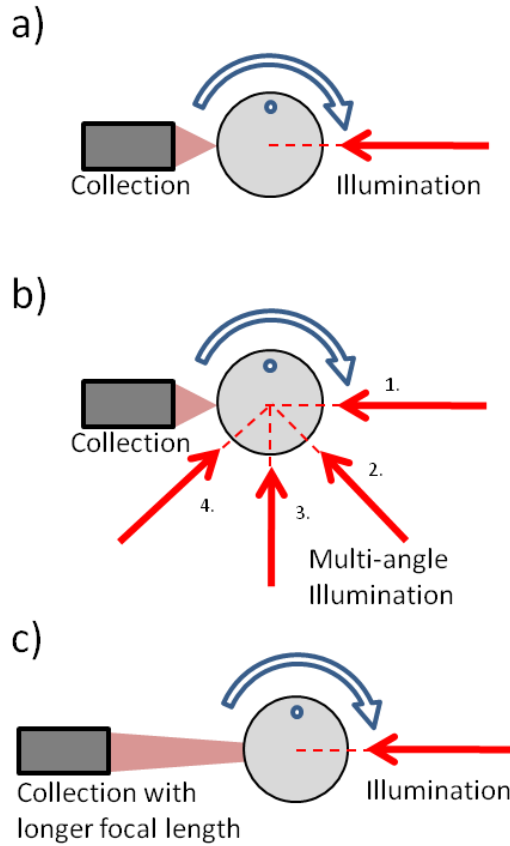


Figure 8) Three instrumentation configurations corresponding to the three experiments performed. a) Illumination and collection are fixed at a 180 degree angle. Measurements are taken as the phantom is rotated in 80 steps of  $4.5^\circ$  each. The fiber bundle is treated as a point detector for 80 total measurements. b) Multiple scans are taken with the source forming four positions with the detector ( $180^\circ$ ,  $135^\circ$ ,  $90^\circ$  and  $45^\circ$ ). The total number of measurements taken is 320 ( $4 \times 80$ ). c) Illumination and collection are fixed at a  $180^\circ$  angle as in setup a), but the focal length of the collection has been increased from 75 mm to 200 mm. As a result, the total area of collection is larger and the fiber bundle can no longer be treated as a point detector – the signals from (ten) individual fibers were evaluated for 800 total data points.

A series of experiments involving phantoms with two PTFE spheres were also performed. Using the instrument setup with the longer focal length collection (experiment seen in figure 8c) and an additional 30 mm focal length lens to focus the collimated illumination beam in an approximation of a point source (see later discussion), the response from two spheres was investigated. Additionally, a third series of experiments in which the Intralipid content of the two-sphere phantoms was increased to 0.5%, was performed in the same manner with two spheres and a longer focal length. The quality of the reconstructions was evaluated by comparison to micro-CT images showing absolute sphere positions.

### Data Processing



Zemax was used to model some of the optical configurations, while matlab was found to be more useful in the tomographic reconstructions. All data processing was done in Matlab R2009b (The MathWorks, Nantucket MA). A median filter was applied to all collected data to correct for the cosmic ray ‘spikes’ which appear on the CCD. The two Raman bands of interest are PTFE (732  $\text{cm}^{-1}$ ) and Intralipid ( $\sim 800\text{-}820 \text{ cm}^{-1}$ ). As with the biopsy Raman measurements, a multilinear “rubber band” baselining procedure was used to remove the background, and the area under each band was calculated. During reconstructions, both the absolute intensity of the PTFE signal and that of the Intralipid signal are utilized. The intensity of the Intralipid band is directly proportional to the number of photons reaching the detector for that measurement, and can be considered an internal standard which accounts for any discrepancies in the distance between source and detector or in the amount of light collected. In high-scattering samples where the Intralipid band is obscured by noise, the band’s value is approximated as being proportional to the average intensity of the entire CCD chip.

### Computerized Tomography Reconstruction

Nirfast

[[www.dartmouth.edu/~nir/nirfast](http://www.dartmouth.edu/~nir/nirfast)], is an open-source software package for simulation of DOT experiments and for DOT reconstructions from real or simulated data.<sup>9</sup> Based on a finite-element method for calculating photon fluence through specified geometries, the two processes that can be modeled (NIR absorbance and fluorescence emission) can be seen as analogous to Raman scattering events (conversion of Rayleigh scattered to Stokes scattered light). While the physical processes behind these two are not the same, they are similar enough to warrant the use of Nirfast as a first approximation for 2D reconstructions from experimental Raman data. For reconstructing experimental data, a circular finite element

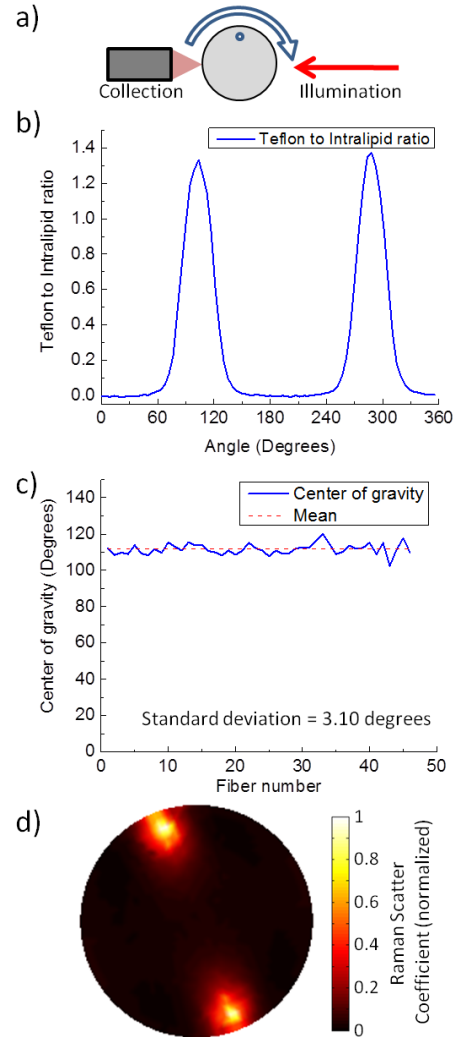


Figure 9) a) Schematic of 180° setup, including the direction of rotation and the approximate starting position of the PTFE target relative to the source and detector. b) PTFE to Intralipid Raman photon ratio as a function of phantom rotation, average of all fibers. Distinct increases in signal occur when the target passes the source or the detector. c) Center of gravity measurements for each fiber-optic in the detector bundle. Due to the small spacing of fibers, little variation is seen in the position of the second peak as seen by each individual fiber. d) Reconstruction from Nirfast. Data predicts two targets at opposite ends of the phantom.

mesh was generated within the program. Source and detector locations were added to match each experimental setup, and the experimental data were ordered and normalized to match the range of the signal from a forward simulation of a 'blank' mesh with no absorbing target.

Also evaluated was a Monte Carlo simulation written in-house for modeling photon fluence. Using a 2D pixel mesh, the reconstruction mathematics and assumptions conserved between the two methods. Although more computationally intensive, Monte Carlo simulations allow the user to overcome certain assumptions made by the radiative transport equation (including the use of a non-idealized point source, implementation of geometrically-accurate detectors, and photon migration that does not follow the diffusion regime) which may not be appropriate for certain Raman experiments. Monte Carlo studies which simulate the generation and propagation of Raman photons through turbid media have been performed recently.<sup>10-12</sup> In a similar manner, we compare the results of Monte Carlo simulations to those of Nirfast to show that the physical processes that govern Raman tomography experiments differ significantly from DOT experiments and that these two modalities need to be treated as separate entities.

### ***Results from these experiments***

#### **A: Radiative transport calculations (NIRFAST)**

Figure 9a illustrates the simplest configuration and the recorded Raman signal of a PTFE sphere relative to Intralipid as a function of rotation (Figure 9b). Two maxima are observed: one when the target passes the source and another when the target passes the detector. These two maxima are spaced by approximately 180°, which is explained by uniform rotation of the target through 360°. In-between the two maxima, no

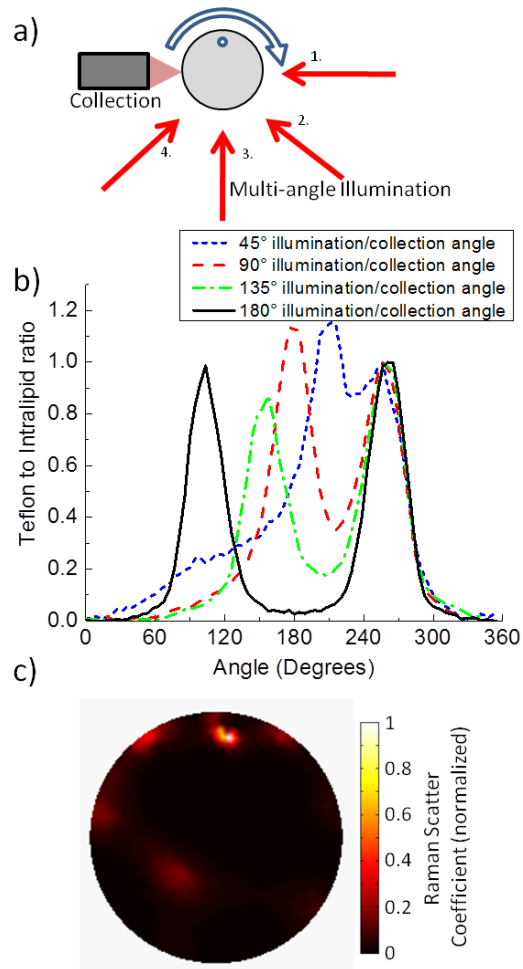


Figure 10) a) Schematic for the multi-angle setup, including the direction of rotation and the approximate starting position of the PTFE target relative to the sources and detector. b) PTFE to Intralipid Raman photon ratio as a function of both phantom rotation and source/detector angle. Signal maxima occur when the target passes near the source or the detector. As expected, the four peaks representing the target passing the detector are separated by about 45 degrees each. c) Reconstruction from Nirfast. Even though there are shadows, the data correctly predicts the location of the target. These shadows are due to normalization errors and deviations from point source illumination.

In-between the two maxima, no

Raman signal is observed; the collected photon count at these points is below the spectrograph's limit of detection.

Each of the 50 fibers from the detector is mapped onto a different region of the CCD camera, and the response from each fiber can be individually determined. The behavior of individual fibers (detectors) set along the waist of the phantom would be similar to the results seen in Figure 9b: the PTFE target will pass by each fiber and the source during rotation, resulting in two maxima with slight position shifts as a result of fiber position. If the fibers are all packed closely together, we expect this difference to be minimal; if the fibers are spaced at larger intervals, this difference will be much more pronounced. Figure 9c plots each fiber's (48 total) center of gravity for the second maximum (when the target is closest to the detector) as a function of phantom rotation. The fibers show a standard deviation of 3.1 degrees, indicating that the majority of the fibers 'see' the target

pass by within six degrees of rotation. This small variation is to be expected because the assembly's collection area spans one square millimeter, contributing a very small angular response of less than three degrees. The two maxima (target near source and target near detector) are similar in height, width, and shape. Without angular information it is not obvious how to distinguish one from the other. Performing a 2D reconstruction on the data with Nirfast, as shown in Figure 9d, confirms this observation: the program predicts two targets separated by 180 degrees. This result reinforces the well-accepted notion that multiple collection angles are needed to accurately determine the position of targets buried in scattering analyte.<sup>1</sup>

Figure 10 displays Raman signal versus rotation angle for multiple source locations ("circular fan-beam" geometry). The data have been normalized to the second maxima (when the phantom is nearest to the detector). As in the previous example, each full rotation shows two maxima corresponding to when the target passes the source and the detector. While the 180° configuration shows a separation of roughly 180°, the other angles show corresponding separations close to 135°, 90° and 45°. It is clear that the maxima corresponding to the target passing the detector do not change in position. The Nirfast reconstruction in Figure 10c supports the observation that multiple illumination/collection angles gives greater insight as to the location of the target.

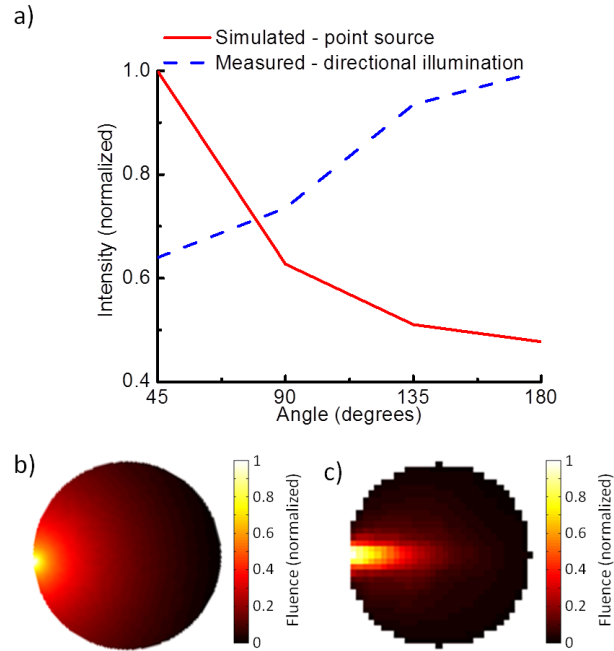


Figure 11) a) Illumination fluence at the phantom border at four different angles relative to the point of illumination. Solid line: calculated fluence from the radiative transport equation. Dashed line: measured fluence using a tissue phantom (0.1% Intralipid, no targets). b) Illumination structure for an idealized point source. c) Ray tracing simulation showing the illumination structure for a directionalized laser source.

Although one target is predicted, ‘shadowing’ occurs in regions not occupied by the target. The primary cause of this stems from a discrepancy between how illumination is modeled and how the phantom is actually illuminated by our instrument. The radiative transport equation is forced to assume a perfect point source for illumination – for measurements over long distances with samples with high scattering coefficients and fiber-launched illumination in contact with the sample, the effective angle of illumination is very large and, after travel, many scattering events will occur, making a point-source illumination approximation very appropriate. In this experiment, a collimated beam is used as the source, meaning that the illumination is highly directionalized within the sample. The difference between these two models is illustrated in Figure 11a, which compares the photon fluence at four points on a homogeneous phantom as simulated in Nirfast and measured using the experimental setup. It is immediately apparent that these two models are not equivalent. With a point source illumination, photon density at any position in the phantom is directly proportional to the distance from the source. Collection at 45° relative to the source is more intense than 90°, etc. In the experimental setup, fluence is greatest at a collection point 180° relative to the source, which is the exact opposite of the simulation. In this particular experimental setup, the source directionality, scattering level, and measurement distance are such that the assumption of photon diffusion behavior does not hold.

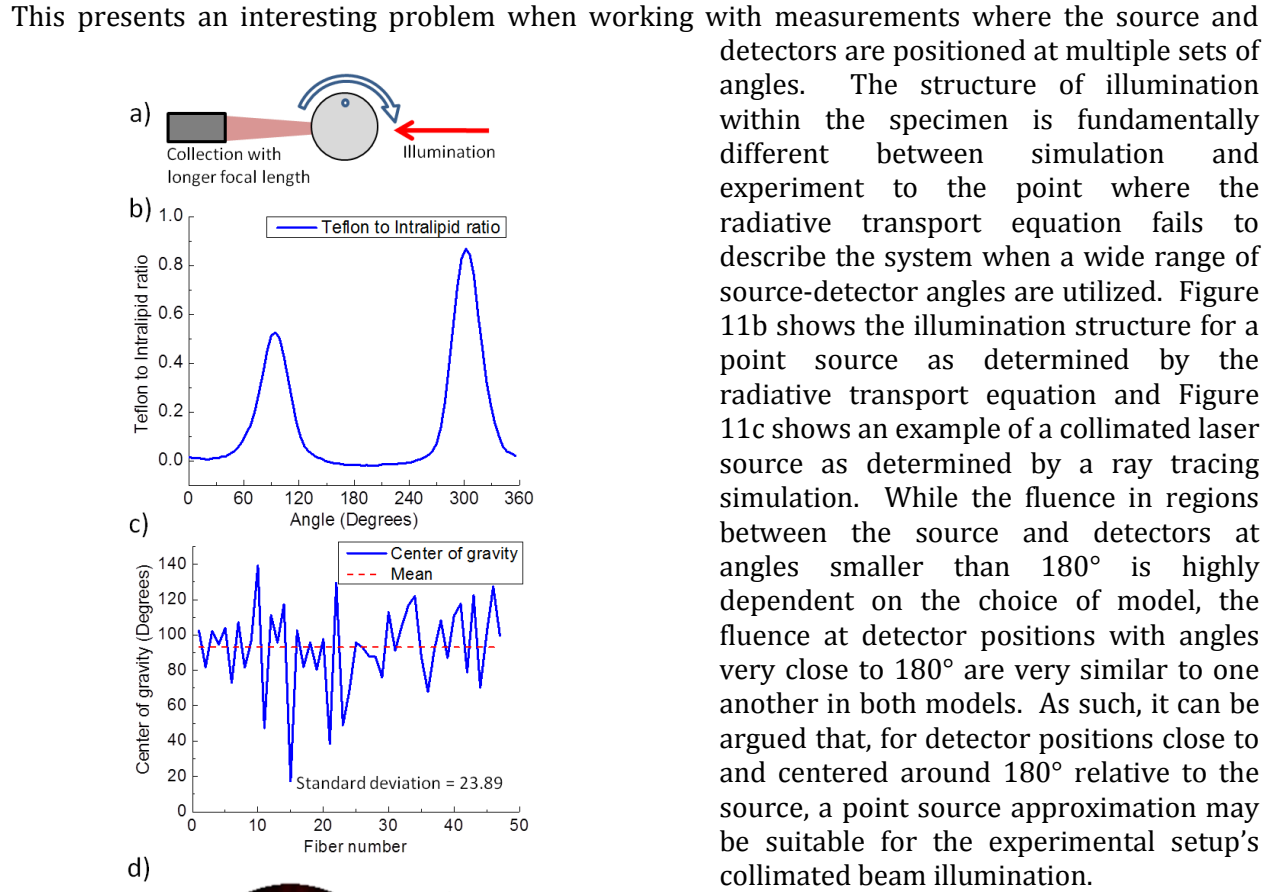


Figure 12) a) Schematic indicating a longer detector focal length and, in turn, a larger collection area by the detector. b) PTFE to Intralipid Raman signal ratio averaged over all fibers. Due to the larger area of collection, the peak corresponding to the target passing the detector is broader than the peak corresponding to the target passing the source. c) Fiber optic center of gravity is much more varied when the area of collection is increased, possibly leading to more angular information during collection. d) Nirfast reconstruction using 10 individual fibers spanning the length of the fiber pattern per rotation angle. One target is predicted with no shadowing.

detectors. This reasoning is confirmed in Figure 12c, in which the standard deviation of the peak

position for all fibers is increased to 23.9. The wider spacing of the fibers implies that more angular information is collected. Upon performing a Nirfast reconstruction using 10 individual fibers spaced across the width of the fiber pattern (and, as a result, tenfold the number of data points as compared to a single detector at 180° from the source), the image in Figure 12d is generated. A single target is predicted with minimal ‘shadowing’ artifacts seen from collecting at angles smaller than 180° from the source, indicating that errors resulting from an incorrectly predicted illumination structure are reduced when source-detector angles are large and span a small range.

While it has been demonstrated that the correct number of targets (and an approximation of target position) can be recovered using this large fiber pattern setup, the validity of this technique cannot be determined unless a) the separation of two closely-spaced targets and b) the accurate determination of the positions of these targets can be demonstrated. In order to do this, three changes were made to the experiment summarized in Figures 8c and 12a: two 1/16” diameter spheres (instead of one 1/8” diameter sphere) were embedded in the phantom with close spacing ( $\leq$  sphere diameter), ‘fluorescence’ Nirfast reconstructions were used (as to separate PTFE and Intralipid responses and normalize each to a simulated blank), and micro-CT was performed on each phantom in order to determine the exact target positions.

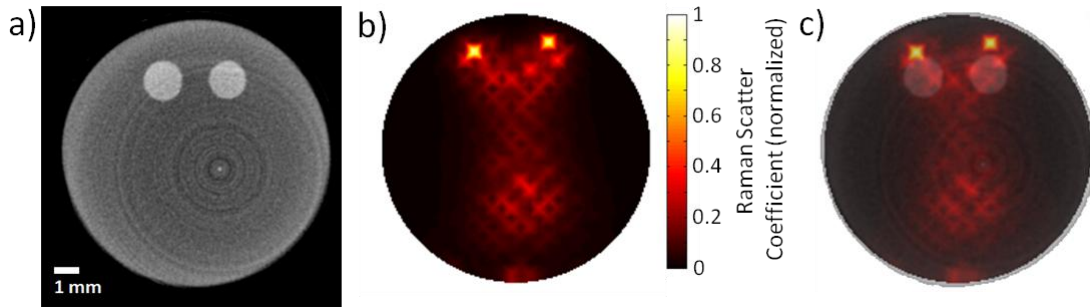


Figure 13) a) Micro-CT reconstruction of the phantom with two PTFE spheres. b) Nirfast reconstruction. c) Micro-CT and Nirfast reconstruction overlay.

Figure 13a shows the micro-CT reconstruction of a phantom with two small embedded PTFE spheres, illustrating their small separation relative to target size. Figure 13b shows the Nirfast reconstruction using data from the Raman tomography experiment. Two closely-spaced targets are predicted with some shadowing seen in the center of the reconstruction. In order to determine how accurate the positions and spacing of these predicted targets are, Figure 13c shows an overlay of the micro-CT reconstruction atop the Nirfast reconstruction. We see that the error in the position of each target is less than 1mm.



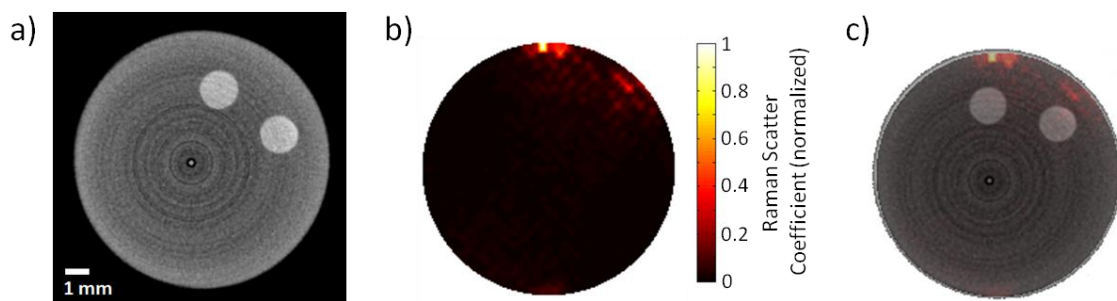


Figure 14) a) Micro-CT reconstruction of phantom with two targets and an increased (0.5%) Intralipid content. b) Nirfast reconstruction. c) Micro-CT and Nirfast reconstruction overlay.

The 0.1% Intralipid phantoms are opaque to the eye, but have only about 1/5 the scattering power of some epithelial tissues.<sup>9</sup> The next step towards translating this method to tissue measurements is to increase the scattering level of the phantoms fivefold to 0.5% Intralipid. The same experiment as shown in Figure 13 was performed on a phantom consisting of 0.5% Intralipid. Figure 14a shows the micro-CT reconstruction of the phantom, Figure 14b shows the Nirfast reconstruction, and Figure 14c shows the overlay of the two. It is immediately noticeable that the positions of the targets are not correct. Although the angular spacing between the targets is correctly reconstructed, their positions are ‘projected’ onto the edge of the phantom. While the width of these projections are similar to the widths of the PTFE spheres, the ‘depths’ of these targets cannot be resolved at this level of scattering using the current instrumentation and reconstruction methods.

## B: Monte Carlo simulations

Thus far it has been shown that Raman tomography reconstructions with Nirfast can provide reasonable size and position information for buried spheres. As experimental parameters become more ‘extreme,’ such as a fivefold increase in the scattering power of the medium, reconstruction accuracy is rapidly degraded. Consideration on the improvement of reconstruction accuracy begins with an exploration of factors which limit reconstruction quality. Three general causes for poor reconstructions that will be discussed here include not acquiring enough total data (absolute undersampling), not acquiring enough unique data (spatial undersampling), and misinterpreting acquired data (incorrect modeling of system response).

Iterative image reconstruction of this sort often falls under the regime of ill-posed inverse problems, meaning that the number of unknown variables to be solved (the number of pixels in the resulting mesh) is larger than the number of known variables (data points collected). When the number of measurements performed meets or exceeds the number of pixels in the resulting mesh, a direct solution is theoretically possible. In any case, increasing the number of measurements increases the maximum potential reconstruction quality. At the same time, care must be taken to ensure that each of these measurements contributes an amount of unique or orthogonal information to the resulting data set. An increase in the absolute number of measurements cannot improve reconstruction quality if these new data points do not add new information to the resulting data set. With the end goal of determining accurate spatial distributions, the combination of source and detector sizes and positions needs to be intelligently chosen such that no region of the specimen is poorly probed or under-sampled as compared to the specimen as a whole.

These first two issues, both related to under-sampling, can be addressed to a certain degree without the use of computer modeling or an exact knowledge of the system response. The total number of measurements to acquire can be chosen based on the desired number of pixels in the reconstruction mesh (or vice-versa), whereas choosing a wide range of different source-detector configurations lends itself to probing a number of different regions of the specimen. Neither of these approaches is sufficient. Without a strong knowledge of both which regions of a specimen are probed in a given source-detector configuration and the collection efficiency of each configuration, it is not possible to determine the effectiveness of a given instrument setup. With such knowledge, an ideal instrument configuration can be determined and the maximum reconstruction quality can be predicted.

Knowledge of source-detector responses with regards to a given specimen (system-analyte response) can be determined through the computer modeling of photon fluence. This is precisely what happens during a reconstruction using Nirfast: photon fluence from each source and the spatial collection efficiency of each detector is determined through radiative transport calculations in order to quantify the sampled region of each source-detector pairing. As mentioned previously, the use of radiative transport equations in the diffusion regime requires several assumptions about both the instrument and the specimen. One such assumption is that all sources are perfect point sources and all detectors have a numerical aperture of one (equal collection efficiency over all angles, the detector equivalent of a point source). Additionally, specimens are assumed to be heavily isotropically light scattering to the point that the movement of photons is governed by the diffusion regime.

While these assumptions sufficiently describe DOT instrumentation, instruments that are simply similar to DOT will deviate from these assumptions by some amount, and this is exemplified by the instrument described in this report. The illumination is not a point source directly in contact with the specimen, but is instead a collimated beam. Detectors are also not in contact with the specimen such that each detector's response changes as a function of the angle it makes with the specimen surface. Because of the strong directionalization of the incoming light, the scattering power of the analyte, and the small distances over which measurements are taken, the diffusion approximation does not hold (as shown in Figure 11).

Significant deviations from the idealized diffusion regime have two main impacts on Raman tomography imaging and instrument design: optimal instrumentation configuration and measurement parameters cannot be determined if accurate specimen illumination and light collection cannot be modeled, and correct reconstructions cannot be obtained if reconstruction algorithms are misinterpreting the experimental data due to the inability to accurately determine the specimen region probed for each source-detector pairing. Correcting for these differences requires abandoning the diffusion regime and its required assumptions in favor of a modeling technique that allows for more accurate descriptions of instrument sources, detectors, and light-specimen interactions.

Ray tracing through an iterative Monte Carlo script represents a solution for light modeling that accommodates a full description of an instrument's sources, detectors, and specimens without operating under the previously discussed assumptions of diffusion-regime radiative transport calculations. Such a simulation models the travel of individual photons as they are generated at a



source, enter a specimen, travel through the specimen, and eventually exit the specimen or become absorbed. The path traveled is a ‘random walk’ governed by statistical distributions determined by user-input properties of the instrument and specimen (source placement, width, and angular distribution; specimen refractive index, mean scattering length, and mean absorbance length; detector placement, width, and numerical aperture). By simulating and recording the paths of thousands of such photons, a detailed description of how the specimen is illuminated and the distribution of collected photons is generated. The power of this approach is that it is relatively simple and straightforward to ray trace individual photons and predict their behaviors during interaction with the specimen via Beer’s Law, Snell’s Law, Fresnel Principle, etc. Modeling thousands of these photons does not require additional mathematics, only additional computing power. As there is no analytical solution for the radiative transport equation outside of the diffusion regime, such a photon modeling approach represents a reasonable solution to more accurate modeling of a range of instruments and specimens.

Monte Carlo approaches are not without drawbacks. Modeling a single photon is a mildly computationally intensive iterative process; modeling thousands of photons for each source and detector can increase this computational burden by several orders of magnitude. While there have been solutions in the literature to increase computational efficiency, including modeling ‘big’ photons which undergo multiple absorbance events<sup>13</sup> and the use of graphics processing units (GPUs) for code speedup,<sup>14</sup> at the present time Monte Carlo methods take strictly more computing power than radiative transport calculations. Additionally, simulations driven by underlying random processes do not converge on an exact solution. Just as the measurement of a signal containing white noise approaches the true value as acquisition time is increased, Monte Carlo simulations approach an ideal solution as more photons are modeled, but there will always be variability in the result. Reducing this variability to an acceptable level through increased runtimes is another consideration when employing these methods. If these computational difficulties can be handled, these methods can provide a straightforward and fully customizable means of modeling specimen illumination and performing reconstructions from experimental data.

Feature	Radiative Transport + Diffusion	Monte Carlo
Photon migration	Diffusion behavior	No diffusion assumption
Source	Point sources	Directionalized (laser) illumination
Detectors	NA of 1	NA < 1

Table 1. Comparison of the three main differences between radiative transport (Nirfast) and Monte Carlo simulations. The lack of an analytical solution to radiative transport equation outside of the diffusion regime requires that photons migration mimics diffusion and that all point sources and detectors are idealized. Monte Carlo simulations do not require these assumptions, as photons can migrate outside of the diffusion regime and sources and detectors can be modeled to have small numerical apertures.

To demonstrate some of these advantages, a Monte Carlo photon ray tracing code was written in-house with Matlab. The cylindrical specimen was represented by a circular mesh (similar to that used in the Nirfast reconstructions) comprised of 709 square pixels (as compared to ~1750 triangular elements in the Nirfast reconstructions), each with a defined mean scattering length,

mean absorbance length, refractive index, etc. For the following discussion, fluence modeling was performed on a simulated homogeneous circular tissue phantom with 16 equally-spaced sources and detectors spread equally over the surface. This is often referred to as a standard ‘fan’ geometry in DOT literature.<sup>[1]</sup> For the Nirfast simulations, all sources were treated as point sources, all detectors had an effective numerical aperture of one, and photon migration occurred under the assumption of the diffusion regime. These three characteristics are required for Nirfast simulations and diffusion-regime radiative transport calculations in general. In contrast, the Monte Carlo simulations utilized directionalized laser sources, small numerical aperture detectors, and a Poissonian distribution to model scattering such that diffusion behavior was not assumed. While the assumptions required by radiative transport calculations have worked well in the DOT field, the small specimen size and directionalized laser illumination utilized in these Raman tomography experiments are not well described by these assumptions. These differences are summarized in Table 1. The images from the Monte Carlo simulation shown below look significantly more ‘pixelated’ than their Nirfast counterparts because the data are not heavily interpolated before being presented to the user.

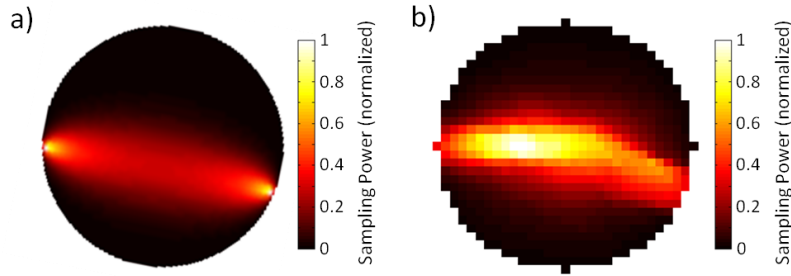


Figure 14. Simulated sampling regions of a homogeneous tissue phantom for two detectors separated by 157.5 degrees. a) Nirfast simulation with a point source, idealized detector, and diffusion-regime photon migration. b) Monte Carlo simulation modeling a directionalized laser source, a small numerical aperture detector, and non-diffusion photon migration.

Visualizing the sampling region of a single source-detector pair using the adjoint source approximation illustrates the differences between point and directionalized sources and detectors. The adjoint source approximation, employed by both Nirfast and the Monte Carlo simulation, states that if a source and a detector switch positions the detected power will remain the same as the detected photons must travel through the same region. Simulating the fluence from a source and the fluence from a detector (as though it were a source) and multiplying these two regions together shows the mutual ‘sampling’ region of the two. This approximation holds true as long as scattering is assumed to be isotropic or if the optical process bridging the two regions (spontaneous Raman scattering) is isotropic. Figure 14 depicts a homogeneous circular mesh with a source-detector pair at an angle of 157.5°. Using the adjoint source approximation, the effective sampling region for both a point source with a ‘point’ detector and a directionalized laser source with a less-than-unity numerical aperture detector are shown. The Monte Carlo simulation shows that the majority of the collected signal originates from the bulk, while in the diffusion regime the most intense signal originates from the phantom’s surface. Quantitatively, the sampling power distribution of these two regions differs by approximately 23%. These differences in sampling region are more

pronounced when all source-detector combinations are taken into account, representing the sampling region for

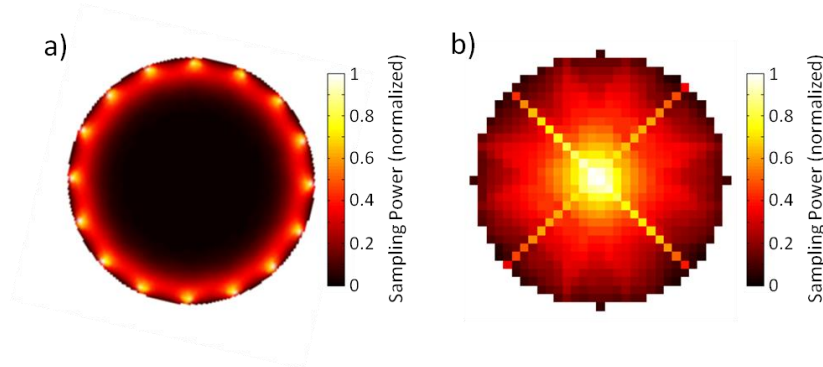


Figure 15) Simulated sampling regions from all 240 source-detector pairs for a homogeneous circular tissue phantom. A) In the diffusion regime (very high scattering, large sampling distances), the majority of the collected signal originates from near the phantom's surface. B) In a lower-scattering regime with directionalized illumination, there is a strong preference for signal originating from the bulk. An X-shaped artifact is present due to the coarse pixel mesh.

an entire experiment. The results from summing the sampling regions for all 240 source-detector combinations are shown in Figure 15. For the Monte Carlo simulation representing our Raman tomography setup, the majority of the collected signal originates from the phantom's bulk, while a diffusion regime behavior results in a collection preference for the phantom's surface. A strong preference for bulk signal agrees with previous Monte Carlo simulations regarding to transmission Raman measurements.<sup>11</sup>

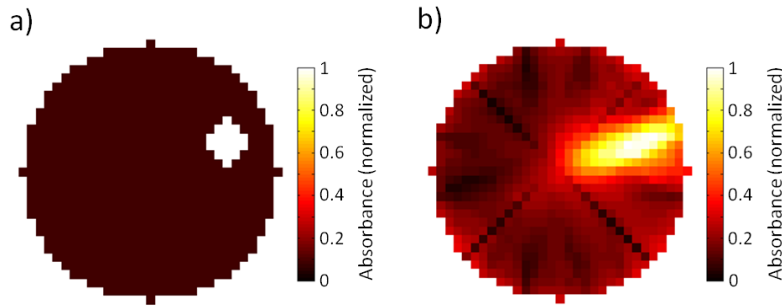


Figure 16) Monte Carlo simulations can be used for the fluence-modeling 'forward' step in an attenuation-based reconstruction. a) A homogeneous mesh with an anomalous region of absorbance that is 10x higher than the bulk. b) After five iterations, a Monte Carlo-based reconstruction algorithm can identify the region of the anomaly, albeit with artifacts.

Fluence modeling simulations through Monte Carlo methods can also be used for reconstruction purposes. Using the same mesh, a region of anomalous absorbance was added (Figure 16), simulated experimental data was generated by Monte Carlo fluence modeling, and the data was supplied to a reconstruction algorithm utilizing the same Monte Carlo method and homogeneous absorbance properties for a starting guess. It should be noted that this reconstruction type is fundamentally different from those discussed in the rest of this report, as Raman/fluorescence reconstructions investigate a photon generation process and require measured values for both the

Raman signal and the fundamental frequency, while an 'absorbance' reconstruction is attenuation based and only utilizes one data point per source-detector pair. Even so, this demonstrates that Monte Carlo fluence simulations have sufficient repeatability to be useful in reconstruction algorithms. In order to maximize this utility, processing times need to be decreased significantly through the use of graphics processing units (GPUs).

These simulation comparisons suggest that while diffuse optical tomography and Raman tomography are similar in form and function, they can differ drastically in analyte response. Radiative transport calculations have been an invaluable tool in the DOT field, as the results are highly reproducible and accurately model those experiments. Upon moving to lower scattering levels, smaller sample sizes, and the use of laser sources and small-NA detectors, the diffusion-regime radiative transport equation becomes a less accurate model. In order to develop the field of transmission Raman tomography, elegant fluence modeling simulations allowing for the accurate modeling of arbitrary sources, detectors, and sample geometries will need to be realized. Monte Carlo simulations bolstered by the processing speed of graphics processing units represent one possible means to this development.

An additional point worth adding to this report is in our collection scheme. Through the research conducted in the above experiments and through modeling we determined a fiber placed in contact with the tissue surface should provide the highest collection efficiency. The maximum collection efficiency occurs with the fiber in contact with the breast tissue. The collection efficiency of a fiber optic probe (the absolute number of photons that reach the CCD camera) increases when the fiber is in direct contact with the tissue as opposed to collection through a distance of air via a focusing lens. The two phenomena that govern this effect, Fresnel reflection and numerical aperture, are primarily functions of the refractive indices of tissue ( $n \sim 1.3-1.5$ )<sup>15</sup>, silica glass ( $n \sim 1.5-1.6$ ), and air ( $n = 1$ ). The magnitude of Fresnel reflections at the boundary of two materials decreases as the difference between the materials' refractive indices ( $\Delta n$ ) approaches zero. First, eliminating a 'layer' of air between tissue and the fiber probe reduces the number of interfaces at which reflections occur. Furthermore, the difference in refractive index for a tissue-fiber boundary ( $\Delta n \sim 0$  to  $0.3$ ) is smaller than either a tissue-air boundary ( $\Delta n \sim 0.3-0.5$ ) or an air-fiber boundary ( $\Delta n \sim 0.6$ ). In addition, the effective numerical aperture (or collection angle) of a fiber optic or lens increases as the refractive index interfacing with the specimen increases. Just as an oil-immersion microscope objective has a larger numerical aperture than a standard objective that operates in air<sup>16</sup>, 'immersing' the tissue in a refractive index  $n \sim 1.5-1.6$  medium by directly interfacing the fiber and the tissue increases both the collection angle and the total number of photons coupled into the fiber. Therefore in our instrument's design we have included breast paddles with slots for positioning fibers so that we are able place individual fiberoptics in direct contact with the skin's surface.

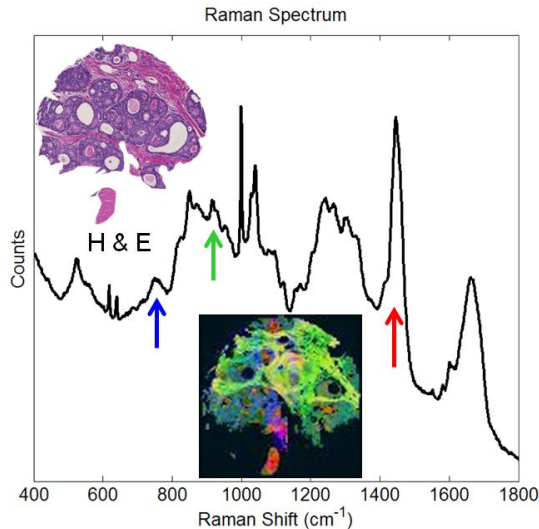


Figure 17) Raman image of a breast tissue biopsy and corresponding H&E Serial section

#### Task 1.4 Justification of correlations (month 13-18):

This task was successfully completed. Data from year 1 was analyzed and additional Raman images were acquired to further understand the complex Raman signal observed from the different cell types that make-up breast tissue. Through Raman imaging the chemical contrast achieved through various spectral bands is apparent. The Raman image displayed in figure 17 is comprised of a red, green, and blue pixels corresponding to the intensities of 3 Raman bands ( $781\text{ cm}^{-1}$  shift in blue,  $936\text{ cm}^{-1}$  shift in green, and  $1450\text{ cm}^{-1}$  shift in red.) The contrast observed in an H&E serial section is mirrored in the Raman image. The challenge lies in identifying the different tissue types and then comparing the different Raman signals to determine the spectral source of the contrast. While a first pass at identifying this contrast was completed in year 1, here the additional imaging experiments are in support of these results

By acquiring a Raman image and then observing histological stains of serial sections we can choose pixels

that are over the desired cell-types. As a simple example, we are able to distinguish epithelium from stromal tissue by masking-out only the tissue type of interest and then looking at the Raman spectrum of only that tissue type. This approach is illustrated in figure 18. We first collect a Raman image and then compare it to a serial section stained with H&E. The serial section allows us to identify which tissue structures are present in the Raman image. We then identify and mark the pixels that correspond to epithelium and to stromal tissue. We are able to then categorize all the spectra that are associated with stromal tissue and all the spectra that are associated with epithelial tissue and thus compare the differences in the spectra and compare that to the literature.<sup>17,18</sup>

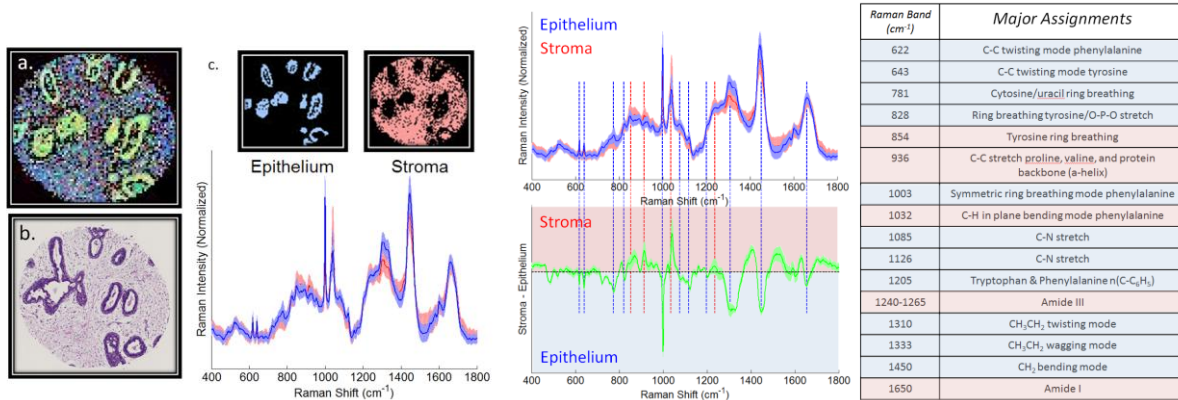
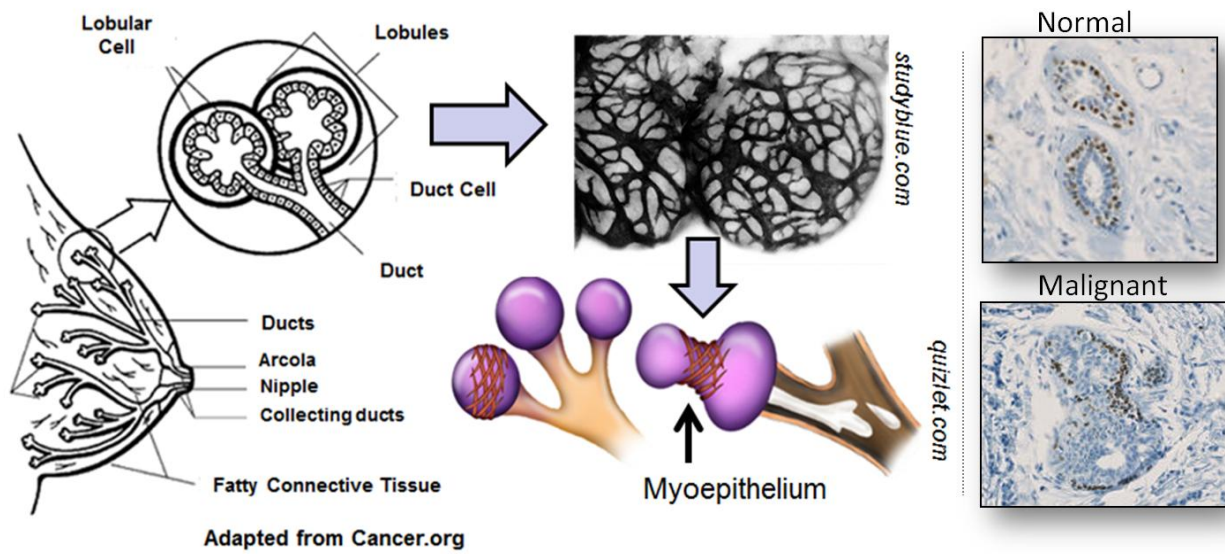


Figure 18) a. Raman image from an unstained tissue biopsy b. serial section H&E c. corresponding cell type masks and spatially recovered spectra along with the difference spectra (green) and band assignments

While the spatial distribution of epithelium and stromal tissue is of diagnostics importance, the clinical utility of imaging these two components alone is not significant. A significant tissue with diagnostic utility is myoepithelium.<sup>19,20</sup> As depicted in figure 19, myoepithelium is comprised of a mesh-like network that surrounds lobules and ducts. These cells have the ability to contract in order to secrete milk from the lobule into the duct.





They are present in healthy breast tissue even if a woman is not lactating. Myoepithelial cells are on the order of 1-2 micrometers thick and are not visualized with H&E staining. These cells are a main diagnostic marker for determining whether suspect tissue is benign or malignant. A pathologist will use the immunohistochemical stain P63 to specifically visualize these cell types.<sup>21</sup> A P63 stain of normal vs malignant lesion is illustrated in figure 19. Myoepithelial cells are stained a dark brown color. The normal tissue has a continuous layer of myoepithelial tissue surrounding the lobules. In the malignant case, the myoepithelial layer is discontinuous and this would be diagnosed as an invasive carcinoma.

Using the same masking approach described in figure 18. We collected high resolution images of a biopsy section to determine if Raman spectroscopy has the chemical contrast to be able to discern myoepithelial tissue from epithelium and stromal tissue. From the comparison of Raman spectra between masked regions several bands of contrast are evident. In figure 20, the masked regions were determined by looking at H&E, P63, and SMA stained serial sections. The Raman spectra were then averaged between the marked sections to identify differences in the spectra. To visualize the chemical distribution within the tissue, three bands were chosen and those pixels were marked as red, green, and blue pixels. The resulting Raman image shows the contrast achieved by these 3 spectral bands. The resulting image is segmented well into the three components highlighted by the stained tissue. This

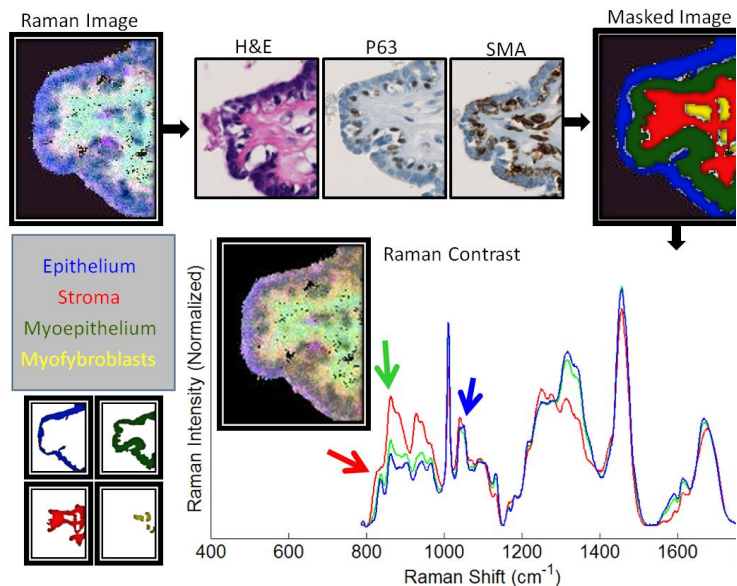


figure demonstrates the ability to obtain label free contrast of myoepithelial cells using Raman spectroscopy. This is an exciting prospect because Raman is conducive to in vivo measurements and the identification/quantification of myoepithelium is an extremely important diagnostic marker. We have sufficient data with spontaneous Raman to put together a manuscript; however we aim to increase our statistical power by increasing our image data-set using a higher speed complementary technique.

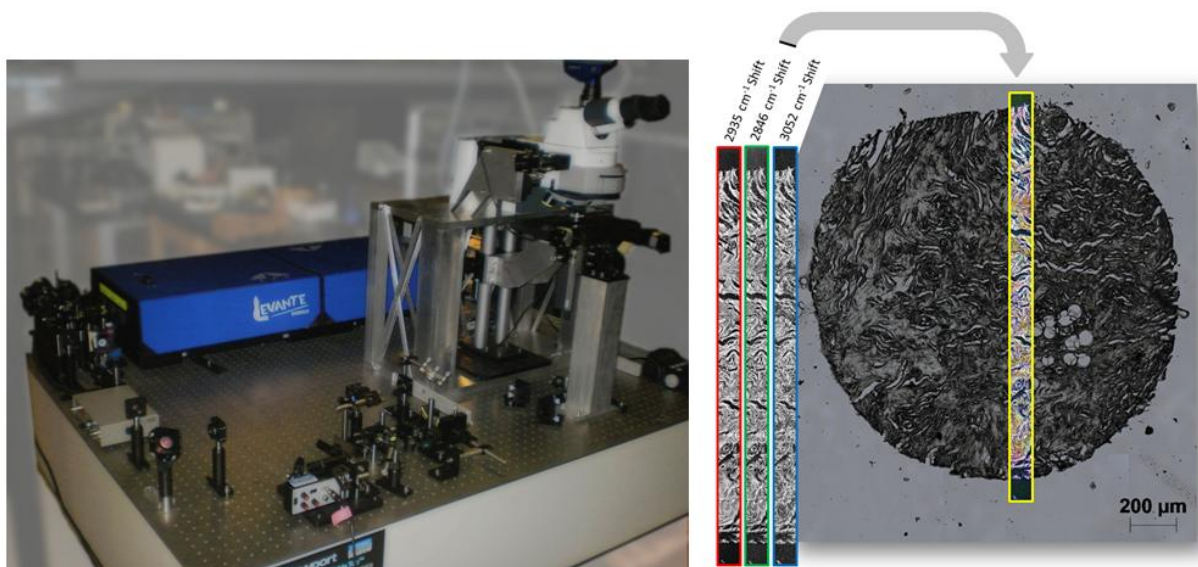


Figure 21) Preliminary data for future work made possible by the study we report here

To explore myoepithelial band assignments further, as future work, we are interested in collecting large images of multiple biopsy sections using stimulated Raman spectroscopy (SRS)<sup>22,23</sup>. The information gained from the spontaneous Raman imaging give us insight into which spectral bands are worth pursuing in order to gain cellular/tissue type contrast. With SRS imaging we are able to collect large image areas on the order of 1mm squared in about one hour per band. This same size would take days to weeks with spontaneous Raman approaches severely limiting the practical statistical power we can achieve. However before one is able to do SRS it is important to know which spectral bands will give chemical contrast. The spontaneous Raman images presented above along with some others we have collected give us a good starting point to conduct an SRS study. As a first step towards this effort we have built and are currently optimizing an SRS microscope for the evaluation of Breast tissue. A photo of this instrument and some preliminary data are depicted in figure 21.

#### Task 1.5 Classification Algorithm (month 19-30):

To complement the Raman data that was acquired, Mid-IR Spectroscopy was used to develop classification algorithms<sup>24</sup>. Similar to the Raman approach, stains were employed to identify regions of pathological significance. A modified Bayesian classification algorithm was used with spectral metrics to calibrate a transfer function on identifying epithelial cells, fibroblast rich stroma, collagen rich stroma, myofibroblast rich stroma, blood, necrosis, lymphocytes, and mucin pixels. Multiple students and postdocs worked on developing this classification algorithm and to-date we have trained on ca.250 breast tissue biopsy specimen and validated on an additional ca.250 breast tissue biopsy specimen. Early results from the validation set are presented in figure 22. Training was performed by taking a 5μm tissue section for FT-IR imaging and then taking serial sections which were stained using multiple special and IHC stains. IR pixels corresponding to deduced cell types were identified (>500,000 pixels) for training. This was further validated on an entirely separate cohort of over 200 patients. An average Area Under the Curve (AUC) for cell type classification of 0.93 using 33 spectral-metrics was achieved in the training array and 0.91 AUC for the validation array. Figure 22, demonstrates the potential of FT-IR imaging coupled with this Bayesian classifier to reduce the burden on the pathologist with the ability to accurately classify the cell types in the example

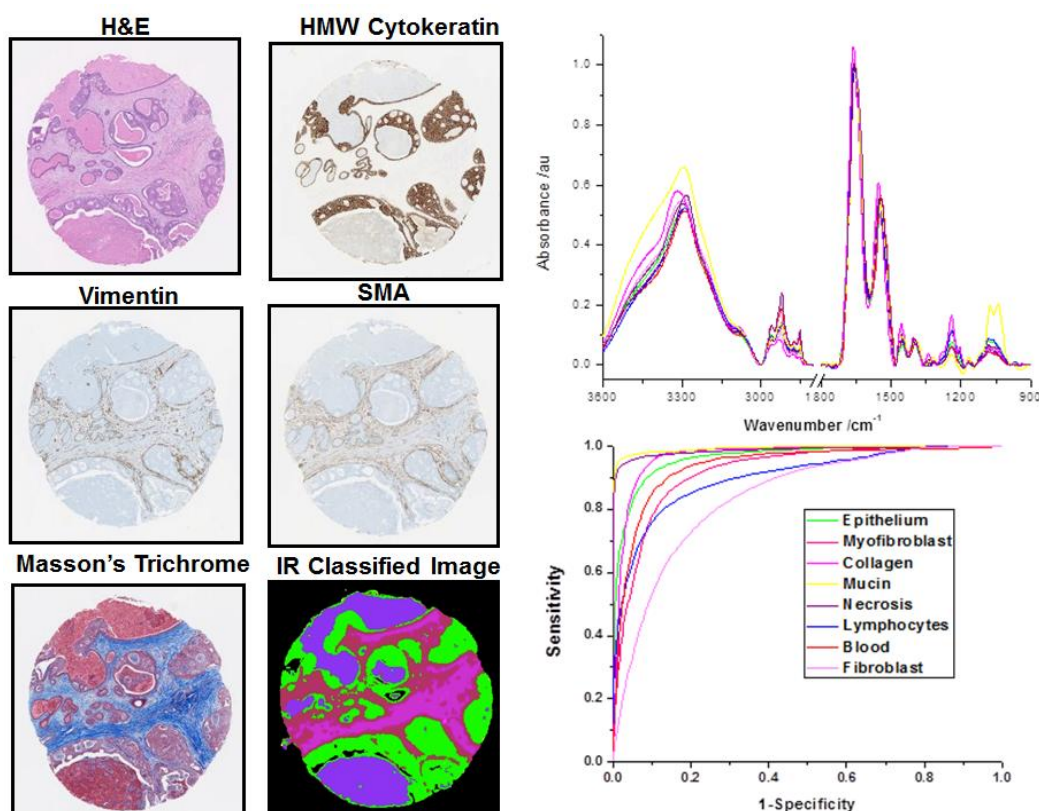


Figure 22) Example of a Bayesian tissue classification result and the validation results

core from a single unstained IR classified tissue section. To otherwise identify the cell types within this example core would have involved a panel of 5 stains to be performed with the pathologist then deducing cell types based on the pattern of positive and negative staining.

With this imaging technology, one aim is to improve or classification accuracy. However we are limited by the spatial resolution of our instrumentation. Some of my effort was spent improving the optics and alignment of our FTIR imaging instrumentation<sup>25</sup>. The results from this work successfully improve our classification accuracy as we are able to obtain proper sampling of the specimen in the microscopes field of view. Figure 23 illustrates the improved classification as highlighted by the red arrows. In this figure the green pixels have been classified as epithelium and the pink pixels have been classified as stromal tissue. By improving the spatial resolution the structure of the tissue-type distribution becomes clearer and will lead to more accurate diagnosis. For example in figure 8, the standard IR approach leads to the appearance of masses of epithelium. A mass of epithelium tissue generally warrants a closer look, such as additional staining to look for the presence or absence of myoepithelial cells. However, on inspection of the HDIR image the tissue looks normal and there would be no need for further investigation as the epithelial cells are simply part of a

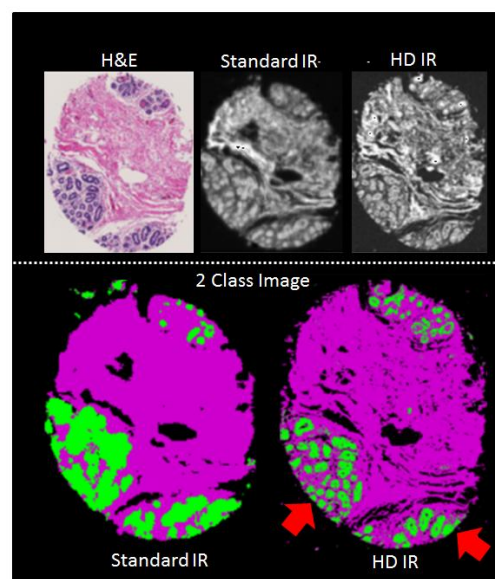


Figure 23) High Definition IR imaging leads to better classification



terminal ductal lobular unit that are a normal part of breast anatomy.

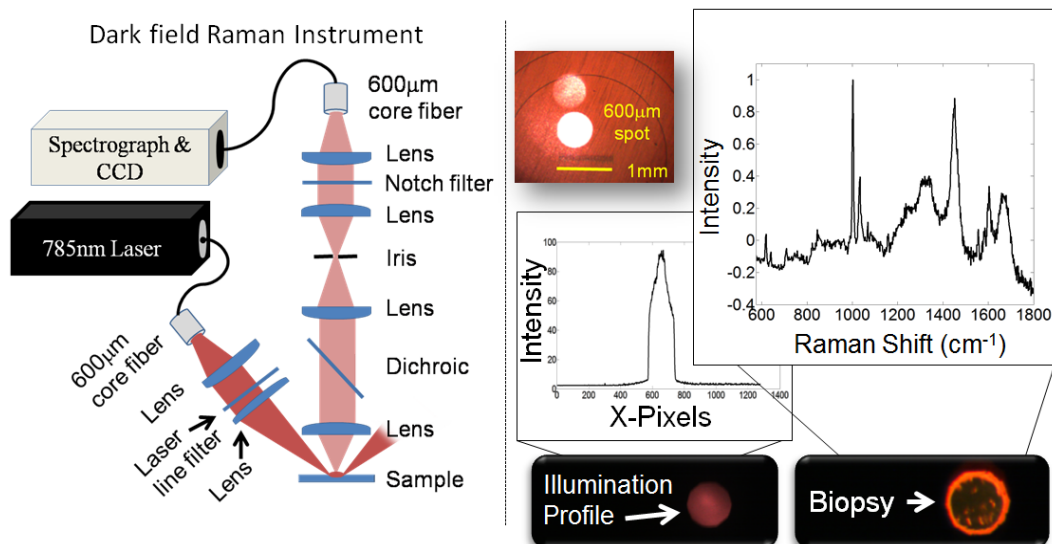


Figure 24) Dark field Raman schematic and characterization for large spot Raman spectroscopy of tissue biopsies

This tissue type classification algorithm that we have developed and validated is extremely useful for Raman experiments to look into the classification accuracy of Raman spectroscopy which is something we will need to understand as we progress into *in vivo* work with Raman. Towards the development of a Raman classification model we have built an instrument to collect a single Raman spectrum from a millimeter or smaller sectioned biopsy specimen. The IR classification model described above is used as a reference to determine the number of cell types that are present for a given core specimen. We can then use that information to train an algorithm to quantify the number of cell types that exist under the Raman field of view. In addition to training for cell types that are present we are also able to train for disease states, ie hyperplasia, dysplasia, malignant, benign.

The instrumentation has been built and characterized using archived tissue that was present in the lab from completed experiments. A schematic of the instrument is depicted in figure 24. The Raman excitation is incident at angles oblique to the collection optics. This leads to only collecting Raman signal from the scattered light and as a result rejects the subsurface signal<sup>26</sup>. In the configuration presented here we adjusted the collection aperture to

collect light from a spot size of 600 micrometers. We have also optimized the system for collection from a 1mm biopsy specimen. The data in figure 24 shows the illumination profile, which we would want to be as top-hat shaped as possible, along with the Raman spectrum of a biopsy section placed in this profile.

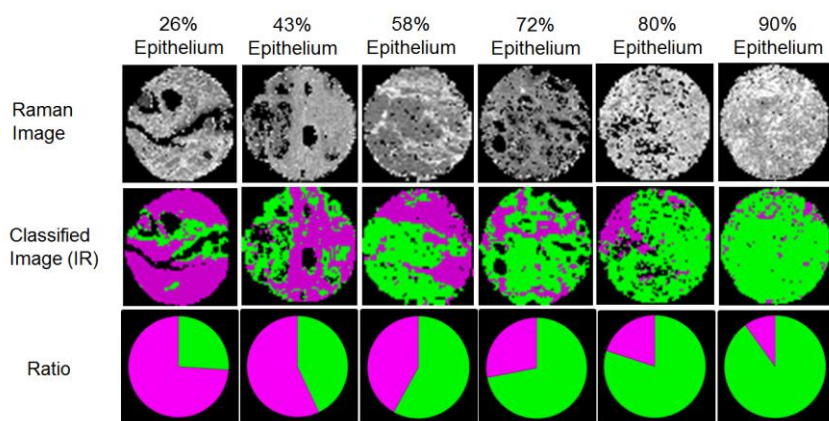


Figure 25) (top) Raman images of biopsy specimens with varying ratios of epithelium and stromal tissue (middle) classified IR images illustrating the distribution of epithelium and stromal tissue. (bottom) the ratio of epithelium and stromal tissue quantified by the IR classification

The information we anticipate to obtain from this single Raman spectrum is illustrated in figure 25. While one approach is to collect images and understand the distribution of tissue in order to diagnose disease, perhaps simply obtaining the representative chemical information is enough as this would be the type of information obtained with Raman tomography as the technique has low spatial resolution, but high chemical specificity. Therefore, by using the IR images and classification algorithm described in figure 22, we can quantify the percentage of epithelium as compared to total area of the image giving us an epithelium to stromal tissue ratio. With this ratio as a reference value we are able to develop a transfer function that will take an input a Raman spectrum and calculate the percentage of epithelium in the core it was collected from. Some preliminary results for this technique are presented in figure 26. A leave-one-out cross-validation model was employed to evaluate the technique's ability to quantify multiple cores for epithelium. In this example we are able classify a biopsy core for the % epithelium with an error of about 13%. Work is currently underway with a larger sample size to quantify biopsy cores for the 8 tissue types described in the classifier above (figure 22). In addition evaluating tissue types we are also using this approach to classify disease diagnosis. This work is currently underway and will continue in future efforts.

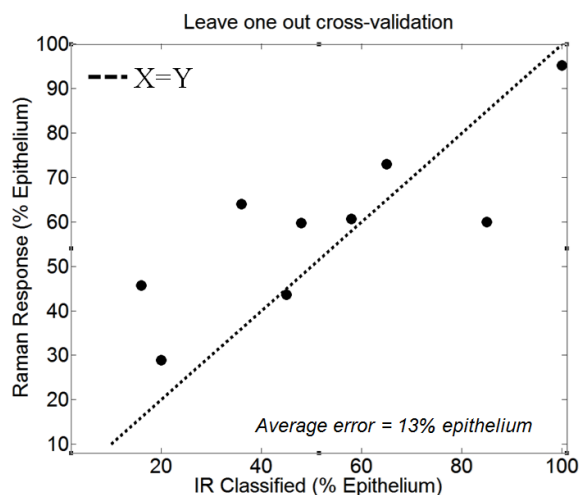


Figure 26) Single spectrum Raman calibration model for predicting % epithelium from a biopsy specimen

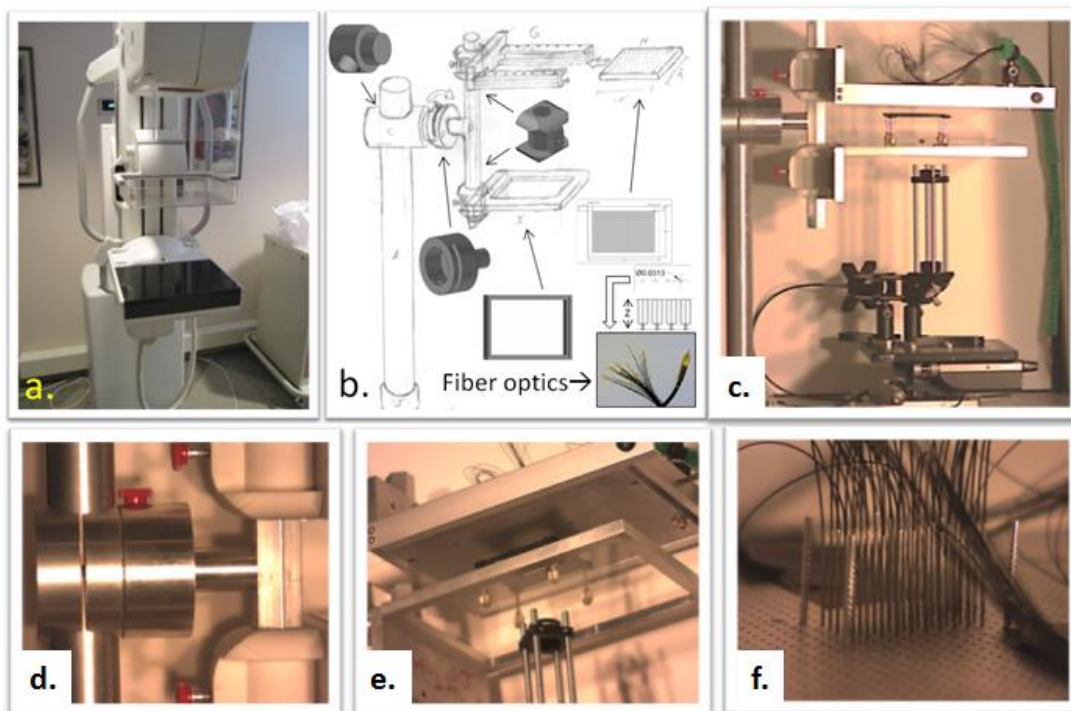


Figure 27) a) Photo taken at Provena Covenant Medical Center of a mammogram instrument b) Conceptual design and AutoCAD files for a breast cancer screening Raman instrument c) a photograph of the prototype instrument d) 0-90 degree hinge and adjustable paddles e) View looking up from the bottom plate e) collection fibers

### Task 2.3 Construction of Instrumentation and calibration standards (month 13-18):

All major instrumentation and components have been purchased and are assembled. The Raman tomography instrument design is depicted in figure 27a and 27b (this is the same figure reported in the year 1 updated).

Photographs of the constructed instrument are now included in figures 27c-27f. The Raman excitation light enters into the sample at the bottom plate (figure 27e). After the excitation light travels through the sample it is collected by the optical fibers that can be freely arranged for mapping purposes. The illumination arm is also freely adjustable and is combined with automated translation stages for control in the x and y dimension. The depicted instrument configuration illuminates all 50 fibers independently resulting in 2500 spectra all with known coordinates for illumination and collection. The light from the collection fiber travels to a Raman spectrograph as depicted in figure 28.

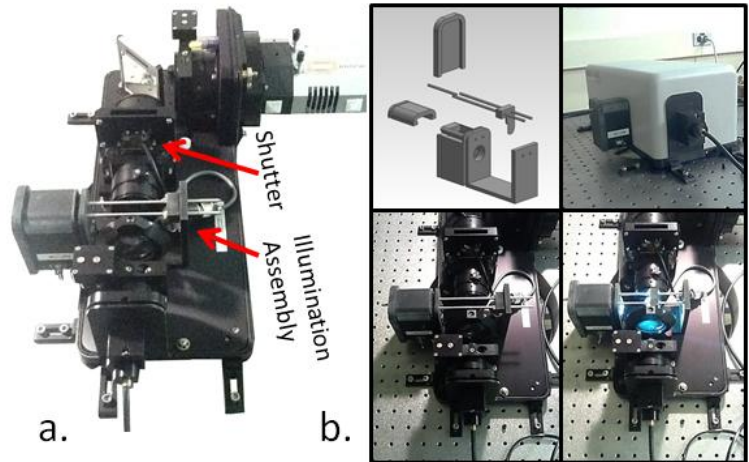


Figure 28) a) Modified spectrograph b) Solid works rendering and photos of the illumination assembly

At the spectrograph the fibers are transposed into a line and the collected light travels through a pre-stage notch filter. The collected light is then focused through a 100x1000 micrometer slit and is then collimated. Finally, the signal is dispersed onto a CCD. The spectrograph depicted in figure 28 was modified to include a home-built internal illumination source. This is a white-light LED with a pull lever that allows us to illuminate through the fibers to see where the collection regions will be on the sample. This is useful in sample alignment. For each fiber

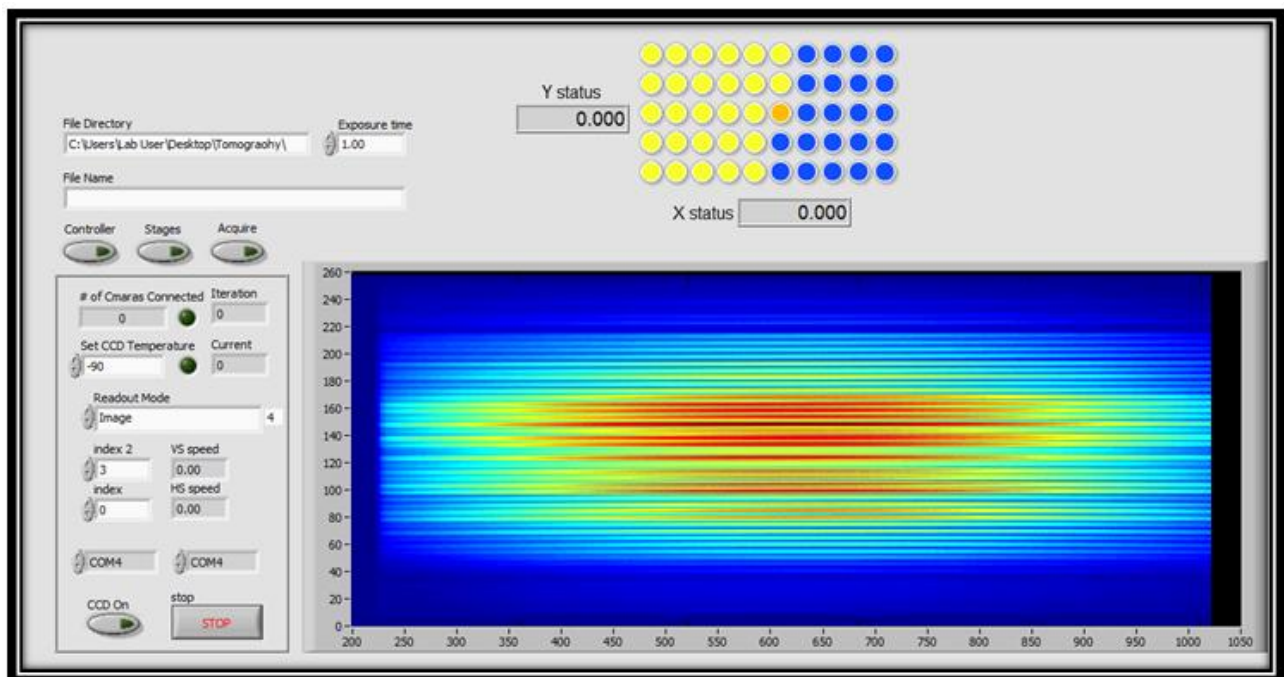


Figure 29) Screenshot of LabView front panel and data collected from white light illumination of all fibers



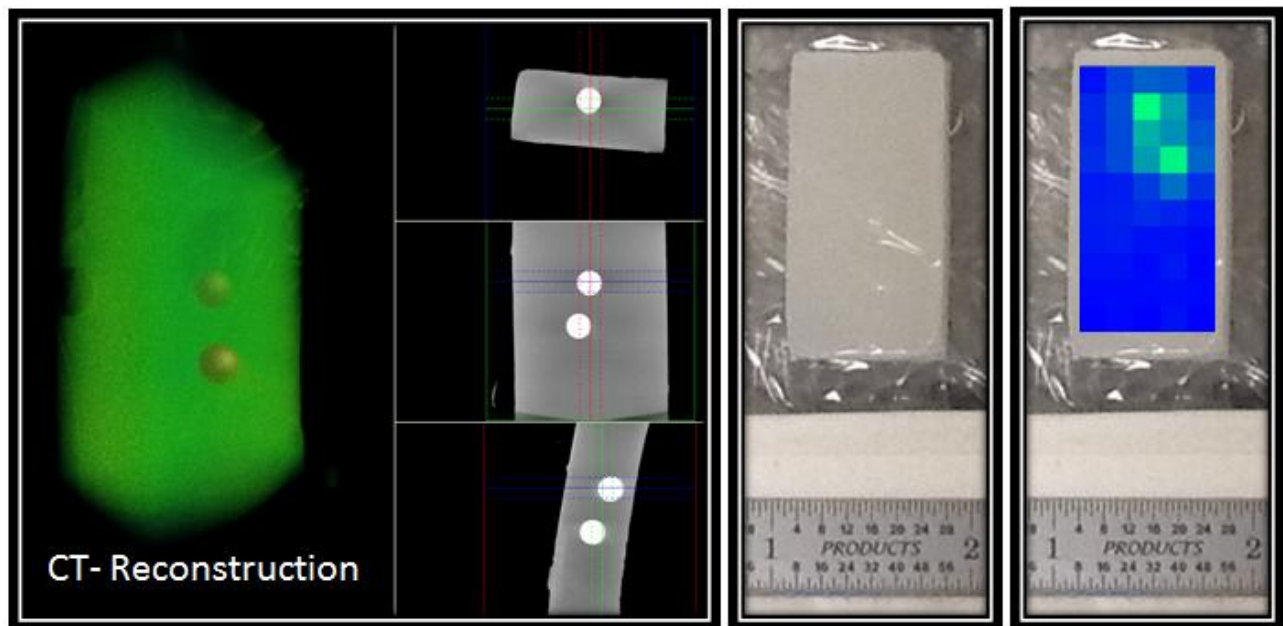


Figure 30) (left) a computed tomography reconstruction of an Intralipid tissue phantom (center) and image of the tissue phantom (right) a transmission Raman pixel map collected with the instrument depicted in figure 12 illustrating the location of the Teflon inclusions

we have mapped the positional correspondence of where the fiber is on the top paddle grid and where the fiber enters the spectrograph. The entire instrument is controlled by LabView and is now completely automated. A screen shot of the current LabView front panel and a CCD frame of all the fibers is illustrated in figure 29. A sample can be put into the instrument and the illumination point will be translated according to the specified stage coordinates. The Completed positions are then marked as yellow, the current position is marked as orange, and the future positions are marked in blue.

To aid in aligning the tomography instrument and processing the resulting data, simple Intralipid and agar phantoms were fabricated. As an example the phantom in figure 30 was an agar phantom with 0.1% Intralipid dispersed through the agar, The target for this phantom was two Teflon sphere place 3mm apart. We verified the location of the spheres using computed tomography. The center image of figure 30 depicts a photograph of the Intralipid phantom and it is clear that the two spheres are not visible. We then put the phantom on the tomography instrument and mapped-out the fiber signals. It is clear from figure 30 that the location of the spheres has been determined by the Raman instrument. A manuscript is preparation for this work and we are currently optimizing our reconstruction methods for the new instrument design.

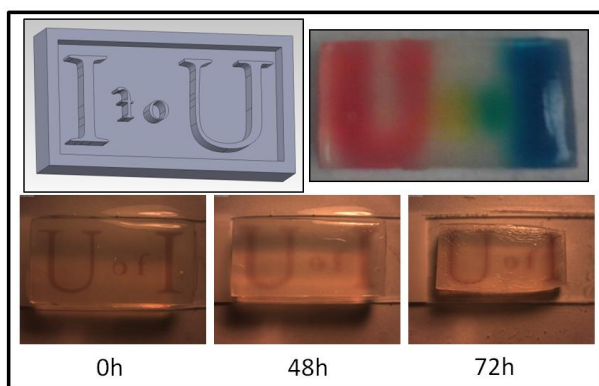


Figure 31) U of I tissue phantom to investigate storage conditions and shelf-life

#### Task 2.4 Collect data using more realistic tissue phantoms (month 19-24):

Tissue phantoms with a reasonable shelf life (1-2weeks) and more geometrical accuracy are important steps to developing and characterizing the tomography instrument. This has proved challenging. As depicted in figure 31, we observe two

significant problems. The first is that the phantoms evaporate quickly resulting in a change in their dimensions and optical properties. Second, any liquid inclusions, such as dyes, pigments, or nanoparticles, tend to diffuse and spread-out throughout the phantom thus blurring any structure intentionally introduced into the phantom. Several experiments are currently underway to investigate approaches to mitigating these two experimental challenges. To-date we have been able to make the evaporation no-long an issue. We simply vacuum seal the phantom in a thin polyethylene film. This preserves the phantom's structure and does not interfere with the Raman signal. The diffusion of liquid inclusions is still an on-going challenge. We have considered including 3-D printed sugar structures as inclusions to avoid the use of liquids.

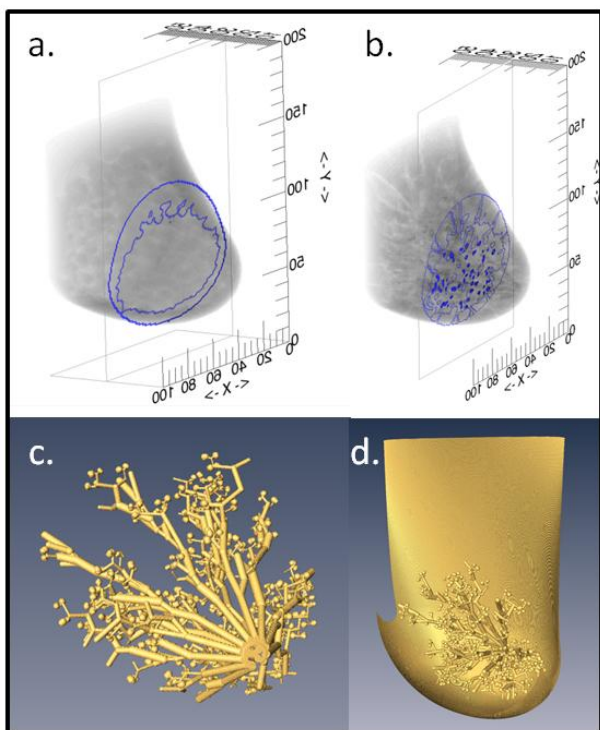


Figure 32) a) IDL in silico model b) IDL in silico model highlighting ductal structures c) Isolated ductal system d) Breast phantom model

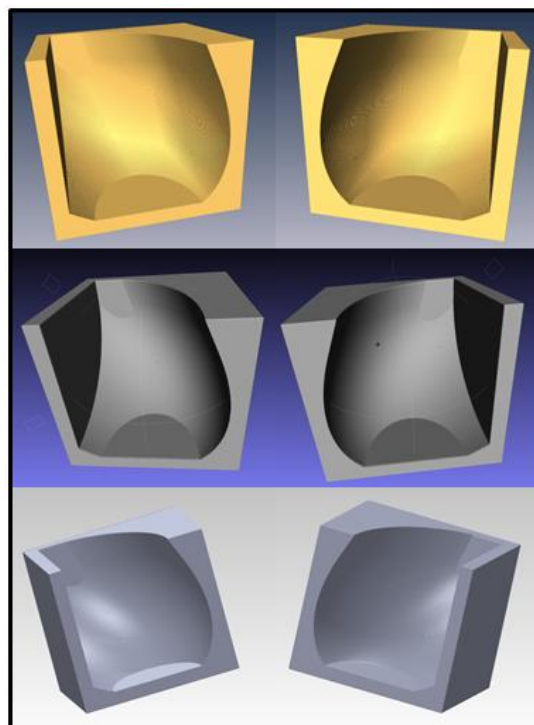


Figure 33) The breast mold rendered in Amira (top) Meshlab (middle) and Solid Works (Bottom)

More accurate tissue phantoms also were constructed. Using a model based on breast CT-scans we constructed a scalable 3-D model of a breast in IDL<sup>27</sup>. We were able to highlight isolate the various structural components including ducts and lobules. The shape of these structures can therefore be either independently molded or printed with a 3-D printer. For our early work here we started-off by molding the outer shape of the breast with plans to include internal structure in future work. An image of the IDL in silico model and isolated ducts and lobular structures are depicted in figure 32 and 33. This model is scalable so that we can change the size of the molded phantoms and the correlated structure will scale proportionally.

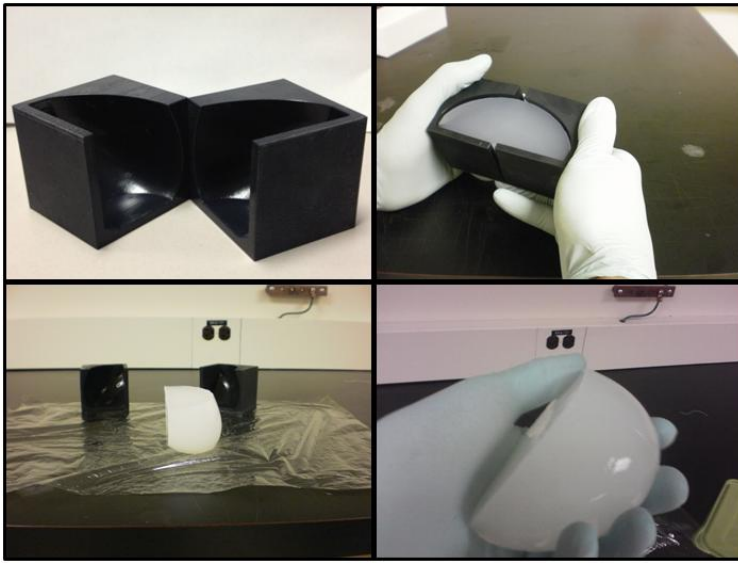


Figure 34) 3-D printed Breast phantom mold and an agar intralipid molded tissue phantom

The size and shape of the breast structure was then exported from IDL into matlab to image in 2-D slices. This allowed us to generate a RAW file format that was readable by Amira as a 5x5x10cm array which was necessary to create a surface stereolithography file format (stl). The stl file was then simplified using MeshLabs, followed by Solid works. The solid works file was then 3-D printed to create the Breast phantom mold. The resulting breast phantom mold is depicted in figure 34. We have successfully molded agar Intralipid tissue phantoms using this mold. Raman

tomography measurements of these phantoms along with the creation of inclusions representing internal structures are currently underway and will continue with future graduate students.

### Future Work:

The work present here has developed a nice foundation and platform for a wide variety of Raman tomography studies. The Raman breast paddles are entirely modular and can be configured in systematic configurations to study light propagation and resulting Raman spectra. Our breast phantoms and inclusions are becoming more sophisticated in structure and we are studying the potential Raman contrast agents to include in these tissue phantoms. The work currently being continued by a first year graduate student includes 1) studying the pigment diffusion in the gel phantoms to characterize diffusion rates with efforts towards preserving the phantoms shelf-life. 2) Work is being carried-out to develop a 3D tissue phantom printer to construct geometry's that cannot be molded. 3) Soybeans are being considered as an inclusion because they have very similar spectral properties to tissue and it is possible to obtain soybeans with varying amino acid levels. The use of soybeans as a targeted inclusion would allow for the characterization of spectral sensitivity as a function of light scattering (ie. Can we discern to spectrally similar targets positioned next to each other and to what degree must these target be spectrally different in order to tell them apart). 4) The addition of physiologically relevant absorption and fluorescent pigments will be studied to determine what effect they have on our spectral and spatial resolution. 5) Stimulated Raman images are being acquired on breast tissue containing myoepithelial cells. This is in an effort to increase the statistical power from the work detailed in figure 20.

#### KEY RESEARCH ACCOMPLISHMENTS:

- Became familiar with clinical practices associated with breast cancer screening, breast cancer histology, how breast tissue is sampled and biopsied for diagnosis, and breast cancer pathology.
- Built-up a comprehensive database consisting of micrographs and IR spectral images for identifying breast tissue histology and tissue chemistry. This database contains tissue cases diagnosed as hyperplasia, dysplasia, malignant carcinomas, and normal tissue.
- Using this database we identified several locations on each biopsy to acquire Raman measurements
- Acquired Raman measurements on all biopsy sections as well as several surgical resections.
- Identified Raman spectral bands that can be used for distinguishing between different tissue types.
- Used the information obtained from the point Raman measurements to achieve cell-level contrast in Raman spectral images
- Used clinical observations and interaction with clinicians to develop a conceptual design for a Raman Tomography instrument aimed at breast cancer screening.
- Put together autoCad files and have begun construction on the instrument
- Evaluated existing diffuse optical tomography algorithms for Raman tomography and have adapted a Monte Carlo framework for Raman tomographic reconstruction
- Investigated through modeling and experimentation different instrument configurations and have implemented the transmission fan style configuration into our instrument design
- Determined that a fiber in-contact with tissue should give us the maximum collection efficiency
- Through Raman imaging we identified spectral markers correlated with epithelial tissue and stromal tissue.
- Through Raman imaging we demonstrated chemical contrast capable of resolving myoepithelial tissue which is an important diagnostic marker for malignant cancer.
- Contributed effort to build a stimulated Raman microscope for faster Raman imaging towards imaging larger data sets with myoepithelial tissue.
- Worked with an infrared classification model to classify 8 different tissue types present in breast tissue. This information will be used for calibrating and validating large-spot Raman acquisitions from biopsy sections.
- Improved spatial resolution achieved in Raman imaging of biopsy sections for improved tissue classification.
- Built a large-spot dark field Raman instrument for acquiring a single spectrum from a breast tissue biopsy and have collected a data set with ~80 biopsy cores.
- Built a Raman tomography instrument.
- Modified an existing Raman spectrograph to include white light illumination.
- Wrote labview software to control and automate the Raman tomography instrument.
- Collected Raman tomography data from tissue phantoms with Teflon inclusions
- Developed methods for tissue phantom fabrication and storage
- Developed a molding approach for geometrically accurate tissue phantoms

#### REPORTABLE OUTCOMES:

- **6 publications (See appendices for bibliography and reprints)**
  - **Discrete Frequency Infrared Microspectroscopy and Imaging with a Tunable Quantum Cascade Laser** - This work investigates the use of a tunable infrared laser for imaging and is the result of efforts to improve speed and spatial resolution in the infrared imaging of breast tissue biopsies.
  - **High-definition infrared spectroscopic imaging** - This manuscript is indirectly a result of this work in that we were trying to obtain high resolution IR images for identifying the tissue chemistry of biopsies. This information was employed in determining regions for Raman point measurements.
  - **Off-resonance surface-enhance Raman Spectroscopy from gold nanorods suspensions as a function of aspect ratio: not what we thought** - This work investigates the optimal plasmon resonance for a colloidal suspension of surfaced enhanced Raman spectroscopy nanoparticles. This is significant for our tomography work as these nanoparticles could be potential contrast agents for inclusion in phantoms or potentially as contrast agents in vivo.
  - **Competition Between Extinction and Enhancement in Surface Enhanced Raman Spectroscopy** - This paper investigates the counterintuitive insight that the Raman signal vanishes when nanoparticles are excited at their plasmon resonance, while increasing nanoparticle concentrations at off-resonance excitation sometimes leads to decreased signal. This is significant for our tomography work as these nanoparticles could be potential contrast agents for inclusion in phantoms or potentially as contrast agents in vivo
  - **Surface-Enhanced Raman Spectroscopy of Polyelectrolyte-Wrapped Gold Nanoparticles in Colloidal Suspension** - This work investigates shape dependent response of colloidal suspensions in surfaced enhanced Raman spectroscopy. This is significant for our tomography work as these nanoparticles could be potential contrast agents for inclusion in phantoms or potentially as contrast agents in vivo.
  - **Real-time interactive data mining for chemical imaging information: application to automated histopathology** - This manuscript was the result of looking for spectral correlations in different tissue types and reports an approach for efficient visualization of such a data set.
- **Two manuscripts are in preparation (See appendices for drafts)**
  - **Large infrared absorbance of biomaterial microcantilevers based on silicon high contrast gratings** -this manuscript investigates the use of a using an atomic force microscopy cantilever to obtain both structural and spectroscopic contrast from a sample. The work is being extended to gain topology and chemical information from tissue. The cantilever itself could be used as a next generation infrared detector that does not need to be cooled and is conducive to an array configuration which has potential in clinically relevant instrumentation for imaging diagnostics.
  - **Discrete-frequency infrared spectroscopic microscopy with narrow-bandwidth high-contrast guided resonance photonic crystal slab filters** - This manuscript employs optical filters for doing infrared spectroscopy. These filters are intended to replace and interferometer in compressed sensing instrumentation



designed for looking at tissue biopsies and classifying tissue types for automated histopathology.

- **5 Presentations (see appendices for abstracts)**

- Oct. 2011- **Poster Presentation** 46<sup>th</sup> Midwest Regional ACS Meeting, Saint Louis MO
- Feb. 2012- **Oral Presentation** at the University of Michigan, Ann Arbor
- March 2012 – **Poster presentation** at the University of Illinois Chicago Cancer Center Forum
- October 2012 - **Oral Presentation** at SciX (Formally called FACSS –Federation of Analytical Chemistry and Spectroscopy Societies)
- May 2013 – **Oral Presentation** at The American Chemical Society's Central Michigan Regional Meeting

## CONCLUSION:

The work presented here has developed a nice foundation and platform for a wide variety of Raman tomography studies. The Raman breast paddles are entirely modular and can be configured in systematic configurations to study light propagation and resulting Raman spectra.

We have made good progress towards the research described in the approved statement of work for years 1 and 2 of this research program. We now have a working relationship with local clinicians and have become familiar with clinical practices associated with breast cancer screening, breast cancer histology, how breast tissue is sampled and biopsied for diagnosis, and breast cancer pathology. We have built-up a comprehensive database consisting of micrographs and IR spectral images with identified breast tissue histology and tissue chemistry. This database has tissue showing cases diagnosed as hyperplasia, dysplasia, malignant carcinomas, and normal tissue. Using this database we have identify several locations on each biopsy to acquire Raman measurements and have acquired Raman measurements on biopsy sections as well as several surgical resections. Through careful analysis we have identified Raman spectral bands that can be used for distinguishing between different tissue types and have applied those Raman spectral bands to achieve cell-level contrast in Raman spectral images.

We now have a working knowledge of some important Raman spectral bands to achieve chemical contrast between tissue types including epithelium, stroma and myoepithelium. We have a plan to collect larger data-sets with stimulated Raman imaging. We can validate the tissue-types that are present in our biopsy samples with infrared imaging through classification algorithms developed for breast tissue. Our infrared imaging capabilities now include higher spatial resolution imaging which should lead to better classification.

Additionally, we have used clinical observations and interaction with clinicians to develop a conceptual design for a Raman Tomography instrument aimed at breast cancer screening. From this conceptual design we put together autoCad files and have begun construction on a prototype instrument for conducting Raman tomography on breast tissue. We have built a Raman tomography instrument and have collected data on light scattering tissue phantoms and polymer inclusion. The tomography instrument is automated and controlled by labview code. For Raman tomographic

reconstruction, we have evaluated existing diffuse optical tomography algorithms for specifically for Raman measurements and have adapted a Monte Carlo framework for our Raman tomographic reconstruction. Through modeling and experimentation we characterized different instrument configurations and have implemented the transmission fan style configuration into our prototype instrument design which uses fiber-optics in-contact with tissue to give the maximum collection efficiency. With these accomplishments we are closer to achieving prototype instrument capable of Raman tomography in breast tissue. We are excited to continue this work in year 2.

Finally we have made good progress towards developing geometrically accurate tissue phantoms and plan to include accurate internal structures. With these accomplishments we are closer to realizing the capabilities of Raman tomography in breast tissue.

## References

1. Pogue, B.W.; McBride, T.O.; Osterberg, U.L.; Paulsen, K.D. Comparison of imaging geometries for diffuse optical tomography of tissue. *Optics Express* **1999**, *4*, 270-286.
2. Flock, S.T.; Jacques, S.L.; Wilson, B.C.; Star, W.M.; Van Gemert, M.J.C. Optical properties of intralipid: A phantom medium for light propagation studies. *Lasers Surg. Med.* **1992**, *12*, 510-519.
3. Mourant, J.R.; Fuselier, T.; Boyer, J.; Johnson, T.M.; Bigio, I.J. Predictions and measurements of scattering and absorption over broad wavelength ranges in tissue phantoms. *Appl. Opt.* **1997**, *36*, 949-957.
4. Cubeddu, R.; Pifferi, A.; Taroni, P.; Torricelli, A.; Valentini, G. A solid tissue phantom for photon migration studies. *Phys. Med. Biol.* **1997**, *42*, 1971-1979.
5. Collier, T.; Arifler, D.; Malpica, A.; Follen, M.; Richards-Kortum, R. Determination of epithelial tissue scattering coefficient using confocal microscopy. *IEEE Journal on Selected Topics in Quantum Electronics* **2003**, *9*, 307-313.
6. Durduran, T.; Choe, R.; Culver, J.P.; Zubkov, L.; Holboke, M.J.; Giammarco, J.; Chance, B.; Yodh, A.G. Bulk optical properties of healthy female breast tissue. *Phys. Med. Biol.* **2002**, *47*, 2847-2861.
7. Gibson, A.P.; Hebden, J.C.; Arridge, S.R. Recent advances in diffuse optical imaging. *Phys. Med. Biol.* **2005**, *50*, R1-R43.
8. Siewerdsen, J.H.; Jaffray, D.A. Optimization of x-ray imaging geometry (with specific application to flat-panel cone-beam computed tomography). *Med. Phys.* **2000**, *27*, 1903-1914.
9. Dehghani, H.; Eames, M.E.; Yalavarthy, P.K.; Davis, S.C.; Srinivasan, S.; Carpenter, C.M.; Pogue, B.W.; Paulsen, K.D. Near infrared optical tomography using NIRFAST: Algorithm for numerical model and image reconstruction. *Communications in Numerical Methods in Engineering* **2009**, *25*, 711-732.
10. Everall, N.; Matousek, P.; Macleod, N.; Ronayne, K.L.; Clark, I.P. Temporal and spatial resolution in transmission raman spectroscopy. *Appl. Spectrosc.* **2010**, *64*, 52-60.
11. Everall, N.; Priestnall, I.A.N.; Dallin, P.; Andrews, J.; Lewis, I.A.N.; Davis, K.; Owen, H.; George, M.W. Measurement of spatial resolution and sensitivity in transmission and backscattering raman spectroscopy of opaque samples: Impact on pharmaceutical quality control and raman tomography. *Appl. Spectrosc.* **2010**, *64*, 476-484.
12. Matousek, P.; Everall, N.; Littlejohn, D.; Nordon, A.; Bloomfield, M. Dependence of signal on depth in transmission Raman spectroscopy. *Appl. Spectrosc.* **2011**, *65*, 724-733.

13. Wang, L.; Jacques, S.L.; Zheng, L. MCML - Monte Carlo modeling of light transport in multi-layered tissues. *Comput. Methods Programs Biomed.* **1995**, *47*, 131-146.
14. Alerstam, E.; Svensson, T.; Andersson-Engels, S. Parallel computing with graphics processing units for high-speed Monte Carlo simulation of photon migration. *J. Biomed. Opt.* **2008**, *13*,
15. Parrish, J.A. New concepts in therapeutic photomedicine: Photochemistry, optical targeting and the therapeutic window. *J. Invest. Dermatol.* **1981**, *77*, 45-50.
16. Hell, S.; Reiner, G.; Cremer, C.; Stelzer, E.H.K. Aberrations in confocal fluorescence microscopy induced by mismatches in refractive index. *J. Microsc.* **1993**, *169*, 391-405.
17. Stone, N.; Kendall, C.; Smith, J.; Crow, P.; Barr, H. Raman Spectroscopy for Identification of Epithelial Cancers. *Faraday Discuss.* **2004**, *126*, 141-157.
18. Stone, N.; Kendall, C.; Shepherd, N.; Crow, P.; Barr, H. Near-infrared Raman spectroscopy for the classification of epithelial pre-cancers and cancers. *J. Raman Spectrosc.* **2002**, *33*, 564-573.
19. Hu, M.; Yao, J.; Carroll, D.K.; Weremowicz, S.; Chen, H.; Carrasco, D.; Richardson, A.; Violette, S.; Nikolskaya, T.; Nikolsky, Y.; Bauerlein, E.L.; Hahn, W.C.; Gelman, R.S.; Allred, C.; Bissell, M.J.; Schnitt, S.; Polyak, K. Regulation of In Situ to Invasive Breast Carcinoma Transition. *Cancer Cell* **2008**, *13*, 394-406.
20. Livasy, C.A.; Karaca, G.; Nanda, R.; Tretiakova, M.S.; Olopade, O.I.; Moore, D.T.; Perou, C.M. Phenotypic evaluation of the basal-like subtype of invasive breast carcinoma. *Modern Pathology* **2006**, *19*, 264-271.
21. Barbareschi, M.; Pecciarini, L.; Cangi, M.G.; Macrì, E.; Rizzo, A.; Viale, G.; Doglioni, C. p63, a p53 homologue, is a selective nuclear marker of myoepithelial cells of the human breast. *Am. J. Surg. Pathol.* **2001**, *25*, 1054-1060.
22. Min, W.; Freudiger, C.W.; Lu, S.; Xie, X.S. Coherent nonlinear optical imaging: Beyond fluorescence microscopy. *Annual Review of Physical Chemistry* **2011**, *62*, 507-530.
23. Freudiger, C.W.; Min, W.; Saar, B.G.; Lu, S.; Holtom, G.R.; He, C.; Tsai, J.C.; Kang, J.X.; Xie, X.S. Label-free biomedical imaging with high sensitivity by stimulated raman scattering microscopy. *Science* **2008**, *322*, 1857-1861.
24. Fernandez, D.C.; Bhargava, R.; Hewitt, S.M.; Levin, I.W. Infrared spectroscopic imaging for histopathologic recognition. *Nat. Biotechnol.* **2005**, *23*, 469-474.
25. Reddy, R.K.; Walsh, M.J.; Schulmerich, M.V.; Carney, P.S.; Bhargava, R. High-definition infrared spectroscopic imaging. *Appl. Spectrosc.* **2013**, *67*, 93-105.
26. Schulmerich, M.V.; Reddy, R.; Kodali, A.K.; Elgass, L.J.; Tangella, K.; Bhargava, R. Dark field Raman microscopy. *Anal. Chem.* **2010**, *82*, 6273-6280.

27. Mahr, D.M.; Bhargava, R.; Insana, M.F. Three-dimensional in silico breast phantoms for multimodal image simulations. *IEEE Trans. Med. Imaging* **2012**, *31*, 689-697.

## APPENDICES:

*Personnel receiving pay from this research effort: Matthew Schulmerich*

Paper 1: Kole, Matthew R; Reddy, Rohith K.; Schulmerich, Matthew V.; Gelber, Matthew K.; Bhargava, Rohit; Discrete Frequency Infrared Microspectroscopy and Imaging with a Tunable Quantum Cascade Laser, *Analytical Chemistry*, (2012), DOI 10.1021/ac302513f

Paper 2: Reddy, Rohith; Walsh, Michael; Schulmerich, Matthew; Carney, P. Scott; Bhargava, Rohit; High-definition infrared spectroscopic imaging, *Applied Spectroscopy*, (2013), 67(1), 93-105, DOI 10.1366/11-06568

Paper 3: Sivapalan, Seant; DeVetter, Brent M; Yang, Timothy K.; Van Dijk, Thomas; Schulmerich, Matthew V.; Carney P. Scott; Bhargava, Rohit; Murphy, Catherine J.; Off-resonance surface-enhance Raman Spectroscopy from gold nanorods suspensions as a function of aspect ratio: not what we thought, *ACS Nano* (2013), DOI 10.1021/nn305710k

Paper 4: Dijk, Thomas van; Sivapalan, Sean T.; DeVetter, Brent M.; Yang, Timothy K.; Schulmerich, Matthew V.; Murphy, Catherine J.; Bhargava, Rohit; Carney, P. Scott; Competition Between Extinction and Enhancement in Surface Enhanced Raman Spectroscopy, *J. Phys. Chem. Let.* (2013), 4(7), DOI: 10.1021/jz4005043

Paper 5: Sivapalan, Seant; DeVetter, Brent M; Yang, Timothy K.; Schulmerich, Matthew V.; Bhargava, Rohit; Murphy, Catherine J.; Surface-Enhanced Raman Spectroscopy of Polyelectrolyte-Wrapped Gold Nanoparticles in Colloidal Suspension, *J. Phys. Chem. C*, (2013), 117(20), DOI: 10.1021/jp402392y

Paper 6: Mayerich, David; Walsh, Michael; Schulmerich, Matthew; Bhargava, Rohit; Real-time interactive data mining for chemical imaging information: application to automated histopathology, *BMC Bioinformatics* (2013), 14:156 DOI:10.1186/1471-2105-14-156

Manuscript 1: Large infrared absorbance of biomaterial microcantilevers based on silicon high contrast gratings –this.

Manuscript 2: Discrete-frequency infrared spectroscopic microscopy with narrow-bandwidth high-contrast guided resonance photonic crystal slab filters

Meeting abstract 1: Poster Presentation 46<sup>th</sup> Midwest Regional ACS Meeting, Saint Louis MO

Meeting abstract 2: Oral Presentation at the University of Michigan, Ann Arbor



Meeting abstract 3: Poster presentation at the University of Illinois Chicago Cancer Center Forum

Meeting abstract 4: Oral Presentation at SciX (Formally called FACSS –Federation of Analytical Chemistry and Spectroscopy Societies)

Meeting abstract 5: Oral Presentation at The American Chemical Societie's Central Michigan Regional Meeting

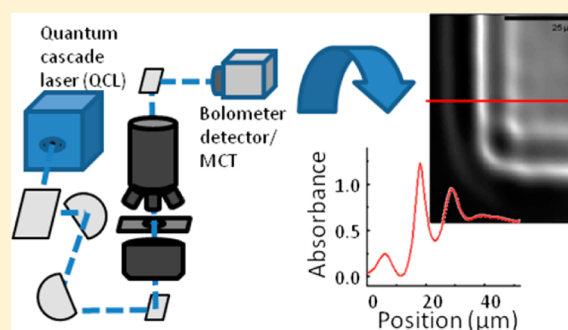
# Discrete Frequency Infrared Microspectroscopy and Imaging with a Tunable Quantum Cascade Laser

Matthew R. Kole,<sup>†</sup> Rohith K. Reddy,<sup>†</sup> Matthew V. Schulmerich,<sup>†</sup> Matthew K. Gelber,<sup>†</sup> and Rohit Bhargava<sup>\*,†,‡</sup>

<sup>†</sup>Department of Bioengineering and Beckman Institute for Advanced Science and Technology, University of Illinois at Urbana–Champaign, Urbana, Illinois 61801, United States

<sup>‡</sup>Department of Mechanical Science and Engineering, Electrical and Computer Engineering, Micro and Nanotechnology Laboratory and University of Illinois Cancer Center, University of Illinois at Urbana–Champaign, Urbana, Illinois 61801, United States

**ABSTRACT:** Fourier-transform infrared (FT-IR) imaging is a well-established modality but requires the acquisition of a spectrum over a large bandwidth, even in cases where only a few spectral features may be of interest. Discrete frequency infrared (DF-IR) methods are now emerging in which a small number of measurements may provide all the analytical information needed. The DF-IR approach is enabled by the development of new sources integrating frequency selection, in particular of tunable, narrow-bandwidth sources with enough power at each wavelength to successfully make absorption measurements. Here, we describe a DF-IR imaging microscope that uses an external cavity quantum cascade laser (QCL) as a source. We present two configurations, one with an uncooled bolometer as a detector and another with a liquid nitrogen cooled mercury cadmium telluride (MCT) detector and compare their performance to a commercial FT-IR imaging instrument. We examine the consequences of the coherent properties of the beam with respect to imaging and compare these observations to simulations. Additionally, we demonstrate that the use of a tunable laser source represents a distinct advantage over broadband sources when using a small aperture (narrower than the wavelength of light) to perform high-quality point mapping. The two advances highlight the potential application areas for these emerging sources in IR microscopy and imaging.



Fourier-transform infrared (FT-IR) spectroscopy is strongly emerging for chemical mapping and imaging<sup>1</sup> in a variety of scientific areas<sup>2–6</sup> due to technological advances since its commercial inception.<sup>7</sup> FT-IR microscopic imaging<sup>8</sup> is now well established for fast, spatially resolved spectroscopy,<sup>9</sup> using a combination of multiplexing via rapid-scan interferometry<sup>10,11</sup> and multichannel detection via array detectors. The development of multiple-element linear and faster 2D array detectors has been the principal driving force for improving widefield FT-IR microscopy via advancing hardware.<sup>3</sup> While these detector improvements have resulted in tremendous progress, sources and spectrometer advancements have not taken place at the same rate. With notable exceptions,<sup>12,13</sup> instruments use an interferometer coupled to a thermal source. Setups based on thermal sources are exceptionally efficient, stable, and commercially successful; however, practitioners have to acquire a large bandwidth of data even if they are interested in only a small set of wavelengths. A smaller set has been shown to be particularly useful, for example, in tissue classification<sup>14</sup> or for monitoring dynamic processes in polymers.<sup>15</sup> Techniques which save time by probing only bands of interest may facilitate rapid data acquisition and analyses. As opposed to FT-IR spectroscopic methods, hence, measurements of a few, selected spectral features may be desirable in some areas.

Approaches to accomplish the same may be termed discrete frequency IR (DF-IR) spectroscopy methods.<sup>1</sup> One straightforward approach to DF-IR spectroscopy and imaging is to use a grating. The use of a dispersive or scanning monochromator for IR microscopy is uncommon due to the inherent low blackbody illumination intensity at individual wavelengths, thereby forfeiting Jacquinot's advantage as well as the spectral multiplexing ( Fellgett ) advantage.<sup>16</sup> In imaging, the multiplexing advantage may be recovered somewhat by using an array detector, but a configuration in which part of the array is used for spectral and part for spatial measurements compromises the imaging potential. While sources such as a synchrotron can potentially provide the flux to overcome the throughput disadvantage,<sup>17,18</sup> a recent emphasis in the use of synchrotrons has instead been to use the brightness of the source to perform high-resolution imaging,<sup>19</sup> which would not provide sufficient flux for nonmultiplexed methods. Narrow-band filters may enable both widefield imaging and DF-IR spectroscopy but are only now maturing as a technology and are intensity limited by the coupled broadband source.<sup>20</sup>

Received: August 31, 2012

Accepted: October 31, 2012

Published: October 31, 2012

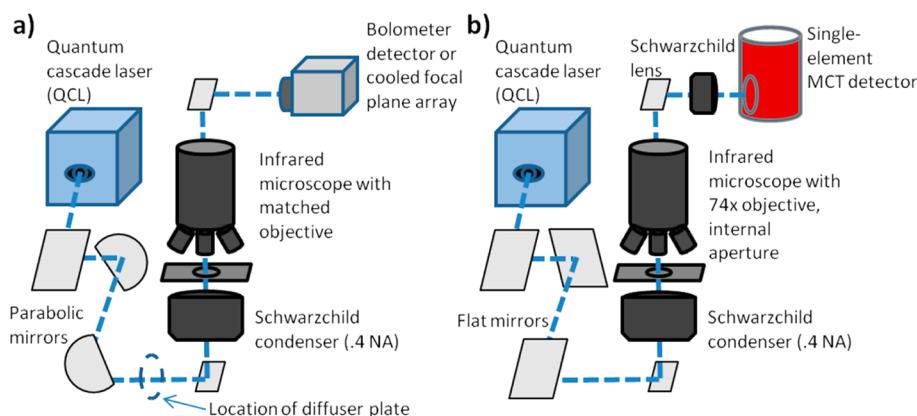


**Figure 1.** Schematics of the two DF-IR systems evaluated in these experiments. Both utilize a tunable, narrow-bandwidth mid-infrared QCL and the same infrared microscope frame. (a) QCL coupled to an uncooled bolometer camera. A parabolic mirror pair is used for 10:1 beam expansion before the microscope. For one experiment, a cooled focal plane array (FPA) was substituted for the bolometer. (b) A cooled single-element MCT detector is utilized with an adjustable aperture that focuses at the sample plane for point measurements. Flat mirrors replace the parabolic mirror pair so that the beam is not expanded.

Recently, narrow-bandwidth quantum cascade lasers (QCLs) have become available. In their most common implementation, QCLs are tunable, external-cavity mid-infrared lasers with outputs on the order of hundreds of milliwatts and grating-assisted spectral selection. First developed in the 90's,<sup>21</sup> these devices have been previously used in the detection of trace particles in gases,<sup>22</sup> wavelength-modulation absorption measurements,<sup>23</sup> and in photoacoustic spectroscopy.<sup>24</sup> Early QCLs featured too limited a spectral range to be useful for general spectroscopic analyses. While the tunable range of individual QCLs still covers only a small region of the mid-IR spectrum (for example, here we use a QCL over the range 980–1204  $\text{cm}^{-1}$ ), these devices represent emerging sources with broad tunable ranges, high power, and narrow bandwidths which are suitable for mid-IR spectroscopy. Additionally, these characteristics may render these new lasers suitable as sources for discrete frequency infrared spectroscopy or microscopy. The use of QCLs for IR imaging has been proposed and demonstrated<sup>25–27</sup> but not in a microscopy format. It is presently unclear whether QCLs offer a microscopy advantage over FT-IR imaging and what specific advances may be enabled by the higher flux. In this manuscript, we describe the use of a QCL as a source in microscopic imaging and point-mapping. By coupling the bright source to an infrared microscope, we take advantage of the laser's high power to perform imaging in a DF mode and compare the results to FT-IR imaging. We also examine whether a low-cost bolometer can be used as a widefield detector alternative to the current standard of expensive liquid nitrogen-cooled detectors. Further extending attainable data quality, we examine the possibility for high-resolution point mapping based on recent theory<sup>28</sup> using a micrometer-sized aperture. As QCLs are a coherent source, finally, we describe the implications of spatial coherence with regards to imaging.

## EXPERIMENTAL SECTION

**Instrumentation.** The instrumentation, set up in-house, consists of three main components: a narrow bandwidth ( $<1 \text{ cm}^{-1}$  spectral bandwidth over the tunable range of 980–1204  $\text{cm}^{-1}$ ) quantum cascade laser (Daylight Solutions, San Diego, CA, prototype of model UT-9), an infrared microscope (Varian Inc., Palo Alto, CA), and detectors. Two detectors were used: a

microbolometer camera with a  $324 \times 256$  pixel detector (Photon series, FLIR, Boston, MA) and a liquid nitrogen-cooled single element mercury cadmium telluride (MCT) detector (InfraRed Associates, Stuart, FL), and in a second widefield imaging configuration, we employed a cooled focal plane array (FPA) in place of the bolometer (Santa Barbara Focal Plane, Santa Barbara, CA). For widefield imaging, the output beam from the QCL was expanded 10:1 (from a 6 mm beam diameter to approximately 60 mm) via two gold-coated parabolic mirrors. The expanded beam was passed through an iris and entered the side port of the infrared microscope. In transmission mode, the beam was condensed through a 0.5 NA Schwarzschild objective lens before passing through the sample stage. The beam exiting the sample stage was collected using a matched 15 $\times$  Schwarzschild reflecting objective. The image was then passed through the microscope's open aperture and imaged onto the bolometer. For point-mapping measurements, the same configuration was used, but apertures of variable openings were placed in the beam path after the sample to restrict light to be from a defined spatial region of the sample. Beam expansion optics were removed, and the single element detector was also used in place of the array detector.

A rotating diffuser plate consisting of a one inch diameter, scratched calcium fluoride plate, and a small motor was employed in certain portions of the experiment to reduce coherence effects. When in use, it was placed between the second parabolic mirror and the iris, after beam expansion but before the microscope entrance. With the rotating diffuser in place, 64 sequential frames were acquired for each wavelength. These were averaged in order to correct for the changing position of the plate. Acquiring a series of individual frames was necessary because the limited dynamic range of the bolometer prevented integration times from being equal to one period of the diffuser rotation. Single frames were acquired for images without the diffuser. While obviously affecting the signal-to-noise ratio of the data, we do not consider this aspect here as our aim was to obtain imaging contrast.

A commercial FT-IR imaging spectrometer (Spotlight 400, Perkin-Elmer, Waltham, MA) was also used as a performance standard to compare with the instrument described above. The spectrometer was operated in rapid scan mode at a mirror speed of 1  $\text{cm/s}$ . Data were acquired and truncated to the 4000–720  $\text{cm}^{-1}$  range of interest. N–B medium apodization

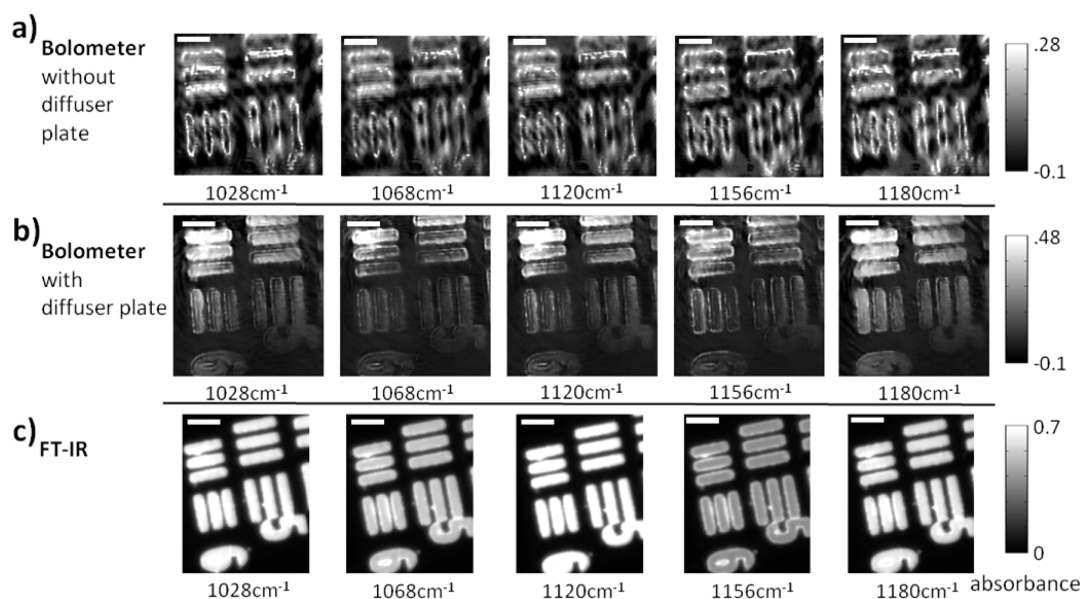


**Figure 2.** USAF 1951 optical resolution target absorption images (cycle 3, elements 5 and 6) as acquired by three different instruments. (a) QCL + bolometer system without diffuser plate. (b) QCL + bolometer system with rotating diffuser plate. (c) Commercial FT-IR instrument. Please note the differences in the color bars between the three sets of images. The scale bar in the images denotes 100  $\mu\text{m}$ .

was used for spectral transformation, and a suitable background was acquired from a region adjacent to the sample.

**Data Acquisition and Processing.** The test sample in this manuscript was a USAF 1951 optical resolution (bar) target fabricated in-house. Briefly, during the fabrication process, uncured SU-8 photoresist resin was spin-coated onto a barium fluoride substrate to a desired thickness, cured, postbaked, and solvent-developed. The target is evaluated using optical microscopy to confirm geometric fidelity. Elements 5 and 6 of cycle 3 were imaged in all instances. All image processing was performed in ENVI (ITT Visual Information Solutions, Boulder, CO) and Matlab (The MathWorks, Nantucket, MA) using code written in-house. Single-beam images had no correction applied, while absorbance images had been divided by a reference image consisting of an unmodified barium fluoride substrate. Images taken at discrete frequencies with the QCL and the bolometer also have a “dark current” chip image subtracted from both the single-beam and background images.

**Safety Considerations.** The quantum cascade laser is the single most hazardous component of the experiments outlined in this manuscript. Depending on the operating wavelength, the output can exceed 400 mW. As a well-collimated beam with a diameter of  $\sim 6$  mm, the maximum permissible exposure (MPE) of this radiation is reached in less than one second as defined by ANSI Z136.1.<sup>29</sup> Additionally, all output frequencies are invisible to the eye, adding to the potential risk of exposure. Lab personnel operating these devices should be trained in laser safety and wear high optical density (OD7+) eye protection at all times.

## RESULTS AND DISCUSSION

Optical microspectroscopy and imaging configurations to conduct experiments described in this manuscript were set up. A schematic of the two major setups is shown in Figure 1. These flexible configurations allowed us to perform a number of experiments by changing aspects of the optical train, as needed, to understand the different effects associated with using QCLs. For this preliminary study, we chose to image a USAF

1951 optical resolution bar target, which has historically been used as a standard for measuring the performance of imaging instrumentation. The target features a motif of three equally spaced rectangles which is patterned many times in decreasing sizes. The particular target used in this manuscript consisted of an approximately 10  $\mu\text{m}$  thick layer of an SU-8 polymer (which has a distinctive IR absorption spectrum) on a barium fluoride substrate (which is transparent to mid-infrared light). In all examples, we examined one region of the target: cycle 3, elements 5 and 6, which contain “bars” of widths approximately 39 and 35  $\mu\text{m}$ , respectively. This particular structure was chosen because it approaches the size limit for targets which are well-resolved by commercial FT-IR imaging instruments.

We first acquired images of the standard USAF sample using a bolometer array detector, shown in Figure 2a. Uncooled detectors have also been proposed for use in IR spectroscopic-imaging measurements, but coupling a bolometer to a global source produced exceptionally low signal-to-noise data.<sup>30</sup> The higher flux of the QCL (hundreds of milliwatts with a spectral width  $< 1$   $\text{cm}^{-1}$  versus tens of microwatts from wavelength 5–10  $\mu\text{m}$  for a typical global source<sup>31</sup>) makes imaging with a microbolometer feasible. The lower cost of the microbolometer, as well as its larger format compared to the majority of cooled array detectors available, makes this a very attractive technology. With a more even illumination, such an imaging system could compete against the established FT-IR imaging systems that usually employ a thermal source (global) and a cooled array detector. The data acquired using a QCL were compared to those acquired from a commercial FT-IR imaging spectrometer in Figure 2c. It is notable that the QCL-based system used a low-performance bolometer, while the FT-IR imaging system is the best available today in terms of signal-to-noise ratio (SNR). The data demonstrate that the coupling of a QCL to an imaging system can be achieved and presents an opportunity to compare with FT-IR imaging systems, even though the two sources are significantly different in nature.

A fine structure overlay with the target was apparent in the QCL-based data and was the most striking difference from the



FT-IR imaging data. We hypothesized that this effect arose from multiple reflections and scattering from the sample as well as etaloning, both of which were exacerbated by the spatial coherence of the laser. To alleviate this problem, we placed a diffusing element in the beam path. With the use of this diffuser (Figure 2b), the fringes and interference were not entirely eliminated but image quality was substantially improved. Such a diffuser has been used in at least one other study,<sup>32</sup> but its effect was not presented, and the effects of laser coherence on images were not shown. The diffuser employed was a transparent salt plate that was heavily scratched on one face to induce random phase shifts in the beam. Simply placing the plate in the path of the beam had little effect, as a structure to the spatial correlation in the beam was still transmitted (images not shown). As a result, the diffuser plate was rotated. Rotating the plate allows energy to be evenly distributed over the specimen, but a drawback is that multiple images have to be acquired in order to average out rotation artifacts. Images acquired by the QCL/bolometer instrument with the diffuser plate can be seen in Figure 2b. Compared to Figure 2a, the fine structure is markedly reduced. A slight shadowing effect can be seen in both sets of images, partly the result of an imperfectly aligned system and the presence of a central obscuration in all Schwarzschild objectives. Even with rotation, the collected image is a function of the exact rotational position of the plate at the time of acquisition. Scratching the plate cannot yield completely randomized scattered light in general; consequently, regions of pronounced scratches or less scratching retain some coherence and are projected through the sample and onto the bolometer. A series of 64 sequential images was captured and averaged to “smooth out” this enduring structure. As it is not a perfect solution, the “swirling” pattern caused by the rotating diffuser plate is evident in the images, but this degrades the images far less than without the diffuser in place. In addition to reducing the coherence of light, the scratched diffuser plate also causes additional scattering. This is ordinarily undesirable, as light scattered (or absorbed) by the plate cannot be used for imaging, but in this setup the losses were small compared to the available flux.

The effects of the beam's spatial coherence are clearly an issue of concern if QCLs are to be used for IR imaging. A theoretical framework to explain image formation including the light coherence is desirable. Using coherent light, every detector element ( $P'$ ) has electric field contribution, not only from the corresponding point ( $P$ ) on the sample being imaged but also from every other point around  $P$  within a radius determined by the coherence area.<sup>33</sup> If the source is coherent, photons incident at different spatial locations of the sample are in phase with one another. The electric field associated with light scattered at any point from the sample can interfere with light transmitted from other points. The amplitude of the interfered electric fields are added and quadratically encoded in the resulting intensity, which is measured by the detector. Hence, the detector image is the result of both the corresponding image that would be observed using an incoherent source as well as the effects of spatial interference. A complete description of the recorded absorbance is possible using recently developed electromagnetic theory-based models of image formation in IR microscopes and specific sample shapes.<sup>34–36</sup> Here, we extend a more recent formulation that is especially useful for examining the effects on recorded data of periodic structures in the samples.<sup>37</sup> For the purposes of simulation in this study, we modified the previously reported

framework to include beam coherence, and the resulting scattered and transmitted fields were added. To improve image quality and more accurately document the effects of coherence, the bolometer was temporarily replaced with a cooled FPA. The results are shown in Figure 3.

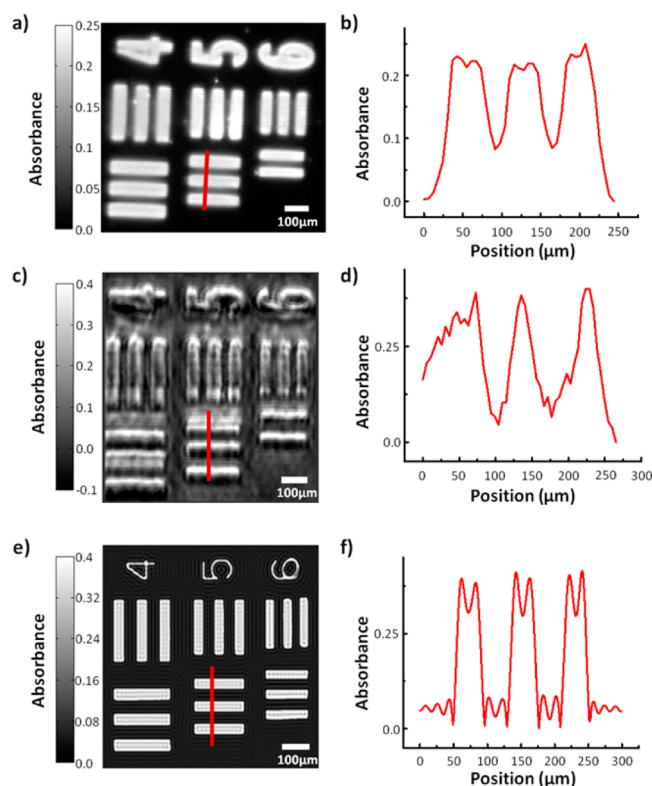


**Figure 3.** (a) Commercial (global source) infrared absorbance image of a USAF 1951 optical resolution target (cycle 3, elements 4 through 6) at  $1180\text{ cm}^{-1}$ . (b) A profile of three bars of element 5, indicated by the red line in (a). (c) QCL + FPA absorbance image of the same target at  $1180\text{ cm}^{-1}$ . Note that there is no longer a diffuser plate in the beam path such that full coherent effects are present. (d) A profile of three bars of element 5, indicated by the red line in (c). (e) Simulated absorbance image of the same region at  $1180\text{ cm}^{-1}$  assuming a coherent source. (f) A profile of three simulated bars of element 5, indicated by the red line in (e).

The simulations indicate that the effects of coherence are to impart a fine structure in the recorded absorbance. The most striking feature of the source can be seen in the extracted absorbance profiles at an edge. While data from the global-equipped system showed an apparent absorbance increase at the edge due to scattering,<sup>38</sup> the fine structure of the beam extends considerably beyond the edge in the QCL-based system. Although this observation and modeling of the fine structure serves as a caution to the use of QCLs and interpretation of recorded data, it also presents new opportunities in modeling and, perhaps, extracting additional information about the structure of the sample. At this time, however, the expectation that the only outcome of a simple coupling of QCLs to existing microscopy systems would be to obtain an equivalent system but with higher SNR is unfounded. The fringes in the recorded images contain information about sample structure which can be extracted via careful theory, modeling, and signal processing. While the formulation of these reconstructions is beyond the scope of this manuscript, a



practical concern is that the signal-to-noise ratio needs to be high for the reconstruction to be reliable. Comparison of theoretical and experimental data demonstrate that further optimization of the optical setup and experimental parameters is required.

In comparing bolometer measurements to those acquired by a commercial FT-IR system, “image quality” can be described by several different factors, including spatial resolution, spectral quality, and signal-to-noise ratio. The spatial resolution of a system is defined completely by wavelength, numerical aperture, and effective detector pixel size. While the QCL instrument utilizes a smaller numerical aperture objective, it can be observed from the measured profiles that resolution does not appear to differ wildly between the two, as is expected. Figure 4a shows the bar motif profiles for target 5, cycle 3 for

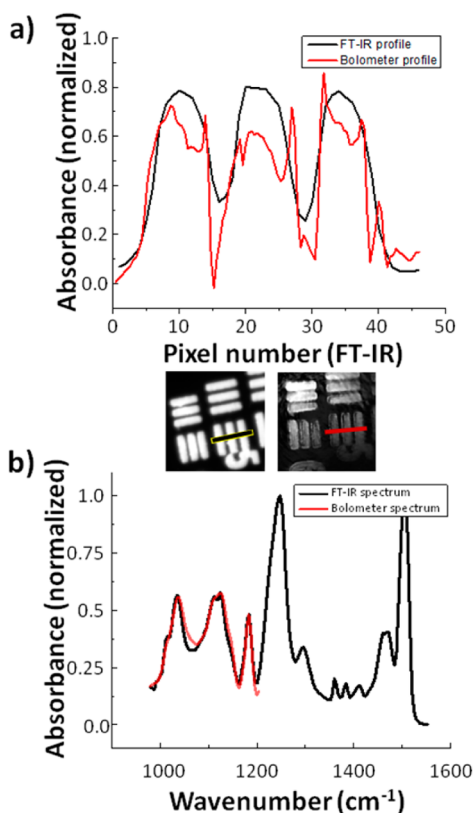


**Figure 4.** (a) Bar-target profile for a commercial FT-IR instrument and the QCL + bolometer system as indicated by the black and red line segments. Because the two detectors contain a different number of pixels, the scale of the measured bolometer profile was adjusted to match that of the commercial instrument. (b) Overlaid absorption spectra of the SU-8 polymer for both the commercial FT-IR system and the QCL + bolometer system. The commercial system recovers the spectrum using an inverse Fourier transform recorded by an interferometer with a 0.25 cm maximum retardation ( $\sim 4$  cm<sup>-1</sup> resolution). The discrete absorbance measurements were taken every 4 cm<sup>-1</sup> for the bolometer system by tuning the QCL sequentially.

both the commercial FT-IR instrument and the bolometer plus diffuser plate setup. After a correction for pixel size (the size per pixel in the FT-IR images is almost 2.5 times as large as those in the bolometer images), it is apparent that the two are on the same order. As there are more pixels representing the same area for the bolometer images, this system has the potential to achieve higher quality images. The relative equivalence of

images is not surprising as the optical setup is similar; however, the relative equivalence in the presence of coherence effects is encouraging. This may indicate that QCL-based systems could be effective for qualitative imaging and will reasonably correlate with FT-IR imaging data, provided that absorbance is high and scattering is not especially strong. For weak absorbance and domain sizes on the order of the wavelength, results between the two would deviate significantly.

Arguably more important than the resolution in chemical imaging is the quality of the recorded spectra. When sequential images across a range of evenly spaced wavelengths are acquired, an absorption spectrum at each pixel is generated. Figure 4b shows the spectrum of SU-8 as acquired by the bolometer instrument with a diffuser plate and as acquired by the commercial FT-IR system. It is clear from the similarity of the band shapes that the bolometer instrument is capable of collecting a representative spectrum. While the band intensities are not identical to those determined by the commercial instrument, this is to be expected. Bolometers are inherently noisier than cooled focal plane arrays and are generally not considered capable of quantitative measurements. While not explicitly observed, it is probable that these power fluctuations can be exacerbated at the far limits of the laser's tunable range. The differences may also be due to optical effects, as reported previously for other configurations,<sup>34–38</sup> but need to be examined in detail using available theory and simulations. The SNR of acquired data is another important aspect of image quality which should be evaluated. Due to uneven illumination in this unoptimized setup, we have measured the signal-to-noise ratio as varying from less than 1 to as large as 32. These values are for images whose acquisition time is on the order of milliseconds and signal averaging may well-improve the SNR if the noise is detector dominated. It can be argued that the QCL system has a higher capacity for signal-to-noise ratio than does the FT-IR instrument: not only is the source power much higher at each individual wavelength measured (between 200 mW and 400 mW at most wavelengths), but the entire dynamic range of the detector is used for a single wavelength at a time rather than evaluating all wavelengths simultaneously. Finally, the QCL-bolometer system underperforms the commercial FT-IR imaging system, indicating the need for further improvement. When these challenges are addressed, the QCL-bolometer system will offer advantages over FT-IR imaging for certain applications. The higher flux makes measurement in aqueous environments possible.<sup>39</sup> Only a handful of bands are required for certain biological analyses,<sup>14</sup> making acquisition of the entire spectrum redundant. Discrete frequency methods could offer a distinct speed advantage in cases where only some bands are required for measurement. Additionally, due to the direct acquisition of data without the need for performing a Fourier transform, the possibility for real-time infrared microscopy and monitoring becomes available.

Given the multichannel detection advantage and the emergence of IR imaging systems with exceptional quality,<sup>2,19</sup> we focused on widefield microscopy applications of the QCL source. Interferometric instrumentation is not appropriate for point-mapping applications due to the very low throughput of a broadband source through a small aperture. In comparison, a potential use for QCLs as IR spectroscopy sources may lie in high-throughput point-mapping measurements. The large flux, focused into a single channel, may offset some of the speed advantages of multichannel detection and the need to diffuse the beam over a large area. The use of point illumination may

also be used to circumvent the fine structure seen in images, as there would not be a scattered and transmitted wave at two different points to interfere. As a final instrumentation setup, we examined the use of QCL for point mapping.<sup>9</sup> For point mapping, the expansion optics (gold-coated parabolic mirrors, iris) and diffuser plate were removed from the DF-IR setup. This kept the unaltered beam tightly focused (less than 2 mm diameter) upon entering the microscope. The bolometer camera was replaced with a cooled single-element MCT detector, allowing for enhanced sensitivity. For simple point measurements by rastering large areas, a QCL system will not be able to best an FT-IR imaging system with a global source. The speed of these conventional widefield systems would far outperform QCL point mapping; the advantage of a QCL source lies in the ability to create truly diffraction-limited spot sizes with large NA objectives and small apertures. We replaced our objective with a 74 $\times$  Schwarzschild objective of 0.65 NA. The high magnification of the objective meant that the microscope's built-in adjustable square aperture could be used to create a very small effective aperture (0.72  $\mu\text{m}$ ) for point-imaging. This aperture size is significantly smaller than the range of illumination wavelengths for imaging and smaller than any objective reported for a global or synchrotron-based system.<sup>40–42</sup> Even with this small aperture in place, a large SNR was observed, and by rastering the stage in increments of 1 or 0.5  $\mu\text{m}$ , spectral data were obtained over larger areas. To date, this is the smallest far-field aperture and smallest point spacing reported. While we caution that diffraction still limits the spot size and therefore the resolution that can be achieved, the image improvement over the use of  $\sim 10$   $\mu\text{m}$  apertures is obvious in the recorded data. Figure 5 demonstrates data

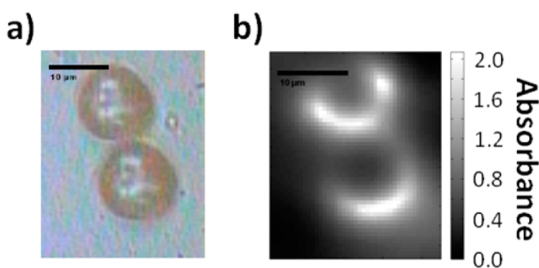


**Figure 5.** (a) White-light image of two touching polystyrene spheres, diameter 10  $\mu\text{m}$ . (b) Point-mapping IR absorption image of the same two spheres at 1080  $\text{cm}^{-1}$ , 0.5  $\mu\text{m}$  steps, 0.72  $\mu\text{m}$  aperture.

acquired from two polystyrene spheres that are approximately 10  $\mu\text{m}$  in diameter. The pixel density is over 100 times that of a synchrotron and nearly 1000 times more than that of a global.<sup>19</sup> For localizing samples in a microscopy configuration, QCL-based point-mapping systems present a new opportunity to image small regions and generate images that are of high pixel density for small feature recognition. The reproduction of structure is quite faithful. At  $\sim 10$   $\mu\text{m}$  of imaging wavelength, the 10  $\mu\text{m}$  diameter spheres can be clearly seen and easily separated.

This point-mapping method also allows for the investigation of scattering effects with enhanced clarity. Scattering by the edges of structural features in infrared imaging is extensive but difficult to quantify in a widefield regime. The corner of one of the bars in the USAF 1951 optical resolution target from the first set of experiments was imaged with both a commercial FT-IR instrument and the point-mapping setup to compare the

clarity of scattering effects. As imaged by the commercial system in Figure 6a, the feature shows an increased loss of

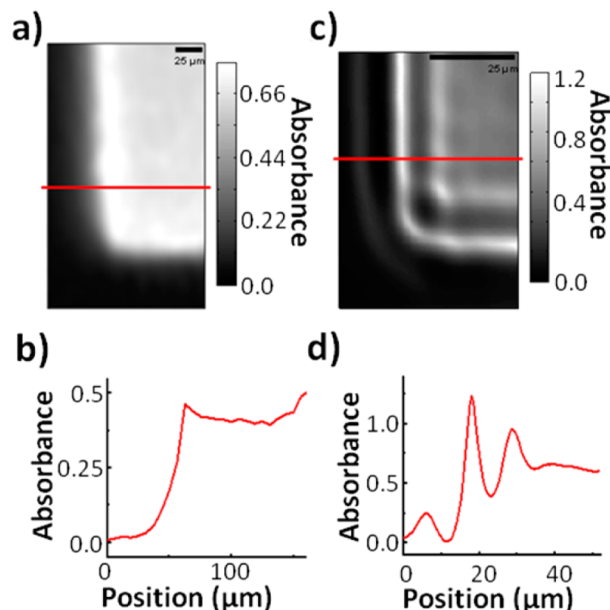


**Figure 6.** (a) Image of a USAF 1951 bar target corner with a commercial FT-IR instrument. The increased “absorbances” at the sharp feature edges are actually due to increased scattering. (b) Graphical profile of one row of pixels from (a). Aside from some blurring, there does not appear to be a well-defined interference pattern at the feature edges due to scattering. (c) Image of the corner with the point-mapping instrument and a 0.72  $\mu\text{m}$  aperture. The edge structure looks starkly different from that of (a). (d) Graphical profile of one row of pixels from (c). Each edge shows a series of minima and maxima that were not discernible with a commercial FT-IR instrument.

transmission at the edges (misinterpreted by the instrument as increased absorbance). The image shows no well-defined structure to the increased scattering. This is evidenced by Figure 6b which shows an absorbance profile of one row of pixels in the image. When imaged by the point-mapping QCL system in 0.5  $\mu\text{m}$  steps, it becomes apparent that there is a well-defined structure to the scattering that was not discernible in the global image. Figure 6c shows the multiple spatial maxima and minima that occur with edge scattering, and Figure 6d shows one row of pixels in greater detail. The richness of information from the edge deserves increased examination and is likely to spur further interest in understanding image formation in the IR.

## CONCLUSION

The latest developments in tunable QCL technology have large tuning ranges, narrow spectral linewidths, and high fluxes to the point where these become feasible sources for discrete-frequency infrared imaging. We have demonstrated an application of a QCL for use as a source in infrared microscopy. When coherence is reduced and the beam is expanded, images of an optical resolution target can be acquired on a bolometer-type camera. These images are comparable to commercial FT-IR measurements in spatial resolution but lack in spectral clarity and signal-to-noise ratio. When used for point mapping, the QCL provides a throughput advantage unmatched by incoherent broadband sources and allows for high-resolution

infrared imaging through a small aperture. These properties of QCLs as an infrared source allow for additional advantages, including rapid widefield imaging at single wavelengths, enhanced localization of signal, and the possibility for real-time infrared monitoring.

## AUTHOR INFORMATION

### Corresponding Author

\*E-mail: rxb@illinois.edu. Address: 4265 Beckman Institute, University of Illinois at Urbana–Champaign, 405 N. Mathews Avenue, Urbana, IL 61801. Tel: (217) 265-6596.

### Notes

The authors declare no competing financial interest.

## ACKNOWLEDGMENTS

The described work was supported by the National Science Foundation (CHE 0957849) and the National Institutes of Health (R01EB009745). M.V.S. would like to acknowledge support through the Congressionally Directed Medical Research Program Postdoctoral Fellowship (BC101112).

## REFERENCES

- (1) Bhargava, R. *Appl. Spectrosc.* **2012**, 66 (10), 1091–1120.
- (2) Walsh, M. J.; Reddy, R. K.; Bhargava, R. *IEEE J. Sel. Top. Quantum Electron.* **2012**, 18 (4), 1502–1513.
- (3) Levin, I. W.; Bhargava, R. *Annu. Rev. Phys. Chem.* **2005**, 56, 429–474.
- (4) Bhargava, R.; Wang, S. Q.; Koenig, J. L. *Adv. Polym. Sci.* **2003**, 163, 137–191.
- (5) Prati, S.; Joseph, E.; Sciotto, G.; Mazzeo, R. *Acc. Chem. Res.* **2010**, 43 (6), 792–801.
- (6) Bellisola, G.; Sorio, M. *Am. J. Cancer Res.* **2012**, 2, 1–21.
- (7) Kwiatkowski, J. M.; Reffner, J. A. *Nature* **1987**, 328 (27), 837–838.
- (8) Lewis, E. N.; Treado, P. J.; Reeder, R. C.; Story, G. M.; Dowrey, A. E.; Marcott, C.; Levin, I. W. *Anal. Chem.* **1995**, 67 (19), 3377–3381.
- (9) Bhargava, R.; Wall, B. G.; Koenig, J. L. *Appl. Spectrosc.* **2000**, 54 (4), 470–479.
- (10) Huffman, S. W.; Bhargava, R.; Levin, I. W. *Appl. Spectrosc.* **2002**, 56 (8), 965–969.
- (11) Snively, C. M.; Katzenberger, S.; Oskarsdottir, G.; Lauterbach, J. *Opt. Lett.* **1999**, 24 (24), 1841–1843.
- (12) Elmore, D. L.; Tsao, M. W.; Frisk, S.; Chase, D. B.; Rabolt, J. F. *Appl. Spectrosc.* **2002**, 56 (2), 145–149.
- (13) Liu, J. N.; Schulmerich, M. V.; Bhargava, R.; Cunningham, B. T. *Opt. Express* **2011**, 19 (24), 24182–24197.
- (14) Bhargava, R. *Anal. Bioanal. Chem.* **2007**, 389 (4), 1155–1169.
- (15) Lendl, B.; Schindler, R. *Vib. Spectrosc.* **1999**, 19 (1), 1–10.
- (16) Griffiths, P. R.; De Haseth, J. A. *Fourier Transform Infrared Spectrometry*, 2nd ed.; John Wiley & Sons: Hoboken, NJ, 2007.
- (17) Hirschmugl, C. J.; Gough, K. M. *Appl. Spectrosc.* **2012**, 66 (5), 475–491.
- (18) Petibois, C.; Piccinini, M.; Guidi, M. C.; Marcelli, A. J. *Synchrotron Radiat.* **2010**, 17 (1), 1–11.
- (19) Nasse, M. J.; Walsh, M. J.; Mattson, E. C.; Reininger, R.; Kajdacsy-Balla, A.; Macias, V.; Bhargava, R.; Hirschmugl, C. J. *Nat. Methods* **2011**, 8, 413–416.
- (20) Kodali, A. K.; Schulmerich, M.; Ip, J.; Yen, G.; Cunningham, B. T.; Bhargava, R. *Anal. Chem.* **2010**, 82 (13), 5697–5706.
- (21) Faist, J.; Capasso, F.; Sivco, D. L.; Sirtori, C.; Hutchinson, A. L.; Cho, A. Y. *Science* **1994**, 264 (5158), 553–556.
- (22) Kosterev, A. A.; Tittel, F. K. *IEEE J. Quantum Electron.* **2002**, 38 (6), 582–591.
- (23) Namjou, K.; Cai, S.; Whittaker, E. A.; Faist, J.; Gmachl, C.; Capasso, F.; Sivco, D. L.; Cho, A. Y. *Opt. Lett.* **1998**, 23 (3), 219–223.
- (24) Paldus, B. A.; Spence, T. G.; Zare, R. N.; Oomens, J.; Harren, F. J. M.; Parker, D. H.; Gmachl, C.; Capasso, F.; Sivco, D. L.; Baillargeon, J. N.; Hutchinson, A. L.; Cho, A. Y. *Opt. Lett.* **1999**, 24 (3), 178–180.
- (25) Weida, M. J.; Buerki, P. R.; Pushkarsky, M.; Day, T. *Micro- and Nanotechnology Sensors, Systems, and Applications* **2011**, 8031, 803127.
- (26) Brandstetter, M.; Genner, A.; Anic, K.; Lendl, B. *Procedia Eng.* **2010**, 5, 1001–1004.
- (27) Phillips, M. C.; Ho, N. *Opt. Express* **2008**, 16 (3), 1836–1845.
- (28) Reddy, R.; Davis, B.; Carney, P. S.; Bhargava, R. *IEEE I. S. Biomed. Imaging* **2011**, 738–741.
- (29) American National Standard for Safe Use of Lasers; ANSI Z136.1; Laser Institute of America: Orlando, 2007.
- (30) Haka, A. S.; Levin, I. W.; Lewis, E. N. *Appl. Spectrosc.* **2000**, 54 (5), 753–755.
- (31) Kwon, B.; Schulmerich, M. V.; Elgass, L. J.; Kong, R.; Holton, S. E.; Bhargava, R.; King, W. P. *Ultramicroscopy* **2012**, 116, 56–61.
- (32) Amrania, H.; McCrow, A.; Phillips, C. *Rev. Sci. Instrum.* **2009**, 80, 123702.
- (33) *Principles of Optics: Electromagnetic Theory of Propagation, Interference and Diffraction of Light*, 6th ed.; Born, M., Wolf, E., Eds.; Cambridge University Press: Cambridge, United Kingdom, 2006.
- (34) Davis, B. J.; Carney, P. S.; Bhargava, R. *Anal. Chem.* **2010**, 82, 3487–3499.
- (35) Davis, B. J.; Carney, P. S.; Bhargava, R. *Anal. Chem.* **2010**, 82, 3474–3486.
- (36) Davis, B. J.; Carney, P. S.; Bhargava, R. *Anal. Chem.* **2011**, 83, 525–532.
- (37) Reddy, R. K.; Walsh, M. J.; Schulmerich, M. V.; Carney, P. S.; Bhargava, R. *Appl. Spectrosc.* **2012**, In press.
- (38) Bhargava, R.; Wang, S. Q.; Koenig, J. L. *Appl. Spectrosc.* **1998**, 52, 323–328.
- (39) Schaden, S.; Haberkorn, M.; Frank, J.; Baena, J. R.; Lendl, B. *Appl. Spectrosc.* **2004**, 58 (6), 667–670.
- (40) Dumas, P.; Carr, G. L.; Williams, G. P. *Analysis* **2000**, 28 (1), 68–74.
- (41) Jamin, N.; Dumas, P.; Moncuit, J.; Fridman, W.-H.; Teillaud, J.-L.; Carr, G. L.; Williams, G. P. *Proc. Nat. Acad. Sci. U.S.A.* **1998**, 95 (9), 4837–4840.
- (42) Miller, L. M.; Smith, R. J. *Vib. Spectrosc.* **2005**, 38 (1–2), 237–240.



# High-Definition Infrared Spectroscopic Imaging

Rohith K. Reddy,<sup>a,b</sup> Michael J. Walsh,<sup>b</sup> Matthew V. Schulmerich,<sup>a,b</sup> P. Scott Carney,<sup>b,c</sup>  
Rohit Bhargava<sup>a-d\*</sup>

<sup>a</sup> Department of Bioengineering;

<sup>b</sup> Beckman Institute for Advanced Science and Technology;

<sup>c</sup> Department of Electrical and Computer Engineering;

<sup>d</sup> Department of Mechanical Science and Engineering, Micro and Nanotechnology Laboratory and University of Illinois Cancer Center  
University of Illinois at Urbana-Champaign, Urbana, IL 61801 USA

The quality of images from an infrared (IR) microscope has traditionally been limited by considerations of throughput and signal-to-noise ratio (SNR). An understanding of the achievable quality as a function of instrument parameters, from first principals is needed for improved instrument design. Here, we first present a model for light propagation through an IR spectroscopic imaging system based on scalar wave theory. The model analytically describes the propagation of light along the entire beam path from the source to the detector. The effect of various optical elements and the sample in the microscope is understood in terms of the accessible spatial frequencies by using a Fourier optics approach and simulations are conducted to gain insights into spectroscopic image formation. The optimal pixel size at the sample plane is calculated and shown much smaller than that in current mid-IR microscopy systems. A commercial imaging system is modified, and experimental data are presented to demonstrate the validity of the developed model. Building on this validated theoretical foundation, an optimal sampling configuration is set up. Acquired data were of high spatial quality but, as expected, of poorer SNR. Signal processing approaches were implemented to improve the spectral SNR. The resulting data demonstrated the ability to perform high-definition IR imaging in the laboratory by using minimally-modified commercial instruments.

Index Headings: Mid-infrared; Fourier transform infrared; Spectroscopic imaging; FT-IR imaging; Resolution; Image quality; Modeling; Theory; Scalar wave theory; Microscopy.

## INTRODUCTION

Instrumentation for Fourier transform infrared (FT-IR) microspectroscopic imaging typically consists of an interferometer for multiplexed spectral encoding, microscope optics for condensing light and image formation, as well as a focal plane array (FPA) detector for multichannel data recording.<sup>1</sup> The instrumentation has benefited from nearly 60 years of development, with its genesis in point-by-point mapping,<sup>2,3</sup> and FT-IR microscopy instrumentation that was developed in the 1980s<sup>4</sup>. The first instruments contained a single-element detector that collected all light transmitted by the microscope, while apertures were used to define the spatial resolution. The use of far-field apertures to localize the region illuminated at the focal plane of the microscope implied that the smallest spot size attained was primarily determined by the wavelength of light. Most studies, however, involved larger spot sizes to achieve higher throughput and, consequently, higher signal-to-noise ratio (SNR) in acquired data. Two dogmatic ideas then emerged to dominate IR imaging technology. The first was that

significant information could not be derived from areas smaller in dimension than the wavelength of light. While this was indeed true because of a lack of throughput for the point-microscopy case, the elimination of apertures in IR imaging meant that there would still be significant throughput at smaller pixels sizes. The second misconception was that there was no benefit to increasing pixel density beyond the optical diffraction limit imposed by the wavelength, as it would not result in more spatial details being accessible. Evidence to the contrary was available with the use of subwavelength apertures along with the higher throughput of a synchrotron source, making the approach feasible and providing excellent quality data.<sup>5</sup>

In other studies, there was also evidence of improved image quality by subpixel stepping<sup>6</sup> in mapping experiments, which did not gain much favor on two grounds. The first objection was a practical consideration. Long acquisition time became even longer. The second objection arose due to the lack of an appropriate theory, leading to a mixing of the concepts of the resolution of optical microscopy with the quality of images arising from IR absorption. As emphasized in this manuscript, the two are often used interchangeably while not being equivalent. Though it is correct that a resolution higher than that determined by the optical configuration and wavelength cannot be attained, there is also no denying the improvement in image quality by recording far-field data from areas of dimensions smaller than wavelength. For example,<sup>7-9</sup> aperture sizes as small as  $3\mu\text{m} \times 3\mu\text{m}$  provided excellent data when using a synchrotron source at wavelengths much longer than  $3\mu\text{m}$ . Spectral quality was retained in this study and maps were sharper. More recent studies<sup>10</sup> showed improved image quality by combining subpixel images. However, the data themselves have not been collected at the optimal pixel sizes. Coupling an FPA to synchrotron-based microscope systems<sup>6,11,12</sup> has recently provided stunning improvements in image quality.<sup>13</sup> Spectra of reasonable quality could be acquired in minutes by using multiple beams, and the multichannel advantages of FPAs allowed for large area coverage. In these advances, the brightness of a synchrotron has been a key factor, and it is unclear if the same benefits are achievable in conventional instruments when using a global source. While the above are considerable advances in instrumentation, few theoretical analyses and validation of resolution and imaging properties have been undertaken.<sup>14,15</sup> These analyses, however, did not provide for a rigorous model of the IR microscope and did not examine the case of pixel sampling beyond the conventional wavelength-limited designs. The lack of an appropriate theory to optimize image quality thus remains as a gap in our understanding. This gap is also a barrier to design of tabletop

Received 9 September 2012; accepted 9 October 2012.

\* Author to whom correspondence should be sent. E-mail: rxb@illinois.edu.

DOI: 10.1366/11-06568

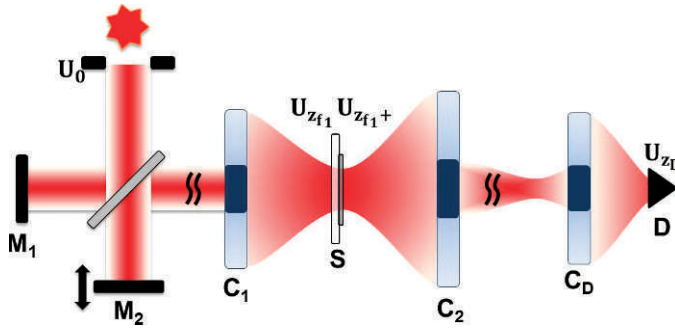


FIG. 1. Model for a FT-IR imaging system. The system consists of an interferometer coupled to a microscope system. Schwarzschild  $C_1$  focus light on to the sample  $S$ ,  $C_2$  and  $C_D$  transmit light from the sample to the detector  $D$ . The fields in different planes are also indicated.

instruments of optimal quality as it is difficult, at present, to make design trade-offs in a quantitative manner.

In this manuscript, we first undertake a theoretical analysis of image formation in IR microspectroscopic imaging. In particular, we focus on determining the best configuration for optimal image quality. We emphasize that attainable resolution and image quality, though related by wavelength and parameters of the optical setup, might not be determined by the same rules. Once the optimal image quality is determined, only then can an examination of the attainable resolution be undertaken. Hence, this is not a detailed discussion of resolution; we focus instead on criteria for obtaining images of the highest possible quality. By using the developed theory, we first determine the pixel size for highest image quality permitted by the optical components. While we focus here only on the capabilities of the microscope, there are other theoretical approaches dealing comprehensively with the effects of optical properties of the sample; size and shape of domains;<sup>16</sup> geometry of acquisition; and microscopy optics on both spectral distortions<sup>17,18</sup> and image formation.<sup>19,20</sup> The approach here, therefore, is a more general model that neglects sample detail in the interests of understanding microscope performance. Second, we implement the theoretical recommendations by modifying a commercial system. Finally, we present the integration with previously described noise-reduction strategies to provide improved data quality.

**A Model for FT-IR Spectroscopic Imaging.** A theoretical analysis is presented here for the system shown in Fig. 1. Models based on ray (geometric) optics have been especially popular for IR microscopy, but are inadequate for analysis of wavelength-associated effects. Full-scale electromagnetic models, at the other extreme, not only capture all of the physics of image formation including polarization effects, but also involve increased complexity. It is prudent to choose the simplest model that incorporates all the phenomena of interest. Hence, we forgo the full electromagnetic treatment in favor of using the simpler scalar wave theory framework.

Our analysis is based on explicitly calculating the electric field at every plane in the microscope system. To simplify the analysis, we consider a monochromatic component of the field with a wavenumber  $\bar{\nu}$  and complex amplitude  $U$ .<sup>1</sup> Dependence on  $\bar{\nu}$  is implied throughout unless otherwise stated. The field can be expressed as a superposition of plane waves described

by functions of the form  $U(\mathbf{f})\exp\{i2\pi[\mathbf{f}\cdot\mathbf{r}+f_z(\mathbf{f})z]\}$ , where  $\mathbf{f}$  is a two-dimensional vector, for instance in Cartesian coordinates,  $\mathbf{f} = (f_x, f_y)$ . The function  $f_z(\mathbf{f})$  is defined so that  $|\mathbf{f}|^2 + f_z^2(\mathbf{f}) = \bar{\nu}^2$ , that is, the plane waves satisfy the Helmholtz equation. For each plane wave constituting the field, its relative contribution, determined by its amplitude, and its relative position, determined by its phase, are both necessary for a complete description of the field. The field and all linear transformations of the field can be represented as a linear combination of these plane waves, which travel at various angles. The term “angular spectrum” is often used<sup>21</sup> to describe such decomposition. We emphasize that the use of the word “spectrum” in this context should not be confused with the absorption spectrum that is commonly encountered in spectroscopy, and that “spectrum” without the modifier “angular” is meant to be the usual absorption spectrum. Similarly, the term “spatial frequency” refers to the vector  $\mathbf{f}$  used above and should not be confused with spectral “frequency.” For the convenience of the reader, we have summarized the notation used in the Appendix.

## OPTICAL SYSTEM

The system shown in Fig. 1 can be analyzed by using a modular approach. To that end, we describe each component in the optical system with an operator. This approach provides a convenient means of modifying the analysis to accommodate changes in the instrument. As the system is linear, it is convenient to work in a notation designed for linear algebra, namely the Dirac notation.<sup>22</sup> Vectors describing the field in a plane at constant axial coordinate  $z$  are written  $|U_z\rangle$  with Hermitian adjoint  $\langle U_z|$ . The two-dimensional Fourier component of the field at spatial frequency  $\mathbf{f}$  is written  $\tilde{U}(\mathbf{f}) = \langle \mathbf{f}|U_z\rangle$ , and the value of the field at a point  $\mathbf{r}$  is given by  $U(\mathbf{r}) = \langle \mathbf{r}|U_z\rangle$ . The sample is assumed to be thin, as described by a vector,  $|S\rangle$ . The detector plane is taken to be at  $z_D$ . Thus the goal of the analysis is to produce an equation of the form

$$|U_{z_D}\rangle = \mathbf{A}|S\rangle \quad (1)$$

where  $\mathbf{A}$  describes the optical system.

We first address the operator for propagation through free space between two parallel planes separated by a distance  $d$ , denoted  $\mathbf{K}_d$ . We assume unidirectional propagation along the axis normal to the planes so that propagation is simply the accumulation of phase. The matrix elements of  $\mathbf{K}_d$  are given by:

$$\langle \mathbf{f}_1|\mathbf{K}_d|\mathbf{f}_2\rangle = \delta(\mathbf{f}_2 - \mathbf{f}_1)e^{i2\pi f_z(\mathbf{f}_1)d} \quad (2)$$

where  $\delta$  is the Dirac delta function, and  $\mathbf{f}_1$  and  $\mathbf{f}_2$  denote spatial frequencies. Alternatively, the operator can be constructed as:

$$\mathbf{K}_d = \int d^2f |\mathbf{f}\rangle e^{i2\pi f_z(\mathbf{f})d} \langle \mathbf{f}| \quad (3)$$

It is useful to note that  $\mathbf{K}_d \mathbf{K}_{d'} = \mathbf{K}_{d+d'}$ .

An interferometer can be thought of as a beam splitter, followed by propagation of two different axial distances. Given arms of length  $d_{A_1}$  and  $d_{A_2}$ , measured from the beam splitter to each of the mirrors, the interferometer is represented by an operator

$$\mathbf{I}_{d_{A_1}, d_{A_2}} = \frac{1}{2}(\mathbf{K}_{2d_{A_1}} + \mathbf{K}_{2d_{A_2}}) \quad (4)$$

Next, we consider the effect of a Schwarzschild (also known

<sup>1</sup> Please consult Table II for a detailed description of the symbols used in the equations throughout this paper.



as a Cassegrain in the literature). Much like a Fresnel lens, the Schwarzschild can be considered to impart onto the field a quadratic phase factor. We represent the Schwarzschild  $C$  with an operator  $\mathbf{G}_C$ :

$$\mathbf{G}_C = \int d^2r |\mathbf{r}\rangle Q_C(\mathbf{r}) \exp \left[ -i \frac{\pi \bar{v}}{L_f} r^2 \right] \langle \mathbf{r}| \quad (5)$$

where  $L_f$  is the focal length of the Schwarzschild. The quadratic phase factor converts each plane wave incident on the Schwarzschild into a spherical wave converging on its focal plane. The phase relation between plane waves incident on the Schwarzschild along with the imparted quadratic phase determine the final image position and size.  $Q_C$  is the aperture function (described in detail in the Appendix). It is often the case that the Schwarzschild appears between two propagation steps in the form  $\mathbf{K}_{d_2} \mathbf{G}_C \mathbf{K}_{d_1}$ . As shown in the Appendix, to a good approximation, when  $d_1^{-1} + d_2^{-1} = L_f^{-1}$ , the Schwarzschild focuses light from the first plane into the second with a magnification factor  $M_C = d_2/d_1$ . Thus, it is convenient to define

$$\mathbf{H}_C = \mathbf{K}_{d_2} \mathbf{G}_C \mathbf{K}_{d_1} \approx \int d^2f |\mathbf{f}\rangle Q_C(\mathbf{f}) \langle -M_C \mathbf{f}| \quad (6)$$

Clearly,  $\mathbf{H}_C$  is not uniquely defined unless  $d_1$  and  $d_2$  are specified, and care should be taken in observing the context in which it is placed. When the image plane is out-of-focus by a distance  $d_0$ , for example, the propagation operator  $\mathbf{K}_{d_0}$  can be used to obtain the out-of-focus image using the operator  $\mathbf{K}_{d_0+d_2} \mathbf{G}_C \mathbf{K}_{d_1} = \mathbf{K}_{d_0} \mathbf{H}_C$ .

Given a field produced at the source  $|U_0\rangle$ , at  $z = z_0$  then propagated to the interferometer at  $z = z_1$ , acted on by the interferometer, then propagated to the first Schwarzschild,  $C_1$ , at  $z = z_{C_1}$  and then from the Schwarzschild to its focal plane,  $z = z_{f_1}$ , the resultant field is

$$|U_{z_{f_1}}\rangle = \mathbf{K}_{z_{f_1}-z_{C_1}} \mathbf{G}_{C_1} \mathbf{K}_{z_{C_1}-z_1} \mathbf{I}_{d_{A_1}, d_{A_2}} \mathbf{K}_{z_1-z_0} |U_0\rangle \quad (7)$$

The sample is modeled as a thin screen. That is, the field on the far side of the sample is assumed to be the product of the sample structure function and the field incident on the sample in the coordinate domain. We formally construct an operator that effects this multiplication. Given a field  $|U\rangle$ , the operator  $\mathbf{U}$  is defined:

$$\mathbf{U} = \int d^2r |\mathbf{r}\rangle \langle \mathbf{r}| \mathbf{U} \langle \mathbf{r}| = \int d^2f d^2f' |\mathbf{f}\rangle \langle \mathbf{f}'| \mathbf{U} \langle \mathbf{f}'| \quad (8)$$

The sample,  $|S\rangle$ , then interacts with the incident field,  $|U_{z_{f_1}}\rangle$ , to produce a transmitted field at a plane  $z = z_{f_1} +$  just past the sample:

$$|U_{z_{f_1}+}\rangle = \mathbf{U}_{z_{f_1}} |S\rangle = \int d^2f d^2f' |\mathbf{f}\rangle \langle \mathbf{f}'| \mathbf{U}_{z_{f_1}} |U_{z_{f_1}}\rangle \langle \mathbf{f}'| |S\rangle \quad (9)$$

Substituting from Eq. 7 we find that:

$$\begin{aligned} |U_{z_{f_1}+}\rangle &= \int d^2f d^2f' |\mathbf{f}\rangle \langle \mathbf{f}'| \mathbf{K}_{z_{f_1}-z_{C_1}} \mathbf{G}_{C_1} \mathbf{K}_{z_{C_1}-z_1} \mathbf{I}_{d_{A_1}, d_{A_2}} \mathbf{K}_{z_1-z_0} |U_0\rangle \\ &\quad \times \langle \mathbf{f}'| |S\rangle \end{aligned} \quad (10)$$

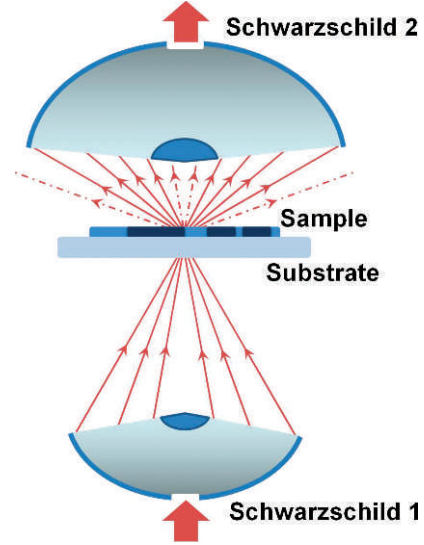


FIG. 2. Schwarzschild  $C_1$ , which focuses light on to the sample, and  $C_2$ , the collection Schwarzschild, are shown.

Note that  $\mathbf{I}_{d_{A_1}, d_{A_2}} = \mathbf{K}_{2d_{A_1}} \mathbf{I}_{0, d_{A_2}-d_{A_1}}$ . Assuming no misalignment, i.e., when the system is in focus, the propagation operators can be absorbed into the magnification factor of  $\mathbf{H}_{C_1}$ . Thus,

$$|U_{z_{f_1}+}\rangle = \int d^2f d^2f' |\mathbf{f}\rangle \langle \mathbf{f}'| \mathbf{H}_{C_1} \mathbf{I}_{0, d_{A_2}-d_{A_1}} |U_0\rangle \langle \mathbf{f}'| |S\rangle \quad (11)$$

where  $\mathbf{H}_{C_1} = \mathbf{K}_{z_{f_1}-z_{C_1}} \mathbf{G}_{C_1} \mathbf{K}_{z_{C_1}-z_0+2d_{A_1}}$ . Evaluating Eq. 11 explicitly, we find that the field just past the sample is given by:

$$\begin{aligned} |U_{z_{f_1}+}\rangle &= \frac{1}{2} \int d^2f d^2f' |\mathbf{f}\rangle Q_{C_1}(\mathbf{f}'/M_{C_1}) \\ &\quad \times \{1 + \exp[i2\pi f_z(\mathbf{f}')(2d_{A_2} - 2d_{A_1})]\} \\ &\quad \times \langle \mathbf{f}'| U_0\rangle \langle \mathbf{f} + \mathbf{f}'/M_{C_1} | S\rangle \end{aligned} \quad (12)$$

where it can be noted that  $\langle \mathbf{f}'| S\rangle$  is the Fourier component of the sample at spatial frequency  $\mathbf{f}'$ . In the case that the source consists of a point source far from the first Schwarzschild,  $\langle \mathbf{f}'| U_0\rangle \approx A_0$ , where  $A_0$  is a constant and inclination factors of the form  $1/f_z$  have been neglected. Then the field is given by:

$$\begin{aligned} |U_{z_{f_1}+}\rangle &= \frac{A_0}{2} \int d^2f d^2f' |\mathbf{f}\rangle Q_{C_1}(\mathbf{f}'/M_{C_1}) \\ &\quad \times \{1 + \exp[i2\pi f_z(\mathbf{f}')(2d_{A_2} - 2d_{A_1})]\} \langle \mathbf{f} + \mathbf{f}'/M_{C_1} | S\rangle \end{aligned} \quad (13)$$

Light propagation from the Schwarzschild  $C_1$  to the sample and to the Schwarzschild  $C_2$  are illustrated in Fig. 2.

The propagation of the field after the sample,  $|U_{z_{f_1}+}\rangle$ , to the field at the detector,  $|U_{z_D}\rangle$ , takes place through two more Schwarzschilds. The Schwarzschild  $C_2$ , located effectively at  $z = z_{C_2}$ , focuses the sample plane to a plane  $z = z_{f_2}$  such that  $1/(z_{f_1} - z_{C_2}) + 1/(z_{C_2} - z_{f_2}) = 1/L_{f_2}$ , where  $L_{f_2}$  is the focal length of Schwarzschild  $C_2$ . Similarly, the Schwarzschild  $C_D$  located at  $z = z_{C_D}$ , focuses light from the plane  $z = z_{f_2}$  onto the detector plane at  $z = z_D$  such that  $1/(z_{C_D} - z_{f_2}) + 1/(z_D - z_{C_D}) = 1/L_{f_D}$ , where  $L_{f_D}$  is the focal length of Schwarzschild  $C_D$ . Misalignment of the focal planes such that  $z_{f_2} \neq z_{f_D}$  can be taken into account with the propagator  $\mathbf{K}_{z_{f_D}-z_{f_2}}$ . Thus,

$$\begin{aligned}
|U_{z_d}\rangle &= \mathbf{H}_{C_D} \mathbf{K}_{z_{f_D}-z_{f_2}} \mathbf{H}_{C_2} |U_{z_{f_1}+}\rangle \\
&= \int d^2f d^2f' \mathbf{H}_{C_D} \mathbf{K}_{z_{f_D}-z_{f_2}} \mathbf{H}_{C_2} |\mathbf{f}\rangle \langle \mathbf{f}'| \mathbf{H}_{C_1} I_{0,d_{A_2}-d_{A_1}} |U_0\rangle \\
&\quad \times \langle \mathbf{f}'|S\rangle
\end{aligned} \quad (14)$$

This expression is now straightforward to evaluate. We assume that  $z_{f_D} = z_{f_2}$  (the focal planes are aligned). We find explicitly that:

$$\begin{aligned}
|U_{z_D}\rangle &= \frac{1}{2} \int d^2f d^2f' |\mathbf{f}\rangle Q_{C_D}(\mathbf{f}) Q_{C_2}(-M_{C_D}\mathbf{f}) Q_{C_1}(-\mathbf{f}'/M_{C_1}) \\
&\quad \times \{1 + \exp[i2\pi f_z(\mathbf{f}')(2d_{A_2} - 2d_{A_1})]\} \langle \mathbf{f}'|U_0\rangle \\
&\quad \times \langle \mathbf{f}'/M_{C_1} + M_{C_2}M_{C_D}\mathbf{f}|S\rangle
\end{aligned} \quad (15)$$

Define  $M = M_{C_D}M_{C_2}$  and compute

$$\begin{aligned}
\langle \mathbf{f}|U_{z_D}\rangle &= \frac{1}{2} Q_{C_D}(\mathbf{f}) Q_{C_2}(-M_{C_D}\mathbf{f}) \int d^2f' Q_{C_1}(-\mathbf{f}'/M_{C_1}) \\
&\quad \times \{1 + \exp[i2\pi f_z(\mathbf{f}')(2d_{A_2} - 2d_{A_1})]\} \\
&\quad \times \langle \mathbf{f}'|U_0\rangle \langle \mathbf{f}'/M_{C_1} + M\mathbf{f}|S\rangle
\end{aligned} \quad (16)$$

The above expression is true for any spatially heterogeneous sample and has no restriction on its constituent spatial frequencies. Note that  $M$  is typically larger than 1 (i.e., the detector elements are bigger than the corresponding areas on the sample).

In order to illustrate the significance of Eq. 16, consider a case where the sample is a point object. In this case,  $\langle \mathbf{f}'/M_{C_1} + M\mathbf{f}|S\rangle = 1$ , giving

$$\begin{aligned}
\langle \mathbf{f}|U_{z_D}\rangle &= \frac{1}{2} Q_{C_D}(\mathbf{f}) Q_{C_2}(-M_{C_D}\mathbf{f}) \int d^2f' Q_{C_1}(-\mathbf{f}'/M_{C_1}) \\
&\quad \times \{1 + \exp[i2\pi f_z(\mathbf{f}')(2d_{A_2} - 2d_{A_1})]\} \langle \mathbf{f}'|U_0\rangle
\end{aligned} \quad (17)$$

$$= \frac{1}{2} Q_{C_D}(\mathbf{f}) Q_{C_2}(-M_{C_D}\mathbf{f}) B_0 \quad (18)$$

Here,  $B_0$ , the integral from Eq. 17, is independent of  $\mathbf{f}$  and physically denotes the field at the sample plane for a point object. The corresponding intensity at the detector plane is

$$\begin{aligned}
\langle U_{z_D}|\mathbf{f}\rangle \langle \mathbf{f}|U_{z_D}\rangle &= \frac{B_0^2}{4} [Q_{C_D}(\mathbf{f}) Q_{C_2}(-M_{C_D}\mathbf{f})] \\
&\quad * [Q_{C_D}(\mathbf{f}) Q_{C_2}(-M_{C_D}\mathbf{f})]
\end{aligned} \quad (19)$$

where  $*$  represents convolution.

In a case where the source is completely incoherent, i.e.,  $\langle \langle U_0|\mathbf{r}'\rangle \langle \mathbf{r}|U_0\rangle \rangle_{en} = I_0(\mathbf{r})\delta(\mathbf{r} - \mathbf{r}')$ , the intensity at the detector plane is

$$\langle \langle U_{z_D}|\mathbf{r}'\rangle \langle \mathbf{r}|U_{z_D}\rangle \rangle_{en} = \int d^2r I_0(\mathbf{r}') |h(\mathbf{r};\mathbf{r}')|^2 \quad (20)$$

Where  $h(\mathbf{r};\mathbf{r}')$  is the transfer function from the coherent case and  $I_0(\mathbf{r})$  is the source intensity. The subscript *en* above denotes an ensemble average over constituent random processes. By using the equations presented in this section, we proceed to compute the spatial sampling rate and pixel size required to record all the information available from the FT-IR spectroscopic imaging system.

**Pixel Size.** An analysis of the equations for the FT-IR

imaging system provides insight into optical design and image formation. The explicit form of  $Q_{C_i}$  in terms of NA is derived in the Appendix (Eq. A29, Eq. A30, and Eq. A31). It can be observed from Eq. 16 that the spatial frequencies on the detector are always less than  $\min(\bar{v}NA_{C_2\text{out}}/M, \bar{v}NA_{C_D\text{out}})$  because the support of the data is the intersection of the support of  $Q_{C_2}(-M_{C_D}\mathbf{f})$  and  $Q_{C_D}(\mathbf{f})$ . When the pre-optics to the detector are well designed, then  $\bar{v}NA_{C_2\text{out}}/M \leq \bar{v}NA_{C_D\text{out}}$ , providing the limiting field on the detector to be a spatial frequency of  $\bar{v}NA_{C_2\text{out}}/M$ . As the detector records intensity and not fields,<sup>21</sup> the intensity  $I(\mathbf{r}) = U^*(\mathbf{r})U(\mathbf{r})$  has a spatial frequency bound of  $2 \times \bar{v}NA_{C_2\text{out}}/M$ . We emphasize that in order to faithfully record the entire intensity image without any loss of information, the spatial sampling rate according to the Nyquist criterion<sup>21</sup> has to be at least twice this limiting frequency, or  $4\bar{v}NA_{C_2\text{out}}/M$ . The pixel size is inversely related to the sampling rate, i.e.,  $L_{\text{pixel}} = M/4\bar{v}NA_{C_2\text{out}}$ . The wavenumber,  $\bar{v}$ , in mid-IR spectroscopic imaging typically varies between 600 and 4000  $\text{cm}^{-1}$  ( $0.4 \mu\text{m}^{-1}$ ). Therefore, when using Eq. 16, the equivalent pixel size on the sample has to be  $1/(4 \times 0.4 NA_{C_2\text{out}}) \mu\text{m}$ . Thus, for  $NA_{C_2\text{out}} = 0.5$ , the effective pixel size on the sample is 125  $\mu\text{m}$  and for  $NA_{C_2\text{out}} = 0.65$ , the effective pixel size is 0.96  $\mu\text{m}$ . It must be emphasized that the value of pixel size calculated above is *not* the same as resolution. It is in fact smaller than the resolution as defined by the Rayleigh criterion.<sup>21</sup> However, it reflects the least sampling rate required to utilize all the information passed by the system in FT-IR spectroscopic imaging.

While we have focused on image quality, a number of other insights are also apparent. In some detectors, for example, it can be advantageous to have a concave mirror (instead of a Schwarzschild) that can be easily be incorporated into the model by making the term corresponding to the central obscuration i.e., an inner numerical aperture of zero  $NA_{C_D\text{in}} = 0$ . The absence of a central obscuration increases light throughput significantly. We suggest that the Schwarzschild used in commercial instruments be replaced with this mirror. This modification will result both in better image quality and lower instrument costs. Although the above derivation uses a transmission mode measurement, the same analysis can be performed for transflection mode. In the case of transflection-absorption measurement when using a beam-splitter and full Schwarzschild illumination, Schwarzschilds  $C_1$  and  $C_2$  correspond to the same Schwarzschild, and light travels through the sample twice, once before reflection and once after. Hence the sampling rates and pixel sizes are the same in both cases.

**Experiments and Simulations. Instrumentation.** A Varian 7000 spectrometer coupled to a UMA-400 microscope was used to perform two sets of experiments with parameters listed in Table I. System 1 uses accessories standard to the Varian microscope. System 2 uses an Edmund Optics ( $NA = 0.65$ , 74 $\times$  magnification) Schwarzschild for  $C_2$ . The two systems make comparisons easy, because parameters other than Schwarzschild  $C_2$  are the same. The only difference is in the effective pixel size on the sample and  $NA_{C_2\text{out}}$ . The detector's pixel size is 40  $\mu\text{m}$ . The interferometer is operated in the step-scan mode at a stepping rate of 200 Hz. Data were acquired at every other zero crossing (a undersampling ratio of 2) of an He-Ne laser for a free-scanning spectral range of 7900–0  $\text{cm}^{-1}$ . Time to acquire a 128  $\times$  128 pixel data set by using system 2 was 25 s for eight co-additions. For the full format of the

**TABLE I.** Experimental parameters used for data acquisition and modeling.

Parameter	System 1	System 2
$NA_{C1out}$	0.5	0.5
$NA_{C2out}$	0.5	0.65
$NA_{C_Dout}$	0.5	0.5
$MC_1$	$15\times$	$15\times$
$MC_2$	$15\times$	$74\times$
$MC_D$	$3\times$	$3\times$
Pixel size (effective)	$5.5\text{ }\mu\text{m}$	$1.115\text{ }\mu\text{m}$
Spectral resolution	$8\text{ cm}^{-1}$	$8\text{ cm}^{-1}$
No. of scans per pixel	8	128
No. of scans (background)	128	128
No. of detector elements	$128 \times 128$	$128 \times 128$
Undersampling ratio	2	2

detector ( $128 \times 128$  pixels), the fastest acquisition of an  $8\text{ cm}^{-1}$  resolution data set (undersampling ratio of 4) is less than 1 s and is limited by FPA speed (1.6 kHz). A Fourier transform of the recorded data was carried out with the Norton–Beer medium apodization function. Data were truncated and stored as absorbance after a ratio against an appropriate background data set.

Data extraction and image processing were performed with a hyperspectral imaging software package, ENvironment for Visualizing Images (ENVI). In ENVI, the two-dimensional Fourier transform routines are in built. Modules for further data processing were written in-house using IDL 7.1 and MATLAB 7. The two imaging systems, with parameters shown in Table I (parameters 1 through 6) are simulated. The simulations were performed on a quad core computer with a NVIDIA GeForce GTX 580 GPU and 12 GB of RAM. Modules and functions for the simulations were written in house by using MATLAB 7. The simulations compute the detector field and intensity for incoherent illumination by using the system parameters (Table I, parameters 1 through 6) and object as inputs. Software is implemented based on the theory and algorithms described here. Simple structures can be simulated in minutes, while entire data sets for morphologically complex samples can require days of computational time on a desktop computer. The run time for simulations is about 20 s for each wavenumber for the samples described here.

Prostate and breast tissue microarrays (TMAs) were used as a platform for high-throughput sampling.<sup>23</sup> TMAs consist of a large number of small ( $\cong 1\text{ mm}$  in diameter) tissue sections arranged in a grid pattern on a substrate. This technique facilitates and streamlines acquisition of data from several patients and provides diversity to the sample population under observation. Breast and prostate tissue microarrays were obtained from the University of Illinois–Chicago (kindly provided by Dr. Andre Kajdacsy-Balla) and from US Biomax (no. BR1003). One  $5\text{ }\mu\text{m}$ -thick tissue section from each array was placed on a  $BaF_2$  substrate for IR imaging and serial  $5\text{ }\mu\text{m}$ -thick sections were placed on standard glass slides for hematoxylin and eosin staining. IR imaging data were acquired from a normal breast tissue core that contained a region comprising terminal ductal lobular units, as well as from a normal prostate tissue core from the region of a small blood vessel. A standard chrome-on-glass USAF 1951 target (Edmund Optics) was used as a test sample to test both spectral and spatial performance. The thickness of chrome is of

the order of (100 nm) and about 10% of incident light is transmitted through the chrome (experimentally measured).

## RESULTS AND DISCUSSION

Our first step in analyzing the performance of the imaging systems was to validate simulations with recorded data by using a gold standard for comparison. As common in other forms of microscopy, a standard USAF 1951 target, consisting of chrome on glass, was chosen. The chrome provides a large attenuation (absorbance) with negligible thickness. It also provides high contrast for visible light microscopy. Hence, it is an ideal sample for simulation and validation. We first recorded visible-light images for a standard USAF microscope target. The recorded image was binarized to remove any edge blurring or grayscale values in the simulation. An absorbance of unity was assigned to the chrome region, and the resulting image was used for simulation. Regions without the chrome were assigned a transmittance of unity (zero absorbance). Simulations were carried out for both the instrument configurations described previously. The light source is assumed to be spatially incoherent, as in Eq. 20. Spectroscopic imaging data were also recorded with the target. We analyzed groups 6 and 7, and elements 1 through 6, as these represent the highest image quality typically encountered in IR microscopy. Images of the standard sample employed for simulation, absorbance images from simulated data, and absorbance images from the recorded data corresponding to the two instrument configurations are shown in Fig. 3. In order to facilitate comparison of simulations, we used the same pixel size for both optical configurations (although different NA lenses are often associated with different magnifications). The chosen pixel size for simulations of  $0.36\text{ }\mu\text{m}$  will not be a limiting factor in the resulting image quality. The USAF target is designed to enable facile calculation of the frequency response of the imaging systems as well as to illustrate resolution capabilities via images. In simulations, we emphasize again that the sample is assumed to be infinitesimally thin to avoid effects associated with thickness. Comparing the two simulated absorbance images (Figs. 3b and 3f) with the same pixel size shows the effects of increasing NA. As expected, an increase in the NA provides for higher quality and higher resolution images. Nevertheless, the enhancement is not especially striking. A more obvious degradation in image quality is evident when the pixel size increased from 1.1 (Fig. 3f) to  $5.5\text{ }\mu\text{m}$  (Fig. 3g), while all other parameters were constant. This dramatic change in image quality emphasizes the need for carefully choosing the pixel size. The combined effects of choosing a higher-NA lens and the appropriate sampling (small pixel size) can result in significantly improved image quality (cf. Figs. 3b and 3g). To experimentally validate these predicted improvements in image quality, we set up two optical configurations described in Table I on the same commercial microscope and obtained data on the same USAF 1951 target used in simulations. Our goal was to minimally modify (by changing one lens) the existing commercial system. Hence, we did not alter the condenser. Matching the throughput via the image formation lens and condenser is likely to result in better SNR, but will not materially change the appearance of the images, as the image quality depends only on the angular spectral bandwidth of the image formation lens. Experimental results for Fig. 3c,  $NA = 0.65$ , pixel size =  $1.115\text{ }\mu\text{m}$ , and Fig. 3h,  $NA = 0.50$ , pixel size =  $5.5\text{ }\mu\text{m}$ , are presented for comparison. A dramatic



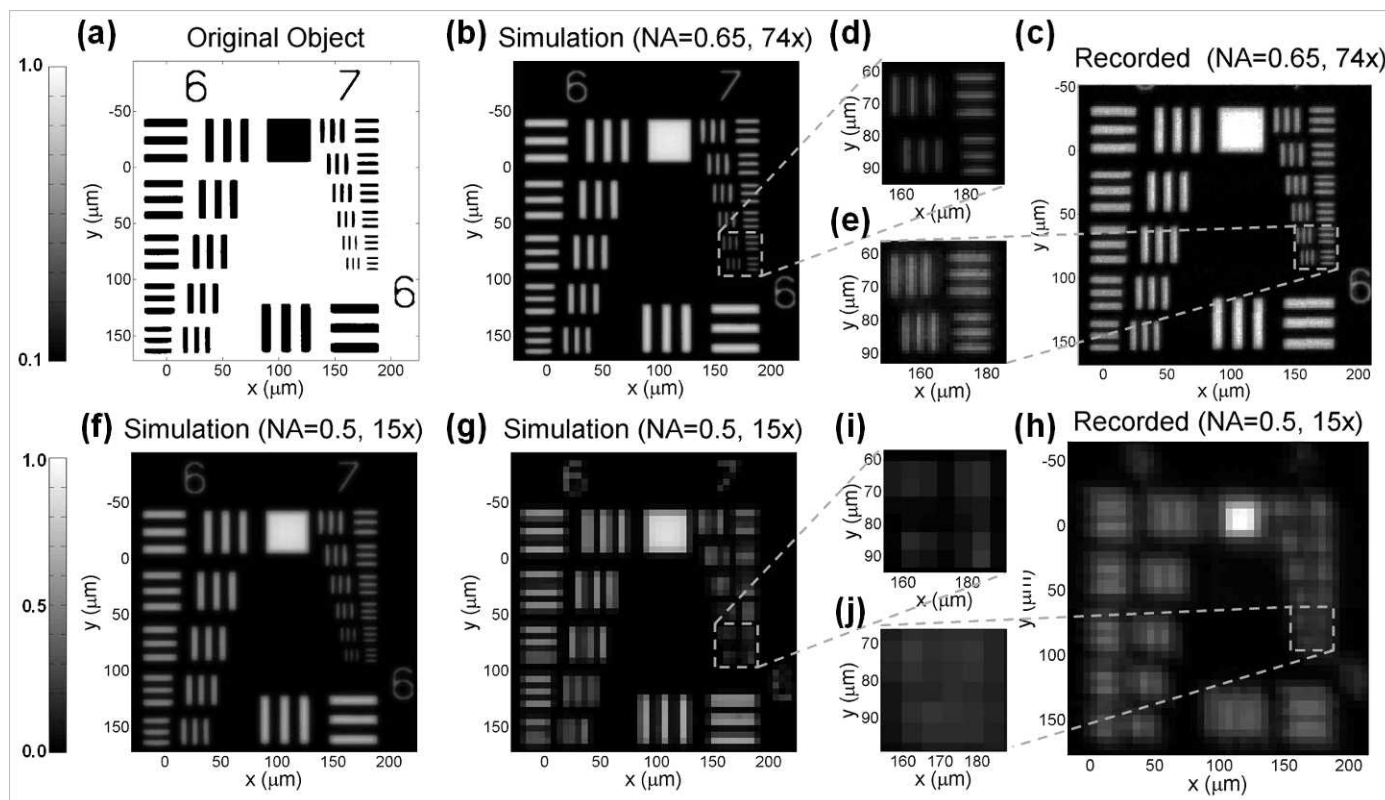


FIG. 3. (a) The original object consists of a set of bars of different sizes with transmittance indicated to the left. Absorbance images from simulations at  $\bar{\nu} = 3850 \text{ cm}^{-1}$  are shown when Schwarzschild  $C_2$  has (b) NA = 0.65, (f) NA = 0.50, (g) NA = 0.50. The pixel size in (b) and (f) are  $1.1 \mu\text{m}$ , whereas the pixel size in (g) is  $5.5 \mu\text{m}$ . Experimental absorbance images from  $\bar{\nu} = 3950 \text{ cm}^{-1}$  are shown with configurations (c) NA = 0.65, pixel size =  $1.1 \mu\text{m}$ ; (h) NA = 0.50, pixel size =  $5.5 \mu\text{m}$ ; (d), (e), (i), (j) magnified regions from corresponding images.

improvement in image quality is observed experimentally for the smaller pixel size. Expanding a smaller region for comparison in Figs. 3d and 3e, and 3i and 3j, the three smaller bars are distinguishable only in the higher NA, smaller pixel-size setup. This qualitatively demonstrates the gain in image quality and resolution when using a higher-NA system along with the appropriate pixel spacing. In all cases, as expected, we also note that the recorded data are of somewhat lower quality than the simulations. This is a result of edge effects in the sample, finite detector sizes, imperfect optics and experimental noise in the recorded data.

While the images from simulation and recorded data agree well, they do not provide a quantitative understanding of the performance improvement and limits of the two configurations. Therefore, we quantitatively analyzed the performance of the systems as a function of the spatial frequency. The frequency response of the optical system is often characterized by the modulation or contrast transfer function of the system. While optical systems typically employ intensity values to examine the imaging system performance, here we use the spatial frequencies in Fig. 3a and the corresponding absorbance values from simulations and recorded data to plot the absorbance contrast. The absorption contrast ratio (ACR) is defined as the difference in maximum and minimum absorbance observed at a specific spatial frequency compared with that observed in the ideal case. The ideal difference between high and low absorbance is obtained by comparing absorbance values from regions on the sample with no absorbance (for example, the

region used to collect a background spectrum) and a relatively homogeneous region of high absorbance (for example, on the large square in a USAF 1951 target). Figure 4a shows a plot of the absorbance contrast ratio as a function of spatial frequency at  $3950 \text{ cm}^{-1}$ . As expected, ACR is highest at low spatial frequencies and decreases with increasing spatial frequency until zero (no measurable contrast). The absorption contrast ratio for the lower-NA system reaches zero at a lower spatial frequency than that of the high NA one as is evident from the polynomial fit (solid lines in the figure) to simulation data. It can be seen in the experimental data that the high-NA system resolves all bars including the smallest bars (group no. 7) available on the USAF 1951 target. The frequency at which ACR reaches zero can be predicted via simulations to be about  $0.4 \mu\text{m}^{-1}$  ( $\cong 400$  line pairs per mm). Contrast decreases with reduction in pixel size, because light intensity per pixel reduces. As a result, the increased imaging capability is partially offset by a decreased spectral SNR in the resulting absorbance images. While predictions from simulations agree well with measured ACR for the high-NA system, there is some disagreement for the lower-NA setup at high spatial frequencies. This difference is observed at approximately  $0.08 \mu\text{m}^{-1}$  ( $\cong 80$  line pairs per mm). Experimentally, the lower-NA system cannot resolve bars beyond a spatial frequency of  $0.115 \mu\text{m}^{-1}$  ( $\cong 115$  line pairs per mm). This is lower than the theoretically predicted  $0.15 \mu\text{m}^{-1}$  ( $\cong 150$  line pairs per mm). This can be attributed to the finite pixel size preventing an accurate recording of the data. This comparison between ACR

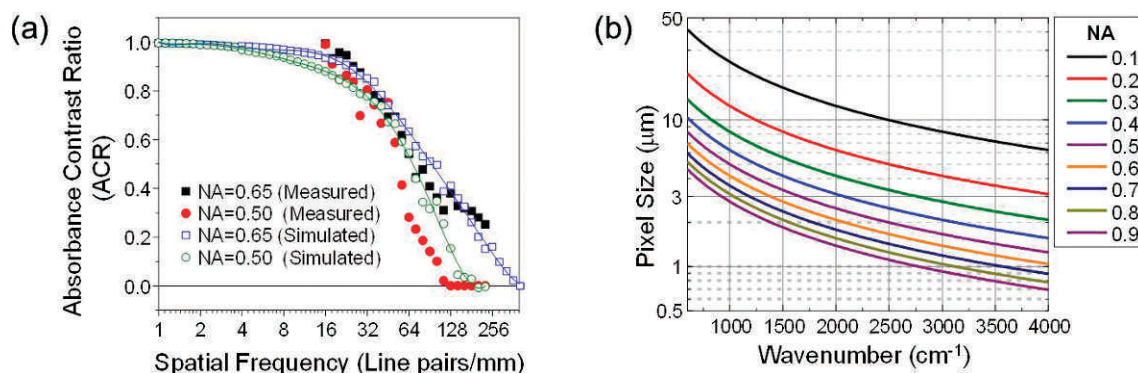


FIG. 4. (a) Plot of absorbance contrast ratio (ACR) measured from both simulation and recorded experimental data as a function of spatial frequency at  $\bar{\nu}=3850$   $\text{cm}^{-1}$  for the two systems in Table I. (b) Plot of minimum pixel size required for correctly sampling allowable spatial frequencies as a function of  $\bar{\nu}$  and NA is shown. The pixel size corresponds to the effective pixel size at the sample.

of the high- and low-NA systems, enabled by the developed theoretical understanding, provides convincing proof that the designs of present-day instrumentation are not permitting optics-limited performance and can be rapidly and easily reconfigured to provide significantly higher imaging performance.

Though the previous analysis provides the smallest observable features, the relationship of these features to the optimal pixel size needs to be quantified. We examined the pixel size at the sample plane required for optimally sampling the signal as a function of NA and wavelength (Fig. 4b). While the optimal pixel size can also be calculated analytically, this figure provides the design parameters for instruments should a practitioner develop an instrument for high performance at any specific wavelength while using a specific lens. As expected, the recommended pixel size decreases with decreasing design wavelength. The dependence on NA is rather striking as well. It is noteworthy that most commercially available systems provide reasonably high NA, but the pixel size is not commensurate with the optical components. Thus, an improvement in incorporating a higher-NA lens is not likely to be as dramatic as using the optimal pixel size in current commercial systems. We note that this plot is based on the maximum attainable spatial frequencies for thin objects, and larger sample thicknesses are likely to achieve poorer contrast for the limiting spatial frequency.

The pixel sizes recommended will provide the highest image quality provided by the microscope, unless limited by the sample. The optimal pixel size and the resolution of an imaging system are also related. According to the Rayleigh criterion, for example, the attainable resolution is  $0.61/(\bar{\nu}\text{NA})$ . We propose to sample at  $0.25/(\bar{\nu}\text{NA})$  in order to convert the analog signal into a digital readout without information loss. We note that the pixel size proposed is significantly smaller than the resolution. This result is contrary to prevailing wisdom in that it is widely believed that no further improvement is possible once a pixel size equal to the resolution has been attained. Indeed, mixing the concepts of resolution and pixel sizes for correct signal sampling has led to significant confusion in IR microscopy. We emphasize that our suggestions for improved data quality are not a contravention of the resolution criterion. Consider the case of pixel spacing resulting in optimal resolution. To resolve two objects, we need more than two measurements when the data are digitized. For example, consider two point objects that

are centered on a pixel each. To entirely resolve these objects, appropriate sampling implies that there be a pixel on either side of the object to separate them from each other and any other neighboring objects. Therefore, at least five pixels are needed to resolve two point objects. A more formal discussion of sampling for optical microscopy<sup>6, 24</sup> and its extension to IR microscopy using this signal processing approach is provided elsewhere. Our approach is distinct from these methods and incorporates light transmission through an entire imaging system and provides calculations based on absorbance. We note that the resolution of an instrument cannot be correctly evaluated unless the pixel size is appropriate (smaller). Even if two objects cannot be resolved into their appropriate shapes by using smaller pixels, the detail in higher pixel-density images is higher. Two point objects, for example, will appear as dumbbells or ovals. Hence, even for systems or wavelengths in which the pixel size is smaller than required for correctly sampling the spatial frequencies permitted by the optics, an improvement in image quality might be observed. For a detailed discussion, we refer the reader to the Appendix.

Data from the two optical configurations described in Table I are shown in Fig. 5. Data are recorded on prostate tissue that is prepared with methods previously reported,<sup>25–27</sup> and images are obtained with the absorbance of the asymmetric C–H stretching vibrational mode (at 2962  $\text{cm}^{-1}$ ). The top row demonstrates the improvement in image quality attained with the higher-NA lens. The bottom row presents the spatial frequency content of corresponding images. It can be observed from Figs. 5e–5h that there are relatively higher spatial frequencies present in the data acquired with the higher-NA lens, signifying that there is degradation of image quality, i.e., information loss in increasing the pixel size from 1.115 to 5.5  $\mu\text{m}$ . There is a noticeable set of high spatial frequencies present in the data acquired at the higher NA at the shorter wavelength. Even for longer wavelengths, the information content difference is relatively small, but not zero. To capture the highest image quality across the spectrum, hence, the pixel size should be calculated based on the highest wavenumber measured in the experiment. This statement is both rigorously and intuitively correct. From a practical perspective, however, a small pixel size calculated at the highest wavenumber also reduces the throughput significantly across the rest of the spectrum. To address this trade-off in an optimal manner, we recommend that the highest wavenumber at which pixel size



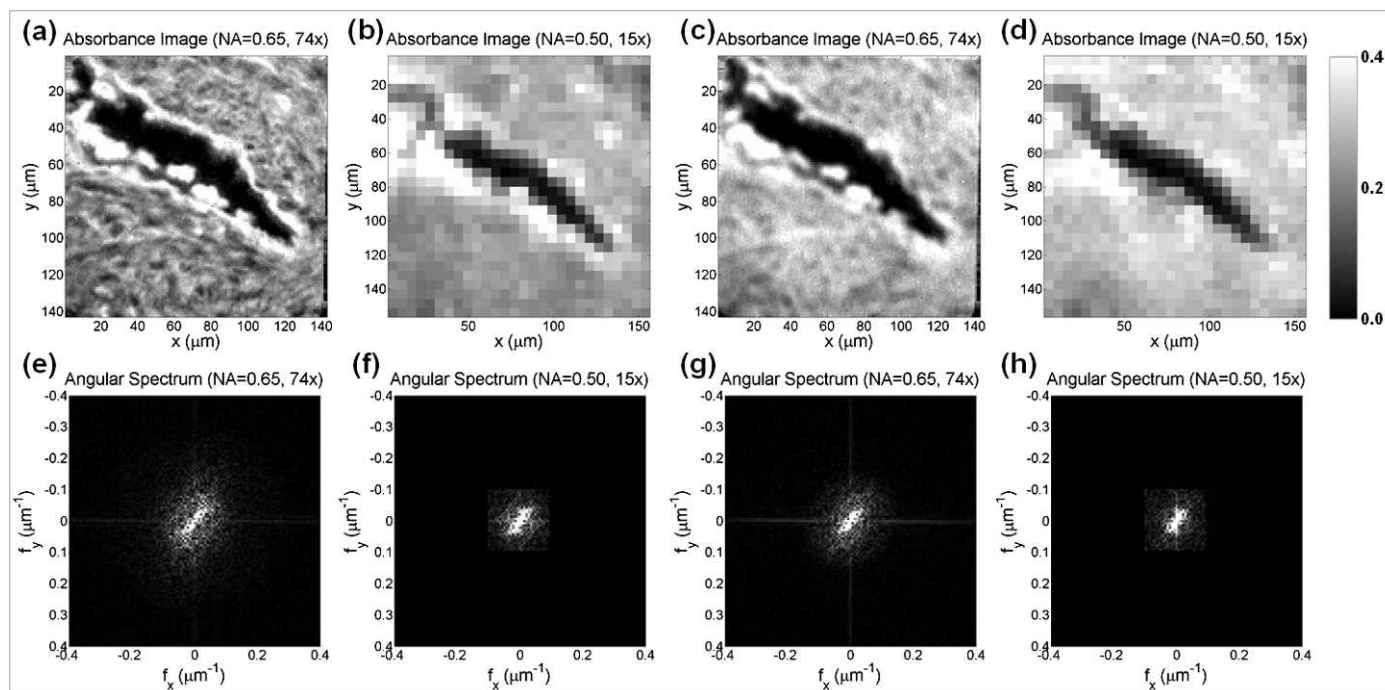


FIG. 5. Absorbance images from spectroscopic imaging data obtained from the two configurations ( $NA = 0.65$ ,  $NA = 0.50$ ) are shown on top. The corresponding angular spectra are shown at the bottom. Images for the system with (a)  $NA = 0.65$  and (b)  $NA = 0.50$  obtained by plotting the absorbance at  $\bar{\nu} = 2962 \text{ cm}^{-1}$ . Similarly, the absorbance at  $\bar{\nu} = 1650 \text{ cm}^{-1}$  is shown for systems with (c)  $NA = 0.65$  data and (d)  $NA = 0.50$ .

should be calculated should depend on the typical experiments to be performed by the imaging system. This small adjustment from the correct sampling at the highest *recorded* wavenumber to that at the highest *usable* wavenumber for image generation leads to the concept of an optimal pixel size. For most studies in the mid-IR, the  $4000$  to  $400 \text{ cm}^{-1}$  spectral region is most interesting. For He-Ne laser reference-based systems, an undersampling of the reference signal by a factor of four typically implies that the allowable free-scanning spectral range is  $3950$ – $0 \text{ cm}^{-1}$ . An optimal pixel size at the high end of this range is  $0.974 \text{ }\mu\text{m}$ . In most experiments, especially with biological systems, vibrational modes at this high limit are very rarely encountered. A more practical high wavenumber region is  $3400 \text{ cm}^{-1}$ , which is in the vicinity of the absorption peak of O–H and N–H stretching-associated vibrational modes. Therefore, we calculate the optimal pixel size at this wavenumber and the predicted pixel size is  $1.13 \text{ }\mu\text{m}$  on a side. As we sought to implement the concept of optimal pixel sampling on a commercial imaging system without extensive hardware modifications, the measured pixel size of  $1.115 \text{ }\mu\text{m}$  can be deemed acceptably close. Our suggested optimal pixel size is approximately fourfold larger than a similar setup when using the synchrotron.<sup>13</sup> It is notable that intensity considerations are secondary for a synchrotron source-based system because of the exceptional flux and a pixel size of  $0.54 \text{ }\mu\text{m}$  on a side was used. Relaxing the very strict condition with a more practical calculation here, we maximize the spectral quality when using a globar source, without compromising the image quality in any appreciable manner. The image quality presented here is likely of the highest quality that will be observed in commonly analyzed biomedical material or forensic samples regardless of the source.

Though image quality is improved with a smaller pixel size,

there is a corresponding decrease in throughput if the same source and fore-optics are employed. The approximate 25-fold reduction in pixel area between the two configurations here implies that acquisition time would need to be increased 625-fold (other factors being constant) if the data quality is to be recovered by signal averaging.<sup>28,29</sup> Some of the loss is mitigated by increased throughput, as proposed when using a synchrotron,<sup>13</sup> or by increased integration time of the FPA, as in the experiments conducted here. We observed a six- to eightfold decrease in recorded signal when using the higher-NA lens compared with the lower-NA system. Hence, the need to signal average is not especially drastic. Further, there are other methods to increase SNR. We previously proposed computational noise reduction<sup>30,31</sup> to obtain a significant gain in SNR without the corresponding increase in data collection time. The utility of this idea is presented in Fig. 6. A significant increase in spectral SNR (Fig. 6c) without observable loss in image quality (Figs. 6a and 6b) can be observed. Thus, a tabletop, high-definition IR imaging system is indeed feasible and can provide both excellent spectra and spatial image quality.

## CONCLUSION

A complete theoretical understanding of the image formation in an IR microscope was provided by using a rigorous theoretical model. The model was used to predict the optimal pixel size at the sample plane that would provide the highest image quality. Simulations demonstrated that the effects of the higher-NA systems arose from an increased acceptance of angular frequencies and resulted in higher-resolution images, whereas optimal pixel sampling demonstrated dramatic improvements in image detail for a specific NA. The results of simulations were validated with measurements on two different

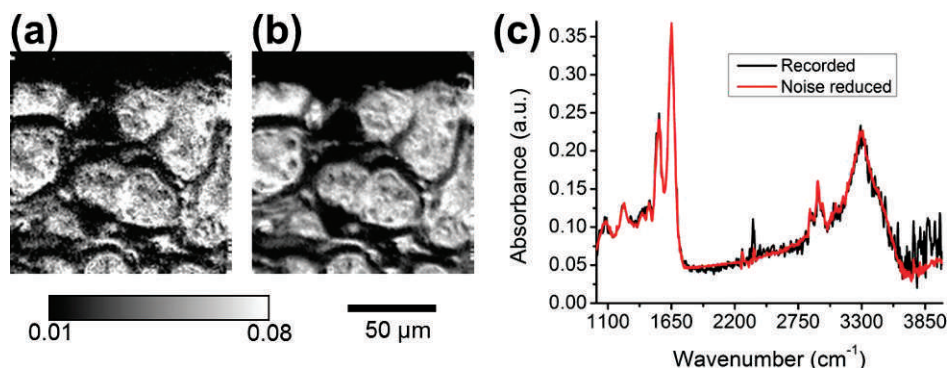


FIG. 6. Infrared spectroscopic imaging data from breast tissue before and after noise reduction. (a) An absorbance image at the asymmetric C–H stretching mode before noise reduction and the corresponding image (b) after noise reduction. (c) Spectra corresponding to recorded data and data after noise reduction from the same pixel.

configurations. A tabletop, high-definition FT-IR spectroscopic imaging system was demonstrated by minimally modifying a commercial system. The resulting data when using this high-definition system can be of high spatial and spectral quality by using conventional signal averaging and/or emerging signal

processing methods. The development of a theoretical understanding and its application to microscope design and acquisition of high-definition data should spur improved applications in many fields where IR imaging is applied.<sup>33</sup>

#### ACKNOWLEDGMENTS

The project described was supported by awards R01CA138882 and R01EB009745 from the U.S. National Institutes of Health. M.V. Schulmerich acknowledges support through Congressionally Directed Medical Research Program Postdoctoral Fellowship BC101112.

#### APPENDIX

#### DERIVATION OF THE TRANSFER FUNCTION OF THE SCHWARZSCHILD

We model the Schwarzschild as a focusing system with two concentric apertures, one outer aperture with  $NA_{out} = \sin(\theta_{out})$  and a second inner circular obstruction with  $NA_{in} = \sin(\theta_{in})$  (see Fig. A1). The focal length, which is the distance between the Schwarzschild and the focal point, is assumed known.

Consider an object placed a distance  $d_1$  from the Schwarzschild-

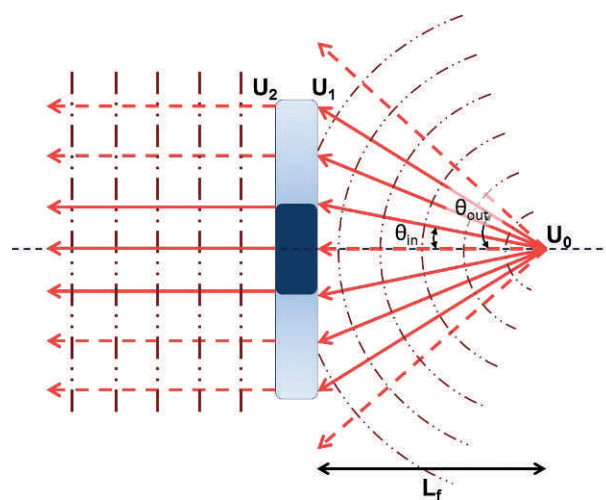


FIG. A1. A Schwarzschild model. A point source placed at the focus results in a plane wave. The outer and inner numerical apertures limit the angles that enter the Schwarzschild.

TABLE II. A list of symbols used along with their description.

Symbol	Description
$\bar{\nu}$	Wavenumber
$NA_{C_{out}}, NA_{C_{in}}$	Outer and inner numerical aperture of Schwarzschild $C_i$
$\mathbf{r} = (x, y), \mathbf{r}' = (x', y')$	Coordinate space variables
$\mathbf{f} = (f_x, f_y), \mathbf{f}_1, \mathbf{f}_2$	Transverse spatial frequency variables
$f_z$	Longitudinal spatial frequency variable
$z$	Axial position (along the principal axis of light propagation)
$z_D$	Axial detector position
$z_1$	Beam splitter position
$z_{C_i}$	Axial position of Schwarzschild $C_i$
$z_{f_i}$	Axial position where light is focused by Schwarzschild $C_i$
$d_1, d_2$	Light propagation distances
$d_{A_1}, d_{A_2}$	Light propagation distances along each arm of the interferometer
$L_{f_i}$	Focal length of Schwarzschild $C_i$
$L_{pixel}$	Length of (one side of) a pixel
$A_0, B_0$	Constants
$U(\mathbf{r}), U^*(\mathbf{r})$	Field in any plane and its corresponding complex conjugate respectively
$\tilde{U}(\mathbf{f})$	Fourier transform of the field in a plane
$\delta(\mathbf{f})$	Two-dimensional Dirac delta function
$I_0(\mathbf{r})$	Source intensity
$I(\mathbf{r})$	Intensity in a plane
$h(\mathbf{r}; \mathbf{r}')$	Transfer function for coherent light
$ U_{z_1}\rangle$	Field in a plane at $z = z_1$
$\langle U_{z_1} $	Hermitian adjoint of field in a plane at $z = z_1$
$ U_{z_{f_i}+}\rangle$	Field immediately after the plane at $z = z_{f_i}$
$ U_0\rangle$	Field from the source
$ U_i\rangle$	Field in plane $i$ , for $i = 1, 2, 3$
$ S\rangle$	Sample
$Q_{C_i}$	Aperture function of Schwarzschild $C_i$
$M_{C_i}$	Magnification of Schwarzschild $C_i$
$M = M_{C_D} M_{C_2}$	Net magnification between the sample and the detector
$\mathbf{A}$	Operator for the entire optical imaging system
$\mathbf{K}_d$	Propagation operator for a propagation distance $d$
$\mathbf{I}_{d_{A_1}, d_{A_2}}$	Operator for the interferometer where $d_{A_1}, d_{A_2}$ are path lengths along the arms
$\mathbf{H}_{C_i}$	Transfer function (operator) for a Schwarzschild $C_i$ in focus
$\mathbf{G}_{C_i}$	Transmission function (operator) of Schwarzschild $C_i$

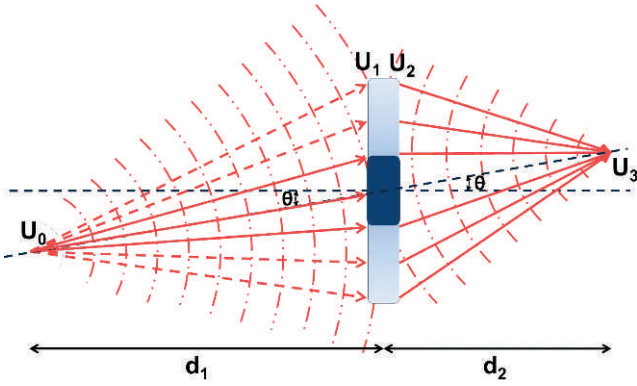


FIG. A2. An object placed at distance  $d_1$  from the Schwarzschild produces an image at position  $d_2$  on the other side.

child, as shown in Fig. A2. Let the field in a plane perpendicular to the principal axis at the object be  $|U_0\rangle$ . The field,  $|U_1\rangle$ , just before the Schwarzschild is given by:

$$|U_1\rangle = \mathbf{K}_{d_1}|U_0\rangle \quad (\text{A1})$$

The field immediately after the Schwarzschild,  $|U_2\rangle$ , can be expressed in terms of  $|U_1\rangle$  and an operator,  $\mathbf{G}_C$ , corresponding to the transmission function of the Schwarzschild as:

$$|U_2\rangle = \mathbf{G}_C|U_1\rangle \quad (\text{A2})$$

$$\mathbf{G}_C = \int d^2r |\mathbf{r}\rangle Q_C(\mathbf{r}) \exp\left[i\frac{\pi\bar{v}}{L_f}r^2\right] \langle\mathbf{r}| \quad (\text{A3})$$

where  $L_f$  is the focal length of the Schwarzschild. Note that the quadratic phase function in Eq. A3 is present because we have used a thin lens like approximation for the focusing system.  $Q_C(\mathbf{r}) = Q_{R_1}^{R_2}(\mathbf{r})$  is defined in Eq. A4, and  $R_1$  and  $R_2$  are the inner and outer aperture radii.

$$Q_a^b(\mathbf{r}) = \begin{cases} 1 & a < r < b \\ 0 & \text{else} \end{cases} \quad (\text{A4})$$

The field  $|U_3\rangle$  in the image plane is

$$|U_3\rangle = \mathbf{K}_{d_2}|U_2\rangle \quad (\text{A5})$$

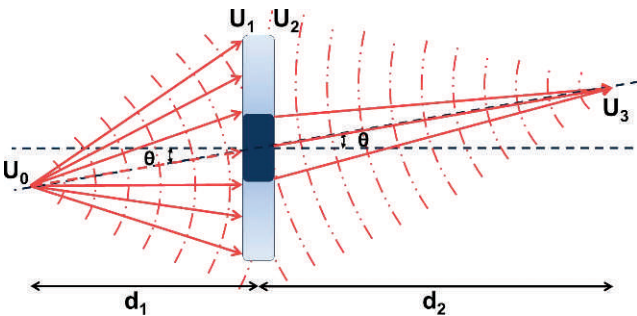


FIG. A3. The Schwarzschild is flipped, and the object distance  $d_1$  is smaller than the image distance  $d_2$  on the other side. Equivalently, a larger range of angles are accepted by the Schwarzschild from the object side.

The term  $f_z(\mathbf{f})$  in  $\mathbf{K}_d$  can be approximated as  $f_z(\mathbf{f}) \approx v(1 - (f^2/2\bar{v}^2))$ . After substituting Eq. A2 and Eq. A1 in Eq. A5 and simplifying we obtain

$$\begin{aligned} |U_3\rangle &= \mathbf{K}_{d_2} \mathbf{G}_C \mathbf{K}_{d_1} |U_0\rangle \\ &= \int d^2r d^2r' d^2r'' |\mathbf{r}\rangle Q_{R_1}^{R_2}(\mathbf{r}') \langle\mathbf{r}'| U_0\rangle \exp\left[i\frac{2\pi\bar{v}}{d_1} \mathbf{r} \cdot \mathbf{r}'\right] \\ &\quad \times \exp\left[i\frac{2\pi\bar{v}}{d_2} \mathbf{r}'' \cdot \mathbf{r}\right] \exp\left[i\frac{2\pi\bar{v}}{2d_2} r''^2\right] \exp\left[i\frac{2\pi\bar{v}}{2d_1} r'^2\right] \\ &\quad \times \exp\left[i\frac{2\pi\bar{v}}{2} \left(\frac{1}{d_1} + \frac{1}{d_2} - \frac{1}{L_f}\right) r^2\right] \end{aligned} \quad (\text{A6})$$

This is the relation between the image and the object for a Schwarzschild. In most FT-IR imaging systems, we can make a few approximations and simplify Eq. 26. The object size (illuminated area of the sample) is typically much smaller than the size of the Schwarzschild. This means that  $\exp[i(2\pi\bar{v}/2d_1)r'^2] \approx 1$ . The image size is also much smaller than the Schwarzschild dimensions; therefore,  $\exp[i(2\pi\bar{v}/2d_2)r''^2] \approx 1$ . We know that<sup>32</sup> for a thin lens (or, more generally, for a system that focuses light like a thin lens), the position of the image and object are related by  $(1/d_1) + (1/d_2) = (1/L_f)$ . Therefore,  $\exp\{i(2\pi\bar{v}/2)[(1/d_1) + (1/d_2) - (1/L_f)](x^2 + y^2)\} = 1$ .

With these approximations, Eq. A6 reduces to:

$$\begin{aligned} |U_3\rangle &= \int d^2r d^2r' d^2r'' |\mathbf{r}\rangle Q_{R_1}^{R_2}(\mathbf{r}') \langle\mathbf{r}'| U_0\rangle \\ &\quad \times \exp\left[i\frac{2\pi\bar{v}}{d_1} \mathbf{r} \cdot \mathbf{r}'\right] \exp\left[i\frac{2\pi\bar{v}}{d_2} \mathbf{r}'' \cdot \mathbf{r}\right] \end{aligned} \quad (\text{A7})$$

Defining magnification  $M_C = (d_2/d_1)$  and evaluating this integral after projecting on the Fourier basis yields

$$\langle\mathbf{f}|U_3\rangle = Q_{R_1}^{R_2}\left(-\frac{\mathbf{f}d_2}{\bar{v}}\right) \langle-M_C\mathbf{f}|U_0\rangle \quad (\text{A8})$$

It can be noted that the system is linear, but *not* shift invariant (because of the magnification term). With this caveat, we can think of  $Q_{R_1}^{R_2}(-\mathbf{f}d_2/\bar{v})$  as the Schwarzschild transfer function. In our model, the exact values of focal lengths are not required, provided that the system is in focus. Only the outer and inner numerical apertures of the Schwarzschilds and the magnification factors are required.

For a Schwarzschild with an orientation as in Fig. 8, typically the image is close to the focus. Thus, we can make approximations that  $d_2 \approx d_2 \approx L_f$  ( $L_f$  is focal length),  $\text{NA}_{\text{out}} \approx (R_2/d_2)$  and  $\text{NA}_{\text{in}} \approx (R_1/d_1)$ . Also note that  $\mathbf{Q}$  is an even function. This gives

$$\langle\mathbf{f}|U_3\rangle = Q_{\bar{v}\text{NA}_{\text{in}}}^{\bar{v}\text{NA}_{\text{out}}}(\mathbf{f}) \langle-M_C\mathbf{f}|U_0\rangle \quad (\text{A9})$$

Note that propagation in free space is a spatial frequency band pass  $Q_0^{\bar{v}}(\mathbf{f})$  and spatial frequencies beyond  $\bar{v}$  do not reach the detector. For a Schwarzschild with an orientation as in Fig. A9, the object is close to the focus and so we can make the approximations that  $d_1 \approx L_f$ ,  $\text{NA}_{\text{out}} \approx (R_2/d_1)$  and  $\text{NA}_{\text{in}} \approx (R_1/d_1)$ . This gives

$$\langle\mathbf{f}|U_3\rangle = Q_{\bar{v}\text{NA}_{\text{in}}}^{\bar{v}\text{NA}_{\text{out}}}(M_C\mathbf{f}) \langle-M_C\mathbf{f}|U_0\rangle \quad (\text{A10})$$

$$\langle-\mathbf{f}/M_C|U_3\rangle = Q_{\bar{v}\text{NA}_{\text{in}}}^{\bar{v}\text{NA}_{\text{out}}}(\mathbf{f}) \langle\mathbf{f}|U_0\rangle \quad (\text{A11})$$



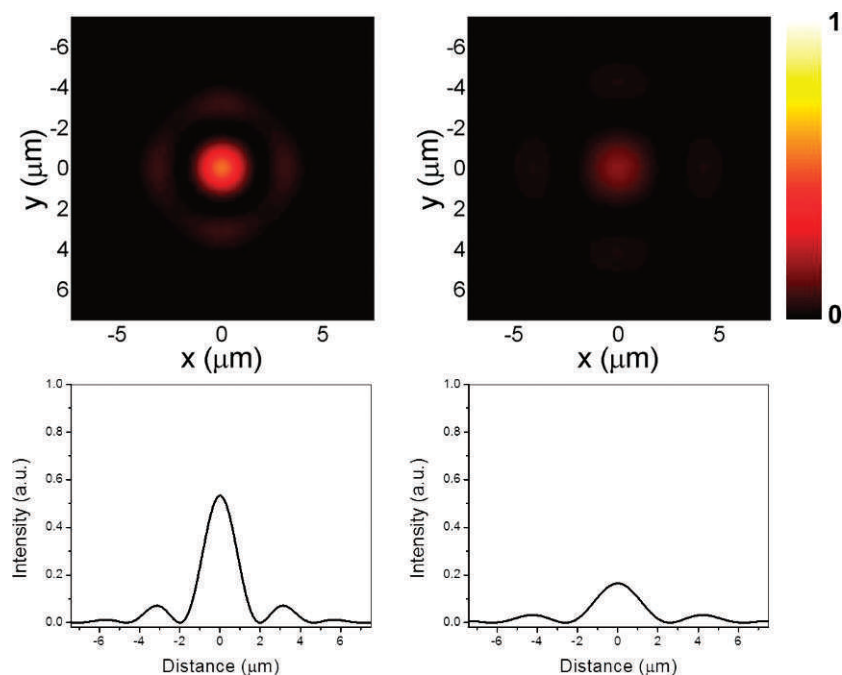


FIG. A4. Point-spread functions. Data on the left correspond to a configuration with  $NA_{C_2out} = 0.65$  and data on the right corresponds to a configuration with  $NA_{C_2out} = 0.5$ .

**Point-Spread Functions and Resolution.** Point-spread functions for the two configurations in the article Table I are presented in Fig. A4.

Simulation data for two point objects separated by four different distances are presented in Figs. A5 and A6. Data in Fig. A5 correspond to the high-NA configuration in the article Table I, and Fig. A6 corresponds to the lower-NA configuration. All data are at  $3950\text{ cm}^{-1}$ . Axes in all the images are

scaled to the effective size of the detector-intensity-image at the sample. From these images, it is evident that two points separated by  $1\text{ }\mu\text{m}$  cannot be resolved with either  $NA_{C_2out} = 0.65$  or  $NA_{C_2out} = 0.5$ , whereas they can be resolved in both configurations at a separation of  $4\text{ }\mu\text{m}$ . However,  $NA_{C_2out} = 0.65$  can resolve two points separated by  $2.4\text{ }\mu\text{m}$  (which is the resolution according to Rayleigh criterion), while  $NA_{C_2out} 0.5$  cannot. Points at a separation of  $3\text{ }\mu\text{m}$  can be just resolved with

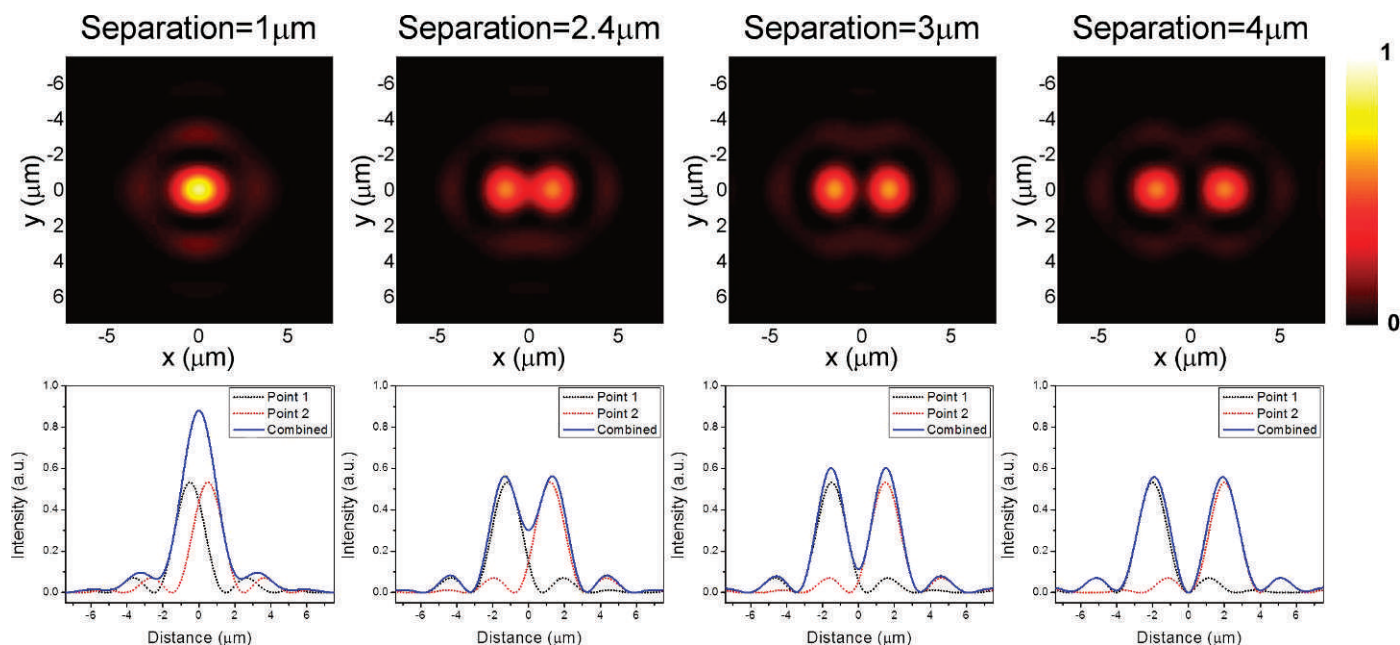


FIG. A5. Intensity at the detector plane at  $3950\text{ cm}^{-1}$  for two point objects separated by distances (indicated on top). Corresponding profile plots at  $y = 0$  are presented in the bottom row. Schwarzschild  $C_2$  has  $NA_{C_2out}$  0.65. Axes are scaled to the effective image size at the sample.

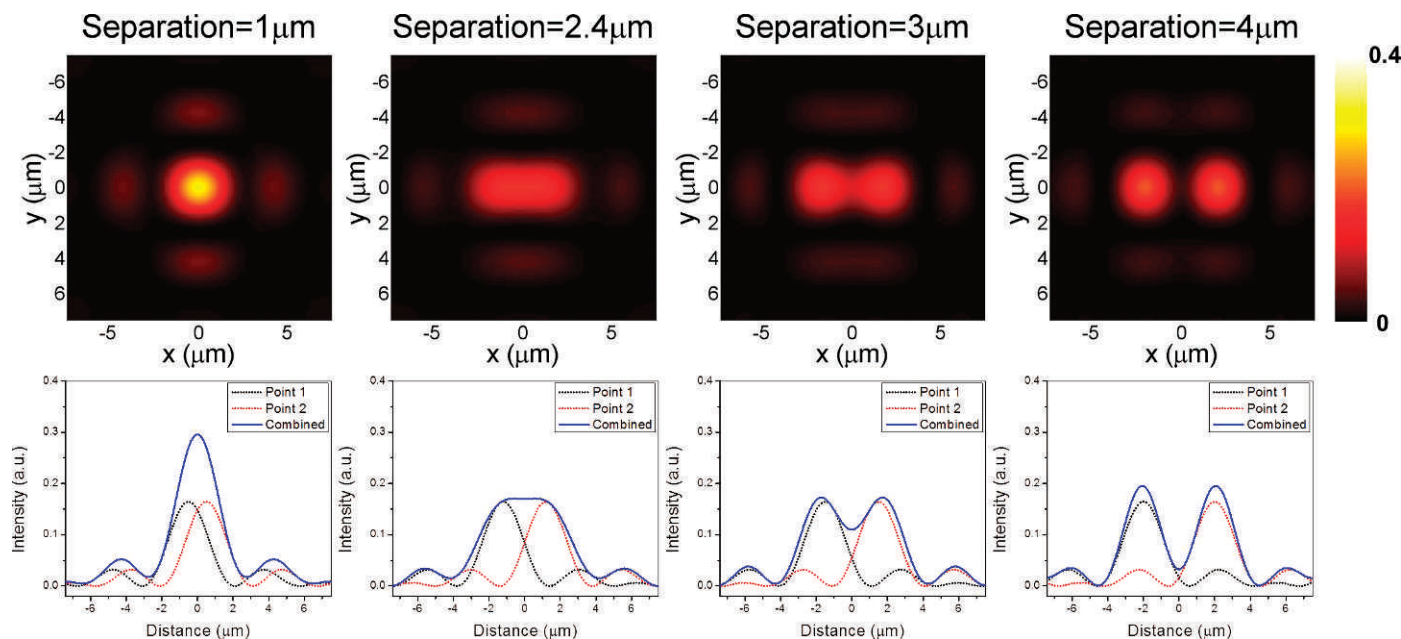


FIG. A6. Intensity at the detector plane at  $3950\text{ cm}^{-1}$  for two point objects separated by distances (indicated on top). Corresponding profile plots at  $y = 0$  are presented in the bottom row. Schwarzschild  $C_2$  has  $NA_{C_{2out}} = 0.5$ . Axes are scaled to the effective image size at the sample.

$NA_{C_{2out}} = 0.5$ . Data presented here illustrate the best image quality obtainable from systems with the optical configurations in the article Table I, without discretization (i.e., using an analog detector). Discretized data obtained at the optimal pixel size (as calculated in section “Pixel Size” in the article) have all the information needed to construct images of this quality.

1. E.N. Lewis, P.J. Treado, R.C. Reeder, G.M. Story, A.E. Dowrey, C. Marcott, I.W. Levin. “Fourier Transform Spectroscopic Imaging Using an Infrared Focal-Plane Array Detector”. *Anal. Chem.* 1995. 67(19): 3377-3381.
2. R. Barer, A.R.H. Cole, H.W. Thompson. “Infra-red Spectroscopy with the Reflecting Microscope in Physics, Chemistry and Biology”. *Nature*. 1949. 163(4136): 198-201.
3. R.C. Gore. “Infrared Spectrometry of Small Samples with the Reflecting Microscope”. *Science*. 1949. 110(2870): 710-711.
4. J.M. Kwiatkowski, J.A. Reffner. “FT-IR Microspectrometry Advances”. *Nature*. 1987. 328: 837-838.
5. N. Jamin, P. Dumas, J. Moncuit, W.H. Fridman, J.L. Teillaud, G.L. Carr, G.P. Williams. “Highly Resolved Chemical Imaging of Living Cells by Using Synchrotron Infrared Microspectrometry”. *P. Natl. Acad. Sci. USA*. 1998. 95(9): 4837-4840.
6. G.L. Carr. “Resolution Limits for Infrared Microspectroscopy Explored with Synchrotron Radiation”. *Rev. Sci. Instrum.* 2001. 72: 1613-1619.
7. P. Dumas, N. Jamin, J.L. Teillaud, L.M. Miller, B. Beccard. “Imaging Capabilities of Synchrotron Infrared Microspectroscopy”. *Faraday Discuss.* 2004. 126: 289-302.
8. F. Briki, B. Busson, L. Kreplak, P. Dumas, J. Doucet. “Exploring a Biological Tissue from Atomic to Macroscopic Scale Using Synchrotron Radiation: Example of Hair.” *Cell. Mol. Biol. (Noisy-le-Grand, France)* 2000. 46(5): 1005-1016.
9. L.M. Miller, P. Dumas. “Chemical Imaging of Biological Tissue with Synchrotron Infrared Light”. *Biochim. Biophys. Acta*. 2006. 1758(7): 846-857.
10. M. Offroy, Y. Roggo, P. Milanfar, L. Duponchel. “Infrared Chemical Imaging: Spatial Resolution Evaluation and Super-Resolution Concept”. *Anal. Chim. Acta*. 2010. 674(2): 220-226.
11. R. Bhargava, I. Levin. *Spectrochemical Analysis Using Infrared Multichannel Detectors*. New York: Wiley-Blackwell, 2005.
12. C. Petibois, M. Cestelli-Guidi, M. Piccinini, M. Moenner, A. Marcelli. “Synchrotron radiation FTIR imaging in minutes: A First Step Towards Real-Time Cell Imaging”. *Anal. Bioanal. Chem.* 2010. 397(6): 2123-2129.

13. M.J. Nasse, M.J. Walsh, E.C. Mattson, R. Reininger, A. Kajdacsy-Balla, V. Macias, R. Bhargava, C.J. Hirschmugl. “High-Resolution Fourier-Transform Infrared Chemical Imaging with Multiple Synchrotron Beams”. *Nature Methods*. 2011. 8(5): 413-416.
14. P. Lasch, D. Naumann. “Spatial Resolution in Infrared Microspectroscopic Imaging Of Tissues”. *Biochimica et Biophysica Acta*. 2006. 1758(7): 814-829.
15. J. Widengren, U. Mets. “Single Molecule Detection in Solution”. Wiley Online Library. 2002.
16. B.J. Davis, P.S. Carney, R. Bhargava. “Theory of Infrared Microspectroscopy for Intact Fibers”. *Anal. Chem.* 2011. 83(2): 525-532.
17. B.J. Davis, P.S. Carney, R. Bhargava. “Theory of Midinfrared Absorption Microspectroscopy: I. Homogeneous Samples”. *Anal. Chem.* 2010. 82(9): 3474-3486.
18. R. Reddy, B. Davis, P.S. Carney, R. Bhargava. “Modeling Fourier Transform Infrared Spectroscopic Imaging of Prostate and Breast Cancer Tissue Specimens”. *International Symposium on Biomedical Imaging*. 2011: 738-741.
19. B.J. Davis, P.S. Carney, R. Bhargava. “Theory of Mid-infrared Absorption Microspectroscopy: II. Heterogeneous Samples”. *Anal. Chem.* 2010. 82(9): 3487-3499.
20. J. Filik, M.D. Frogley, J.K. Pijanka, K. Wehbe, G. Cinque. “Electric Field Standing Wave Artifacts in FTIR Micro-spectroscopy of Biological Materials”. *Analyst*. 2012. 137(4): 853-861.
21. J.W. Goodman. *Introduction to Fourier Optics*. Englewood, CO: Roberts and Company Publishers, 2005.
22. P.A.M. Dirac. *The Principles of Quantum Mechanics*. Oxford, UK: Oxford University Press, 1958.
23. I.W. Levin, R. Bhargava. “Fourier Transform Infrared Vibrational Spectroscopic Imaging: Integrating Microscopy and Molecular Recognition”. *Annu. Rev. Phys. Chem.* 2005. 56: 429-474.
24. E.H.K. Stelzer. “Contrast, Resolution, Pixelation, Dynamic Range and Signal-To-Noise Ratio: Fundamental Limits to Resolution in Fluorescence Light Microscopy”. *Journal of Microscopy*. 1998. 189(1): 15-24.
25. D.C. Fernandez, R. Bhargava, S.M. Hewitt, I.W. Levin. “Infrared Spectroscopic Imaging for Histopathologic Recognition”. *Nat. Biotechnol.* 2005. 23(4): 469-474.
26. R. Bhargava, D.C. Fernandez, S.M. Hewitt, I.W. Levin. “High-Throughput Assessment of Cells and Tissues: Bayesian Classification of Spectral Metrics from Infrared Vibrational Spectroscopic Imaging Data”. *Biochim. Biophys. Acta*. 2006. 1758(7): 830-845.
27. R. Bhargava, R. Schwartz Perlman, D.C. Fernandez, I.W. Levin, E.G. Bartick. “Non-invasive Detection of Superimposed Latent Fingerprints and

- Inter-Ridge Trace Evidence by Infrared Spectroscopic Imaging". *Anal. Bio. Chem.* 2009. 394(8): 2069-2075.
28. R. Bhargava, I.W. Levin. "Fourier transform infrared imaging: theory and practice". *Anal. Chem.* 2001. 73(21): 5157-5167.
29. P.R. Griffiths, J.A. De Haseth. *Fourier Transform Infrared Spectroscopy*. New York: John Wiley and Sons, 1986.
30. R. Bhargava, S.Q. Wang, J.L. Koenig. "Route to Higher-Fidelity FTIR Imaging". *Appl. Spectrosc.* 2000. 54(4): 486-495.
31. R.K. Reddy, R. Bhargava. "Accurate Histopathology from Low Signal-To-Noise Ratio Spectroscopic Imaging Data". *Analyst.* 2010. 135(11): 2818-2825.
32. B.E.A. Saleh, M.C. Teich. *Fundamentals of Photonics*. New York: John Wiley and Sons, 2007.
33. R. Bhargava. "Infrared Spectroscopic Imaging: The Next Generation". *Appl. Spectrosc.* 2012. 66(10): 1091-1120.



# Off-Resonance Surface-Enhanced Raman Spectroscopy from Gold Nanorod Suspensions as a Function of Aspect Ratio: Not What We Thought

Sean T. Sivapalan,<sup>†</sup> Brent M. DeVetter,<sup>‡,§</sup> Timothy K. Yang,<sup>‡</sup> Thomas van Dijk,<sup>||</sup> Matthew V. Schulmerich,<sup>§,||</sup> P. Scott Carney,<sup>‡,§</sup> Rohit Bhargava,<sup>‡,§,||,\*</sup> and Catherine J. Murphy<sup>†,‡,\*</sup>

<sup>†</sup>Department of Materials Science and Engineering, <sup>‡</sup>Department of Electrical and Computer Engineering, <sup>§</sup>Beckman Institute for Advanced Science and Technology, <sup>||</sup>Department of Chemistry, <sup>||</sup>Department of Bioengineering, and <sup>†</sup>Department of Mechanical Science and Engineering, Micro and Nanotechnology Laboratory and University of Illinois Cancer Center, University of Illinois at Urbana—Champaign, Urbana, Illinois 61801, United States

**ABSTRACT** Design of nanoparticles for surface-enhanced Raman scattering (SERS) within suspensions is more involved than simply maximizing the local field enhancement. The enhancement at the nanoparticle surface and the extinction of both the incident and scattered light during propagation act in concert to determine the observed signal intensity. Here we explore these critical aspects of signal generation and propagation through experiment and theory. We synthesized gold nanorods of six different aspect ratios in order to obtain longitudinal surface plasmon resonances that incrementally spanned 600–800 nm. The Raman reporter molecule methylene blue was trap-coated near the surface of each nanorod sample, generating SERS spectra, which were used to compare Raman signals. The average number of reporter molecules per nanorod was quantified against known standards using electrospray ionization liquid chromatography mass spectrometry. The magnitude of the observed Raman signal is reported for each aspect ratio along with the attenuation due to extinction in suspension. The highest Raman signal was obtained from the nanorod suspension with a plasmon resonance blue-shifted from the laser excitation wavelength. This finding is in contrast to SERS measurements obtained from molecules dried onto the surface of roughened or patterned metal substrates where the maximum observed signal is near or red-shifted from the laser excitation wavelength. We explain these results as a competition between SERS enhancement and extinction, at the excitation and scattered wavelengths, on propagation through the sample.



**KEYWORDS:** surface-enhanced Raman spectroscopy · extinction · gold nanorods

Surface-enhanced Raman scattering (SERS) is a vibrational technique whose promise for chemical sensing has been debated since the 1970s.<sup>1</sup> A primary design objective in SERS optimization is to tailor the surface plasmon resonance relative to the laser excitation wavelength. This is because the on-resonance field enhancement at the surface of the plasmon-active material can increase the Raman signal intensity of nearby molecules by several orders of magnitude. In the case of SERS on immobilized silver nanostructures, the maximum signal enhancement was observed if the plasmon band position was red-shifted compared to the laser excitation wavelength.<sup>2</sup> On the basis of these studies, researchers have

fabricated rationally designed nanoparticles for biomedical applications<sup>3</sup> such as highly sensitive assays<sup>4</sup> and multiplexed imaging.<sup>5</sup> The stable signals and multiplexing capabilities of these nanoparticles offer an attractive alternative to fluorescence-based techniques.<sup>6,7</sup> For example, a recent report notes that a SERS-based approach can outperform an enzyme-linked immunosorbent assay (ELISA).<sup>8</sup> Nanoparticle-based SERS assays could, thus, provide novel sensing capabilities that complement or improve present technologies and lead to next-generation clinical diagnostics. For example, Moskovits *et al.* have extended such studies to quantitatively confirm the ratio of cancerous to noncancerous cells in samples with two different reporter molecule—antibody

\* Address correspondence to [murphyjc@illinois.edu](mailto:murphyjc@illinois.edu), [rxb@illinois.edu](mailto:rxb@illinois.edu).

Received for review September 24, 2012 and accepted February 25, 2013.

Published online February 25, 2013  
10.1021/nn305710k

© 2013 American Chemical Society

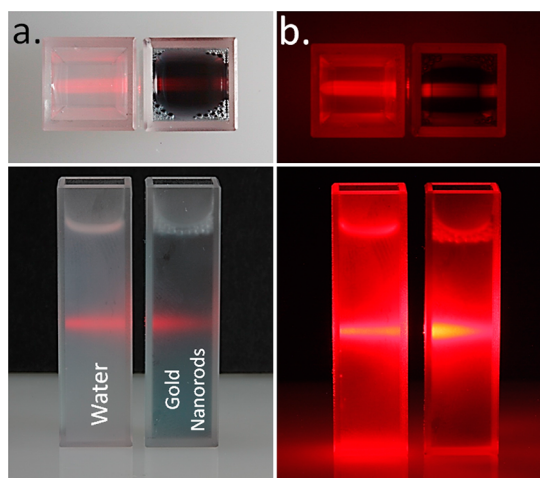


**Figure 1.** Photographs demonstrating extinction effects in solution. Upon laser illumination, minimal extinction (scattering + absorption) is observed in water (left cuvette). In contrast, suspensions of gold nanorods in water exhibit extinction under illumination (right cuvette). (a) Laser illumination under ambient lighting. (b) Laser illumination without ambient lighting.

combinations.<sup>9</sup> Using labeled nanoparticles as Raman reporters to achieve contrast in deep-tissue measurements is currently an active area of research.<sup>10,11</sup>

Light scattering, absorption, and fluorescence arising from the tissue limit the choice of Raman excitation wavelengths to the near-infrared (NIR) spectral region.<sup>12</sup> In this spectral region (700–1100 nm), gold nanorods<sup>13</sup> and nanoshells<sup>14</sup> can be used as effective SERS-active nanoparticles as they exhibit a tunable plasmon band<sup>15</sup> where tissue has low absorption.<sup>12</sup> Additionally, the presence of the nanoparticles dispersed throughout the tissue adds absorption and scattering effects to the Raman measurement as the light propagates. In this way, nanoparticles that would be injected into tissue behave much like in colloidal suspensions.

For suspensions, as opposed to substrates, accounting for light propagation and attenuation is vital. While the resonant plasmon helps to enhance the Raman signal, attenuation by absorption and scattering complicates experimental design and optimization.<sup>16</sup> Upon plasmonic excitation for anisotropic shapes like rods, the maximum electric field, on average, is at the tips of the rods; therefore, SERS signals will be dominated by events at the tips of the rods. The overall extinction of the nanorods depends not only on their shape but also on their absolute size: larger nanorods, for the same aspect ratio, lead to more extinction, with little relation to the qualities of the rod tips. Therefore, it is not a surprise that, in colloidal solution, SERS and extinction effects need to be unraveled.

This effect is clearly visible in a solution of nanoparticles. For example, Figure 1 shows a photograph of a laser beam traversing two cuvettes, illustrating extinction effects in solution. The cuvette on the left in both

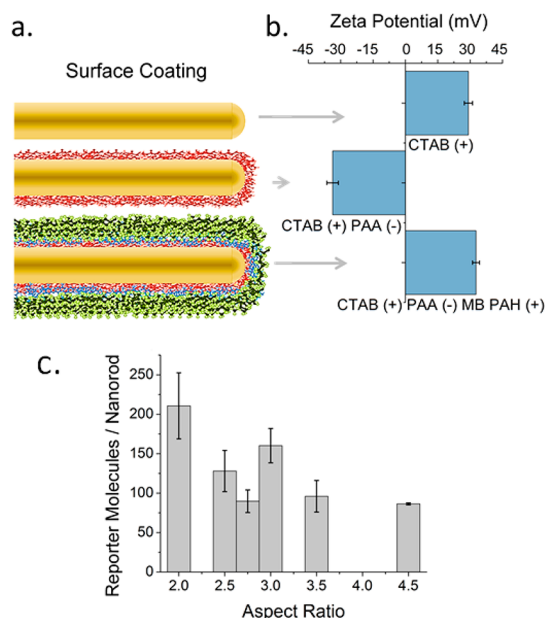


**Figure 2.** (a) Schematic of a gold nanorod with a (red) poly(acrylic acid) coating, followed by methylene blue reporter molecules (blue) and a polyallylamine hydrochloride (green) trap coat. (b) Corresponding zeta-potential for aspect ratio 3 gold nanorods as a function of layer coating corresponding to the stages in (a). (c) Quantification of the number of methylene blue reporter molecules per gold nanorod as a function of aspect ratio.

panels, containing water, displays minimal scattering and absorption, resulting in minor attenuation of the laser beam. The cuvette on the right, containing gold nanorods in suspension, shows that the laser beam is unable to penetrate effectively through the cuvette, due to a combination of absorption and scattering of light by the nanorods. Therefore, when performing SERS experiments on such nanorods in solution, Raman-scattered light would be similarly extinguished. Therefore, it is important to understand that there is an antagonistic interplay between extinction and SERS enhancement in the observed Raman signal collected from colloidal suspensions and therefore in biological sensing.

Here we explore the competition between SERS enhancement and extinction on propagation through the sample. We investigate the dependence on plasmon resonance frequency by using gold nanorods of six different aspect ratios which provide longitudinal surface plasmon resonances at wavelengths spanning 600–800 nm. The Raman reporter, methylene blue, was trap-coated with a polyelectrolyte layer near the surface of each nanorod. SERS spectra were acquired using a 785 nm excitation wavelength in transmission mode. In order to compare signals across batches of nanorods, the average number of reporter molecules per nanorod was quantified using electrospray ionization liquid chromatography mass spectrometry (ESI-LC-MS). We report the Raman signal per nanorod as a function of aspect ratio, correcting for the attenuation

due to extinction in suspension using methanol as an internal standard.

## RESULTS AND DISCUSSION

SERS measurements are typically based on Raman reporter molecules attached directly to the surface of the nanoparticles by either covalent or electrostatic interactions.<sup>17</sup> Other reports have examined the use of SERS using reporter molecules separated at fixed distances from the surface of the nanoparticles by employing a dielectric silica shell.<sup>18</sup> Here, we utilize a polyelectrolyte dielectric layer to wrap gold nanorods of a variety of aspect ratios.<sup>19</sup> A schematic of this technique is illustrated in Figure 2a. First, positively charged CTAB-capped gold nanorods were wrapped with negatively charged poly(acrylic acid) (PAA). We then attached methylene blue reporter molecules by electrostatic interactions. The reporter molecules were then trap-coated by an additional polyallylamine hydrochloride (PAH) polyelectrolyte layer.<sup>20</sup> Layer wrapping was confirmed at each step by zeta-potential measurements (Figure 2b) and electronic absorption spectra as previously described.<sup>21</sup> Shifts in the longitudinal plasmon peak of 5 nm or less are observed as the surface functionalization proceeds (Supporting Information Figure S1). The polyelectrolyte coating also stabilizes the as-synthesized CTAB-capped gold nanorods from aggregating in polar protic solvents.<sup>22</sup> As an approximate guide, assuming a 2.5 nm thick CTAB bilayer and 1.5 nm thicknesses for the polyelectrolyte layers,<sup>19,21</sup> the Raman reporter dyes should be about 4 nm from the metal surface. There is no apparent aggregation in solution, as suggested by the lack of plasmon band broadening. In the case that two nanorods are in contact, the spacer layers guarantee that the reporter molecule is approximately 4 nm away from the proximal metal surface and about 12 nm away from the distal metal surface. Although we cannot rigorously prove that there are zero aggregates in solution, these relative distances suggest that the reporter molecules are not expected to lie in hot spots.

The number of reporter molecules per nanorod was quantified for each aspect ratio by ESI-LC-MS.<sup>21</sup> We found that the average number of reporters per gold nanorod was 100–300 reporter molecules (Figure 2c). These ESI-LC-MS measurements were carried out in triplicate for three independent batches, for each aspect ratio of nanorods. The means of 9 measurements per aspect ratio, with attendant error bars of one standard deviation from the means, are shown in Figure 2c with further details in Figure S2. The values of 100–300 reporters per nanorod are far fewer than monolayer coverage. For example, methylene blue adsorbs to charged surfaces from water with a footprint of 0.66 nm<sup>2</sup>.<sup>23</sup> A full monolayer of methylene blue, hence, would imply approximately 3000 molecules per nanorod. Therefore,

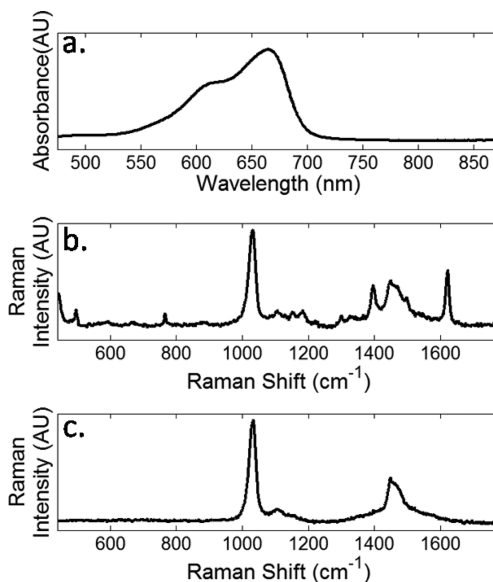


**Figure 3.** Reference spectra. (a) UV/vis of 15  $\mu\text{M}$  methylene blue in methanol. (b) Raman spectrum of 500  $\mu\text{M}$  methylene blue in methanol. (c) Raman spectrum of neat methanol.

experimental loadings are less than 10% of monolayer coverage. Using these values, we compare the experimentally observed SERS signal intensity from each gold nanorod suspension and relate them to theory.

To characterize the observed spectral signatures, we present three reference spectra in Figure 3. The electronic absorption spectrum of methylene blue in methanol is shown in Figure 3a. An absorption maximum can be seen around 670 nm with a shoulder at 650 nm, both of which are blue-shifted from the Raman laser excitation wavelength of 785 nm. This should minimize any chemical resonance effects such as those observed in surface-enhanced resonance Raman spectroscopy (SERRS).

For Raman measurements, we collected the signal from a sample of methylene blue polyelectrolyte-coated gold nanorods resuspended in methanol. This approach was first introduced by Kneipp and co-workers<sup>24</sup> and has the benefit that the methanol Raman band at 1030 cm<sup>-1</sup><sup>25</sup> can serve as an internal standard. For reference, the Raman spectra of methylene blue in methanol and of neat methanol are shown in Figure 3b,c.

We synthesized gold nanorods with aspect ratios from 2 to 4.5, resulting in a systematic variation of the longitudinal plasmon resonance band. Figure 4a shows the electronic absorption spectra of each of the gold nanorod suspensions after the final PAH polyelectrolyte trap coating. On the same spectral axes, we also depict the laser excitation wavelength with a red dotted line and the resulting Raman spectrum (black curve) for reference. Traditionally, Raman spectra are reported in terms of Raman shift from an excitation wavelength, as shown in Figure 4b, where the spectra are normalized for concentration and the number of reporter molecules per rod and then offset for clarity. From the shaded region in Figure 4a, it is obvious that

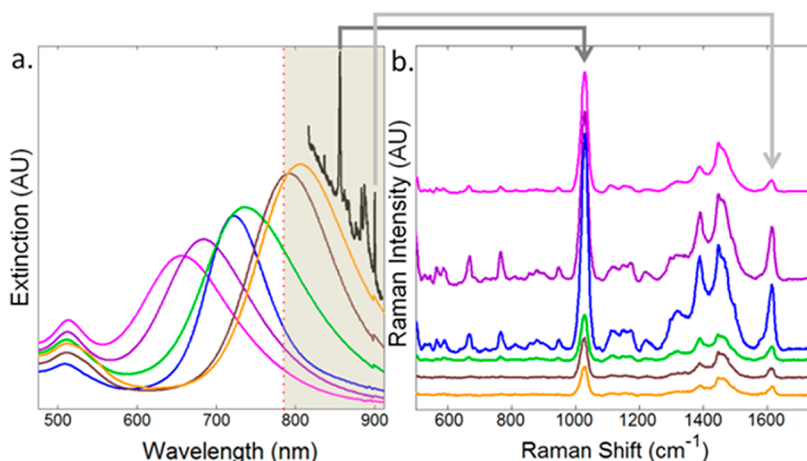


**Figure 4.** (a) Extinction spectra for gold nanorods (AR 2, pink; AR 2.5, purple; AR 2.75, blue; AR 3, green; AR 3.5, brown; and AR 4.5, orange), normalized to concentration plotted on the same axes as the position of the Raman excitation wavelength (red dots) and the resulting Raman spectrum (black). The spectral region shown in Figure 5b is highlighted by shadow in Figure 5a. (b) Surface-enhanced Raman spectrum of methylene blue attached to six different aspect ratios of gold nanorods bearing PAA polyelectrolyte layer (offset for clarity) normalized for gold nanorods and reporter molecule concentration.

the extinction profile of higher aspect ratio nanorods in suspension overlaps both the spectral profile of the Raman excitation laser and the wavelengths of Raman scattered photons. The largest Raman signal is observed for nanorods that have a plasmon band blue-shifted from the excitation frequency. To quantify the recorded signal, we examined both the reporter Raman signal as well as that of the suspending medium (methanol).

Two spectral features to characterize our suspensions are the Raman band originating from methanol at  $1030\text{ cm}^{-1}$  shift and the Raman band originating from methylene blue at  $1616\text{ cm}^{-1}$  shift (Figure 5).<sup>26</sup> The signal intensity at  $1030\text{ cm}^{-1}$  shift should only decrease from extinction of the Raman excitation wavelength since we assume methanol is not enhanced by the gold nanorods.<sup>24</sup> However, the Raman signal from the reporter at  $1616\text{ cm}^{-1}$  shift will be affected by the location of the longitudinal surface plasmon resonance determined by the aspect ratio of the gold nanorod suspensions. By examining these two bands as a function of aspect ratio, we illustrate the effects of the competing physical processes. In addition, we can select an aspect ratio that would provide the largest Raman signal in suspension.

Extinction measurements (Figure 4a) and Raman measurements of the methanol band (Figure 5) provided two estimates of the extinction due to nanorods. This extinction is quantified in Figure 6a. The competing process of SERS electromagnetic enhancement when extinction effects are considered to be negligible (*i.e.*, substrate measurements) is presented in Figure 6b. A prolate-spheroidal approximation for the rods was used to estimate absorption-free electromagnetic enhancement.<sup>27</sup> It is clear from Figure 6 that maximum extinction of the Raman excitation occurs near the

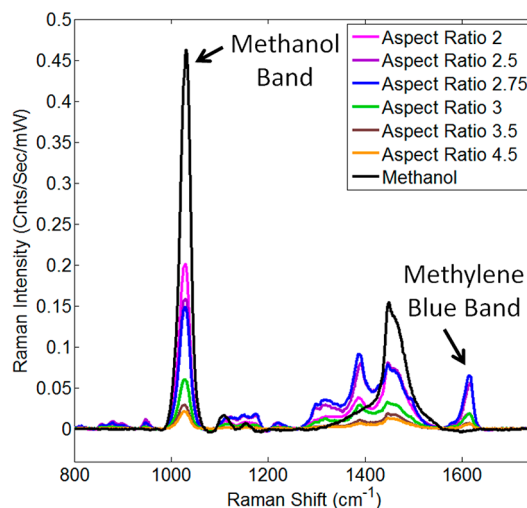


**Figure 5.** Comparison of Raman spectra acquired from gold nanorod suspensions bearing polyelectrolyte layers plus methylene blue reporter in methanol. The variation in Raman intensity for the methanol bands is illustrated by the peak at  $1030\text{ cm}^{-1}$  which varies as a function of aspect ratio. Gold nanorod suspensions are normalized for concentration and the number of reporter molecules per gold nanorod.

maximum of electromagnetic enhancement. The collected signal seen in Figure 5 illustrates this competition.

As the SERS signal will vary as a function of the nanoparticle concentration and the number of reporter molecules per nanoparticle, it is important to account for these variations in order to understand the spectral data. Using theory, we account for these experimental variations between samples. The observed Raman spectra are quantified using the reporter signal at  $1616\text{ cm}^{-1}$  shift for each aspect ratio. These results are shown in Figure 7. The normalized Raman signal in transmission mode from a suspension of gold nanorods can be shown to be equal to<sup>16</sup>



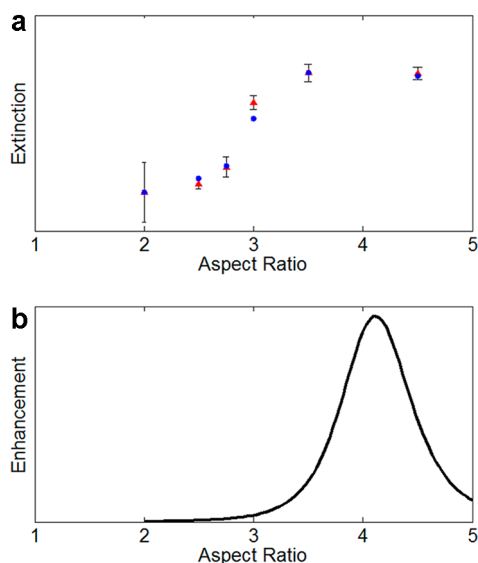


**Figure 6.** (a) Blue dots: Experimentally observed extinction of Raman excitation at 785 nm. Red triangles: Difference in Raman band at 1030 cm<sup>-1</sup> shift with neat methanol and each aspect ratio of gold nanorods suspended in methanol. (b) Predicted electromagnetic enhancement from varying aspect ratios of spheroids in the quasi-static limit. Mean-free electron path and depolarization/radiative damping corrections were applied.

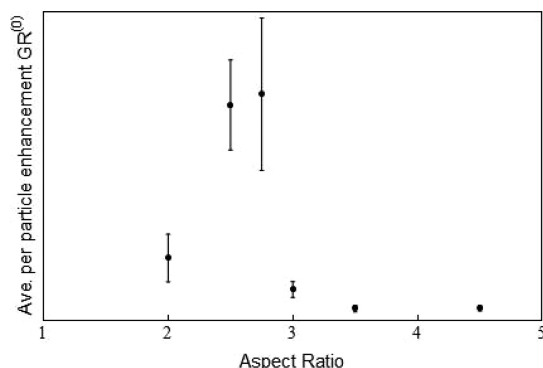


**Figure 7.** Determined average per particle extinction-modified enhancement factor  $GR^{(0)}$  ( $G$  as a function of aspect ratio) from eq 2; some error bars are smaller than the data points.

$$R(\omega, \omega_0, \rho, h) = AR^{(0)}\langle G_N(\omega, \omega_0) \rangle \frac{e^{-mC_{\text{ext}}(\omega_0)hp} - e^{-mC_{\text{ext}}(\omega)hp}}{mC_{\text{ext}}(\omega) - mC_{\text{ext}}(\omega_0)} \quad (1)$$

where the frequencies  $\omega_0$  and  $\omega$  correspond to the incident light and the Stokes' shifted frequencies, respectively,  $A$  is the effective cross-sectional area of the illuminating and collecting beams,  $R^{(0)}$  is the Raman signal from a single reporter molecule absent the nanorod,  $\rho$  is the concentration of the nanorods in the solution,  $N$  indicates the number of bound Raman

reporter molecules,  $h$  is the interaction path length,  $C_{\text{ext}}$  is the extinction cross section of the individual nanorods,  $m$  is the refractive index of the solution, and  $\langle G_N(\omega, \omega_0) \rangle$  is the ensemble-averaged extinction-modified enhancement factor. The ratio in eq 1 models the propagation of incident light and Raman scattered light through the suspension and is a form of Beer's Law. This expression can be simplified if the number of reporter molecules is small, in which case the ensemble-averaged, extinction-modified enhancement factor  $\langle G_N(\omega, \omega_0) \rangle$  can be linearized, that is,  $\langle G_N(\omega, \omega_0) \rangle = \langle G(\omega, \omega_0)N \rangle = \langle G(\omega, \omega_0) \rangle \langle N \rangle$ . This allows us to obtain the averaged per particle extinction-modified enhancement factor.

$$\langle G(\omega, \omega_0) \rangle = \frac{R(\omega, \omega_0, \rho, h)}{R^{(0)}\langle N \rangle} \frac{mC_{\text{ext}}(\omega) - mC_{\text{ext}}(\omega_0)}{e^{-mC_{\text{ext}}(\omega_0)hp} - e^{-mC_{\text{ext}}(\omega)hp}} \quad (2)$$

The single-particle, extinction-modified enhancement factor was computed using eq 2 and is shown in Figure 7. A maximum per-particle signal enhancement is found at an aspect ratio of 2.75, with 2.5 also within error bounds. This implies that maximum observed signal occurs with gold nanorods blue-shifted from the laser excitation wavelength. This differs from the field enhancement maximum expected at an aspect ratio of 4.

## CONCLUSION

In contrast to SERS experiments of immobilized nanoparticle substrates, where absorption effects are minimal, a significant extinction contribution is realized for SERS particles in suspension. In analyzing the signal generation and recording rigorously, we have demonstrated that Raman-active molecules do not provide monolayer coverage of our polyelectrolyte-bearing nanorods as usually assumed. In our experiments, loadings are less than 10% of the expected maximum for monolayer coverage. The calculated ensemble-average signal intensity based on experimentally determined molecular coverage suggests the maximum Raman scattered signal is obtained from that plasmon resonance that is blue-shifted from excitation. This implies the use of nanorods of lower aspect ratios for optimal sensing. Extinction is an important consideration in combination with maximal SERS enhancement when designing tagged Raman probes for suspension applications such as collecting Raman reporter signal through tissue. Efforts toward refining our model by accurately spatially localizing reporter binding sites on the gold nanorods are currently underway in our laboratories.

## MATERIALS AND METHODS

**Materials.** Hydrogen tetrachloroaurate(III) hydrate (HAuCl<sub>4</sub>·3H<sub>2</sub>O, >99.999%), sodium borohydride (NaBH<sub>4</sub>, 99.99%), and silver

nitrate (AgNO<sub>3</sub>, >99.0%) were obtained from Aldrich and used as received. Methylene blue (>82%) with the remainder in organic salts, cetyltrimethylammonium bromide (CTAB, >99%), and ascorbic acid (C<sub>6</sub>H<sub>8</sub>O<sub>6</sub>, >99.0%) were obtained from Sigma



Chemical and used as received. The polyelectrolytes poly(acrylic acid), sodium salt,  $M_w \sim 15\,000$  g/mol (35 wt % solution in  $H_2O$ ) (PAA), and polyallylamine hydrochloride,  $M_w \sim 15\,000$  g/mol (PAH), were obtained from Aldrich and used without further purification. Sodium chloride (NaCl, >99.0%) was obtained and used as received from Fischer Chemicals. All solutions were prepared using Barnstead E-Pure 18  $M\Omega \cdot cm$  water. All glassware used was cleaned with aqua regia and finally rinsed with 18  $M\Omega \cdot cm$  water.

**Gold Nanorod Synthesis.** CTAB-coated gold nanorods of aspect ratio (AR) 2, 2.5, 2.75, 3, 3.5, and 4.5 corresponding to dimensions  $35 \pm 2$  nm  $\times$   $17 \pm 1$  nm,  $39 \pm 6$  nm  $\times$   $16 \pm 4$  nm,  $40 \pm 5$  nm  $\times$   $14 \pm 2$  nm,  $43 \pm 4$  nm  $\times$   $15 \pm 1$  nm,  $45 \pm 3$  nm  $\times$   $12 \pm 1$  nm, and  $48 \pm 3 \times 11 \pm 1$  nm were synthesized as previously described.<sup>28</sup> The gold nanorods were purified twice by centrifugation (8000 rpm, 2 h).

**Polyelectrolyte Layer-by-Layer (LBL) Coating.** We coated the gold nanorods with PAA and PAH using an adapted procedure<sup>19</sup> to maintain the nanoparticle concentration throughout each step. For each polyelectrolyte layer, we prepared stock aqueous solutions of PAA (–) or PAH (+) at concentrations of 10 mg/mL prepared in 1 mM NaCl and a separate aqueous solution of 10 mM NaCl. To 30 mL aliquots of twice centrifuged CTAB gold nanorods (0.15 nM in particles) we added 6 mL of PAA or PAH (+) solution followed by 3 mL of 10 mM NaCl. The solutions were left to complex overnight (12–16 h) before purification using centrifugation (5000 rpm, 2 h). We then centrifuged the supernatant and concentrated the two pellets to minimize losses in gold nanorod concentration. Zeta-potential measurements and UV–vis absorption measurements were made between each layering step to confirm successful coating without aggregation of the gold nanorods.

Zeta potentials were measured on a Brookhaven ZetaPALS instrument. Absorption spectra were recorded on a Cary 500 UV–vis–NIR spectrometer, and transmission electron microscope images were taken on a JEOL 2100 cryo-TEM microscope at a 200 kV accelerating voltage. All TEM grids were prepared by drop-casting 10  $\mu$ L of purified gold nanorods on a holey carbon TEM grid (Pacific Grid-Tech). A ThermoScientific Sorvall Legend X1 centrifuge in a “swinging bucket” orientation was used for purification as detailed below.

**Methylene Blue Gold Nanorod Complexation.** We used the same initial concentration of gold nanorods (0.15 nM) prior to addition of 10  $\mu$ L of a stock 1 mM methylene blue solution to 0.99 mL of gold nanorods, to give a final methylene blue concentration of 1  $\mu$ M during complexation. The mixture was left for an hour before removing excess reporter molecules using centrifugation (2350 rcf, 15 min). The supernatant was also centrifuged, and both pellets were concentrated to maintain gold nanorod concentration. The concentrated pellet was then resuspended to 1 mL with DI water before adding 0.2 mL of PAH (10 mg/mL) in 1 mM NaCl and 0.1 mL of 10 mM aqueous NaCl solutions. This mixture was left overnight before purification by centrifugation (2350 rcf, 15 min); again, the supernatant was also centrifuged (2350 rcf, 15 min), and the pellets were concentrated. For final purification, we dialyzed the aqueous solutions in Spectrum Laboratories 100k MWCO G2 membranes against 4 L of Barnstead E-Pure (18  $M\Omega \cdot cm$ ) water for 48 h. Any remaining unbound methylene blue molecules and excess polyelectrolyte were removed via centrifugation followed by dialysis in a 100 kDa cutoff membrane. By using a membrane pore size 5 times larger than the molecular weight of the polyelectrolyte used, any multilayer polyelectrolyte bundles that may have formed during synthesis should be removed.

**ESI-LC-MS Quantification of Methylene Blue.** For electrospray ionization liquid chromatography mass spectrometry (ESI-LC-MS) quantification of the number of methylene blue molecules, we centrifuged the methylene blue complexed polyelectrolyte gold nanorods (2350 rcf, 15 min) and the supernatant again (2350 rcf, 15 min) before concentrating the pellets. We resuspended the pellet in 50  $\mu$ L of methanol, and the gold nanorod cores were then etched by adding 0.010 mL of 1 M KCN and waiting 1–2 h. It was observed that etching had completed once the solution turned colorless. KCN itself does not disturb the mass spectral analysis of methylene blue (see Supporting Information).

All data in Figure 2c are the results of triplicate measurements for each of three independent batches of nanorods for each aspect ratio.

The ESI-LC-MS analysis was performed in Metabolomics Center at UIUC with a 5500 QTRAP mass spectrometer (AB Sciex, Foster City, CA) which is equipped with a 1200 Agilent LC. Analyst (version 1.5.1, Applied Biosystems) was used for data acquisition and processing. An Agilent Zorbax SB-Aq column (5 $\mu$ , 50  $\times$  4.6 mm) was used for the separation. The HPLC flow rate was set at 0.3 mL/min. HPLC mobile phases consisted of A (0.1% formic acid in  $H_2O$ ) and B (0.1% formic acid in acetonitrile). The gradient was as follows: 0–1 min, 98% A; 6–10 min, 2% A; 10.5–17 min, 98% A. The autosampler was kept at 5  $^{\circ}C$ . The injection volume was 1  $\mu$ L. The mass spectrometer was operated with positive electrospray ionization. The electrospray voltage was set to 2500 V; the heater was set at 400  $^{\circ}C$ ; the curtain gas was 35, and GS1 and GS2 were 50 and 55, respectively. Quantitative analysis was performed via multiple reaction monitoring (MRM) where  $m/z$  284.2 to 240.1 for methylene blue was monitored. Calibration curves were run on methylene blue standards in the presence of cyanide, from 0.01 to 0.1  $\mu$ M concentrations; our data found 0.029–0.108  $\mu$ M concentrations (Figure S2).

**Raman Spectroscopy.** For Raman acquisition, the dialyzed gold nanorod samples were centrifuged to concentrate the pellets (2350 rcf, 15 min) and the supernatant poured off. The samples were then resuspended in 2 mL of methanol (HPLC Fischer Scientific, >99.9% purity) and placed in a quartz cuvette. Triplicate samples were synthesized, with seven spectral acquisitions of each sample collected to minimize the signal-to-noise ratio.

Raman spectra were acquired on liquid samples in transmission mode (LabRAM, Horiba). The excitation wavelength for all measurements was 785 nm with a 30 s acquisition time. The Raman shift from 400 to 1800  $cm^{-1}$  was collected at  $\sim 9$   $cm^{-1}$  spectral resolution. Laser light was focused through a 1 cm path length cuvette with a 40 mm focal length lens and collected with a 125 mm focal length lens to collimate the transmitted light and direct it to the spectrograph. Laser power at the sample was 25 mW. Between measurements, the cuvette was rinsed with aqua regia (3:1 HCl/HNO<sub>3</sub>) followed by multiple rinses with Barnstead E-Pure (18  $M\Omega \cdot cm$ ) water and methanol. For Raman measurements, the gold nanorod concentrations were 0.36, 0.36, 0.31, 0.33, 0.33, and 0.29 nM for aspect ratios 2, 2.5, 2.75, 3, 3.5, and 4.5, respectively, necessitating a small correction to the recorded data which did not change the relative trend observed in the Raman spectra between aspect ratios. Electronic absorption spectra were confirmed before and after Raman measurements.

**Conflict of Interest:** The authors declare no competing financial interest.

**Acknowledgment.** S.T.S. and B.M.D. acknowledge support from the University of Illinois at Urbana—Champaign from NIH National Cancer Institute Alliance for Nanotechnology in Cancer “Midwest Cancer Nanotechnology Training Center” Grant R25 CA154015A. M.V.S. acknowledges support through the Congressionally Directed Medical Research Program Postdoctoral Fellowship BC101112. We also acknowledge support from a Beckman Institute seed grant, AFOSR Grant No. FA 9550-09-1-0246 and NSF Grant Nos. CHE-1011980 and CHE 0957849. The authors thank the Roy J. Carver Biotechnology Metabolomics Center at the University of Illinois at Urbana—Champaign for mass spectrometry analysis.

**Supporting Information Available:** Additional characterization details of mass spectrometry and electronic absorption between synthetic steps. This material is available free of charge via the Internet at <http://pubs.acs.org>.

## REFERENCES AND NOTES

- Haynes, C. L.; McFarland, A. D.; Van Duyne, R. P. Surface-Enhanced Raman Spectroscopy. *Anal. Chem.* **2005**, *77*, 338A–346A.
- McFarland, A. D.; Young, M. A.; Dieringer, J. A.; Van Duyne, R. P. Wavelength-Scanned Surface-Enhanced Raman Excitation Spectroscopy. *J. Phys. Chem. B* **2005**, *109*, 11279–11285.

3. Banholzer, M. J.; Millstone, J. E.; Qin, L.; Mirkin, C. A. Rationally Designed Nanostructures for Surface-Enhanced Raman Spectroscopy. *Chem. Soc. Rev.* **2008**, *37*, 885–897.
4. Porter, M. D.; Lipert, R. J.; Siperko, L. M.; Wang, G.; Narayanan, R. SERS as a Bioassay Platform: Fundamentals, Design, and Applications. *Chem. Soc. Rev.* **2008**, *37*, 1001–1011.
5. Kodali, A. K.; Llorca, X.; Bhargava, R. Optimally Designed Nanolayered Metal-Dielectric Particles as Probes for Massively Multiplexed and Ultrasensitive Molecular Assays. *Proc. Natl. Acad. Sci. U.S.A.* **2010**, *107*, 13620–13625.
6. Zavaleta, C. L.; Smith, B. R.; Walton, I.; Doering, W.; Davis, G.; Shojaei, B.; Natan, M. J.; Gambhir, S. S. Multiplexed Imaging of Surface Enhanced Raman Scattering Nanotags in Living Mice Using Noninvasive Raman Spectroscopy. *Proc. Natl. Acad. Sci. U.S.A.* **2009**, *106*, 13511–13516.
7. Xing, Y.; Chaudry, Q.; Shen, C.; Kong, K. Y.; Zhou, H. E.; Wchung, L.; Petros, J. A.; O'Regan, R. M.; Yezhelyev, M. V.; Simons, J. W.; *et al.* Bioconjugated Quantum Dots for Multiplexed and Quantitative Immunohistochemistry. *Nat. Protoc.* **2007**, *2*, 1152–1165.
8. Wang, G.; Lipert, R. J.; Jain, M.; Kaur, S.; Chakraborty, S.; Torres, M. P.; Batra, S. K.; Brand, R. E.; Porter, M. D. Detection of the Potential Pancreatic Cancer Marker MUC4 in Serum Using Surface-Enhanced Raman Scattering. *Anal. Chem.* **2011**, *83*, 2554–2561.
9. Pallaoro, A.; Braun, G. B.; Moskovits, M. Quantitative Ratio-metric Discrimination between Noncancerous and Cancerous Prostate Cells Based on Neuropilin-1 Overexpression. *Proc. Natl. Acad. Sci. U.S.A.* **2011**, *108*, 16559–16564.
10. Stone, N.; Faulds, K.; Graham, D.; Matousek, P. Prospects of Deep Raman Spectroscopy for Noninvasive Detection of Conjugated Surface Enhanced Resonance Raman Scattering Nanoparticles Buried within 25 mm of Mammalian Tissue. *Anal. Chem.* **2010**, *82*, 3969–3973.
11. Stone, N.; Kerssens, M.; Lloyd, G. R.; Faulds, K.; Graham, D.; Matousek, P. Surface Enhanced Spatially Offset Raman Spectroscopic (SESORS) Imaging—The Next Dimension. *Chem. Sci.* **2011**, *2*, 776–780.
12. Richards-Kortum, R.; Sevick-Muraca, E. Quantitative Optical Spectroscopy for Tissue Diagnosis. *Annu. Rev. Phys. Chem.* **1996**, *47*, 555–606.
13. Huang, X.; El-Sayed, I. H.; Qian, W.; El-Sayed, M. A. Cancer Cells Assemble and Align Gold Nanorods Conjugated to Antibodies To Produce Highly Enhanced, Sharp, and Polarized Surface Raman Spectra: A Potential Cancer Diagnostic Marker. *Nano Lett.* **2007**, *7*, 1591–1597.
14. Lal, S.; Grady, N. K.; Kundu, J.; Levin, C. S.; Lassiter, J. B.; Halas, N. J. Tailoring Plasmonic Substrates for Surface Enhanced Spectroscopies. *Chem. Soc. Rev.* **2008**, *37*, 898–911.
15. Jain, P. K.; Huang, X.; El-Sayed, I. H.; El-Sayed, M. A. Noble Metals on the Nanoscale: Optical and Photothermal Properties and Some Applications in Imaging, Sensing, Biology, and Medicine. *Acc. Chem. Res.* **2008**, *41*, 1578–1586.
16. van Dijk, T.; Sivapalan, S. T.; DeVetter, B. M.; Yang, T. K.; Schulmerich, M. V.; Murphy, C. J.; Bhargava, R.; Carney, P. S. Competition between extinction and enhancement in surface enhanced Raman spectroscopy. **2013**, arXiv:1303.0277.
17. Guerrini, L.; Jurasekova, Z.; Domingo, C.; Perez-Mendez, M.; Leyton, P.; Campos-Vallette, M.; Garcia-Ramos, J. V.; Sanchez-Cortes, S. Importance of Metal-Adsorbate Interactions for the Surface-Enhanced Raman Scattering of Molecules Adsorbed on Plasmonic Nanoparticles. *Plasmonics* **2007**, *2*, 147–156.
18. Li, J. F.; Huang, Y. F.; Ding, Y.; Yang, Z. L.; Li, S. B.; Zhou, X. S.; Fan, F. R.; Zhang, W.; Zhou, Z. Y.; Wu, D. Y.; *et al.* Shell-Isolated Nanoparticle-Enhanced Raman Spectroscopy. *Nature* **2010**, *464*, 392–395.
19. Gole, A.; Murphy, C. J. Polyelectrolyte-Coated Gold Nanorods: Synthesis, Characterization and Immobilization. *Chem. Mater.* **2005**, *17*, 1325–1330.
20. Huang, J. Y.; Jackson, K. S.; Murphy, C. J. Polyelectrolyte Wrapping Layers Control Rates of Photothermal Molecular Release from Gold Nanorods. *Nano Lett.* **2012**, *12*, 2982–2987.
21. Sivapalan, S. T.; Vella, J. H.; Yang, T. K.; Dalton, M. J.; Swiger, R. N.; Haley, J. E.; Cooper, T. M.; Urbas, A. M.; Tan, L. S.; Murphy, C. J. Plasmonic Enhancement of the Two Photon Absorption Cross Section of an Organic Chromophore Using Polyelectrolyte-Coated Gold Nanorods. *Langmuir* **2012**, *28*, 9147–9154.
22. Alkilany, A. M.; Thompson, L. B.; Murphy, C. J. Polyelectrolyte Coating Provides a Facile Route To Suspend Gold Nanorods in Polar Organic Solvents and Hydrophobic Polymers. *ACS Appl. Mater. Interfaces* **2010**, *2*, 3417–3421.
23. Hahner, G.; Marti, A.; Spencer, N. D.; Caseri, W. R. Orientation and Electronic Structure of Methylene Blue on Mica: A Near Edge X-ray Absorption Fine Structure Spectroscopy Study. *J. Chem. Phys.* **1996**, *104*, 7749–7757.
24. Kneipp, K.; Dasari, R. R.; Wang, Y. Near-Infrared Surface-Enhanced Raman Scattering (NIR SERS) on Colloidal Silver and Gold. *Appl. Spectrosc.* **1994**, *48*, 951–957.
25. Dixit, S.; Poon, W. C. K.; Crain, J. Hydration of Methanol in Aqueous Solutions: A Raman Spectroscopic Study. *J. Phys.: Condens. Matter* **2000**, *12*, L323–L328.
26. Naujok, R. R.; Duevel, R. V.; Corn, R. M. Fluorescence and Fourier-Transform Surface-Enhanced Raman-Scattering Measurements of Methylene-Blue Adsorbed onto a Sulfur-Modified Gold Electrode. *Langmuir* **1993**, *9*, 1771–1774.
27. Schatz, G. C.; Van Duyne, R. P. Electromagnetic Mechanism of Surface-Enhanced Spectroscopy. In *Handbook of Vibrational Spectroscopy*; John Wiley & Sons, Ltd.: Chichester, UK, 2002; Vol. 1; pp 759–774.
28. Sau, T. K.; Murphy, C. J. Seeded High Yield Synthesis of Short Au Nanorods in Aqueous Solution. *Langmuir* **2004**, *20*, 6414–6420.

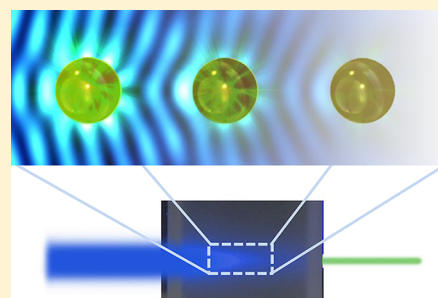
# Competition Between Extinction and Enhancement in Surface-Enhanced Raman Spectroscopy

Thomas van Dijk,<sup>†</sup> Sean T. Sivapalan,<sup>‡</sup> Brent M. DeVetter,<sup>¶</sup> Timothy K. Yang,<sup>§</sup>  
Matthew V. Schulmerich,<sup>‡,||</sup> Catherine J. Murphy,<sup>‡,§</sup> Rohit Bhargava,<sup>‡,||,⊥</sup> and P. Scott Carney<sup>\*,†,¶</sup>

<sup>†</sup>Beckman Institute for Advanced Science and Technology, <sup>‡</sup>Department of Materials Science and Engineering, <sup>¶</sup>Department of Electrical and Computer Engineering, <sup>§</sup>Department of Chemistry, <sup>||</sup>Department of Bioengineering, and <sup>⊥</sup>Department of Mechanical Science and Engineering, Chemical and Biomolecular Engineering and University of Illinois Cancer Center, University of Illinois at Urbana–Champaign, Urbana, Illinois 61801, United States

**ABSTRACT:** Conjugated metallic nanoparticles are a promising means to achieve ultrasensitive and multiplexed sensing in intact three-dimensional samples, especially for biological applications, via surface-enhanced Raman scattering (SERS). We show that enhancement and extinction are linked and compete in a collection of metallic nanoparticles. Counterintuitively, the Raman signal vanishes when nanoparticles are excited at their plasmon resonance, while increasing nanoparticle concentrations at off-resonance excitation sometimes leads to decreased signal. We develop an effective medium theory that explains both phenomena. Optimal choices of excitation wavelength, individual particle enhancement factor, and concentrations are indicated. The same processes that give rise to enhancement also lead to increased extinction of both the illumination and the Raman-scattered light. Nanoparticles attenuate the incident field (blue) and at the same time provide local enhancement for SERS. Likewise, the radiation of the Raman-scattered field (green) is enhanced by the nearby sphere but extinguished by the rest of the spheres in the suspension upon propagation.

**SECTION:** Physical Processes in Nanomaterials and Nanostructures



Several methods for using surface-enhanced Raman scattering (SERS)<sup>1</sup> have emerged for biomedical applications, ultrasensitive sensing, and multiplexed analyses. In particular, nanoparticles have been the focus of recent efforts toward in vitro and in vivo molecular sensing.<sup>2–5</sup> Nanoparticles can dramatically increase the electric field intensity near and at their surface, providing useful SERS-based probes,<sup>6</sup> especially for deep tissue imaging at varying concentrations.<sup>7</sup> Typically, a nanostructured particle is bioconjugated and employed in the same manner as conventional fluorescent probes are used for molecular imaging. SERS probes are postulated to offer bright and stable signals and extensive multiplexing,<sup>8</sup> while it has been assumed that experimental best practice parallels that of fluorescent probes, that is, that one should excite at the strongest resonance and use a high concentration. In fact, it has recently been recognized even in single-particle enhancement of fluorescence that peak signals are observed to be red-shifted from the plasmon reference.<sup>9</sup> Thus far, the design of nanoparticle-based SERS experiments has focused on maximizing the local electromagnetic field enhancement in or around an individual particle.<sup>10,11</sup> This strategy fails to take into account the physics of propagation in the bulk medium where the same processes that give rise to enhancement also lead to increased extinction of both the illumination and the Raman-scattered light. Particles provide enhanced fields for Raman scattering, and the same particles form an effective medium with corresponding absorption. The importance of absorption of

the Raman-scattered light is recognized in ref 12. However, they do not describe the necessary link and competition between the enhancement and the extinction. For example, it is commonly known to experimentalists that gold nanospheres exhibit a plasmon resonance at 520 nm and should produce a large local field enhancement when illuminated at 532 nm; yet, no appreciable Raman signal is observed upon 532 nm excitation commonly ascribed to interband transitions in gold.<sup>13</sup> Away from the plasmon resonance frequency maximum, the Raman signal is again observed and actually increases as the excitation wavelength becomes longer.

In this Letter, we address the issue of extinction by a suspension of nanoparticles in SERS experiments through an effective medium approach. It is shown that extinction and enhancement are tied to each other and compete in such a way that peak signals are acquired off-resonance and that, at any wavelength, an optimal particle concentration exists to maximize the Raman signal. We provide verification of the model with experiments in which the particle concentration is varied.

Propagation of light in a dilute suspension of identical particles is well-approximated by propagation through a

**Received:** March 6, 2013

**Accepted:** March 22, 2013

**Published:** March 22, 2013

homogeneous medium with an effective refractive index  $\tilde{m}$ , given by<sup>14</sup>

$$\tilde{m} = m \left[ 1 + i \frac{2\pi\rho}{k^3} S(0) \right] \quad (1)$$

where  $m$  is the refractive index of the medium in which the particles are embedded,  $k = \omega/c$  is the wavenumber in the medium,  $\rho$  is the number of particles per unit volume, and  $S(0)$  is the scattering amplitude in the forward direction.<sup>14</sup> The absorption coefficient in a medium with a complex refractive index is  $\alpha = 2k \text{Im} \tilde{m}$ . For a suspension with small identical particles, the absorption coefficient is given by  $\alpha = m4\pi\rho k^{-2} \text{Re}[S(0)] = \rho m C_{\text{ext}}$ , where  $C_{\text{ext}}$  is the extinction cross section of a single particle in the suspension, proportional to the real part of the forward-scattering amplitude. The attenuation of a well-collimated beam propagating through the effective medium is described by Beer's law,<sup>15</sup>  $I(h) = I(0)e^{-h\alpha}$ , where  $I$  is the intensity and  $h$  is the propagation distance. The extinction cross section, rather than the absorption cross section, is used to account also for scattering out of the collection and detection optical train or subsequent absorption. Hence, for systems of large particles, where the scattering is mostly in the forward direction, or for high-NA systems, this model may fail or require correction for contribution to the detection by the scattered field. In the system considered here, the particles are small compared to the wavelength, and the optical system is low-NA.<sup>16</sup>

The extinction cross section,  $C_{\text{ext}}$ , for a small metallic sphere with radius  $a$ , to terms of order  $(ka)^4$ , is given by<sup>14</sup>

$$C_{\text{ext}} = 4k\pi a^3 \text{Im} \left\{ \frac{p^2 - 1}{p^2 + 2} \left[ 1 + \frac{(ka)^2}{15} \left( \frac{p^2 - 1}{p^2 + 2} \right) \times \frac{p^2 + 27p^2 + 38}{2p^2 + 3} \right] \right\} + \frac{8}{3}(ka)^4 \times \pi a^2 \text{Re} \left[ \left( \frac{p^2 - 1}{p^2 + 2} \right)^2 \right] \quad (2)$$

where  $p = m_s/m$  is the ratio of the refractive index of the material of the spheres,  $m_s$ , to that of the refractive index of the medium,  $m$ , which both depend on the wavenumber. For dilute suspensions, the change in the real part of the refractive index of the effective medium from the background is negligible. The extinction from gold spheres in a suspension is shown in Figure 1, where the extinction peaks near the Fröhlich frequency ( $\lambda_f \approx 520$  nm); for this calculation the optical constants obtained by Johnson and Christy for gold have been used.<sup>17</sup>

The Raman signal, which we denote as  $R$ , from a single, isolated nanoparticle depends on the incident field amplitude,  $E_0$ , the number of Raman-active molecules,  $N$ , the local field enhancement,  $f(\mathbf{r}, \omega)$ , and the spatial distribution of those molecules. This last point we address through a probability density, which in general will also depend on the number of molecules present,  $p(\mathbf{r}, N)$ . Though not explicitly noted, the local enhancement factor is also dependent on the orientation of the incident electric field vector. The number of molecules attached to the nanoparticle may itself be random and given by the probability of finding  $N$  molecules attached to the particle  $P_N$ . A single molecule at  $\mathbf{r}$  is excited by a field with amplitude  $E_0 f(\mathbf{r}, \omega_0)$ , producing a secondary source proportional to the

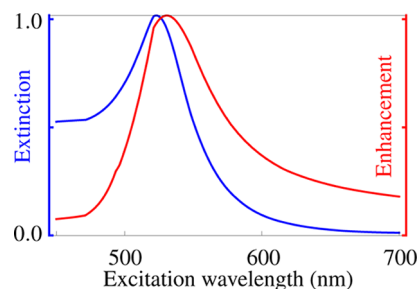


**Figure 1.** (blue) The normalized extinction cross section  $C_{\text{ext}}$  from eq 2. Extinction by gold spheres of 5 nm radius in aqueous suspension as a function of the wavelength of the incident light. (red) The normalized Raman enhancement,  $G(\lambda)$  from eq 4, versus the excitation wavelength for gold spheres of radius much smaller than the wavelength evaluated for a Raman shift of 0 nm.

Raman susceptibility  $\chi$ , which implicitly depends on  $\omega_0$ , and  $\omega$ . The field reradiated at the Raman-shifted frequency  $\omega$  is enhanced by the particle as well, so that, by reciprocity, the reradiated field is proportional to  $\chi E_0 f(\mathbf{r}, \omega_0) f(\mathbf{r}, \omega)$ . We assume that the Raman signal from each reporter molecule is statistically independent; therefore, the intensities add. The ensemble-averaged Raman signal for a single nanoparticle is thus given by

$$R = |\chi|^2 \sum_{N=1}^{\infty} N P_N \int d^3r |E_0 f(\mathbf{r}, \omega_0) f(\mathbf{r}, \omega)|^2 p(\mathbf{r}, N) = \langle N \rangle G R^{(0)} \quad (3)$$

where  $R^{(0)}$  is the Raman signal from one molecule absent the particle and  $G$  is the Raman enhancement factor and generally depends on  $p(\mathbf{r}, N)$  and  $P_N$ . For systems in which the particle placement is independent of the number of particles, the sum and the integral may be carried out independently, the sum yielding the average number of molecules ( $\langle N \rangle$ ), and the integral resulting in a  $G$  independent of the number of molecules.

The enhancement factor for a small sphere of radius  $a$  ( $a \ll \lambda$ ) with a uniform probability of molecule placement over the surface of the sphere can be calculated in closed form<sup>18</sup>

$$G(\omega, \omega_0) = |1 + 2g(\omega_0)|^2 |1 + 2g(\omega)|^2 \quad (4)$$

where  $g = (p^2 - 1)/(p^2 + 2)$ ,  $\omega_0$  is the frequency of the incident field, and  $\omega$  is the frequency of the Raman-scattered field.

The enhancement calculated by eq 4 is shown in Figure 1 alongside the extinction using the optical constants obtained by Johnson and Christy.<sup>17</sup> It is clear that enhancement and extinction are closely linked and that when the enhancement is strong, the correspondingly strong extinction must be taken into account. The light falling on a single particle is attenuated by propagation through the suspension and arrives with amplitude attenuated by the factor  $\exp[-\int_0^z dz' \rho(z') m C_{\text{ext}}(\omega_0)/2]$ . The local Raman signal is then  $\langle N \rangle R^{(0)} G p(z) \exp[-\int_0^z dz' \rho(z') m C_{\text{ext}}(\omega_0)]$ . In transmission mode, this signal must then propagate out through the medium to  $z = h$ , and the intensity is attenuated by a factor of  $\exp[-\int_z^h dz' \rho(z') m C_{\text{ext}}(\omega)]$ . The total signal is a sum over the signal from all particles, so that



$$R = \langle N \rangle A R^{(0)} G \int_0^h dz \rho(z) \exp\left[-\int_0^z dz' \rho(z')\right] \times mC_{\text{ext}}(\omega_0) \exp\left[-\int_z^h dz' \rho(z') mC_{\text{ext}}(\omega)\right] \quad (5)$$

where  $A$  is the integral over the transverse beam profile normalized to the peak value, the effective transverse area of the beam. When the concentration  $\rho(z)$  does not depend on  $z$ , the integrals can be computed in closed form with the result

$$R = \langle N \rangle A R^{(0)} G \frac{e^{-mC_{\text{ext}}(\omega_0)h\rho} - e^{-mC_{\text{ext}}(\omega)h\rho}}{mC_{\text{ext}}(\omega) - mC_{\text{ext}}(\omega_0)} \quad (6)$$

From this expression, it is seen that there are two competing processes that determine the size of the Raman signal, the enhancement,  $G$ , and the extinction that results in an exponential decay of the signal. The same processes that increase the enhancement also increase the extinction. The attenuation due to extinction depends not only on the frequency but also on the concentration of the nanospheres. This is illustrated in Figure 2a, where it is shown that for increasing concentration, the peak

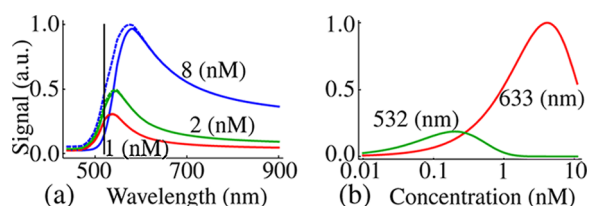


**Figure 2.** (a) Solid lines: Predicted signal in transmission mode versus the wavelength of the incident light. Dashed lines: Predicted signal in reflection mode versus the wavelength of the incident light. Both transmission and reflection signals are with three different concentrations of the nanospheres that have a radius 6 nm; the sample thickness  $h$  is 2 cm. The vertical black line indicates the location of the surface plasmon resonance. (b) Predicted signal in transmission mode versus the concentration for two different incident wavelengths; the radius of the spheres is 15 nm.

of the signal is shifted farther away from the resonant wavelength. This result explains the absence of Raman signal at the plasmon resonance where extinction is so strong that no signal is observed.

In reflection mode, there is always a contribution from the front layer of the sample that is not attenuated, and therefore, the expression for the Raman signal is slightly altered

$$R = \langle N \rangle A R^{(0)} G \frac{1 - e^{-hm\rho[C_{\text{ext}}(\omega) + C_{\text{ext}}(\omega_0)]}}{mC_{\text{ext}}(\omega) + mC_{\text{ext}}(\omega_0)} \quad (7)$$

The Raman signal in reflection mode for three different concentrations of the nanospheres is shown in Figure 2a as the dashed lines. In the reflection mode, there is a slightly higher signal to the blue side of the resonance compared to the signal in transmission mode.

The Raman signal in transmission mode is depicted in Figure 2b for two commonly used wavelengths evaluated for a Raman band at  $1076 \text{ cm}^{-1}$ . For  $\lambda = 532 \text{ nm}$ , the excitation wavelength closest to the plasmon resonance, the signal is very small. A higher signal is found farther away from resonance with the peak shifted to the red. For relatively low concentrations, the biggest signal is obtained with a wavelength of  $632 \text{ nm}$ . Only for concentrations smaller than  $0.1 \text{ nM}$  is the signal bigger for the excitation wavelength closest to resonance, as shown in

Figure 2b. It is seen that there is a concentration that maximizes the signal. This optimal concentration,  $\rho_{\text{opt}}$ , can be found by differentiating eq 6 and equating it to zero, giving the following expression

$$\rho_{\text{opt}} = \frac{\ln[C_{\text{ext}}(\omega)/C_{\text{ext}}(\omega_0)]}{hm[C_{\text{ext}}(\omega) - C_{\text{ext}}(\omega_0)]} \quad (8)$$

When the extinction cross section,  $C_{\text{ext}}(\omega)$ , equals, or is very close to,  $C_{\text{ext}}(\omega_0)$ , the optimal concentration becomes  $\rho_{\text{opt}} = 1/[hmC_{\text{ext}}(\omega_0)]$ . The strong nonlinearity with concentration that these competing phenomena impose on the recorded signal is also a caution in the development of practical assays and must be taken into account to correctly quantify results across samples. Hence, this physics-based analysis enables quantitative molecular imaging for SERS-based microscopy.

The model presented in this paper is validated by measuring the SERS signal of 4,4'-dipyridyl Raman reporter molecules attached to gold nanospheres. Spectra were acquired from the nanoparticles in suspension using a high-resolution Raman spectrometer (LabRAM, Horiba) with a 90 s acquisition time. The Raman shift from  $200$  to  $1800 \text{ cm}^{-1}$  was collected at  $10 \text{ cm}^{-1}$  resolution with  $10 \text{ mW}$  laser power at the sample. Transmission Raman measurements were collected by focusing laser light through a  $1 \text{ cm}$  cuvette with a  $50 \text{ mm}$  focal length lens and collected with a  $100 \text{ mm}$  focal length lens to collimate the transmitted light and direct it to the spectrograph.

The integrated SERS signal under three different bands ( $476$ ,  $1076$ , and  $1600 \text{ cm}^{-1}$ ) is compared for different concentrations of the gold spheres when excited at  $632 \text{ nm}$ . The SERS spectra from 4,4'-dipyridyl for increasing concentrations is illustrated in Figure 3a. The three boxes indicate the Raman bands for which

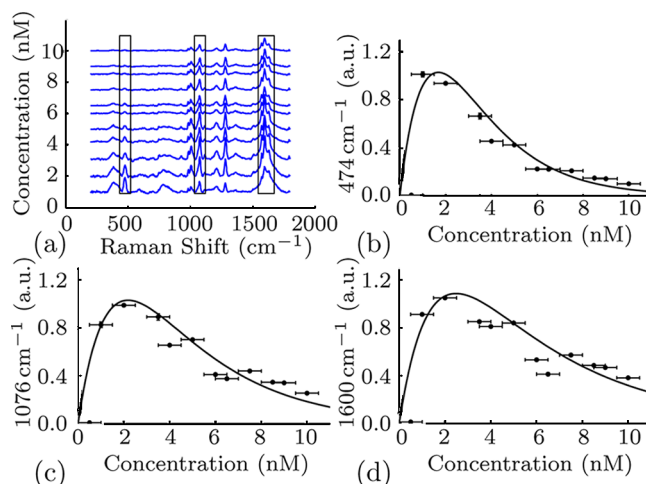


**Figure 3.** (a) SERS spectra of 4,4'-dipyridyl attached to gold nanospheres with a radius of 15 nm at an excitation wavelength of  $633 \text{ nm}$  at different nanoparticle concentrations. Measured Raman signals (points) agree with the theoretical prediction (solid line) for a Raman shift of (b)  $474$ , (c)  $1076$ , and (d)  $1600 \text{ cm}^{-1}$ .

the signal is investigated as a function of concentration. The signal is obtained by integrating the Raman band of interest over the width of the box, as shown in Figure 3.

As predicted, increasing the concentration of nanoparticles in an attempt to increase the signal leads to signal attenuation beyond an optimal concentration. The measurements are in good agreement with the model. Our results suggest that strategies to increase Raman signals using nanoparticles should



not focus on achieving greater local enhancement but instead might strive for designs that maximize total signal by separating the single-particle enhancement and absorption peaks or otherwise tailoring the shape of the enhancement and absorption curves to maximize the gap between absorption and enhancement at frequencies away from resonance. A move toward using thin samples with large areas of collection is also suggested. We see that the signal is increased by moving away from resonance and, in some cases, by lowering the concentration of particles. While we focused on nanospheres, our results apply broadly to particle-based Raman enhancement with nonspherical particles as well.

## ■ EXPERIMENTAL METHODS

Gold nanospheres of 15 nm radius were synthesized by the boiling citrate method.<sup>19,20</sup> For stability against aggregation, 100 mg of bis(*p*-sulfonatophenyl)phenylphosphine dihydrate dipotassium salt (BSPP) was added to 100 mL of as-synthesized nanoparticles.<sup>21,22</sup> The mixture was left to stir overnight (12–16 h), and excess reagents were removed by two centrifugation cycles (3000 RCF, 20 min). For 4,4'-dipyridyl complexation, 1 mL of 10 mM 4,4'-dipyridyl in water was added to 9 mL of BSPP-stabilized gold nanoparticles and left to complex overnight.<sup>23</sup> Excess reagents were removed by two centrifugation cycles (3000 RCF for 20 min). For final purification, we dialyzed the solutions in Thermo Scientific G2 Slide-A-Lyzer G2 cassettes against 4 L of Barnstead E-Pure (18 MΩ cm) water for 48 h.

## ■ AUTHOR INFORMATION

### Corresponding Author

\*E-mail: carney@uiuc.edu.

### Notes

The authors declare no competing financial interest.

## ■ ACKNOWLEDGMENTS

The work was supported in part by the Beckman Fellows program. S.T.S. and B.M.D. acknowledge support from the University of Illinois at Urbana–Champaign from the NIH National Cancer Institute Alliance for Nanotechnology in Cancer “Midwest Cancer Nanotechnology Training Center” Grant R25CA154015A. M.V.S. acknowledges support through the Congressionally Directed Medical Research Program Postdoctoral Fellowship BC101112. We also acknowledge support from a Beckman Institute seed grant, AFOSR Grant No. FA9550-09-1-0246, and NSF Grants CHE-1011980 and CHE-0957849.

## ■ REFERENCES

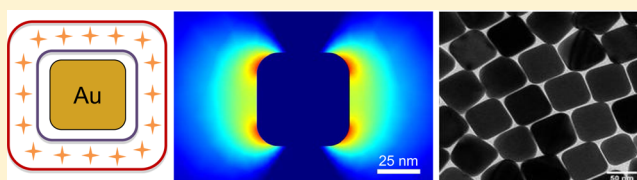
- (1) Schatz, G. C.; Van Duyne, R. P. *Handbook of Vibrational Spectroscopy*; John Wiley & Sons: Chichester, U.K., 2002; Vol. 1, pp 759–774.
- (2) Lyandres, O.; Yuen, J. M.; Shah, N. C.; van Duyne, R. P.; Walsh, J. T.; Glucksberg, M. R. Progress Toward an In Vivo Surface-Enhanced Raman Spectroscopy Glucose Sensor. *Diabetes Technol. Ther.* **2008**, *10*, 257–265.
- (3) Qian, X.; Peng, X.-H.; Ansari, D. O.; Yin-Goen, Q.; Chen, G. Z.; Shin, D. M.; Yang, L.; Young, A. N.; Wang, M. D.; Nie, S. In Vivo Tumor Targeting and Spectroscopic Detection with Surface-Enhanced Raman Nanoparticle Tags. *Nat. Biotechnol.* **2008**, *26*, 83–90.
- (4) von Maltzahn, G.; Centrone, A.; Park, J.-H.; Ramanathan, R.; Sailor, M. J.; Hatton, T. A.; Bhatia, S. N. SERS-Coded Gold Nanorods as a Multifunctional Platform for Densely Multiplexed Near-Infrared Imaging and Photothermal Heating. *Adv. Mater.* **2009**, *21*, 3175–3180.
- (5) Frontiera, R. R.; Henry, A.-I.; Gruenke, N. L.; Van Duyne, R. P. Surface-Enhanced Femtosecond Stimulated Raman Spectroscopy. *J. Phys. Chem. Lett.* **2011**, *2*, 1199–1203.
- (6) Larmour, I. A.; Argueta, E. A.; Faulds, K.; Graham, D. Design Consideration for Surface-Enhanced (Resonance) Raman Scattering Nanotag Cores. *J. Phys. Chem. C* **2012**, *116*, 2677–2682.
- (7) Stone, N.; Faulds, K.; Graham, D.; Matousek, P. Prospects of Deep Raman Spectroscopy for Noninvasive Detection of Conjugated Surface Enhanced Resonance Raman Scattering Nanoparticles Buried within 25 mm of Mammalian Tissue. *Anal. Chem.* **2010**, *82*, 3969–3973.
- (8) Cao, Y. C.; Jin, R. C.; Nam, J. M.; Thaxton, C. S.; Mirkin, C. A. Raman Dye-Labeled Nanoparticle Probes for Proteins. *J. Am. Chem. Soc.* **2003**, *125*, 14676–14677.
- (9) Bharadwaj, P.; Novotny, L. Spectral Dependence of Single Molecule Fluorescence Enhancement. *Opt. Express* **2007**, *21*, 14266–14274.
- (10) Talley, C. E.; Jackson, J. B.; Oubre, C.; Grady, N. K.; Hollars, C. W.; Lane, S. M.; Huser, T. R.; Nordlander, P.; Halas, N. J. Surface-Enhanced Raman Scattering from Individual Au Nanoparticles and Nanoparticle Dimer Substrates. *Nano Lett.* **2005**, *5*, 1569–1574.
- (11) Kodali, A. K.; Llorca, X.; Bhargava, R. Optimally Designed Nanolayered Metal–Dielectric Particles as Probes for Massively Multiplexed and Ultrasensitive Molecular Assays. *Proc. Natl. Acad. Sci. U.S.A.* **2010**, *107*, 13620–13625.
- (12) Jackson, J. B.; Westcott, S. L.; Hirsch, L. R.; West, J. L.; Halas, N. J. Controlling the Surface Enhanced Raman Effect via the Nanoshell Geometry. *Appl. Phys. Lett.* **2003**, *82*, 257–259.
- (13) Alvarez-Puebla, R. A. Effects of the Excitation Wavelength on the SERS Spectrum. *J. Phys. Chem. Lett.* **2012**, *3*, 857–866.
- (14) Bohren, C. F.; Huffman, D. R. *Absorption and Scattering of Light by Small Particles*; John Wiley and Sons: New York, 1983.
- (15) van de Hulst, H. C. *Light Scattering by Small Particles*; Dover Publications: Mineola, NY, 1982.
- (16) Bohren, C. F. Applicability of Effective-Medium Theories to Problems of Scattering and Absorption by Nonhomogeneous Atmospheric Particles. *J. Atmos. Sci.* **1986**, *43*, 468–475.
- (17) Johnson, P. B.; Christy, R. W. Optical-Constants of Noble-Metals. *Phys. Rev. B* **1972**, *6*, 4370–4379.
- (18) Kerker, M.; Wang, D. S.; Chew, H. Surface Enhanced Raman-Scattering (SERS) by Molecules Adsorbed at Spherical-Particles: Errata. *Appl. Opt.* **1980**, *19*, 4159–4174.
- (19) Ji, X.; Song, X.; Li, J.; Bai, Y.; Yang, W.; Peng, X. Size Control of Gold Nanocrystals in Citrate Reduction: The Third Role of Citrate. *J. Am. Chem. Soc.* **2007**, *129*, 13939–13948.
- (20) Kimling, J.; Maier, M.; Okenve, B.; Kotaidis, V.; Ballot, H.; Plech, A. Turkevich Method for Gold Nanoparticle Synthesis Revisited. *J. Phys. Chem. B* **2006**, *110*, 15700–15707.
- (21) Loweth, C. J.; Caldwell, W. B.; Peng, X. G.; Alivisatos, A. P.; Schultz, P. G. DNA-Based Assembly of Gold Nanocrystals. *Angew. Chem., Int. Ed.* **1999**, *38*, 1808–1812.
- (22) Schmid, G.; Lehnert, A. The Complexation of Gold Colloids. *Angew. Chem., Int. Ed. Engl.* **1989**, *28*, 780–781.
- (23) Lim, D. K.; Jeon, K. S.; Hwang, J. H.; Kim, H.; Kwon, S.; Suh, Y. D.; Nam, J. M. Highly Uniform and Reproducible Surface-Enhanced Raman Scattering from DNA-Tailorable Nanoparticles with 1-nm Interior Gap. *Nat. Nanotechnol.* **2011**, *6*, 452–460.

# Surface-Enhanced Raman Spectroscopy of Polyelectrolyte-Wrapped Gold Nanoparticles in Colloidal Suspension

Sean T. Sivapalan,<sup>†,▽</sup> Brent M. DeVetter,<sup>‡,§,▽</sup> Timothy K. Yang,<sup>||</sup> Matthew V. Schulmerich,<sup>§,⊥</sup> Rohit Bhargava,<sup>\*,‡,§,⊥,#</sup> and Catherine J. Murphy<sup>\*,†,||</sup>

<sup>†</sup>Department of Materials Science and Engineering, <sup>‡</sup>Department of Electrical and Computer Engineering, <sup>§</sup>Beckman Institute for Advanced Science and Technology, <sup>||</sup>Department of Chemistry, <sup>⊥</sup>Department of Bioengineering, <sup>#</sup>Department of Mechanical Science and Engineering, Micro and Nanotechnology Laboratory and University of Illinois Cancer Center, University of Illinois at Urbana–Champaign, Urbana, Illinois 61801, United States

**ABSTRACT:** The rapidly expanding field of surface-enhanced Raman spectroscopy (SERS) has helped fuel an intense interest in noble metal nanoparticle synthesis. An in-suspension approach for quantifying SERS enhancement and relating that enhancement to a spontaneous Raman equivalent signal is described. Gold nanoparticles of various shapes were wrapped with polyelectrolyte multilayers that trapped Raman reporter molecules at defined distances from the metal core. Electrospray ionization liquid chromatography mass spectrometry (ESI-LC-MS) on digested samples was employed to measure the average number of bound Raman reporter molecules per gold nanoparticle, and inductively coupled plasma mass spectrometry (ICP-MS) was used to measure the average number of gold atoms per nanoparticle. Using these data, SERS signal intensity was compared to a spontaneous Raman calibration curve to compute a spontaneous Raman equivalent factor. Three different geometries of gold nanoparticles (cubes, spheres, and trisoctahedra) were synthesized to investigate edge and corner effects using these quantitative techniques. Finite element method electromagnetic simulations examined the relationship between the different geometries and the observed SERS signal intensities. The experimental observations and theoretical results indicate that cubic gold nanoparticles have the highest effective signal.



## INTRODUCTION

Plasmonic metal nanoparticles show great promise for biological applications, ranging from diagnostic imaging to in vivo therapies.<sup>1–4</sup> Intense electromagnetic fields near the metal surface, which arise from irradiation into the plasmon bands, promote highly sensitive surface-enhanced Raman scattering (SERS), both in substrate-based assays as well as nanoprobe approaches approaching single-molecule detection limits.<sup>5</sup> SERS has a dynamic range surpassing that of fluorescence spectroscopy<sup>6</sup> and the ability to multiplex vibrational fingerprints of reporter molecules.<sup>4</sup> The design considerations for such probes focus on maximizing the electromagnetic enhancement defined by their shape, size, and polarization of the incident light.<sup>7–11</sup> However, there has been great debate in the SERS community regarding the reproducibility and reliability of reported enhancement factors.<sup>11</sup>

Minor differences in synthesis and quantification approaches can produce varying results in the reported SERS enhancement. This is further complicated by sample preparation, such as whether or not the measurements were performed on dried colloidal suspensions, on SERS-active substrates, or on the colloidal suspensions themselves. In previous work we have demonstrated that gold nanocubes dried on gold substrates bearing an analyte monolayer have a higher SERS enhancement compared to gold nanorods prepared in the same way.<sup>12</sup> However, the structures that form as a result of nanoparticle drying have a complicated impact on the resulting signal;

aggregation of nanoparticles can create electromagnetic hot spots. Our understanding of these effects has rapidly accelerated due to the availability of computational tools based on the discrete dipole approximation (DDA), finite-difference time-domain (FDTD) method, and the finite-element method (FEM), among others.<sup>8–10</sup> From simulations, it is well understood that hot spots are localized areas of high enhancement resulting from interplasmonic coupling between metallic surfaces that may lead to unreliable or difficult-to-reproduce measurements.

In this study we aim to minimize the effects of hot spots by collecting SERS measurements on colloidal suspensions and using polyelectrolyte-coated nanoparticles to reduce the effect of aggregation. Here, three different geometries (cubes, spheres, trisoctahedra) of gold nanoparticles were synthesized to investigate edge and corner effects. Raman-active reporter molecules trapped near the surface of gold nanoparticles were quantified using electrospray ionization liquid chromatography mass spectrometry (ESI-LC-MS). Additionally, the average number of gold atoms per nanoparticle was quantified via inductively coupled plasma mass spectrometry (ICP-MS). Using these data, we compare SERS signal intensity with a spontaneous Raman calibration curve. Finite element method (FEM)

Received: March 8, 2013

Revised: April 21, 2013

Published: April 25, 2013



electromagnetic simulations were performed to examine the relationship between the different geometries and the observed SERS signal intensities.

## ■ EXPERIMENTAL SECTION

**Materials.** Hydrogen tetrachloride ( $\text{HAuCl}_4$ , >99.999%), sodium borohydride ( $\text{NaBH}_4$ ), polyallylamine hydrochloride (PAH, MW  $\approx$  15 000 g/mol), poly(acrylic acid) sodium salt (PAA, MW  $\approx$  15 000 g/mol, 35 wt % in  $\text{H}_2\text{O}$ ), sodium chloride ( $\text{NaCl}$ , >99%), and ascorbic acid ( $\text{C}_6\text{H}_8\text{O}_6$ , >99.0%) were obtained from Aldrich and used as received. Cetyltrimethylammonium bromide (CTAB, >99%) and cetyltrimethylammonium chloride (CTAC, >98%) were obtained from Sigma and used without further purification. All glassware was cleaned using aqua regia and rinsed with Barnstead E-Pure 18  $\text{M}\Omega\text{-cm}$  water.

**Instrumentation.** SERS spectra were obtained on a Horiba LabRAM Raman microscope configured with a 785 nm excitation laser line. Triplicate measurements with integration times of 30 s were performed on the gold nanoparticles in suspension through a 1 cm path length quartz cuvette. Laser power at the sample was measured to be 12.5 mW. Zeta potential measurements were performed on a Brookhaven ZetaPALS instrument. Electronic absorption spectra were measured with a Cary 500 scan UV–vis–NIR spectrophotometer. Transmission electron micrograph (TEM) images were taken on a JEOL 2010F field emission microscope at 200 kV accelerating voltage. For grid preparation, 10  $\mu\text{L}$  of gold nanoparticle suspension was drop cast onto holey carbon TEM grids (Pacific Grid-Tech). Size distributions were verified by analyzing at least 100 representative particles per shape. We use a Thermo Scientific Sorvall Legend X1 Centrifuge for purification as detailed in the synthesis below.

**Synthesis of Seeds for CTAB Cubes (A).** The nanoparticle seeds were synthesized by modification of the method of El-Sayed et al.<sup>13</sup> An aqueous CTAB solution (7.5 mL, 0.1 M) was mixed with 0.25 mL of 0.01 M aqueous  $\text{HAuCl}_4$ . To the stirred solution was quickly added 0.6 mL of ice-cold newly made aqueous 0.01 M  $\text{NaBH}_4$ , which resulted in a light brown solution. After stirring the solution vigorously for 2 min, the solution was kept for 1 h in room temperature before use.

**Synthesis of CTAB Seeds for Trisoctahedra (TOH) Gold Nanocrystals (B).** The nanoparticle seeds were synthesized by following the procedure by El-Sayed et al.<sup>13</sup> An aqueous CTAB solution (7.0 mL, 75 mM) was mixed with 46  $\mu\text{L}$  of 20 mM aqueous  $\text{HAuCl}_4$ . To the solution was quickly added 0.42 mL of ice-cold freshly made aqueous 0.01 M  $\text{NaBH}_4$  under vigorous mixing, yielding a light brown solution. After  $\text{NaBH}_4$  was added, the solution was gently stirred to decompose the excess  $\text{NaBH}_4$ . The solution was used within 2–5 h after preparation.

**Synthesis of CTAB Spheres and Cubes.** Spheres and cubes were synthesized in 40 mL batches. To 32 mL of nanopure water were added aqueous solutions of 6.4 mL of 0.1 M CTAB and 0.8 mL of 0.01 M  $\text{HAuCl}_4$ , respectively. This resulted in a yellow-brown solution. Then, 3.8 mL of aqueous 0.1 M ascorbic acid was added as the reducing agent, which rendered the solution colorless. From here, depending on the seed concentration, spheres or cubes will form. To obtain spheres, a 0.02 mL of 5 times diluted seed (A) was added to the colorless solution. To obtain cubes, 0.03 mL of 10 times diluted seed (A) was added to the colorless solution. Solutions were allowed to react until no further color changes were observed. The spheres were centrifuged at 4000 rcf for 30 min, and the supernatant was removed. The pellet was resuspended in water, and this process

was repeated again to remove excess CTAB. Similarly, cubes were twice centrifuged at 8000 rpm for 20 min.

**Synthesis of TOH Gold Nanocrystals.** Trisoctahedra (TOH) nanocrystals were synthesized by a seed-mediated method used by Lee et al.<sup>14</sup> A 0.125 mL solution of aqueous 20 mM  $\text{HAuCl}_4$  was mixed with 9 mL of 22 mM aqueous CTAC. To this mixture was added 3.06 mL of aqueous 38.8 mM ascorbic acid to make the concentration of ascorbic acid 9.5 mM. The solution was thoroughly mixed. Then, seed (B) was diluted 100-fold with nanopure water, and 50  $\mu\text{L}$  of the diluted seed (B) was added to the solution. This resulted in a red-pinkish solution. Trisoctahedra samples were purified by centrifugation at 4000 rcf for 30 min. The supernatant was discarded, and the sample was resuspended in water. To remove excess CTAC, this process was repeated twice.

**Polyelectrolyte Wrapping and Complexation of Methylene Blue to Gold Nanoparticles.** To 30 mL of as-synthesized CTAB/CTAC stabilized gold nanoparticles, 6 mL of PAA (10 mg/mL) and 3 mL of  $\text{NaCl}$  (10 mM) were added and left overnight. Centrifugation and resuspension into 30 mL of water were performed on each sample to remove excess PAA at the same speeds specified in the synthesis for each shape. To complex the gold nanoparticles with Raman reporter, 1 mL of methylene blue (1 mM) was added to the suspension. After 1 h, centrifugation was performed again to remove unbound methylene blue. To 30 mL of resuspended gold nanoparticles, 6 mL of PAH (10 mg/mL) and 3 mL of  $\text{NaCl}$  (10 mM) were added and left overnight. The samples were again centrifuged to remove excess PAH. Dialysis with 20 000 g/mol dialysis cassettes (Fischer Scientific) was performed for 48 h in 4 L of water to remove residual reagents. To quantify the number of methylene blue molecules via liquid chromatography mass spectrometry, 1 mL of methylene blue complexed polyelectrolyte wrapped gold nanoparticles was centrifuged into pellets and resuspended into 50  $\mu\text{L}$  of water. To this suspension, 10  $\mu\text{L}$  of 1 M KCN was added and allowed to sit for at least 1 h before quantification. The suspension slowly turned colorless as the gold nanoparticles were etched away.

**ESI-LC-MS Quantification of Methylene Blue.** The LC-MS analysis was performed in Metabolomics Center at UIUC with a 5500 QTRAP mass spectrometer (AB Sciex, Foster City, CA) which is equipped with a 1200 Agilent LC. Analyst (version 1.5.1, Applied Biosystems) was used for data acquisition and processing. An Agilent Zorbax SB-Aq column (5  $\mu\text{m}$ , 50  $\times$  4.6 mm) was used for the separation. The HPLC flow rate was set at 0.3 mL/min. HPLC mobile phases consisted of A (0.1% formic acid in  $\text{H}_2\text{O}$ ) and B (0.1% formic acid in acetonitrile). The gradient was: 0–1 min, 98% A; 6–10 min, 2% A; 10.5–17 min, 98% A. The autosampler was kept at 5  $^\circ\text{C}$ . The injection volume was 1  $\mu\text{L}$ . The mass spectrometer was operated with positive electrospray ionization. The electrospray voltage was set to 2500 V; the heater was set at 400  $^\circ\text{C}$ ; the curtain gas was 35; and GS1 and GS2 were 50 and 55, respectively. Quantitative analysis was performed via multiple reaction monitoring (MRM) where  $m/z$  284.2 to  $m/z$  240.1 was monitored.

## ■ RESULTS AND DISCUSSION

Polyelectrolyte-wrapped nanoparticles are highly resistant to aggregation and provide a buffering layer of roughly 5 nm from each metallic surface.<sup>15</sup> Raman-active molecules of methylene blue were electrostatically trapped between a layer of anionic poly(acrylic acid) (PAA) and cationic polyallylamine hydrochloride (PAH). Three nanoparticle geometries (cubes, spheres,



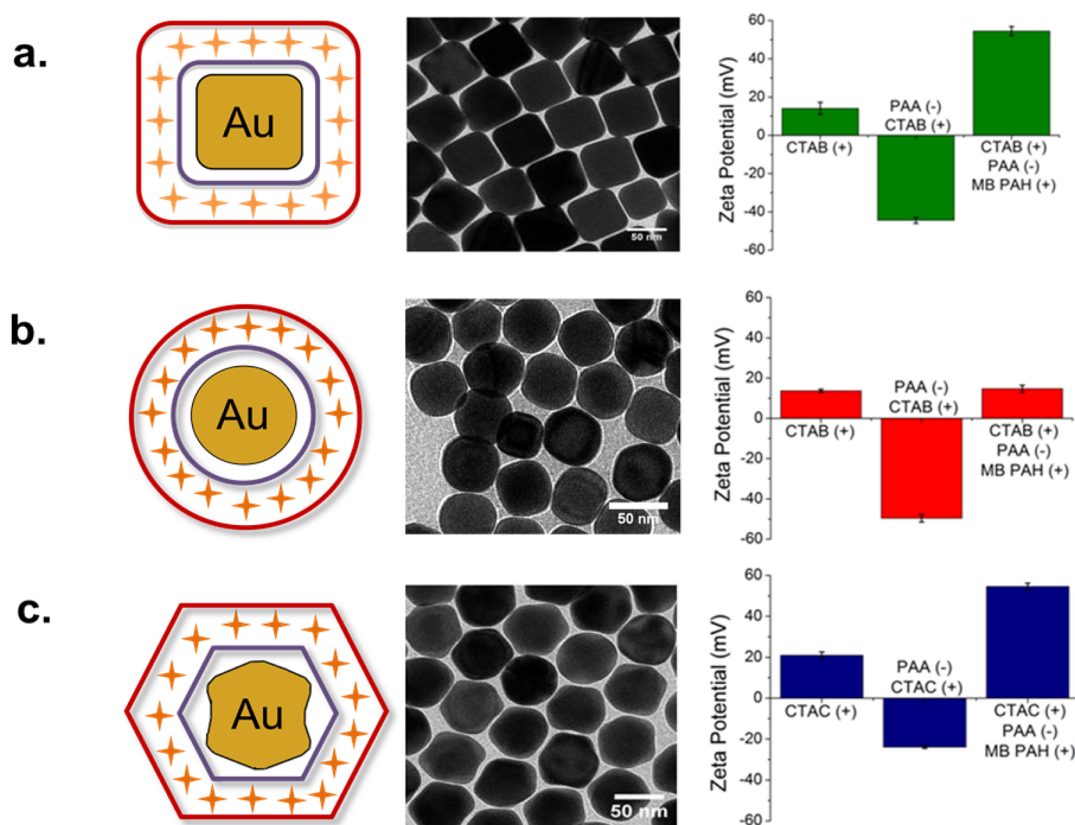


**Figure 1.** Cartoon illustrating polyelectrolyte trap coating of methylene blue (MB, orange crosses) around gold nanoparticles. MB is electrostatically bound to poly(acrylic acid) (PAA, purple) and trapped by polyallylamine hydrochloride (PAH, dark red). Transmission electron micrographs of nanoparticle shapes and corresponding zeta potential for (a) cubes, (b) spheres, and (c) trisoctahedra as a function of wrapping stage.

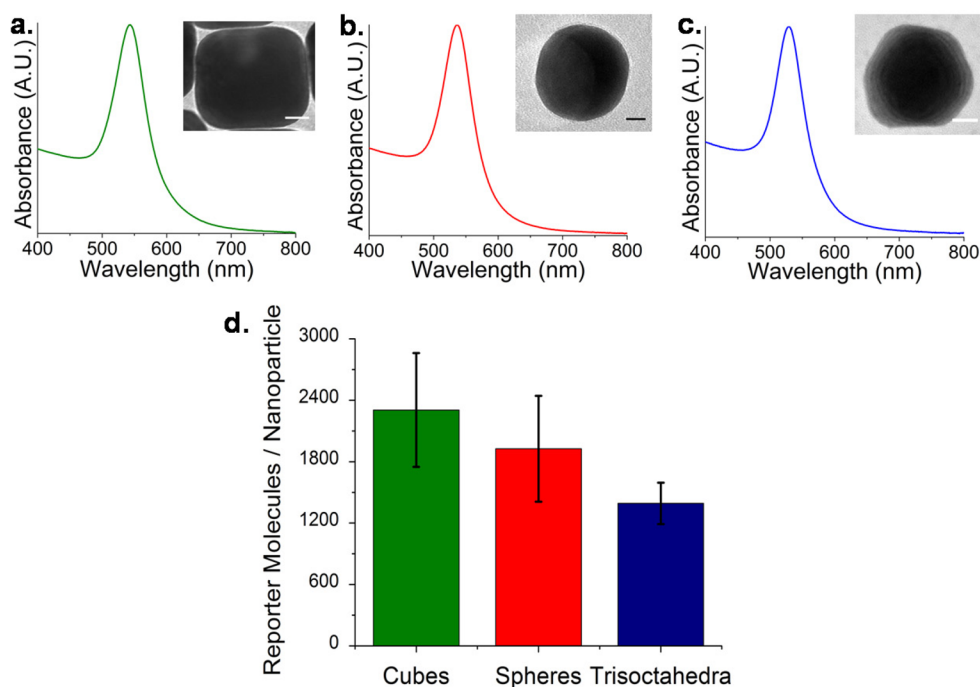


**Figure 2.** Normalized electronic absorption spectra of colloidal suspensions of (a) cubes, (b) spheres, and (c) trisoctahedra. Inset: transmission electron micrographs of each shape. Scale bars = 10 nm. (d) Experimental ESI-LC-MS quantification of the average number of methylene blue molecules per gold nanoparticle shape. Error bars indicate the standard deviation over four independently synthesized samples.

and trisoctahedra) with polyelectrolyte layers and trapped methylene blue molecules are depicted in Figure 1 with their

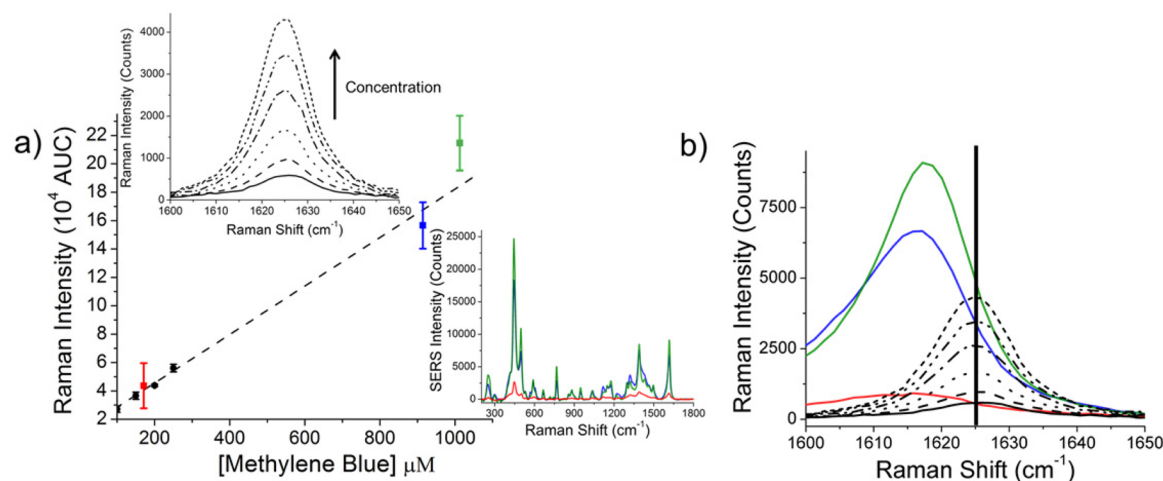


**Figure 3.** (a) Spontaneous Raman calibration curve of the  $\sim 1625\text{ cm}^{-1}$  band of methylene blue (black dots), compared to the same concentration of methylene blue bound to gold nanospheres (red square), gold trisoctahedra (blue square), and gold nanocubes (green square). Error bars correspond to the standard deviation of nanoparticle concentration and reporter molecules per nanoparticle as determined by ICP-MS and ESI-LC-MS, respectively. Top left inset: spontaneous Raman spectra (between  $1600$  and  $1650\text{ cm}^{-1}$ ) of varying concentrations of methylene blue in water ( $25\text{--}400\text{ }\mu\text{M}$ ). Bottom right inset: Example spectra calculated from the spontaneous Raman calibration curve with an assumed  $0.12\text{ nM}$  gold nanoparticle concentration and  $1800$  reporter molecules per nanoparticle. (b) Methylene blue molecules experience a conformational change during the trap-coating process, resulting in a slight shift in the observed Raman band. Raman measurements of free methylene blue molecules (vertical bar at  $1625\text{ cm}^{-1}$ ) versus surface-enhanced trap-coated methylene blue molecules are shown (cubes, green; trisoctahedra, blue; spheres, red).

corresponding transmission electron micrograph (TEM) images. Each synthetic step was verified using zeta potential measurements to indicate successful wrapping.

The far-field optical properties of the colloidal suspensions are nearly identical as shown in the experimental electronic absorption spectra (Figure 2). Recently, we have demonstrated a dependence on realized signal for in-suspension measurements due to an interrelationship between localized surface plasmon resonance (LSPR) and laser excitation wavelength.<sup>16</sup> Nanoparticle suspensions were synthesized with similar LSPR maxima to minimize these effects. Here, four independently synthesized batches of cubes, spheres, and trisoctahedra had LSPR maxima at  $543$ ,  $537$ , and  $529\text{ nm}$ , respectively, to maximize the signal for  $785\text{ nm}$  excitation.<sup>16</sup> Characterization with TEM revealed the average size of each shape to be  $54.3 \pm 3.35$ ,  $46.54 \pm 6.7$ , and  $52.3 \pm 5.8\text{ nm}$  for cubes, spheres, and trisoctahedra, respectively. The average number of reporter molecules (methylene blue) per nanoparticle shape were quantified with ESI-LC-MS against known concentrations of reporter standards (see Experimental Section). On average, there were between  $1200$  and  $2400$  molecules per gold nanoparticle. Both experimental<sup>17</sup> and theoretical<sup>18</sup> reports typically assume monolayer coverage of Raman-active molecules. With an assumed molecular profile of  $0.66\text{ nm}^2/\text{molecule}$  for methylene blue,<sup>19</sup> the expected monolayer coverage was over  $10\,000$  molecules per nanoparticle. In all cases, each nanoparticle shape had less than  $25\%$  coverage (Figure 2(d)).

Quantitative comparison of SERS data was performed by measuring the spontaneous Raman intensity of methylene blue in water with  $25\text{--}400\text{ }\mu\text{M}$  concentrations. All measurements were acquired with exactly the same laser power, acquisition times, and laser configuration used for SERS measurements. From these data, a spontaneous Raman calibration curve was constructed via integration of the band at  $\sim 1625\text{ cm}^{-1}$  (Figure 3). Due to conformational changes in the methylene blue molecules during the binding process, SERS signal intensity was quantified at  $1616\text{ cm}^{-1}$ . SERS measurements were performed in

aqueous solution on nanoparticle ensembles at an average concentration of  $0.074$ ,  $0.12$ , and  $0.17\text{ nM}$  for cubes, spheres, and trisoctahedra, respectively.

An observed Raman intensity (Table 1) may be calculated from extrapolation of the spontaneous Raman calibration curve

**Table 1. Observed Raman Intensity of Each Nanoparticle Shape<sup>a</sup>**

nanoparticle shape	observed Raman intensity
cubes	$5.63 \pm 0.56 \times 10^3$
spheres	$0.87 \pm 0.52 \times 10^3$
trisoctahedra	$4.01 \pm 0.20 \times 10^3$

<sup>a</sup>Intensity values were determined from extrapolation of the spontaneous Raman calibration curve of methylene blue with SERS measurements normalized to nanoparticle concentration (determined by ICP-MS) and the average number of reporter molecules per nanoparticle (determined by ESI-LC-MS).

such that: Observed Raman Intensity =  $(\text{SERS}_{1616} - 12\,472) / 157N_{\text{conc}}M_{\text{molec}}$  where  $N_{\text{conc}}$  is the average concentration of gold nanoparticles and  $M_{\text{molec}}$  is the average number of reporter molecules per nanoparticle. The slope  $m = 157$  and the  $y$ -intercept  $b = 12\,472$  were determined from linear regression of the spontaneous calibration curve. The indicated error corresponds to the averaged standard deviation of reporter molecules per sample as determined by ESI-LC-MS. Gold nanocubes have the highest observed intensity of  $5.63 \times 10^3$ .

Nanostructures with high radii of curvature concentrate optical fields through the so-called “lightning rod” effect of SERS.<sup>20</sup> Recent computational studies have emphasized the importance of edge effects in SERS-based measurements.<sup>21,22</sup> We performed FEM electromagnetic simulations to visualize edge effects on nonspherical geometries. In contrast to other popular techniques such as FDTD and DDA, FEM utilizes adaptive meshes rather than cubic grids, subsequently improving near-field accuracy as well as significantly decreasing solver time.<sup>18</sup> All calculations were performed using a commercial



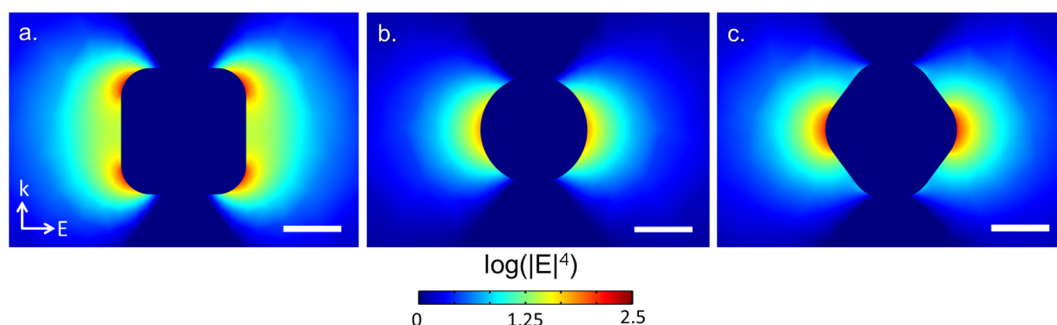


**Figure 4.** Electric field distributions of single nanoparticle shapes: (a) 54 nm diameter cube, (b) 46 nm diameter sphere, and (c) 52 nm diameter trisioctahedra evaluated at  $\lambda = 785$  nm. Water ( $n = 1.33$ ) is assumed to be the surrounding media. Scale bar is 25 nm.

software package (COMSOL Multiphysics 4.2). Bulk gold optical constants were obtained from Johnson and Christy.<sup>23</sup>

Cubes, spheres, and trisioctahedra were simulated in a three-dimensional scattering domain (Figure 4). Electromagnetic enhancement is quantified by a factor  $G$  where it is assumed that the Stokes' shifted wavelength of Raman scattered light is negligible:  $G = |E(\lambda_{\text{inc}})|^2 \cdot |E(\lambda_{\text{inc}} + \delta\lambda)|^2 \approx |E(\lambda_{\text{inc}})|^4$ . Assuming submersion in water ( $n = 1.33$ ), cubes were modeled with an edge length of 54 nm, spheres with a diameter of 46 nm, and trisioctahedra with an effective diameter of 52 nm, corresponding to the average dimensions measured in TEM. The polyelectrolyte layers were not included in the simulation. Furthermore, we neglect any chemical enhancement effects, as they are expected to be minimal with our chosen reporter molecule. Corner roundness was empirically determined from TEM image analysis using ImageJ software developed at the National Institutes of Health (Figure 1). As expected from the lightning rod effect, nanostructures with the sharpest corners have the highest enhancement factor  $G$ . Despite having more corners, trisioctahedra are relatively smooth as compared to the edges of gold nanocubes.

Surface integration of  $|E|^4$  normalized to nanoparticle surface area reveals cubes have a  $2.5\times$  greater field strength as compared to trisioctahedra and spheres. The observed Raman intensity, however, of cubes is over  $5\times$  greater than that of spheres. Trisioctahedra have an observed intensity greater than  $4\times$  that of spheres. Therefore, we suggest that the primary mechanism of enhancement is due to the lightning rod effect because of the sharp edges and corners that exist on the cubes and trisioctahedra. Differences in the simulated versus experimental data arise from variability in the molecular trap coating process. In the absence of definitive imaging results, we propose that the polyelectrolyte coating process uniformly deposits over the entire surface of each nanoparticle shape. However, molecules positioned at corners or edges may be displaced farther from the surface than molecules trapped near smooth features. Mismatch between theory and experiment is likely due to the difficulties in determining the positions of reporter molecules.

The quantitative approach to ensemble SERS measurements presented here demonstrates a novel method to compute observed Raman intensity using a spontaneous Raman calibration curve. In combination with reporter molecule and gold nanoparticle quantification, we have demonstrated that gold nanocubes have the highest SERS signal relative to trisioctahedra and spheres. Trisioctahedra bearing high-index facets such as (221), (331), and (441)<sup>24</sup> are of particular interest due to their increased chemical reactivity.<sup>25</sup> Future work will involve studying

the binding density and binding sites available to SERS-active molecules on high-index nanostructures.

## AUTHOR INFORMATION

### Corresponding Author

\*E-mail: murphycj@illinois.edu (Catherine J. Murphy); rxb@illinois.edu (Rohit Bhargava).

### Author Contributions

▽ These authors contributed equally to this work.

### Notes

The authors declare no competing financial interest.

## ACKNOWLEDGMENTS

STS and BMD acknowledge support from the University of Illinois at Urbana–Champaign from NIH National Cancer Institute Alliance for Nanotechnology in Cancer ‘Midwest Cancer Nanotechnology Training Center’ Grant R25 CA154015A. MVS acknowledges support through the Congressionally Directed Medical Research Program Postdoctoral Fellowship BC101112. We also acknowledge support from a Beckman Institute seed grant, AFOSR Grant Number FA 9550-09-1-0246 and NSF Grant Numbers CHE-1011980 and CHE 0957849. The authors thank the Roy J. Carver Biotechnology Metabolomics Center at the University of Illinois at Urbana–Champaign for mass spectrometry analysis. TEM images were obtained at the Frederick Seitz Materials Research Laboratory Central Facilities, University of Illinois.

## REFERENCES

- (1) Boisselier, E.; Astruc, D. Gold Nanoparticles in Nanomedicine: Preparations, Imaging, Diagnostics, Therapies and Toxicity. *Chem. Soc. Rev.* **2009**, *38*, 1759–1782.
- (2) Qian, X. M.; Peng, X. H.; Ansari, D. O.; Yin-Goen, Q.; Chen, G. Z.; Shin, D. M.; Yang, L.; Young, A. N.; Wang, M. D.; Nie, S. M. In Vivo Tumor Targeting and Spectroscopic Detection with Surface-Enhanced Raman Nanoparticle Tags. *Nat. Biotechnol.* **2008**, *26*, 83–90.
- (3) von Maltzahn, G.; Park, J. H.; Agrawal, A.; Bandaru, N. K.; Das, S. K.; Sailor, M. J.; Bhatia, S. N. Computationally Guided Photothermal Tumor Therapy Using Long-Circulating Gold Nanorod Antennas. *Cancer Res.* **2009**, *69*, 3892–3900.
- (4) Zavaleta, C. L.; Smith, B. R.; Walton, I.; Doering, W.; Davis, G.; Shojaei, B.; Natan, M. J.; Gambhir, S. S. Multiplexed Imaging of Surface Enhanced Raman Scattering Nanotags in Living Mice Using Non-invasive Raman Spectroscopy. *Proc. Natl. Acad. Sci. U.S.A.* **2009**, *106*, 13511–13516.
- (5) Nie, S. M.; Emory, S. R. Probing Single Molecules and Single Nanoparticles by Surface-Enhanced Raman Scattering. *Science* **1997**, *275*, 1102–1106.

- (6) Pieczonka, N. P. W.; Aroca, R. F. Single Molecule Analysis by Surface-Enhanced Raman Scattering. *Chem. Soc. Rev.* **2008**, *37*, 946–954.
- (7) Alvarez-Puebla, R. A. Effects of the Excitation Wavelength on the SERS Spectrum. *J. Phys. Chem. Lett.* **2012**, *3*, 857–866.
- (8) Atkinson, A. L.; McMahon, J. M.; Schatz, G. C. *FDTD Studies of Metallic Nanoparticle Systems*. In *Self Organization of Molecular Systems*; Russo, N., Antonchenko, V. Y., Kryachko, E. S., Eds.; Springer: Netherlands, 2009; pp 11–32.
- (9) Jain, P. K.; Lee, K. S.; El-Sayed, I. H.; El-Sayed, M. A. Calculated Absorption and Scattering Properties of Gold Nanoparticles of Different Size, Shape, and Composition: Applications in Biological Imaging and Biomedicine. *J. Phys. Chem. B* **2006**, *110*, 7238–7248.
- (10) Khoury, C. G.; Norton, S. J.; Vo-Dinh, T. Plasmonics of 3-D Nanoshell Dimers Using Multipole Expansion and Finite Element Method. *ACS Nano* **2009**, *3*, 2776–2788.
- (11) Margueritat, J.; Gehan, H.; Grand, J.; Lévi, G.; Aubard, J.; Féridj, N.; Bouhelier, A.; Colas-Des-Francis, G.; Markey, L.; Marco De Lucas, C.; et al. Influence of the Number of Nanoparticles on the Enhancement Properties of Surface-Enhanced Raman Scattering Active Area: Sensitivity Versus Repeatability. *ACS Nano* **2011**, *5*, 1630–1638.
- (12) Orendorff, C. J.; Gole, A.; Sau, T. K.; Murphy, C. J. Surface-Enhanced Raman Spectroscopy of Self-Assembled Monolayers: Sandwich Architecture and Nanoparticle Shape Dependence. *Anal. Chem.* **2005**, *77*, 3261–3266.
- (13) Nikoobakht, B.; El-Sayed, M. A. Preparation and Growth Mechanism of Gold Nanorods (NRs) Using Seed-Mediated Growth Method. *Chem. Mater.* **2003**, *15*, 1957–1962.
- (14) Yu, Y.; Zhang, Q. B.; Lu, X. M.; Lee, J. Y. Seed-Mediated Synthesis of Monodisperse Concave Trisoctahedral Gold Nanocrystals with Controllable Sizes. *J. Phys. Chem. C* **2010**, *114*, 11119–11126.
- (15) Gole, A.; Murphy, C. J. Polyelectrolyte-Coated Gold Nanorods: Synthesis, Characterization and Immobilization. *Chem. Mater.* **2005**, *17*, 1325–1330.
- (16) Sivapalan, S. T.; DeVetter, B. M.; Yang, T. K.; van Dijk, T.; Schulmerich, M. V.; Carney, P. S.; Bhargava, R.; Murphy, C. J. Off-Resonance Surface-Enhanced Raman Spectroscopy from Gold Nanorod Suspensions as a Function of Aspect Ratio: Not What We Thought. *ACS Nano* **2013**, *7*, 2099–2105.
- (17) Naujok, R. R.; Duevel, R. V.; Corn, R. M. Fluorescence and Fourier-Transform Surface-Enhanced Raman-Scattering Measurements of Methylene-Blue Adsorbed onto a Sulfur-Modified Gold Electrode. *Langmuir* **1993**, *9*, 1771–1774.
- (18) Kerker, M.; Wang, D. S.; Chew, H. Surface Enhanced Raman-Scattering (SERS) by Molecules Adsorbed at Spherical Particles. *Appl. Opt.* **1980**, *19*, 4159–4174.
- (19) Hahner, G.; Marti, A.; Spencer, N. D.; Caseri, W. R. Orientation and Electronic Structure of Methylene Blue on Mica: A Near Edge X-ray Absorption Fine Structure Spectroscopy Study. *J. Chem. Phys.* **1996**, *104*, 7749–7757.
- (20) Liao, P. F.; Wokaun, A. Lightning Rod Effect in Surface Enhanced Raman Scattering. *J. Chem. Phys.* **1982**, *76*, 751–752.
- (21) Angulo, A. M.; Noguez, C.; Schatz, G. C. Electromagnetic Field Enhancement for Wedge-Shaped Metal Nanostructures. *J. Phys. Chem. Lett.* **2011**, *2*, 1978–1983.
- (22) Xu, H.; Aizpurua, J.; Käll, M.; Apell, P. Electromagnetic Contributions to Single-Molecule Sensitivity in Surface-Enhanced Raman Scattering. *Phys. Rev. E* **2000**, *62*, 4318–4324.
- (23) Johnson, P. B.; Christy, R. W. Optical Constants of Noble Metals. *Phys. Rev. B* **1972**, *6*, 4370–4379.
- (24) Ma, Y.; Kuang, Q.; Jiang, Z.; Xie, Z.; Huang, R.; Zheng, L. Synthesis of Trisoctahedral Gold Nanocrystals with Exposed High-Index Facets by a Facile Chemical Method. *Angew. Chem., Int. Ed.* **2008**, *47*, 8901–8904.
- (25) Zhang, J.; Langille, M. R.; Personick, M. L.; Zhang, K.; Li, S.; Mirkin, C. A. Concave Cubic Gold Nanocrystals with High-Index Facets. *J. Am. Chem. Soc.* **2010**, *132*, 14012–14014.

RESEARCH ARTICLE

Open Access

# Real-time interactive data mining for chemical imaging information: application to automated histopathology

David Mayerich<sup>1</sup>, Michael Walsh<sup>2</sup>, Matthew Schulmerich<sup>1,3</sup> and Rohit Bhargava<sup>1,3,4,5,6\*</sup>

## Abstract

**Background:** Vibrational spectroscopic imaging is now used in several fields to acquire molecular information from microscopically heterogeneous systems. Recent advances have led to promising applications in tissue analysis for cancer research, where chemical information can be used to identify cell types and disease. However, recorded spectra are affected by the morphology of the tissue sample, making identification of chemical structures difficult.

**Results:** Extracting features that can be used to classify tissue is a cumbersome manual process which limits this technology from wide applicability. In this paper, we describe a method for interactive data mining of spectral features using GPU-based manipulation of the spectral distribution.

**Conclusions:** This allows researchers to quickly identify chemical features corresponding to cell type. These features are then applied to tissue samples in order to visualize the chemical composition of the tissue without the use of chemical stains.

## Background

Vibrational spectroscopic imaging, or chemical imaging, data is composed of a series of absorption or scattering measurements taken across the electromagnetic spectrum. Materials exhibit a characteristic spectral signature that is indicative of their molecular composition. The speed and versatility of vibrational techniques offer the most potential for label-free microscopy by providing micron-scale resolution and significant molecular detail.

In this paper we focus on mid-infrared spectroscopic imaging [1], which is a form of vibrational spectroscopy with a data rate that is currently viable for clinical applications. We will also show that our methods are applicable to other techniques, such as Raman spectroscopy, which show promise for future *in vivo* imaging. Recent advances in optical detector technology allow the rapid acquisition of spectral signals that are spatially specific, producing multidimensional images that can be extensive in size

(several tens of gigabytes). These techniques have shown promise in biomedicine for cell type classification [2,3] and cancer analysis [4]. However, the interpretation of a spectral signature is a complex task, requiring a significant amount of pre-processing before identifying spectral features that correspond to chemical information.

While the acquisition of data is relatively rapid, there are limited options at present to assist researchers in visualizing data. In this paper, we propose a method for interactively exploring the chemical composition of a tissue sample. The proposed software allows a user to quickly identify spectral features corresponding to specific tissue types within a sample. The results are then applied to other samples in order to identify tissue types without the use of histological labels. This allows us to overcome several disadvantages of current histology methods by using quantitative information that is collected non-destructively. This makes our methods repeatable and provides an array of useful quantitative information that can be used by a pathologist to aid in diagnosis.

In Section 'Mid-infrared spectroscopy', we provide an overview of mid-infrared spectroscopic imaging. Section 'Morphological effects' describes the coupling between tissue morphology and chemistry, which makes

\*Correspondence: rxb@illinois.edu

<sup>1</sup> Beckman Institute for Advanced Science and Technology, University of Illinois at Urbana-Champaign, Urbana, IL, USA

<sup>3</sup> Department of Bioengineering, University of Illinois at Urbana-Champaign, Urbana, IL, USA

Full list of author information is available at the end of the article

the characterization of tissue difficult. Our method and implementation details are described in Section 'Methods' and Section 'Visualization'. Section 'Results and discussion' provides validation using chemical phantoms and demonstrates our results on breast cancer biopsies.

Our *SpecVis* software is open-source and 32-bit Windows binaries available online (<http://www.chemimage.illinois.edu/software>).

### Mid-infrared spectroscopy

Mid-infrared spectroscopy is used to identify molecular content in a sample by determining the fraction of incident light absorbed. Broadband mid-infrared electromagnetic radiation is transmitted through the sample and the absorbed light at each wavelength is quantified (Figure 1). The most common technique for measuring absorption spectra is Fourier Transform Infrared (FT-IR) Spectroscopy [5], which uses an interferometer to encode optical frequencies in time. The recorded data is then decoded using a Fourier transform. The resulting data consist of a spectrum representing the intensity of light transmitted as a function of frequency  $\bar{\nu}$ . The frequency domain is generally recorded in units of *wavenumber* ( $\text{cm}^{-1}$ ). The absorbance at each wavelength is computed using

$$A(\bar{\nu}) = -\log_{10} \left( \frac{I(\bar{\nu})}{I_0(\bar{\nu})} \right) \quad (1)$$

where  $A$  is the absorbance,  $I$  is detected light through the sample, and  $I_0$  is the light detected without the sample present. Molecular bonds are identified by their characteristic pattern where  $A(\bar{\nu})$  is non-zero.

Recent advances in FT-IR spectrometry allow the use of focal plane arrays (FPAs) for acquiring spatially-resolved mid-infrared absorbance spectra at high speeds [6]. This allows the facile collection of hyperspectral images, where each pixel provides the corresponding spatially resolved absorption as a function of wavenumber.

### Morphological effects

The increasing availability of imaging systems now permit the analyses of non-homogeneous samples, where structural changes accompany changes in chemical composition. However, these samples introduce additional

spectral characteristics due to the sample morphology. These effects can dramatically affect the ability to differentiate between chemical constituents. Morphological characteristics can affect the spectrum in two ways: (a) increased absorbance as a function of density and thickness, and (b) scattering affects. Changes in tissue thickness and density result in well-understood spectral changes characterized by the Beer-Lambert Law, while scattering is significantly more difficult to characterize.

### Scattering

Light transmitted through non-homogeneous samples is subject to scattering as it transitions between material interfaces exhibiting different indices of refraction,  $n(\bar{\nu})$ . These effects are prominent in mid-infrared spectroscopy, where the re-direction of light is indistinguishable from absorbance [7-9], resulting in wavelength-dependent changes in the absorbance spectrum that make the determination of the actual tissue absorbance,  $A(\bar{\nu})$ , extremely difficult [7]. The study of scattering effects in FT-IR imaging is an active area of research [8-10]. Current work suggests that a significant portion of scattering through tissue samples is the result of interaction with microscopic structures, such as cell bodies and nuclei [11]. Empirical methods have been proposed for correcting spectra based on Mie theory [12], however these techniques are time consuming and do not provide interactive feedback. In addition, Mie theory is not generally applicable to scattering effects and the prior information required for these estimations is not always available. While computational methods have been proposed for eliminating scattering effects for known structures such as spheres [13], no automated techniques have been proposed that compensate for spectral features introduced by elastic scattering, which accounts for a large amount of variance in mid-infrared spectroscopic images [14].

An alternative method presents a first-order approximation to remove the non-chemical effects of scattering [15]. For each feature, a corrected absorption spectrum  $\hat{A}(\bar{\nu})$  is determined by subtracting a piecewise-linear function  $b$ :

$$\hat{A}(\bar{\nu}) = A(\bar{\nu}) - b(\bar{\nu}) \quad (2)$$

However, the process requires manual specification of points that represent  $b$  as well as either detailed know-

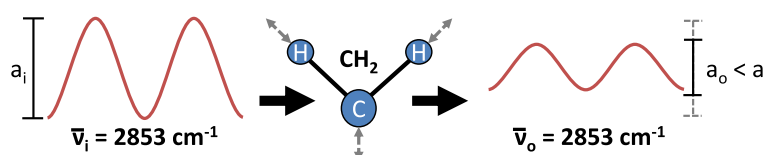


**Figure 1** Mid-infrared spectroscopy measures the light absorbed due to resonance with specific vibrational modes in a molecule. When transmitted through a material containing a  $\text{CH}_2$  functional group, as shown in this example, the output intensity is lower than the incident light when  $\bar{\nu}_i = 2853 \text{ cm}^{-1}$ .

ledge of the chemical compound under consideration or extensive exploration of the data set. This makes the selection of spectral features representing chemical information extremely time-consuming, particularly when the chemical composition of the tissue sample is unknown.

### Beer-Lambert law

Variations in tissue thickness and molecular density cause linear scaling of the absorbance spectrum according to the Beer-Lambert Law:

$$\hat{A}(\bar{\nu}) = \kappa(\bar{\nu})\ell N \quad (3)$$

Here,  $\hat{A}(\bar{\nu})$  is the scattering-corrected absorption as a function of the wavenumber  $\bar{\nu}$ ,  $\kappa(\bar{\nu})$  is the absorption coefficient,  $\ell$  is the path length through the specimen (thickness), and  $N$  is the molecular density. The absorption coefficient  $\kappa$  is the desired material property that defines the chemical composition of the specimen.

Note that there are no methods for separating the path length  $\ell$  and density  $N$  in the general case. However, the function  $\kappa(\bar{\nu})$  can be estimated using a reference band  $\bar{\nu}_r$  within the spectrum. One example of a useful reference is the Amide I peak found in biological tissue at  $\bar{\nu}_r \approx 1650\text{cm}^{-1}$ . By normalizing Amide I absorption across chemical species (setting  $A(\bar{\nu}_r) = 1.0$ ), the combined contributions of path length and density are estimated in terms of the relative protein composition, using  $A(\bar{\nu}_r) = \ell N$ , and determining the normalized spectrum:

$$A_n(\bar{\nu}) = \frac{\hat{A}(\bar{\nu})}{\hat{A}(\bar{\nu}_r)} \quad (4)$$

While a single reference feature is useful, it is not generally applicable to samples containing several unique components, therefore several references are used for classifying multiple chemical species.

### Methods

In this section, we describe our methods for interactive exploration of hyperspectral data. The chemical composition of a sample is identified by finding features, such as absorbance peaks, that can be used as references and to differentiate individual compounds. For example, the biological compound *collagen* exhibits several absorbance peaks between  $1235\text{cm}^{-1}$  and  $1265\text{cm}^{-1}$ . However, these peaks are difficult to distinguish in a raw spectrum, due to morphological characteristics of the sample (Section ‘Morphological effects’).

Given a measured absorption spectrum from a non-homogeneous sample composed of a single chemical

constituent, Equations 2 and 4 indicate that the normalized, corrected spectrum can be computed using:

$$\hat{A}_n(\bar{\nu}) = \frac{A(\bar{\nu}) - b(\bar{\nu})}{A(\bar{\nu}_r) - b(\bar{\nu}_r)} \quad (5)$$

where  $\bar{\nu}_r$  is the location of a spectral feature used for normalization and  $b(\bar{\nu})$  is an estimate of the spectral contribution due to scattering.

For an unknown sample, both the normalization feature and baseline function must be estimated. In addition, if the sample is composed of several unique chemical constituents, multiple normalization features and baseline functions must be utilized for classification. This is an extremely difficult problem to solve computationally, requiring detailed knowledge of both the sample and the relationship between spectral bands and molecular characteristics.

The SpecVis software addresses this problem by allowing interactive visualization of the data set. Our software allows a spectroscopist to specify the baseline function  $b$  (Section ‘Scattering’), dynamically select reference features (Section ‘Beer-Lambert law’), and visualize the chemical characteristics. This is done by allowing the user to specify changes in the distribution of spectra, as reflected using a dynamic 2D histogram. The user then selects chemical features in this histogram, exploring the results through an interactive 2D visualization of the tissue sample. Computing the changing distribution of spectra as well as visualization of user-selected features is computationally expensive, making interactive feature selection impossible on current CPU-based desktop systems. We therefore demonstrate that this problem can be well-formulated for implementation on programmable graphics hardware. In the following sections, we first describe the types of metrics used to identify features in hyperspectral images. We then discuss how spectra in an image are adjusted to remove scattering artifacts and other distortions, based on a histogram describing the distribution of spectral information.

### Metrics

We first identify measures of spectral features, or metrics, that quantify, for example, characteristics in forensic spectroscopy [16] and differentiate cell types in biological samples by acting as features for more complex classification systems [2,17]. The user specifies parameters for these measurements in the spectral domain. Once specified, a metric is immediately applied to all pixels in the image. The metrics described in this paper include the peak height, which is the most basic measure of chemical composition, as well as peak integral and centroid. While these are not all of the possible types of metrics, we limit our study to these as this is an active area of research and they allow us to identify several important chemical differences



in biological tissue samples. Additional types of metrics can be readily added as our approach is general. For each metric, the function  $S(x, y, \bar{\nu})$  represents a generic spectral value, where  $(x, y)$  is the spatial position and  $\bar{\nu}$  is the wavenumber. In the case of absorbance measurements,  $S$  can be either the raw or corrected absorbance spectrum.

### Peak height

This metric is highly sensitive to peak shifts. This is particularly noticeable for the Amide I peak at  $1650\text{cm}^{-1}$ , which is narrow and composed of multiple chemical contributions that make it prone to shift. Absorbance is particularly useful for detecting broad peaks and the density of well-known and localized molecular bonds.

### Peak integral

While the peak absorbance is indicative of the presence of species, the total area under the peak is indicative of the total concentration. Hence, another useful metric is the definite integral of the spectrum on a user-specified interval  $[\bar{\nu}_0, \bar{\nu}_1]$  that provides the area under the peak:

$$M_i(x, y, \bar{\nu}_0, \bar{\nu}_1) = \int_{\bar{\nu}_0}^{\bar{\nu}_1} S(x, y, \bar{\nu}) d\bar{\nu} \quad (6)$$

This metric provides a robust measure of absorbance within a spectral region and is relatively insensitive to noise and peak shifts. This robustness makes it an ideal candidate for use as a spectral reference. It is insensitive, however, to subtle spectral changes that are often found in biological tissue samples.

### Centroid

The centroid of a bounded region of the spectrum is computed using:

$$M_c(x, y, \bar{\nu}_0, \bar{\nu}_1) = \frac{\int_{\bar{\nu}_0}^{\bar{\nu}_1} \bar{\nu} S(x, y, \bar{\nu}) d\bar{\nu}}{\int_{\bar{\nu}_0}^{\bar{\nu}_1} S(x, y, \bar{\nu}) d\bar{\nu}} \quad (7)$$

The resulting value is the wavenumber for the center of mass in the specified region. This metric is useful for measuring shifts in single peak positions as well as the distribution of multiple species' absorption among multiple neighboring peaks. This metric is dependent on the distribution of absorption and therefore does not require a reference. However, it is incapable of detecting the height and is of limited utility for peaks that do not shift as a function of spatial position.

### Interactive histogram

The first step in visualization is to display the distribution of spectra in the image using a 2D histogram. This allows the user to identify chemical compounds by approximately removing morphological effects and selecting metrics. Chemical features are selected using the joint

histogram of wavenumber and absorbance for all spectra in the image. The user selects features in this domain that correspond to the structural and chemical components of the tissue sample. However, the data processing required to separate structural and chemical features is currently time consuming and the results are difficult to visualize. We implement a dynamic approach, which allows the user to explore the data set via interactive feedback in both the spatial and spectral domains, which facilitates meaningful feature selection. Our framework allows the user to interactively adjust points for baseline correction and select reference features. Data processing is performed dynamically on the GPU using CUDA [18] and provides interactive feedback for multi-gigabyte data sets. The unprocessed data set is stored on the GPU as a three-dimensional texture map represented as 32-bit floating point values. The user explores the data in two ways: (a) the insertion of baseline points to build the scattering approximation  $b(\bar{\nu})$  and (b) the selection of a reference metric. The histogram is computed interactively and dynamically as the user changes parameters for the baseline and reference. This is done using a CUDA device kernel. A block of threads is assigned to process each band (wavenumber). We specify a 2D block size of  $\sqrt{w}x\sqrt{w}$  threads, where  $w$  is the maximum warp size supported by the GPU. Therefore, each block consists of one warp that executes data in a single-instruction multiple-data (SIMD) fashion. Each block  $b$  is responsible for computing the complete one-dimensional histogram for a single band  $\bar{\nu}_b$ . The threads within each block are responsible for evaluating a spatially coherent square of pixels, initially positioned at the upper left-hand corner of the image. Each thread then iterates across the image to the lower-right corner at intervals of  $\sqrt{w}$ . Note that all threads within the block are part of the same (SIMD) warp, therefore they will be spatially coherent at each iteration across the spatial domain of the image. This spatial coherence is used to perform faster fetches using texture units, which is particularly useful for fast evaluation on GPUs with compute capability lower than 2.0.

Computing the processed spectrum at each spatial location within a band requires a maximum of four memory fetches: (1) the raw data value at  $A(x, y, \bar{\nu})$ , (2) the raw values at the baseline points  $A(x, y, \bar{\nu}_0)$  and  $A(x, y, \bar{\nu}_1)$ , and (3) the reference value  $r(x, y)$ . Computing the reference value  $A_r(x, y)$  also requires its neighboring baseline points at  $A(x, y, \bar{\nu}_{r0})$  and  $A(x, y, \bar{\nu}_{r1})$ . However, an image of the reference values at each spatial location is pre-computed whenever the reference is changed.

As each thread traverses the image at  $\bar{\nu}$ , the resulting histogram is accumulated in shared memory allocated for the block. Accurate computation of the histogram, however, requires the use of atomic operations for incrementing the counters for each bin. This can reduce

performance when multiple threads encounter similar absorbance values – a common occurrence, given the close spatial proximity of all threads in the  $\bar{v}$  image. In addition, the SIMD execution within a warp will cause the entire block to pause while atomic adds are resolved. We address this issue by allocating a separate shared histogram for each thread and summing the results when the entire  $\bar{v}$  image has been processed. The resulting histogram is then displayed using a *log*-scale intensity filter.

### Visualization

The chemical composition of the tissue sample is visualized by building a 2D image based on user-selected metrics. Each metric is assigned a color value, where the intensity is based on the value of the metric. The metrics are then evaluated for each pixel, and the resulting colors are combined to create a spatially-resolved chemical visualization of the sample. This color-mapping technique is similar to a *transfer function*, which is commonly used in volumetric visualization. We first provide an overview of this technique and describe how it is applied to our algorithm.

### Transfer functions

Transfer functions are used in volume visualization to assign color and opacity values to pixels based on features defined in a separate domain [19,20]. These techniques generally use spatial features such as gradient magnitude [21], curvature [22], size [23], and orientation [24] to assign color values. While these techniques have been applied to gigabyte-scale data sets [25,26], they are difficult to generalize to spectroscopic images since each pixel represents a spatially-resolved absorbance function. The principle behind using spectra to apply transfer functions has been previously explored through contour spectra [27], where spatial characteristics are used to highlight geometric features in the data set. More flexible methods using spatially local statistics have also been proposed [28]. Both contour spectra and spatial statistics may be applicable for

extracting spatial characteristics in heterogeneous samples. In this paper, we focus on visualizing chemical features, and therefore each pixel is considered to be an independent component with a corresponding chemical signature.

Very few techniques currently exist for visualizing spectroscopic images. Li et al. [29] propose a technique for visualizing astrophysical data imaged at various wavelengths. They propose the use of transfer functions for defining opacity when rendering the image stack volumetrically. However, the number of bands in a single image is small and the samples are discontinuous, which limits the amount of chemical information in the data set. More recent work demonstrates a visualization framework for near-infrared spectroscopic images of historical documents sampled regularly in the spectral domain [30]. This technique allows relighting of images, interactive selection of individual bands, and metrics for evaluating similarity between user-specified spectra. However, similarity is difficult to measure for vibrational spectra because of the coupled structural and chemical contributions to the spectrum. Unsupervised techniques, such as principal component analysis (PCA) and vertex component analysis (VCA) [31], have been proposed to perform spectral unmixing. However, these techniques assume homogeneous samples and also make specific assumptions about the data, such as the existence of orthogonal chemical signatures, which are not generally applicable. Comprehensive Data Maps (CDM) have been proposed to examine data [32], but do not provide imaging visualizations.

Color values are assigned to spectra based on metric results. The user specifies a bounding range for a metric value using a lasso tool in the spectral histogram. For all three metrics, the lasso bounds are indicated by a line segment. For metrics that are computed across a specified wavenumber interval, a shaded region highlights these boundaries (Figure 2). When the result of a spectral metric falls within these bounds, a color value is assigned based on the point of intersection using a ramp shader. Our

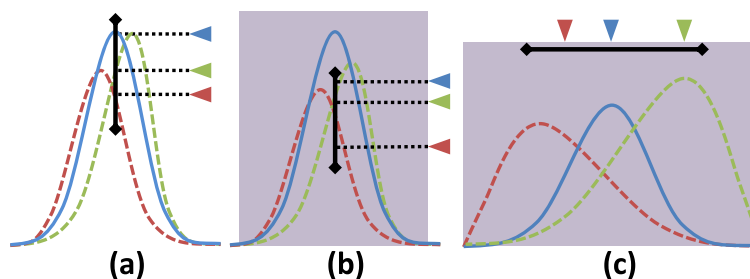


**Figure 2 Metrics for selecting spectral features.** Useful measurements include (a) peak height, (b) average peak height (integral), (c) centroid (center of gravity). Colored arrows indicate the projection of the metric value on the widget (black line). Shaded regions indicate the integral intervals.

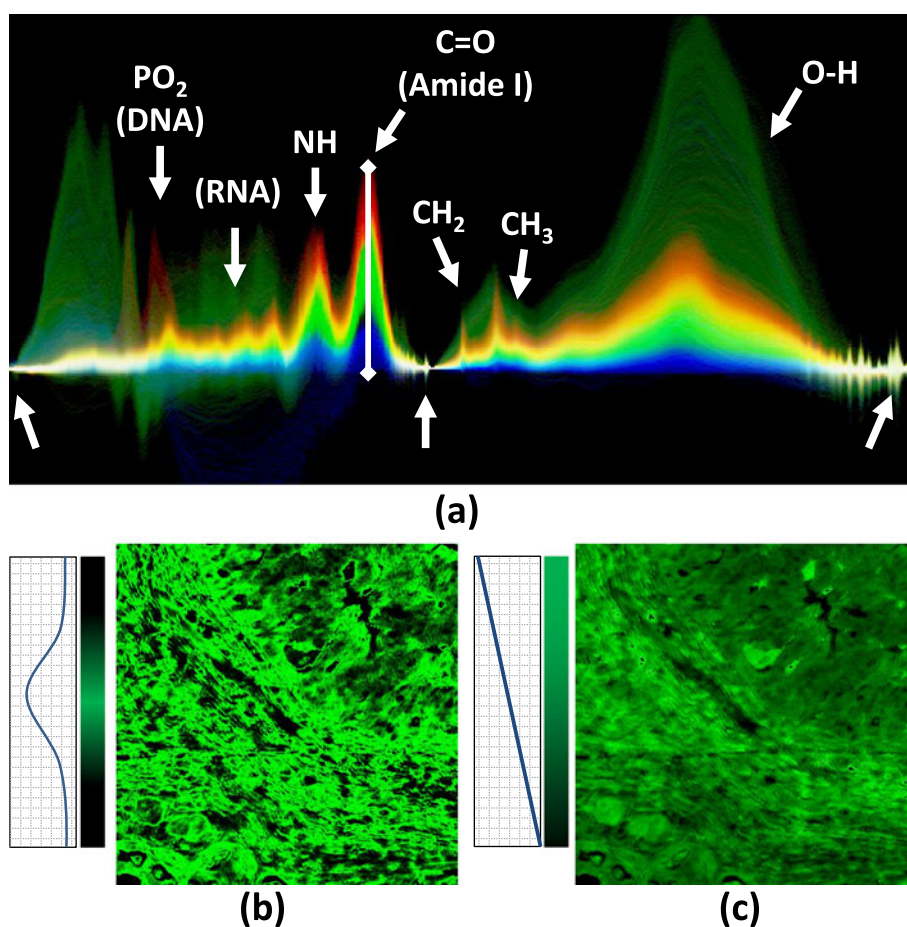


**Figure 3 Color mapping of spectral features in a baseline-corrected image.** Labels indicate peaks representing prominent chemical features. (a) The spectral histogram shows a rainbow color map applied based on the peak height of the Amide I band (vertical white line). The peak height of Amide I is often assumed to correspond to tissue thickness and density in tissue samples. Note how the colors mix as individual spectra cross and overlap with changes in density and chemistry. Spatial images show the result of a (b) Gaussian and (c) linear ramp applied to the lasso.

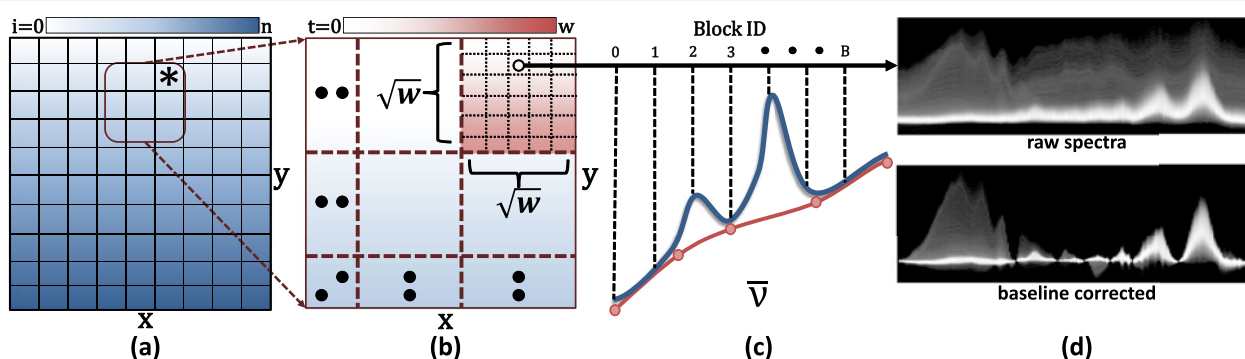


**Figure 4 Parallel implementation for evaluating the corrected spectral distribution.** Each band is evaluated by a block of  $\sqrt{w_x} \times \sqrt{w_y}$  threads. (a) Each block iterates across the spatial dimensions of the image from  $i = 0$  to  $i = n$ , where  $n = \frac{S_x S_y}{w}$  and  $S_x$  and  $S_y$  are the spatial extents. The threads for  $i = 14$  (\*) are shown. (b) The threads are evaluated using SIMD and kept spatially coherent to take advantage of 2D texture caching. (c) Each band is evaluated by an independent thread block and each thread performs a maximum of 3 texture fetches per iteration (1 data point and 2 baseline points). (d) Resulting histogram.

framework allows the user to assign colors using a constant, linear, and Gaussian ramp (Figure 3), as available in most image analysis software. In order to make selection intuitive for the integration metric  $M_i$ , color is assigned based on the average peak height

$$\tilde{M}_i = \frac{M_i}{\bar{v}_1 - \bar{v}_0} \quad (8)$$

rather than the integral. This allows the widget to be placed in the vicinity of the selected spectra.

### Computing metrics

Metrics are computed independently for each spectrum, requiring the appropriate baseline points and reference bands. The data set is partitioned spatially into  $\sqrt{w} \times \sqrt{w}$  blocks, where each thread is assigned an independent spectrum. The baseline bands and reference are applied using a GPU kernel (Figure 4). If the metric requires integration, summation occurs along the spectral axis. Note that a binary search for the neighboring baseline bands is only necessary when a thread is created. If a baseline band is crossed within an interval of integration, the next band  $\bar{v}_n$  in the list is acquired. The metric result is saved to a 2D grid, which can be used as a source for color-mapping to produce the final display image or as a reference for additional metrics.

### Results and discussion

Rendering time is dominated by the computation of the histogram as the user changes processing and visualization parameters. However, the frame rate is interactive for

our largest sample image (700x700x491,  $\approx 1$ GB), requiring  $< 32$ ms for complete evaluation of the histogram ( $< 147$ ms with atomic writes to shared memory) using a GeForce GTX 580 with 1.5GB of global memory. We use the developed software to identify characteristics in mid-infrared spectroscopic images. We first demonstrate the visualization of structural and chemical components from images of synthetic polymer targets that are often used to assess image quality. We then show how these techniques can be used to extract similar information from mid-infrared images of tissue biopsies, including the visualization of chemical components useful for breast cancer diagnosis. Finally, we demonstrate that these techniques can be extended to other forms of spectroscopy by visualizing Raman images of tissue samples.

### Infrared images of tissue

Biological tissue samples pose a unique problem in spectroscopic imaging, since each pixel contains a complex combination of chemical species. Spectral features that correspond to different tissue types are subtle and difficult to identify, making interactive exploration a valuable tool. We first demonstrate the structural and chemical characteristics that can be visualized using the developed techniques. We obtain a tissue sample and place it on a barium fluoride substrate for imaging. The same sample is then stained using a commonly-used clinical dye, Hematoxylin and Eosin (H&E), in order to identify structural and chemical features (Figure 5a).

The developed method is used to find similar features from the hyperspectral image data. Since the unprocessed

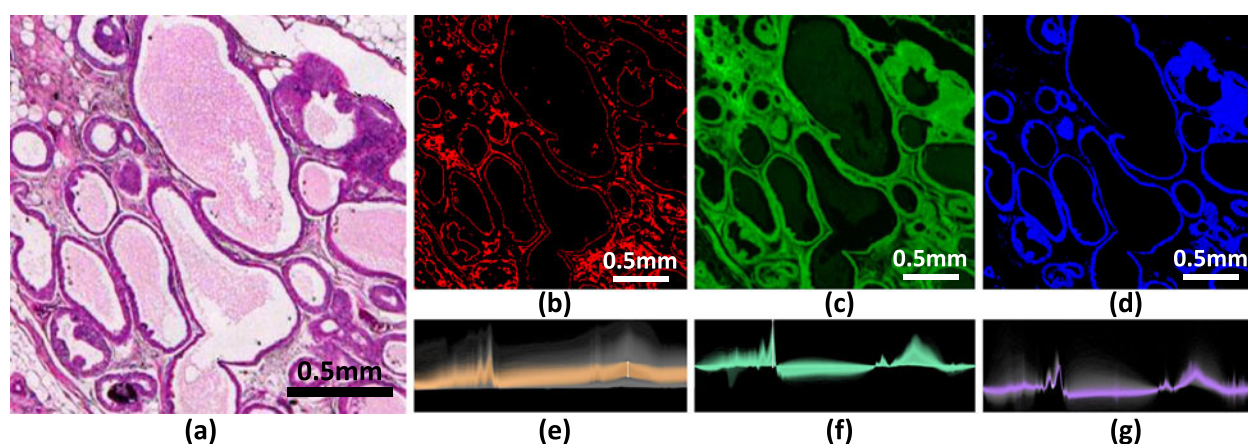


**Figure 5 Using transfer functions to visualize features seen in standard histology.** A surgical resection of a breast biopsy was imaged using IR spectroscopy and then stained and imaged with a standard optical microscope. **(a)** A section of the hematoxylin and eosin (H&E) stained tissue is shown. The proposed techniques can be used to selectively visualize various structural and chemical features using only the IR hyperspectral image. **(b)** Scattering effects are highlighted, indicating regions containing highly scattering structures (edges and collagen fibers). **(c)** Removal of scattering features allows the selection of tissue thickness based on the absorbance of Amide I ( $1650\text{cm}^{-1}$ ). **(d)** Using Amide I as a reference, chemical compounds corresponding to epithelial cells are visualized using the centroid of the Amide II band ( $\approx 1550\text{cm}^{-1}$ ). **(e-f)** The corresponding joint histograms are shown, with selected pixels highlighted.



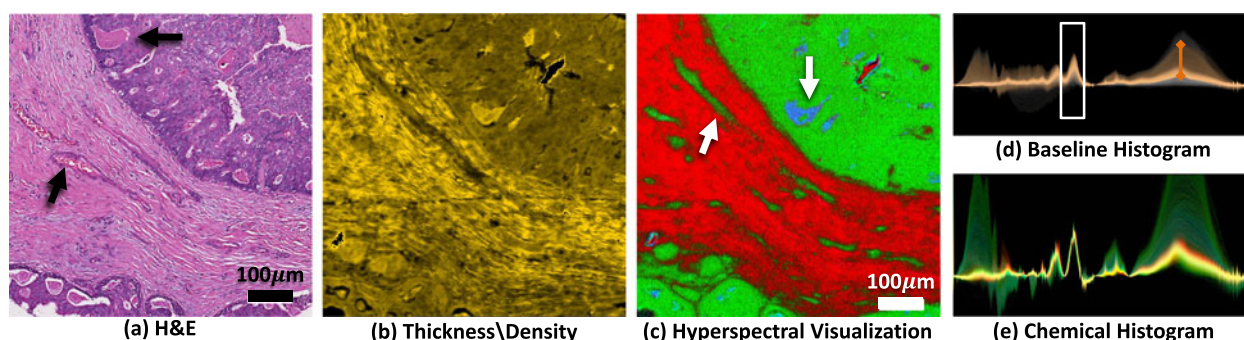


**Figure 6 Visualization of a 1mm needle biopsy from a breast tissue biopsy at 74X magnification (scale bar = 100 $\mu$ m).** (a) An adjacent histology slide stained with H&E is shown. Epithelial cells are purple and stromal cells are pink. Arrows indicate the position of a blood vessel and necrosis. (b) Tissue density is shown after baseline correction. (c) Features are then selected to separate stromal cells (red), epithelium (green), and necrosis (blue). The histogram shows selected spectra for estimating tissue density (d) and chemical composition (e). The composition histogram is normalized to the area under the Amide I peak (white box).

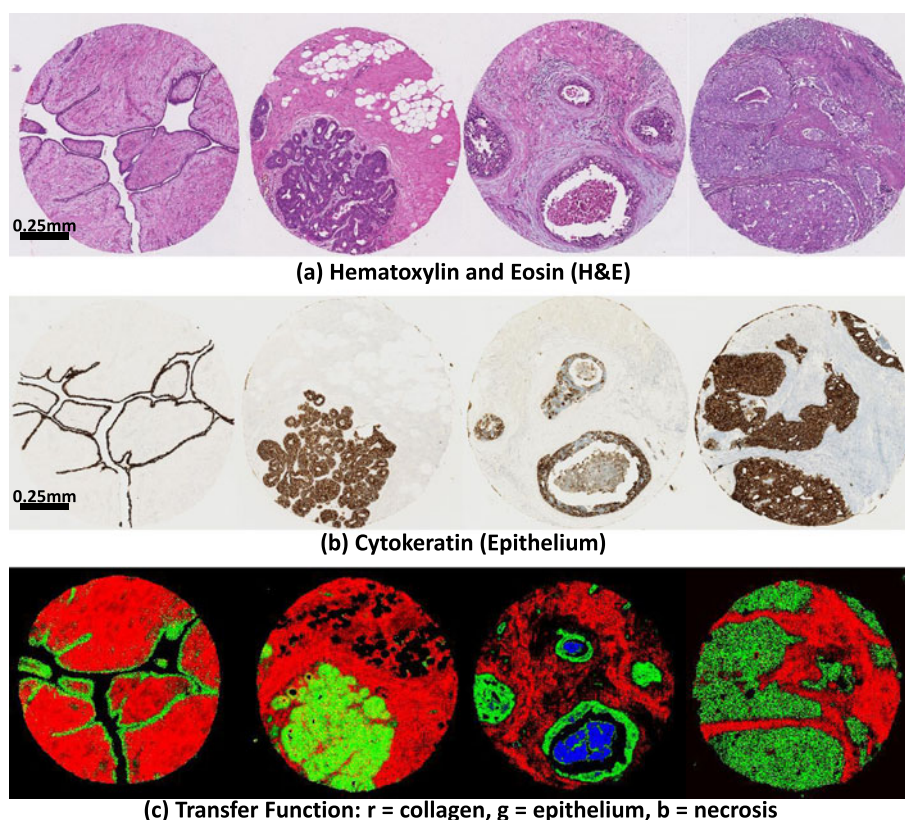


**Figure 7 Standard histology stains (top, middle) and hyperspectral imaging (bottom) applied to adjacent sections of 1mm breast cancer biopsies.** Hyperspectral imaging is quantitative and our methods allow the pathologist to separate several chemical constituents consistently across tissue samples. Adjacent sections of 1mm biopsy cores are shown stained using hematoxylin and eosin (a), cytokeratin for epithelium (b), and visualized using our methods (c). The SpecVis visualization shows epithelial cells in green, collagen in red, and necrosis in blue. Separating epithelium and stromal cells in H&E stained tissue can be difficult (a), however these differences are visible using a cytokeratin stain (b) for epithelium. Necrosis is difficult to identify using chemical staining (a and b), but can be clearly segmented using mid-IR spectroscopic imaging combined with our processing methods (c, blue).



spectra are dominated by scattering in the high-wavenumber regions, we are able to visualize pixels containing edges and boundaries, where scattering is more prominent (Figure 5b and e). We then select baseline points and use a linear gradient to visualize the tissue thickness and density based on Amide I absorption (Figure 5c and f). Using Amide I as a reference, features in the spectra are now dominated by chemical differences between cell types in the tissue. This allows the user to visualize the distribution of tissue types, such as epithelial cells (Figure 5d and g), in which 97% of cancers of the breast arise. The facile delineation of epithelial cells is a desirable, but unmet need, as reported in recent studies using automated computerized analysis of pathologic images [33]. We further demonstrate the possible use of the presented techniques for tissue pathology. Several breast cancer biopsies were commercially obtained and stained using H&E. Adjacent tissue samples were imaged using mid-infrared spectroscopy. We then designed transfer functions to identify tissue characteristics that are useful for cancer diagnosis. This includes structural features, such as tissue density, as well as labeling of various tissue types. These types include epithelial cells, connective tissue (stroma), and necrotic (dead and dying) cells

(Figure 6). The spatial distribution of these features are commonly used in pathology to identify the presence of a tumor.

Once the transfer function is created, it is then applied to other tissue samples (Figure 7). Note that these tissue types are difficult to separate using chemical staining. Often, multiple stains are necessary for diagnosis and these methods are difficult to quality-control. However spectroscopic imaging provides quantitative data that can be used to characterize chemical information reliably across multiple samples. The ability to identify tissue types by interactively exploring the hyperspectral data provides several advantages over existing techniques. Unlike chemical staining, mid-infrared imaging does not perturb the tissue sample in any way. In addition, the effects of scattering on tissue samples are not well understood, and previous methods for classification of tissue types require extensive pre-processing and the application of machine learning [2,34]. Though an extensive comparison between the more complex machine learning methods and the method reported here must be undertaken to quantify advantages, the results seem to be comparable and significantly faster for our method by facilitating interactive analysis. An experienced user was

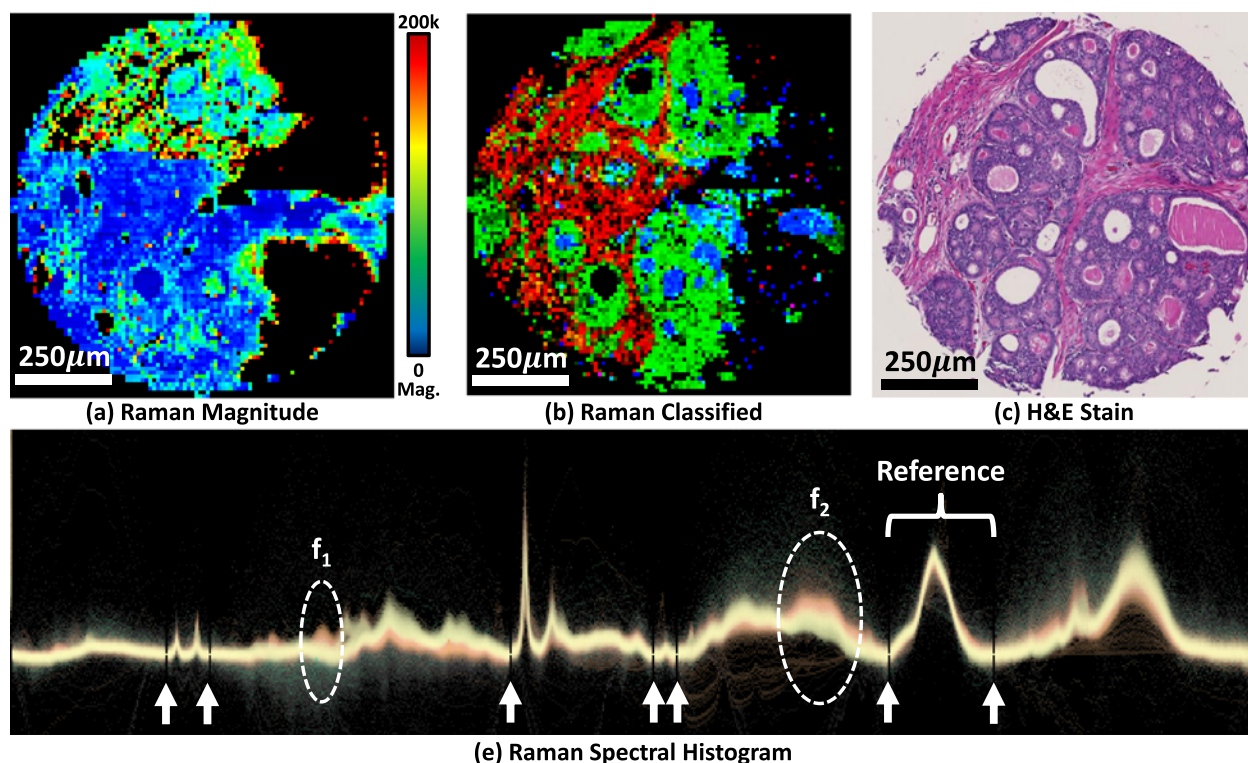


**Figure 8 Application of hyperspectral transfer functions on Raman spectroscopy.** A single breast tumor biopsy was imaged using Raman microscope. The magnitude of the Raman signal is shown using a rainbow color map (a). A new transfer function is applied to separate cell types (b) based on the adjacent histology (c). Colors reflect stroma (red), epithelium (green), and protein deposits (blue). The Raman spectral distribution is shown (e) with features and baseline points indicated.

able to separate, visualize, and evaluate the utility of the extracted tissue characteristics useful for tumor diagnosis in a few minutes, given interactive feedback. Using our older methods, simply computing a metric took several minutes on a CPU.

### Raman spectroscopy

The methods that we propose in this paper can also be extended to hyperspectral imaging in other areas. We demonstrate that transfer functions can be created to effectively visualize the distribution of chemical compounds in Raman images. We collected Raman images of prostate biopsy cores and built a transfer function to discriminate between epithelial and stromal cells (Figure 8). Some advantages of Raman spectroscopy include the ability to choose the excitation frequency, easy coupling to fiber-optic probes, and little to no signal from water in a sample. These features make it useful for taking *in vivo* measurements [35-37]. However, the Raman spectral signal is extremely weak and requires long acquisition times that effectively limit the signal-to-noise ratio (SNR) and the size of image that can be obtained in a reasonable amount of time. Our method is robust and can thus be generally applied.

### Conclusions

The ability to acquire spatially resolved information using hyperspectral imaging is strongly emerging as a promising avenue across a variety of areas, especially biomedical analyses. Vibrational spectroscopy has the potential to provide quantitative histology for disease diagnosis, without the use of chemical stains in an objective and automated manner. Recent work has shown that mid-infrared spectroscopic imaging provides sufficient chemical detail for differentiating between tissue types. Researchers have reported very high accuracy after rigorous scattering correction [12] and classification algorithms [2,3] are applied. These studies demonstrate the potential for applying vibrational spectroscopy to cancer diagnosis.

However, computational methods must be developed to visualize the data quickly and reliably. The size and complexity of the data contained in hyperspectral images makes this a difficult problem, requiring the separation of physical and chemical characteristics from underlying spectra. In this paper, we demonstrate an interactive method for building transfer functions for visualizing hyperspectral images. Our method allows users to dynamically assimilate large collections of spectra using algorithms designed to separate structural and chemical features in real time. These features are then selected using transfer functions which allow the visualization of these characteristics in a spatial image of the sample. To our knowledge, the reported methods are the first to allow interactive processing and visualization of hyperspectral

images at this level of spectral and structural detail, and we have demonstrated their usefulness in biological samples. Applying these features to tissue provides a method for label-free identification of tissue types that is quantitative, non-destructive, and can be performed in a time frame that is clinically viable.

Future directions include applying these techniques to three-dimensional samples, which can be acquired using Raman spectroscopy in combination with a confocal microscope, for example.

Our proposed technique also has several advantages over unsupervised methods, such as PCA and VCA. In particular, the metrics that we use for visualization have finite support, requiring only a narrow band of information within the spectrum. Once useful metrics are identified, the number of collected bands can then be reduced, allowing faster imaging, for example using narrow-band filters for IR [38]. Finally, since the separation of structural and chemical characteristics from an IR image is so difficult, many algorithms for the classification of hyperspectral images rely on the use of user-defined metrics [2]. Our method may provide an efficient method for selecting features for use in more complex classifiers for IR-based clinical histology.

### Competing interests

The authors declare no competing interests.

### Authors' contributions

DM designed the algorithm and developed the software. MW collected mid-infrared images and identified spectral and chemical features corresponding to cell types. MS collected Raman images and identified spectral and chemical features corresponding to cell types. RB designed the experiments and identified chemical and spectral features corresponding to cell types in cancer biopsies. All authors read and approved the final manuscript.

### Acknowledgements

This work was funded in part by the Beckman Institute for Advanced Science and Technology, the National Institutes of Health (NIH) via grant number 1R01CA138882, the National Science Foundation (NSF) Division of Chemistry (CHE) via 0957849, and the Congressionally Directed Medical Research Program Postdoctoral Fellowship via BC101112.

### Author details

<sup>1</sup>Beckman Institute for Advanced Science and Technology, University of Illinois at Urbana-Champaign, Urbana, IL, USA. <sup>2</sup>Department of Pathology, University of Illinois at Chicago, Chicago, IL, USA. <sup>3</sup>Department of Bioengineering, University of Illinois at Urbana-Champaign, Urbana, IL, USA. <sup>4</sup>Department of Mechanical Science and Engineering, University of Illinois at Urbana-Champaign, Urbana, IL, USA. <sup>5</sup>Micro and Nanotechnology Laboratory, University of Illinois at Urbana-Champaign, Urbana, IL, USA. <sup>6</sup>University of Illinois Cancer Center, Urbana, IL, USA.

Received: 1 November 2012 Accepted: 2 April 2013

Published: 8 May 2013

### References

1. Bhargava R: **Infrared spectroscopic imaging: The next generation.** *Appl Spectrosc* 2012, **66**(10):1091-1120. [http://as.osa.org/abstract.cfm?URI=as-66--10-1091].
2. Fernandez D, Bhargava R, Hewitt S, Levin I: **Infrared spectroscopic imaging for histopathologic recognition.** *Nat Biotechnol* 2005, **23**(4):469-474.

3. Kallenbach-Thieltges A, Großerüchkamp F, Mosig A, Diem M, Tannapfel A, Gerwert K: **Immunohistochemistry, histopathology and infrared spectral histopathology of colon cancer tissue sections.** *J Biophotonics* 2013, **6**:88–100. [http://onlinelibrary.wiley.com/doi/10.1002/jbio.201200132/abstract].
4. Kwak JT, Hewitt SM, Sinha S, Bhargava R: **Multimodal microscopy for automated histologic analysis of prostate cancer.** *BMC Cancer* 2011, **11**:62. [http://www.biomedcentral.com/1471-2407/11/62].
5. Griffiths PR, De Haseth JA: *Fourier Transform Infrared Spectrometry*: Wiley-Interscience; 2007.
6. Lewis EN, Treado PJ, Reeder RC, Story GM, Dowrey AE, Marcott C, Levin IW: **Fourier transform spectroscopic imaging using an infrared focal-plane array detector.** *Anal Chem* 1995, **67**(19):3377–3381. [http://dx.doi.org/10.1021/ac00115a003].
7. Bhargava R, Wang SQ, Koenig JL: **FT-IR Imaging of the interface in multicomponent systems using optical effects induced by differences in refractive index.** *Appl Spectrosc* 1998, **52**(3):323–328. [http://www.opticsinfobase.org/as/abstract.cfm?URI=as-52-3-323].
8. Davis BJ, Carney PS, Bhargava R: **Theory of mid-infrared absorption microspectroscopy I: Homogeneous samples.** *Anal Chem* 2010, **82**(9):3474–3486. [http://dx.doi.org/10.1021/ac902067p].
9. Davis BJ, Carney PS, Bhargava R: **Theory of mid-infrared absorption microspectroscopy II: Heterogeneous samples.** *Anal Chem* 2010, **82**(9):3487–3499. [http://dx.doi.org/10.1021/ac902068e].
10. Reddy R, Mayerich D, Walsh M, Schulmerich M, Carney PS, Bhargava R: **Optimizing the design of FT-IR spectroscopic imaging instruments to obtain increased spatial resolution of chemical species.** In *IEEE Int Symp Biomed Imaging*; 2012:354–357.
11. Bassan P, Byrne HJ, Bonnier F, Lee J, Dumas P, Gardner P: **Resonant Mie scattering in infrared spectroscopy of biological materials – understanding the ‘dispersion artefact’.** *Analyst* 2009, **134**(8): 1586–1593. [http://pubs.rsc.org/en/Content/ArticleLanding/2009/652%20AN/B904808A].
12. Bassan P, Kohler A, Martens H, Lee J, Jackson E, Lockyer N, Dumas P, Brown M, Clarke N, Gardner P: **RMieS-EMSC correction for infrared spectra of biological cells: Extension using full Mie theory and GPU computing.** *J Biophotonics* 2010, **3**(8-9):609–620.
13. van Dijk T, Mayerich D, Carney PS, Bhargava R: **Recovery of absorption spectra from Fourier transform infrared microspectroscopic measurements of intact spheres.** *Appl Spectrosc* 2013, **6**(5): 546–552.
14. Kwak JT, Reddy R, Sinha S, Bhargava R: **Analysis of variance in spectroscopic imaging data from human tissues.** *Anal Chem* 2011. [http://dx.doi.org/10.1021/ac2026496].
15. Bhargava R: **Towards a practical Fourier transform infrared chemical imaging protocol for cancer histopathology.** *Anal Bioanal Chem* 2007, **389**(4):1155–1169.
16. Deming SN, Michotte Y, Massart DL, Kaufman L, Vandeginste BGM: *Chemometrics: A Textbook*. 1 edition: Elsevier Science; 1988.
17. Levin IW, Bhargava R: **Fourier transform infrared vibrational spectroscopic imaging: Integrating microscopy and molecular recognition.** *Ann Rev Phys Chem* 2005, **56**:429–474. [http://www.annualreviews.org/doi/abs/10.1146/annurev.physchem.56.092503.141205] [PMID: 15796707].
18. Nvidia C: **Compute unified device architecture programming guide.** *NVIDIA: Santa Clara, CA* 2007, **83**:129.
19. Drebin RA, Carpenter L, Hanrahan P: **Volume rendering.** In *Proceedings of the 15th Annual Conference on Computer Graphics and Interactive Techniques, Volume 22*; 1988:65–74.
20. Pfister H, Lorensen B, Bajaj C, Kindlmann G, Schroeder W, Avila LS, Raghu KM, Machiraju R, Lee J: **The transfer function bake-off.** *IEEE Comput Graph Appl* 2001, **21**(3):16–22.
21. Kniss J, Kindlmann G, Hansen C: **Interactive volume rendering using multi-dimensional transfer functions and direct manipulation widgets.** In *IEEE Conference on Visualization*; 2001:255–262.
22. Kindlmann G, Whitaker R, Tasdizen T, Moller T: **Curvature-based transfer functions for direct volume rendering: methods and applications.** In *IEEE Conference on Visualization*; 2003:513–520.
23. Correa C, Ma KL: **Size-based Transfer Functions: A New Volume Exploration Technique.** *IEEE Trans Vis Comput Graph* 2008, **14**(6):1380–1387.
24. Mayerich D, Hart JC: **Visualization of serial electron microscopy images using local variance.** In *IEEE Symposium on Biological Data Visualization (BioVis)*; 2012:9–16.
25. Crassin C, Neyret F, Lefebvre S, Eisemann E: **GigaVoxels: Ray-guided streaming for efficient and detailed voxel rendering.** In *ACM Symposium on Interactive 3D Graphics and Games (I3D)*; 2009:15–22.
26. Peng H, Ruan Z, Long F, Simpson JH, Myers EW: **V3D enables real-time 3D visualization and quantitative analysis of large-scale biological image data sets.** *Nat Biotech* 2010, **28**(4):348–353. [http://dx.doi.org/10.1038/nbt.1612].
27. Bajaj C, Pascucci V, Schikore D: **The contour spectrum.** In *IEEE Conference on Visualization*; 1997:167–173.
28. Tenginakai S, Lee J, Machiraju R: **Salient iso-surface detection with model-independent statistical signatures.** In *Proceedings of the 12th Annual Conference on Visualization*; 2001:231–238. [http://ieeexplore.ieee.org/xpls/abs\_all.jsp?arnumber=964516].
29. Li H, Fu CW, Hanson A: **Visualizing multiwavelength astrophysical data.** *IEEE Trans Vis Comput Graph* 2008, **14**(6):1555–1562.
30. Kim S, Zhuo S, Deng F, Fu C, Brown M: **Interactive visualization of hyperspectral images of historical documents.** *IEEE Trans Vis Comput Graph* 2010, **16**(6):1441–1448.
31. Nascimento J, Dias J: **Vertex component analysis: a fast algorithm to unmix hyperspectral data.** *IEEE Trans Geoscience Remote Sensing* 2005, **43**(4):898–910. [http://ieeexplore.ieee.org/xpls/abs\_all.jsp?arnumber=1411995].
32. Kong R, Reddy R, Bhargava R: **Characterization of tumor progression in engineered tissue using infrared spectroscopic imaging.** *Analyst* 2010, **135**:1569–1578.
33. Beck AH, Sangoi AR, Leung S, Marinelli RJ, Nielsen TO, van de Vijver MJ, West RB, van de Rijn M, Koller D: **Systematic analysis of breast cancer morphology uncovers stromal features associated with survival.** *Sci Transl Med* 2011, **3**(108):108–113. [http://stm.sciencemag.org/content/3/108/108a113.abstract].
34. Llorà X, Priya A, Bhargava R: **Observer-invariant histopathology using genetics-based machine learning.** *Nat Comput* 2009, **8**:101–120.
35. Schulmerich MV, Finney WF, Fredricks RA, Morris MD: **Subsurface Raman spectroscopy and mapping using a globally illuminated non-confocal fiber-optic array probe in the presence of Raman photon migration.** *Appl Spectrosc* 2006, **60**(2):109–114. [http://as.osa.org/abstract.cfm?URI=as-60--2-109].
36. Schulmerich MV, Dooley KA, Morris MD, Vanasse TM, Goldstein SA: **Transcutaneous fiber optic Raman spectroscopy of bone using annular illumination and a circular array of collection fibers.** *J Biomed Optics* 2006, **11**(6):060502. [http://spiedigitallibrary.org/jbo/resource/1/jbopfo/v11/i6/p060502.s1].
37. Schulmerich MV, Cole JH, Kreider JM, Esmonde-White F, Dooley KA, Goldstein SA, Morris MD: **Transcutaneous Raman spectroscopy of murine bone In Vivo.** *Appl Spectrosc* 2009, **63**(3):286–295. [http://as.osa.org/abstract.cfm?URI=as-63--3-286].
38. Kodali AK, Schulmerich M, Ip J, Yen G, Cunningham BT, Bhargava R: **Narrowband midinfrared reflectance filters using guided mode resonance.** *Anal Chem* 2010, **82**(13):5697–5706. [http://dx.doi.org/10.1021/ac1007128].

doi:10.1186/1471-2105-14-156

Cite this article as: Mayerich et al.: Real-time interactive data mining for chemical imaging information: application to automated histopathology. *BMC Bioinformatics* 2013 **14**:156.

# **LARGE INFRARED ABSORBANCE OF BIMATERIAL MICROCANTILEVERS BASED ON SILICON HIGH CONTRAST GRATING**

## **4.1 Introduction**

Bimaterial cantilever infrared (IR) detectors are based on the photothermal cantilever bending where the IR light absorption induces temperature rise and the thermal expansion mismatch bending of the cantilever [1-10]. The bimaterial cantilevers have shown a potential as a novel uncooled IR detector by exhibiting IR sensitivity similar to traditional methods but with lower cost and faster response time ( $\sim 0.1 - 1$  ms) [11-13]. Published research has shown that a bimaterial cantilever can detect radiative power of  $250 \text{ pW/Hz}^{0.5}$  at the wavelength of 650 nm [6], or  $1.3 \text{ nW/Hz}^{0.5}$  at the wavelength of  $10 \text{ }\mu\text{m}$  [3]. Focal plane array of bimaterial cantilevers have noise equivalent temperature difference (NETD) of  $50 - 200 \text{ mK}$  [2] which is comparable to the NETD of the most recent microbolometer IR detectors,  $35 - 200 \text{ mK}$  [14, 15]. Thus, people have explored the applications of bimaterial cantilevers in portable IR imaging system [2, 7, 9, 16] and IR spectroscopic system [8].

To make bimaterial cantilever IR detectors practical in actual applications, it is still necessary to improve their sensitivity [8, 12]. Optical and thermomechanical properties determine the cantilever sensitivity, which are related to the cantilever material and geometry [3, 9, 17]. To improve the cantilever thermomechanical property, people have designed the



cantilever with large length, small width, and optimum layer thicknesses to achieve large thermal expansion mismatch stress and sufficiently small mechanical stiffness [3, 9, 17]. However, there have been few efforts to improve the cantilever optical property [10]. The most common material combination for bimaterial cantilever IR detectors has been silicon nitride and aluminum [1, 3, 6, 9, 10]. The cantilevers fabricated with these materials have relatively small optical absorbance over large portion of the mid-IR spectral region due to small imaginary part of refractive index ( $\sim 0.001 - 0.01$ ) of silicon nitride [18]. Small optical absorbance has been one of the limiting factors to the cantilever sensitivity.

High-contrast grating (HCG) is periodic grating made of material with higher refractive index than surrounding medium [19], and has recently impacted the device concept of semiconductor optoelectronics and nanophotonics due to its extraordinary features [19-21]. HCG can exhibit broadband high reflection or resonance reflection with high quality factor [19], which are not commonly obtainable from traditional gratings. HCG can also possess resonance absorption by having a metal layer on its bottom which inverts the reflection spectrum of HCG [22]. Thus, the integration of HCG into an optical system can enhance its absorbance at the spectral region of interest. Here, we report a new type of bimaterial cantilever based on silicon HCG with metallic (aluminum) coating on the bottom for the use across a wide range of mid-IR wavelengths ( $3 - 11 \mu\text{m}$ ). By incorporating HCG with the bimaterial cantilever, we aim to enhance cantilever IR absorbance as well as the IR sensitivity of the cantilever. We also demonstrate the application of HCG cantilever into the transmission IR spectroscopy employing a Michelson interferometer as an IR source.

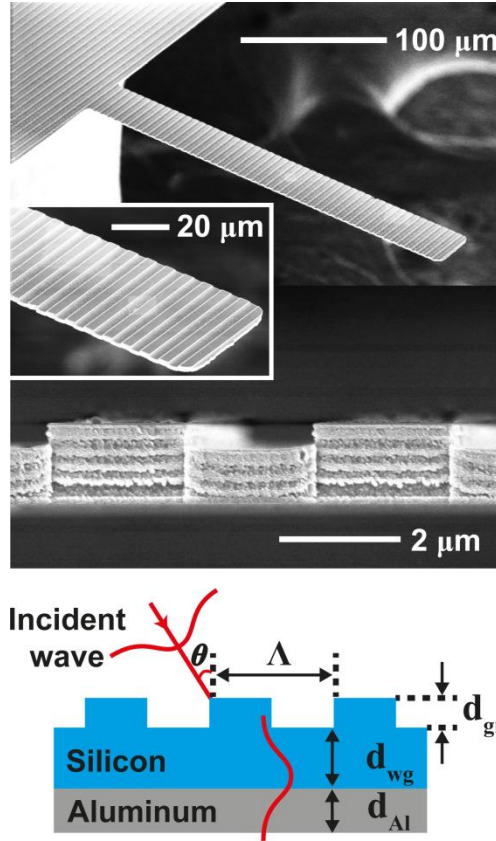


**Figure 0.1** Illustration and SEM micrographs of bimaterial cantilever based on silicon high contrast grating with aluminum coating on the bottom surface. A periodic 1D surface corrugation grating and a waveguide layer consist of single crystal silicon, while the bottom layer is aluminum. At a resonance wavelength of the grating, an incident wave couples to the waveguide layer and creates strong intensity distribution within the cantilever, resulting in strong cantilever absorbance.

## 4.2 Cantilever design and fabrication

Figure 4.1 shows scanning electron microscope (SEM) images of a fabricated cantilever and the cantilever design. The cantilever has a single crystal silicon layer that consists of a periodic 1D surface corrugation grating structure on top of a waveguide layer. The cantilever has an aluminum coating on the bottom surface. We use silicon for a structural material, since

mid-IR light can propagate through silicon with negligible loss due to small extinction coefficient,  $k$ , of silicon ( $k = 10^{-9} - 10^{-4}$ ) [23]. For a coating material, we use aluminum, because it absorbs the wave leaked from the waveguide based on its large extinction coefficient ( $k = 30 - 100$ ) [24]. In addition, the silicon and aluminum are relatively easy to integrate into cantilevers through microfabrication.

From an electromagnetic waveguide perspective, the silicon grating – waveguide on top of an aluminum layer is similar to a grating structure totally surrounded by low index medium or air. The aluminum layer serves as a perfectly reflecting boundary or a mirror for the propagating waves in the silicon waveguide. Hence, the propagating modes in the silicon grating – waveguide on top of an aluminum coating are effectively equal to the propagating modes in an axisymmetric structure composed of twin silicon grating-waveguide structures. Therefore, the cantilever with silicon grating – waveguide structure with an aluminum coating shows similar optical characteristics which are available from HCG grating, which will be shown in the following paragraphs.

Our goal is to integrate gratings structure into the cantilever such that the resonance absorption of HCG occurs in mid-IR spectral region ( $3 - 11 \mu\text{m}$ ). There are several parameters that determine the resonance wavelengths of the grating such as grating period,  $\Lambda$ , grating duty cycle,  $\eta$ , grating depth,  $d_{gr}$ , the waveguide layer thickness,  $d_{wg}$ , the angle of incidence,  $\theta$ , and the light polarization [19-21, 25]. The photolithography resolution limits the ridges of the grating to be larger than  $2 - 3 \mu\text{m}$ , therefore the grating period should be larger than  $5 \mu\text{m}$ . For the simplicity, we set other geometric parameters as follows:  $\eta = 0.5$ ,  $d_{gr} = 0.5 \mu\text{m}$ ,  $d_{wg} = 1 \mu\text{m}$ .

The waveguide layer thickness is related to the cantilever thermal conductance and mechanical compliance which are important factors for the cantilever thermomechanical sensitivity [3].

We used a two-dimensional finite element model (COMSOL Multiphysics) to simulate the absorbance spectra of the cantilevers with different grating periods. Due to the symmetry of the geometry, we simulated a unit cell of the cantilever grating structure which corresponds to a single grating period. In the model, a plane electromagnetic wave is incident on the cantilever with either transverse electric (TE) or transverse magnetic (TM) polarization. The model

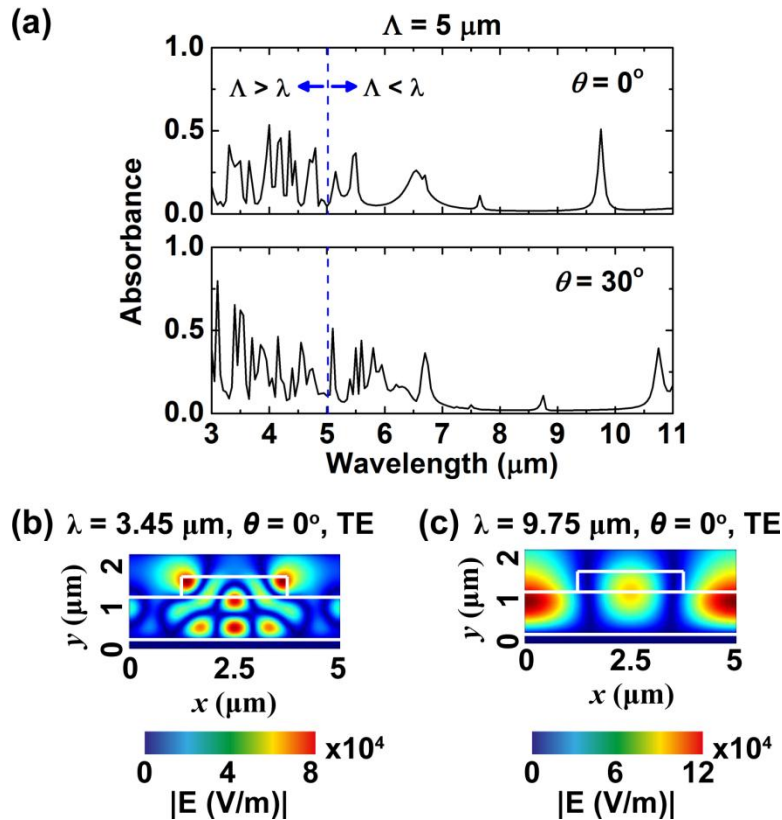


**Figure 0.2** Calculated IR absorbance and electric field amplitude distribution of a cantilever with HCG (grating period  $\Lambda = 5 \mu\text{m}$ , duty cycle  $\eta = 0.5$ , grating depth  $d_{gr} = 0.5 \mu\text{m}$ , waveguide thickness  $d_{wg} = 1 \mu\text{m}$ ) using a finite element model. (a) IR absorbance spectra when both TE and TM polarized wave are incident on the cantilever at either  $0^\circ$  or  $30^\circ$  angle. (b-c) Distribution of the electric field amplitude ( $|E|$ ) in a unit cell of the cantilever when a TE polarized wave is normally incident with a wavelength of either 3.45 or 9.75  $\mu\text{m}$ .

calculated the cantilever absorbance from the ratio of the electromagnetic power loss within

the cantilever to the incident light power. Since we will characterize the cantilever absorbance with randomly polarized light source in later section, we averaged the cantilever absorbance values calculated with TE and TM polarized light.

Figure 4.2a shows the calculated cantilever absorbance when the grating period is 5  $\mu\text{m}$  with an angle of incidence of  $0^\circ$  or  $30^\circ$ . At the wavelength longer than the grating period, an absorption peak due to coupling to resonance mode in HCG appears at 9.75  $\mu\text{m}$  for  $0^\circ$  angle of incidence and at 10.75  $\mu\text{m}$  for  $30^\circ$  angle of incidence [20, 25]. At the wavelength shorter than the grating period, multiple absorbance peaks appear, since higher-order modes of HCG occur [20, 25]. Figure 4.2b and 4.2c show the distribution of the electric field amplitude,  $|E|$ , in a unit cell of a cantilever when a plane wave with TE polarization incident at  $0^\circ$  angle of incidence. At the absorbance peak at 3.45  $\mu\text{m}$ , multiple propagating modes in the waveguide interfere, and create a complex field distribution. At the absorbance peak at 9.75  $\mu\text{m}$ , only a single propagating mode exists in the waveguide, and a simple standing wave pattern appears. In the same manner, we calculated the absorbance spectra of the cantilevers with grating periods of 5.5  $\mu\text{m}$ . The simulation indicated that the grating period of 5.5  $\mu\text{m}$  has resonance at the wavelengths 9.15 – 10.15  $\mu\text{m}$  when the angle of incidence varies from  $0^\circ$  to  $30^\circ$ .

The aluminum layer thickness,  $d_{Al}$ , cantilever length,  $L$ , and cantilever width,  $w$ , are important for both the cantilever thermomechanical sensitivity and the compatibility with the optical cantilever deflection detection system [3]. There is an optimum value for the ratio of coating layer thickness to the structural layer thickness to maximize the thermal expansion mismatch stress [17]. The optimum ratio is typically larger than 0.2, thus the aluminum coating



**Table 0.1** Description of cantilevers

Cantilever	A	B	C
------------	---	---	---

---

Grating Period

5.07    5.45    -

$\Lambda$  ( $\mu\text{m}$ )

Grating Duty

cycle            0.51    0.46    -

$\eta$

Grating Depth

0.43    0.48    -

$d_{gr}$  ( $\mu\text{m}$ )

should be thicker than 200 nm for a 1 $\mu\text{m}$  thick silicon cantilever. However, the evaporated aluminum film typically is under a compressive intrinsic stress [26] such that thick aluminum layer causes the cantilever to bend severely. When the cantilever bending is too large, the laser beam in the deflection readout reflects off the cantilever, deviates from the photodiode, and fails to read the cantilever deflection. For the cantilever to possess large thermomechanical sensitivity, the cantilever has to be long and narrow [3]. However, when the cantilever is too long, the intrinsic stress-induced cantilever deflection becomes too large. In addition, when the cantilever is too narrow, the optical cantilever deflection readout system cannot acquire sufficient signal. Based on this consideration, we select the aluminum coating thickness as 100 nm, cantilever length as 460  $\mu\text{m}$ , and cantilever width as 40  $\mu\text{m}$ .

The HCG cantilevers are fabricated using a silicon-on-insulator (SOI) wafer with a 2.0  $\mu\text{m}$ -thick device layer. We first pattern gratings using a conventional photolithography followed by an anisotropic etching of the silicon. The second photolithography patterns a mask for cantilevers, which is carefully aligned with the gratings. Deep reactive ion etching (DRIE) of the silicon using these patterns follows until the buried oxide is exposed. In order to release the cantilevers, windows around the cantilevers are patterned from the backside of the SOI wafer. We etch through the SOI handle layer from the backside using the buried oxide layer as an etch

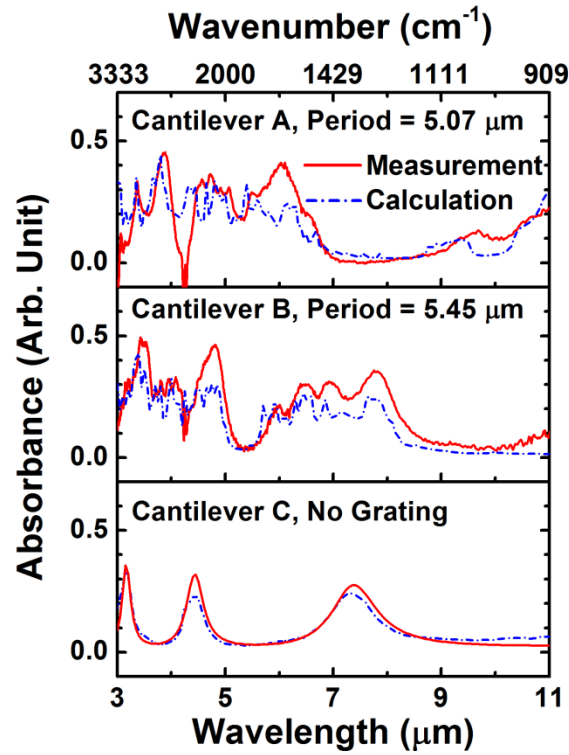


**Figure 0.3** Spectral absorbance of (a) cantilever A, (b) cantilever B, and (c) cantilever C at 3 – 11  $\mu\text{m}$  wavelength region, when randomly polarized waves are incident on a cantilever at a range of angles ( $10 - 30^\circ$ ). The solid lines show cantilever absorbance measured in an FTIR spectrometer. The dashed lines show calculation results from the finite element model.

stop. Finally, we use a hydrofluoric acid (HF) solution to remove the oxide, and release the cantilevers. Table 4.1 lists the dimensions of the fabricated cantilevers and a commercially

obtained cantilever without HCG. The grating period has a length scale of the wavelength of interest. The commercially obtained cantilever also consists of a silicon and aluminum layers (Mikromasch, CSC17) and possesses relatively large IR sensitivity among commercial silicon based bimaterial cantilevers [5].

### 4.3 Cantilever characterization

Figure 4.3 shows the measured and calculated IR absorbance of the cantilevers in the wavelength range 3 – 11  $\mu\text{m}$ . We measured the cantilever IR absorbance using an Fourier transform infrared (FTIR) imaging microspectrometer system (Agilent, 680-IR spectrometer with 620-IR optical microscope). The details of the FTIR measurement protocol are described elsewhere [27]. We also calculated cantilever IR absorbance using the finite element model when a plane wave with TE or TM polarization is incident on a cantilever at incidence angles of 10 – 30° with a step size of 2°. The dash lines in Fig. 4.3 correspond to the arithmetic means of the calculated cantilever absorbance for all the light polarizations and angles of incidence, which compare well with the measured values. Here the absorbance spectra of the cantilevers with HCG, cantilever A and B, have several bands that are the superposition of multiple resonance absorption bands. The multiple absorption bands occur when HCG cantilevers are subject to either randomly polarized light or light from a range of incidence angles. Thus, the superposition of absorption bands occurring in cantilever A and B is due to the optical configuration of the characterization system. The FTIR microspectrometer system uses a non-polarized light source which is a globar source. In addition, a Schwartzschild objective in the

FTIR system has a numerical aperture of 0.5 with central obscuration, thus the FTIR system illuminates light on a cantilever at various angles of incidence ( $10 - 30^\circ$ ) [28].

The amplitudes and bandwidths of the absorption bands increase in the cantilevers with HCG over the wavelengths of  $3 - 11 \mu\text{m}$ . The average absorption peak amplitudes of cantilever A and B range  $0.35 - 0.36$ , while the average peak amplitude of cantilever C is  $0.26$ . More importantly, the total bandwidth (defined as the sum of the bandwidths of the absorption bands with amplitude  $> 0.2$ ) of cantilever A, and B ranges  $2.8 - 4.1 \mu\text{m}$ , while the total bandwidth of cantilever D is  $1 \mu\text{m}$ . Therefore, the cantilevers with HCG have about  $3 - 4\text{X}$  larger total bandwidths as compared to the cantilever with a smooth surface.

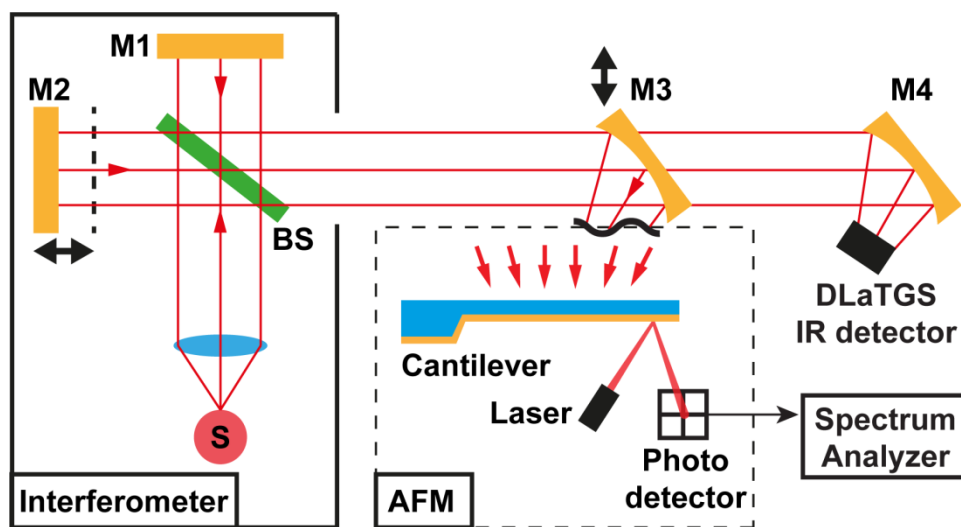


**Figure 0.4** Schematic of the experimental setup that measures cantilever IR responsivity and IR spectrum of a thin film sample. Michelson interferometer includes an IR emitter at  $540^\circ\text{C}$  (S), fixed mirror (M1), a moving mirror (M2), and a beam splitter (BS). A concave mirror (M3) focuses the intensity modulated broadband IR light onto a bimaterial cantilever mounted in a commercial AFM. A spectrum analyzer performs fast Fourier transform on the cantilever deflection signal acquired by the AFM. When M3 is removed from the beam path, the light from interferometer is focused onto a DLaTGS IR detector via a concave mirror (M4).

Figure 4.4 shows an experimental setup that measures cantilever spectral responsivity.

The setup consists of a commercial FTIR spectrometer system (Bruker, Vertex 70) and an AFM

system (Agilent, PicoPlus). Michelson interferometer in the FTIR system produces an intensity modulated broadband light, where the modulation frequency is different for each wavelength. The modulation frequency,  $f$ , is related to the wavelength,  $\lambda$ , by the relation  $f = 2v/\lambda$  where  $v$  is the velocity of the moving mirror in the interferometer. The intensity modulated beam is focused on a cantilever mounted in the AFM, resulting in a periodic cantilever bending. The optical readout in the AFM measures the cantilever tip displacement. A spectrum analyzer (Stanford Research Systems, SR780) performs fast Fourier transform on the optical readout signal, and records cantilever tip displacement as a function of the wavelength. The optical flux at the cantilever position normalizes the cantilever tip displacement to obtain the responsivity value. A deuterated L-alanine-doped triglycine sulfate (DLaTGS) IR detector in the FTIR system can also measure the interferometer output, and is used for IR spectroscopy experiment which is described in the following section.

In addition, we calculated cantilever responsivity employing a model relating incident radiation, heat transfer, temperature distribution in the cantilever, and thermal expansion mismatch bending [27]. This model used the cantilever absorbance values obtained from the finite element model. The finite element model calculated the average values of the cantilever absorbance for TE and TM polarizations and the angles of incidence of  $0 - 15^\circ$ , since the responsivity measurement setup had a non-polarized light source and used a spherical mirror to focus the light onto a cantilever. To account for the heat transfer from the cantilever to air, the responsivity model used an effective thermal conductance to air,  $G_a = 30 \mu\text{W/K}$  for cantilever

A,



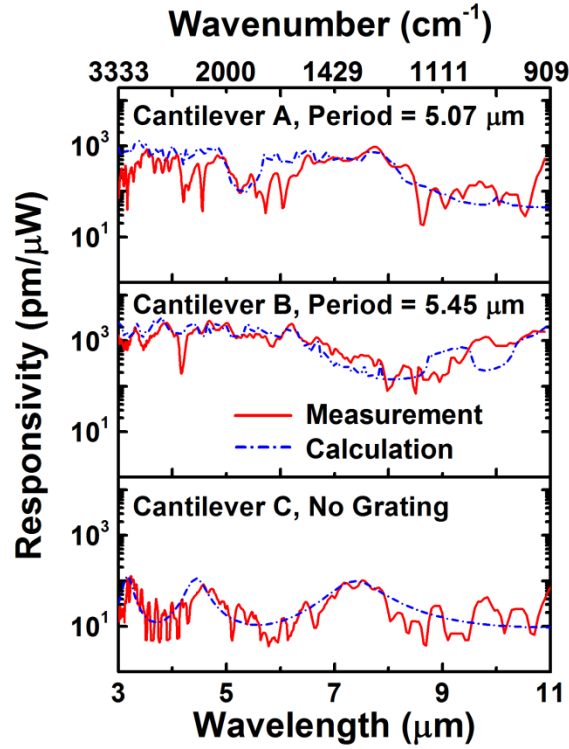


**Figure 0.5** Measured and predicted cantilever responsivity over the 3 – 11  $\mu\text{m}$  wavelength region when randomly polarized waves are incident on a cantilever at a range of angles 0 – 15°.

B, and C, and  $G_a = 20 \mu\text{W/K}$  for cantilever D. These values of  $G_a$  provide model fit and are close to  $G_a$  for a silicon nitride-gold cantilever with similar dimensions [29].

Figure 4.5 shows the measured and calculated IR responsivity of the cantilevers in the wavelength range 3 – 11  $\mu\text{m}$ . In average, the cantilevers with HCG have 13 – 47X greater responsivity values than the cantilever without HCG, cantilever C. Average value of the responsivity is 316  $\text{pm}/\mu\text{W}$  for cantilever A, 1181  $\text{pm}/\mu\text{W}$  for cantilever B, and 25  $\text{pm}/\mu\text{W}$  for cantilever C. Using an average InvOLS value of the cantilevers (248  $\text{nm/V}$ ), the responsivity values of the HCG cantilevers in the unit of  $\text{V/W}$  can be known which range 1.2 – 4.7  $\text{kV/W}$ . Other than enhanced cantilever absorbance, the improvement in the ratio of coating layer thickness to the structural layer thickness,  $d_{Al}/d_{wg}$  is also responsible for the improved

**Table 0.2** Microcantilever performance figures of merit

Cantilever	A	B	C
Responsivity			
$R$ (pm $\mu\text{W}^{-1}$ )	316	1181	25
Noise equivalent power			
	6.7	0.5	47.2

responsivity of the HCG cantilevers [17].  $d_{AI}/d_{wg}$  is 0.07 – 0.1 for the HCG cantilevers, while  $d_{AI}/d_{wg}$  is 0.01 for cantilever C. Since  $d_{AI}/d_{wg}$  value of the HCG cantilevers is close to the optimum value ( $\sim 0.2$ ) as compared to cantilever C, HCG cantilevers are subject to larger thermal expansion mismatch stress when the same amount of heating power is applied.

We characterized the noise equivalent power,  $NEP$ , and detectivity,  $D^*$ , of the cantilevers [3, 6, 17]. Table 4.2 lists the measured  $NEP$ ,  $D^*$  based on the average value of the cantilever responsivity. Thermomechanical noise of the cantilever and the noise from optical readout limit our IR power measurement [9]. The cantilever responsivity measurement setup recorded the noise floor while there is no IR heating on a cantilever. The noise floor equivalent tip displacement of the HCG cantilevers was on the order of 1 pm when a measurement bandwidth was 78 mHz. We normalized the noise equivalent cantilever tip displacement by both its responsivity and square root of the measurement bandwidth to obtain  $NEP$  which was on the order of 1 nW Hz<sup>-1/2</sup>. Another important figure of merit for photodetectors is detectivity which is defined as  $D^* = A^{1/2}/NEP$  where  $A$  is the area of the photosensitive region of the detector. Based on the cantilever surface areas and their  $NEP$ ,  $D^*$  of the HCG cantilevers range 10<sup>6</sup> – 10<sup>7</sup> cm Hz<sup>1/2</sup> W<sup>-1</sup>. For comparison, bolometer type IR detectors have  $D^*$  on the order of 10<sup>8</sup>

$\text{cm Hz}^{1/2} \text{W}^{-1}$  and liquid-nitrogen-cooled mercury-cadmium-telluride (MCT) detectors have  $D^*$  on the order of  $10^{10} \text{ cm Hz}^{1/2} \text{W}^{-1}$  [15].

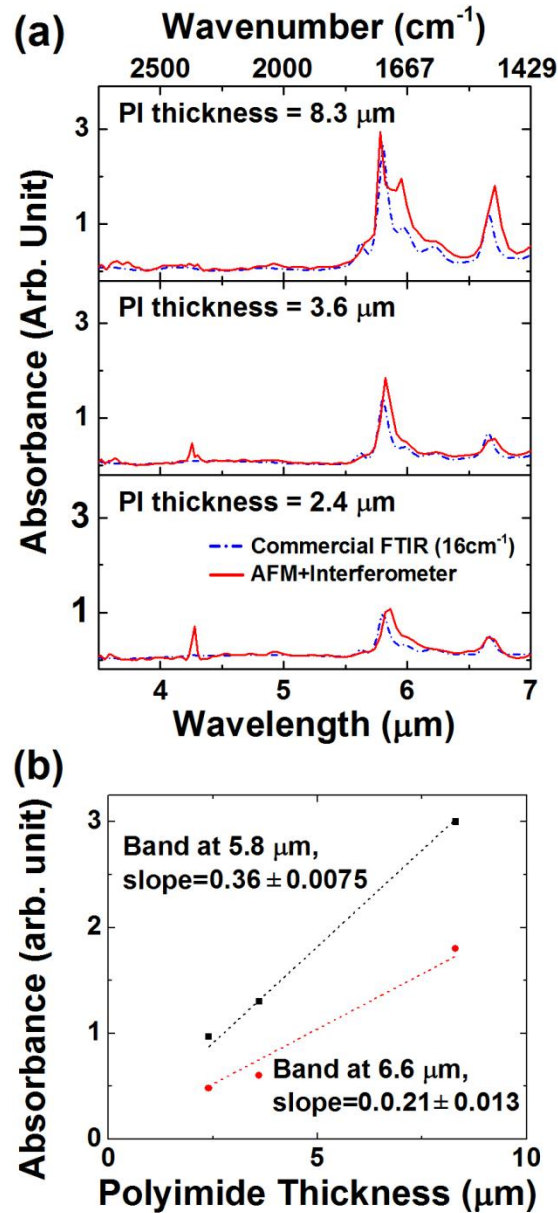


**Figure 0.6** Measured IR absorbance spectra of polyimide (PI) films at the wavelength region between 3.3 and 7  $\mu\text{m}$ . (a) IR absorbance spectra of 2.4, 3.6, and 8.3  $\mu\text{m}$  thick PI films obtained by cantilever B (solid line) and a DLaTGS IR detector (dash line). (b) Absorbance value measured by cantilever B near 5.8 (square) and 6.6  $\mu\text{m}$  (circle) as a function of the PI film thickness.

## 4.4 An application to infrared spectroscopy

The large IR responsivity of the HCG cantilever enables the cantilever based transmission IR spectroscopy with Michelson interferometer shown in Fig. 4.4. To demonstrate the transmission IR spectroscopy, we obtained absorbance spectra of thin polyimide films. The polyimide (PI) films are free-standing membranes with the thicknesses of 2.4, 3.6, and 8.3  $\mu\text{m}$  supported by metallic frames at the edges. To prepare the PI films, we spin coat PI solution (HD Microsystems, PI-2555) on glass substrates and cure them at 300  $^{\circ}\text{C}$  for 1 hour. Then, to transfer the PI films on the metallic frames, we bond the metallic frames on top of the PI films with an adhesive, soak them in hot water (90  $^{\circ}\text{C}$ ) for 12 hours, and detach the metallic frames from the glass substrates. A profilometer measures the thickness of the PI films which are remained on the glass substrates. A PI membrane is positioned in the beam path between the interferometer exit and a cantilever shown in Fig. 4.4. With a sample, we measure the cantilever deflection,  $z_t$ , arising from the transmitted beam intensity. Then, we remove the sample, and measure the cantilever deflection,  $z_0$ , as a reference. Theoretically, the cantilever deflection has a linear relation to the incident radiative power, thus the sample absorbance can be calculated by  $A = -\log_{10}(z_t/z_0)$ . When we measure the absorbance spectrum with a DLaTGS IR detector in the FTIR system, we remove a spherical mirror (M3) in Fig. 4.4 which directs the interferometer output to the cantilever.

Figure 4.6a shows the absorbance spectra of PI films measured by cantilever B and the DLaTGS detector (spectral resolution = 16  $\text{cm}^{-1}$ ) in the wavelength range 3.3 – 7  $\mu\text{m}$ . The spectra measured by both detectors resolve the absorbance bands at 5.8 and 6.6  $\mu\text{m}$  and compare well. Cantilever B provides signal to noise ratio of 2 – 10 at 3.3 – 7  $\mu\text{m}$  with 8.3  $\mu\text{m}$  thick PI sample when the signal is averaged over 20 scan. However cantilever C has low signal

to noise ratio ( $\sim 1$ ) with the same sample such that absorbance spectrum is unobtainable. For this comparison, we average the DLaTGS detector over 20 scans as well. Importantly, we demonstrate that the cantilever response to the incident power is linear such that the absorbance value linearly increases with the increasing sample thickness. Figure 4.6b shows the absorbance value at 5.8 and 6.6  $\mu\text{m}$  as a function of the PI film thickness, which verifies the linear relation between absorbance value measured by the cantilever and the sample thickness. Dissimilar to the bimaterial cantilever, some IR detectors such as mercury-cadmium-telluride (MCT) detector have nonlinear response to the incident radiation, which requires additional data correction process for the quantitative study based on IR spectroscopy.

The integration of HCG into silicon based bimaterial cantilever enhances cantilever responsivity,  $NEP$ , and detectivity. The improved responsivity and linear response of the cantilever to IR light enables IR spectroscopy with Michelson interferometer. The absorbance amplitude, total bandwidth, and the active wavelengths for the HCG cantilever depend on the geometric parameters for HCG. Therefore, the optimization of the geometric parameters [25] will further improve the performance of HCG cantilever for a given incident light.



## 4.5 Conclusion

In conclusion, we designed and fabricated bimaterial cantilevers based on silicon HCG with metallic (aluminum) coating on the bottom. The cantilevers with HCG had about 3 – 4X larger total IR absorbance bandwidths and 30% improvement in absorbance peak amplitude as compared to the cantilever without HCG at the wavelength of 3 – 11  $\mu\text{m}$ . Finite element model for cantilever IR absorbance showed good agreement with the experimental data, indicating that strong IR absorption by HCG cantilevers is due to the resonance modes in HCG. Based on the improved IR absorbance, the HCG cantilevers had 13 – 47X greater responsivity values than the cantilever without HCG. The HCG cantilevers had  $NEP$  as small as  $0.6 \text{ nW Hz}^{-1/2}$  and detectivity,  $D^*$ , as small as  $2.2 \times 10^7 \text{ cm Hz}^{1/2} \text{ W}^{-1}$ . The improved responsivity of the HCG cantilevers enabled transmission IR spectroscopy with a Michelson interferometer. The HCG cantilever obtained IR absorbance spectra of polyimide films, and exhibited linear response to the incident IR light. The IR absorbance amplitude, total bandwidth, and the active wavelengths for the HCG cantilever are dependent on the geometric parameters for HCG, hence the adjustment and optimization of the cantilever performance are available. This study should help the development of bimaterial cantilever IR detectors.

## 4.6 Reference

- [1] Barnes J R, Stephenson R J, Woodburn C N, O Shea S J, Welland M E, Rayment T, Gimzewski J K and Gerber C 1994 A femtojoule calorimeter using micromechanical sensors *Review of Scientific Instruments* **65** 3793-8
- [2] Datskos P G, Lavrik N V, Hunter S R, Rajic S and Grbovic D 2012 Infrared imaging using arrays of SiO<sub>2</sub>micromechanical detectors *Opt. Lett.* **37** 3966-8
- [3] Kwon B, Rosenberger M, Bhargava R, Cahill D G and King W P 2012 Dynamic thermomechanical response of bimaterial microcantilevers to periodic heating by infrared radiation *Review of Scientific Instruments* **83** 015003-7
- [4] Kwon B, Schulmerich M V, Elgass L J, Kong R, Holton S E, Bhargava R and King W P 2012 Infrared microspectroscopy combined with conventional atomic force microscopy *Ultramicroscopy* **116** 56-61
- [5] Kwon B, Wang C, Park K, Bhargava R and King W P 2011 Thermomechanical sensitivity of microcantilevers in the mid-infrared spectral region *Nanoscale Microscale Thermophys. Eng.* **15** 16-27
- [6] Varesi J, Lai J, Perazzo T, Shi Z and Majumdar A 1997 Photothermal measurements at picowatt resolution using uncooled micro-optomechanical sensors *Applied Physics Letters* **71** 306-8
- [7] Zhao Y, Mao M, Horowitz R, Majumdar A, Varesi J, Norton P and Kitching J 2002 Optomechanical uncooled infrared imaging system: design, microfabrication, and performance *Microelectromechanical Systems, Journal of* **11** 136-46
- [8] Van Neste C W, Senesac L R, Yi D and Thundat T 2008 Standoff detection of explosive residues using photothermal microcantilevers *Applied Physics Letters* **92**
- [9] Datskos P G, Lavrik N V and Rajic S 2004 Performance of uncooled microcantilever thermal detectors *Review of Scientific Instruments* **75** 1134-48
- [10] Rosenberger M R, Kwon B, Cahill D G and King W P 2012 Impact of silicon nitride thickness on the infrared sensitivity of silicon nitride–aluminum microcantilevers *Sensors and Actuators A: Physical* **185** 17-23
- [11] Canetta C and Narayanaswamy A 2013 Sub-picowatt resolution calorimetry with a bi-material microcantilever sensor *Applied Physics Letters* **102** 103112-4
- [12] Datskos P G, Lavrik N V, Hunter S R, Rajic S and Grbovic D 2012 Infrared imaging using arrays of SiO<sub>2</sub>micromechanical detectors *Optics Letters* **37** 3966-8
- [13] Rogalski A 2010 *Infrared Detectors, Second Edition* (New York, NY: Taylor & Francis)
- [14] Niklaus F, Vieider C and Jakobsen H 2007 MEMS-based uncooled infrared bolometer arrays: a review 68360D-D
- [15] Rogalski A 2011 *Infrared Detectors* (New York: CSC Press)
- [16] Grbovic D, Lavrik N V, Datskos P G, Forrai D, Nelson E, Devitt J and McIntyre B 2006 Uncooled infrared imaging using bimaterial microcantilever arrays *Applied Physics Letters* **89** 073118-3
- [17] Lai J, Perazzo T, Shi Z and Majumdar A 1997 Optimization and performance of high-resolution micro-optomechanical thermal sensors *Sensors and Actuators A: Physical* **58** 113-9
- [18] Klanjšek Gunde M and Maček M 2001 Infrared Optical Constants and Dielectric Response Functions of Silicon Nitride and Oxynitride Films *physica status solidi (a)* **183** 439-49
- [19] Zhou Y, Huang M C Y, Chase C, Karagodsky V, Moewe M, Pesala B, Sedgwick F G and Chang-Hasnain C J 2009 High-Index-Contrast Grating (HCG) and Its Applications in Optoelectronic Devices *Selected Topics in Quantum Electronics, IEEE Journal of* **15** 1485-99
- [20] Chang-Hasnain C J 2011 High-contrast gratings as a new platform for integrated optoelectronics *Semiconductor Science and Technology* **26** 014043
- [21] Karagodsky V and Chang-Hasnain C J 2012 Physics of near-wavelength high contrast gratings *Opt. Express* **20** 10888-95

- [22] Lin S-F, Wang C-M, Ding T-J, Tsai Y-L, Yang T-H, Chen W-Y and Chang J-Y 2012 Sensitive metal layer assisted guided mode resonance biosensor with a spectrum inversed response and strong asymmetric resonance field distribution *Opt. Express* **20** 14584-95
- [23] Palik E D ed 1985 *Handbook of Optical Constants of Solids* vol III (New York: Academic)
- [24] Brewster Q M 1992 *Thermal Radiative Transfer and Properties* (New York: John Wiley & Sons, Inc)
- [25] Liu J-N, Schulmerich M V, Bhargava R and Cunningham B T 2011 Optimally designed narrowband guided-mode resonance reflectance filters for mid-infrared spectroscopy *Opt. Express* **19** 24182-97
- [26] Abermann R 1990 Measurements of the intrinsic stress in thin metal films *Vacuum* **41** 1279-82
- [27] Kwon B, Jiang J, Schulmerich M V, Xu Z, Bhargava R, Liu L G and King W P Bimaterial Microcantilevers with Black Silicon Nanocone Arrays *Sensors and Actuators A: Physical* (*accepted*)
- [28] Gaylord T K and Kilby G R 2004 Optical single-angle plane-wave transmittances/reflectances from Schwarzschild objective variable-angle measurements *Review of Scientific Instruments* **75** 317-23
- [29] Narayanaswamy A and Gu N 2011 Heat Transfer From Freely Suspended Bimaterial Microcantilevers *J. Heat Transf.-Trans. ASME* **133**

# Discrete-frequency infrared spectroscopic microscopy with narrow-bandwidth high-contrast guided resonance photonic crystal slab filters

Jui-Nung Liu,<sup>1,2,3</sup> Matthew V. Schulmerich,<sup>3</sup> Rohit Bhargava,<sup>2,3,4,5,\*</sup>  
and Brian T. Cunningham<sup>1,2,4,\*</sup>

<sup>1</sup>Department of Electrical and Computer Engineering, University of Illinois at Urbana-Champaign, Urbana, Illinois 61801, USA

<sup>2</sup>Micro and Nanotechnology Laboratory, University of Illinois at Urbana-Champaign, Urbana, Illinois 61801, USA

<sup>3</sup>Beckman Institute for Advanced Science and Technology, University of Illinois at Urbana-Champaign, Urbana, Illinois 61801, USA

<sup>4</sup>Department of Bioengineering, University of Illinois at Urbana-Champaign, Urbana, Illinois 61801, USA

<sup>5</sup>Department of Mechanical Science and Engineering, University of Illinois at Urbana-Champaign, Urbana, Illinois 61801, USA

\*[rxb@illinois.edu](mailto:rxb@illinois.edu)

\*[bcunning@illinois.edu](mailto:bcunning@illinois.edu)

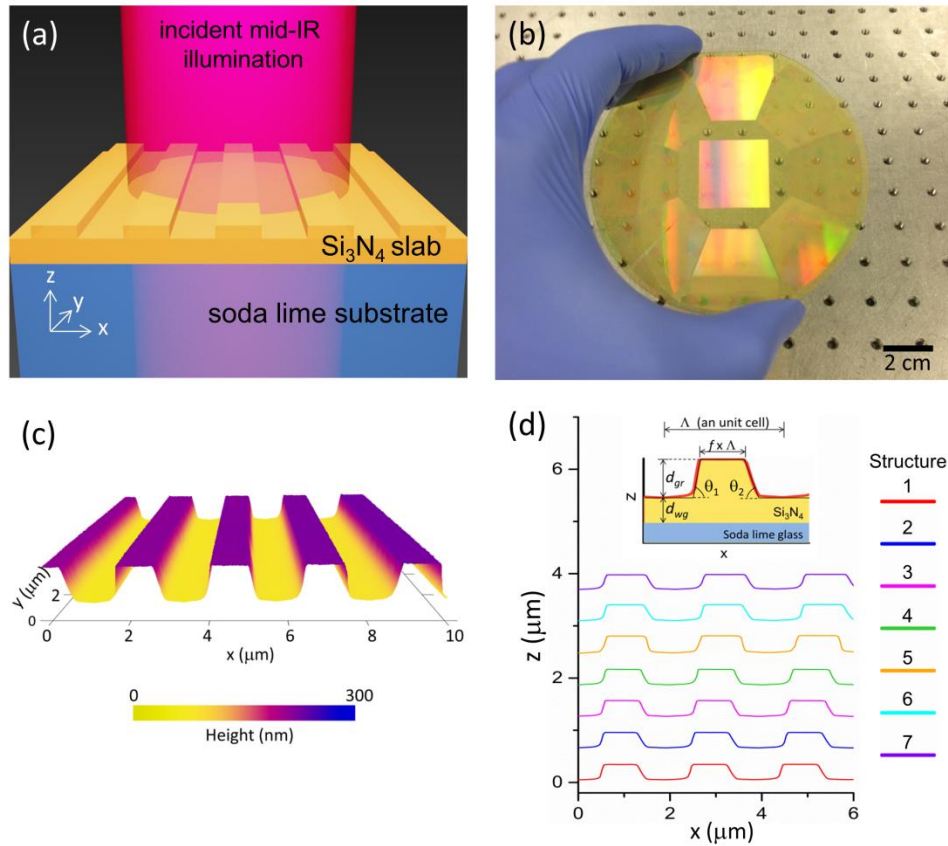


**Figure 1.** Mid-infrared (mid-IR) narrowband guided resonance photonic crystal slab (PCS) filters built on one 4-inch soda lime glass substrate. (a) Schematic of the PCS filters. (b) Image of the fabricated PCS filter set. Visible

light dispersion is made by periodic surface corrugation of the PCS filters. (c) and (d): Atomic force microscopy image of PCS filter surfaces. Structural parameters of the PCS filters can be extracted from the measurement.

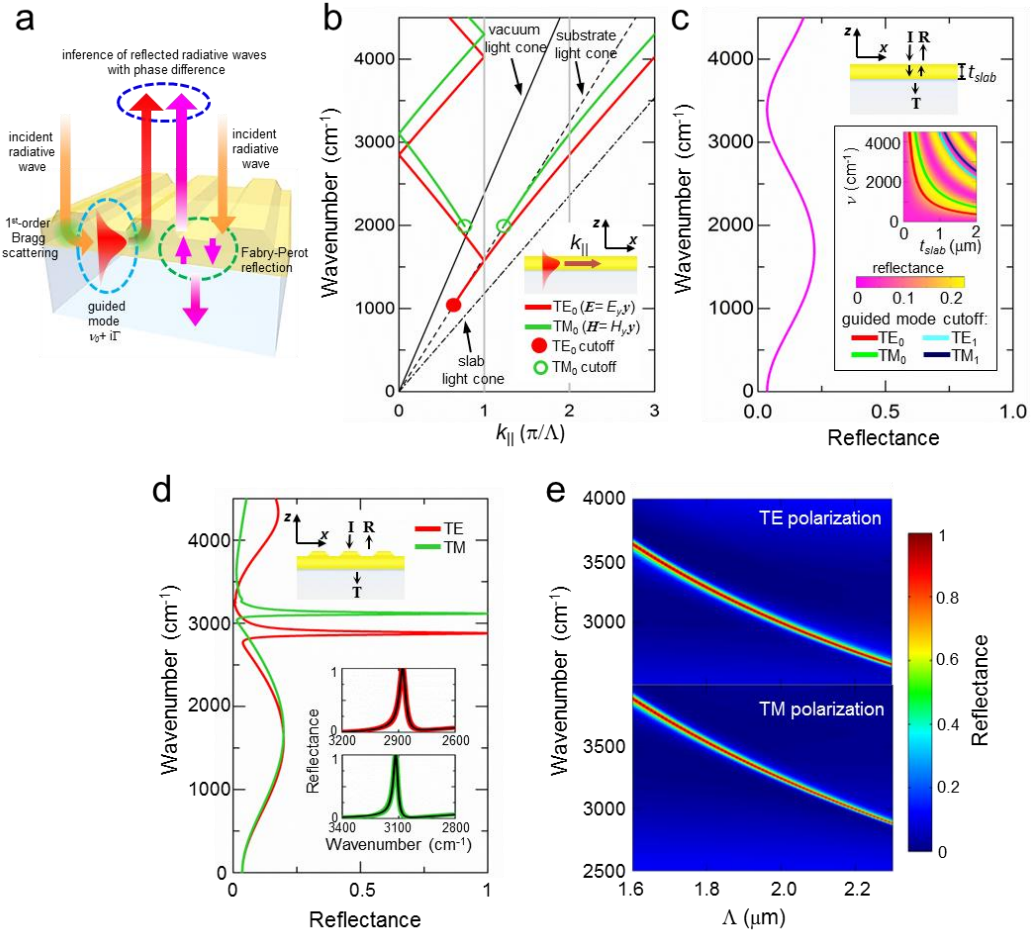


**Figure 2.** Design of mid-IR narrowband PCS filters. (a) Schematic showing reflected radiative wave has contribution from both narrow-linewidth guide mode resonance and broad-linewidth Fabry-Perot background reflections. Interference of the two parts leads to asymmetric lineshape of the PCS filters. (b) Empty-lattice approximation of the PCS with slab thickness=730 nm, period= 2.1 μm,  $n_{SiN}$ = 2.02, and  $n_{SL}$ = 1.47. Narrowband PCS filters require small periodic perturbation of the guided modes, so empty-lattice approximation is employed to predict the spectral location of the guided resonance. Normal incident wave coupled to the guided mode and gains/releases momentum of  $2\pi/\text{period}$  by 1<sup>st</sup>-order Bragg scattering, so guided resonance happens at second Brillouin Zone (BZ) boundary in extended scheme or  $k_{||}=0$  in reduced scheme. (c) Calculation of the Fabry-Perot background reflections by using propagation matrix method for the same flat slab in (b). Inset: reflectance map of the slab as a function of the slab thickness and wavenumbers. Cutoff curves of the guided modes are also shown. For single band guided resonance PCS filter with high contrast ratio, it requires the designed slab thickness to be on the right-hand side of the TE<sub>0</sub> and TM<sub>0</sub> modes (not cutoff), to be on the left-hand side of the higher-order modes (cutoff), and to have small background reflections at the spectral location of guided mode resonance at the same time. (d) Finite-element calculation of the reflection spectra of PCS filters with  $d_{gr}$ =300 nm,  $d_{wg}$ = 580 nm, and period= 2.1 μm. The spectral location of the guided resonance is very close to the predicted ones using empty-lattice approximation in (b). Inset: The finite-element calculated spectra are fitted by narrowband resonance formula and constant background reflection. (e) Spectral location of the resonance as a function of the photonic crystal period. TE- and TM-polarized guided resonances with grating period=2.0-2.2 μm can be used for mid-IR spectroscopy in C-H stretching region (2800-3200 cm<sup>-1</sup>).



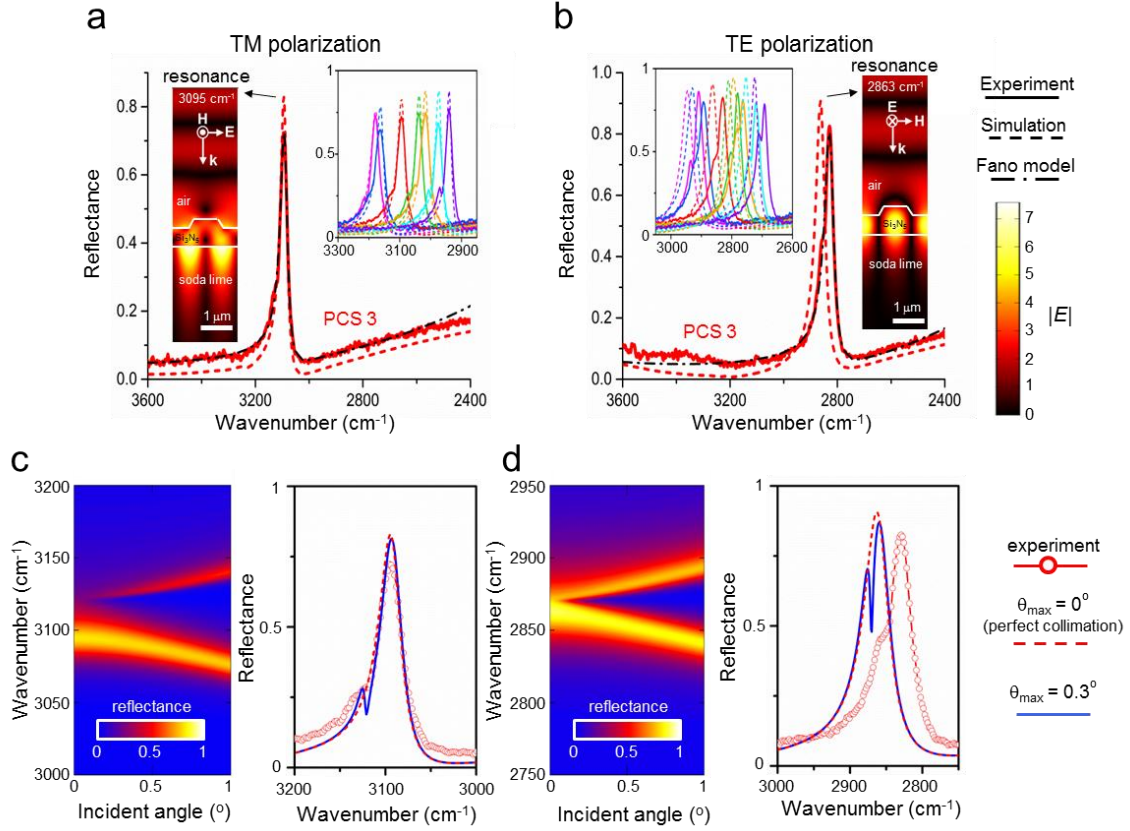


**Figure 3.** Measured and finite-element computed optical properties of narrowband guided resonance PCS filters with high contrast ratio. Far-field reflectivity along with analytical model fit and near-field electric field enhancement distribution at resonance of PCS filter 3 for TM (a) and TE (b) polarizations and normal incidence. Near-field distribution at resonance shows standing wave pattern along  $z$  direction above the PCS structure due to coupling of incident and reflected waves in air and high reflectivity of the PCS at resonance. Two maxima of the electric field strength standing waves in the slab along  $x$  direction confirm that the resonances happen at 2<sup>nd</sup> BZ boundary. Reflectance spectra of a set of fabricated filters on the same substrate are also shown in the insets for mid-IR spectroscopy. (c) and (d): To enhance understanding of the lineshape of the PCS filters, angular response of a PCS filter is computed for small incident angles (0-1 degree) for TM (c) and TE (d) polarizations. By considering contributions from incident waves with different small incident angles, the computed spectra can explain experimental PCS filter lineshapes. The sharp dip in the lineshape is not seen in some filters because of spectral resolution of characterization and inhomogeneous broadening due to fabrication nonuniformity.

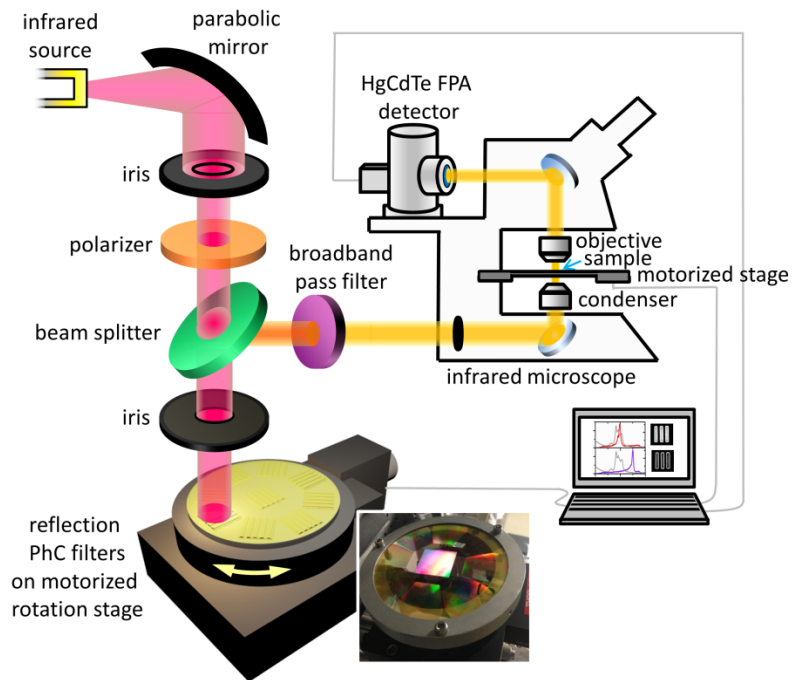


**Figure 4.** Schematic of discrete-frequency infrared (DF-IR) imaging spectroscopy.

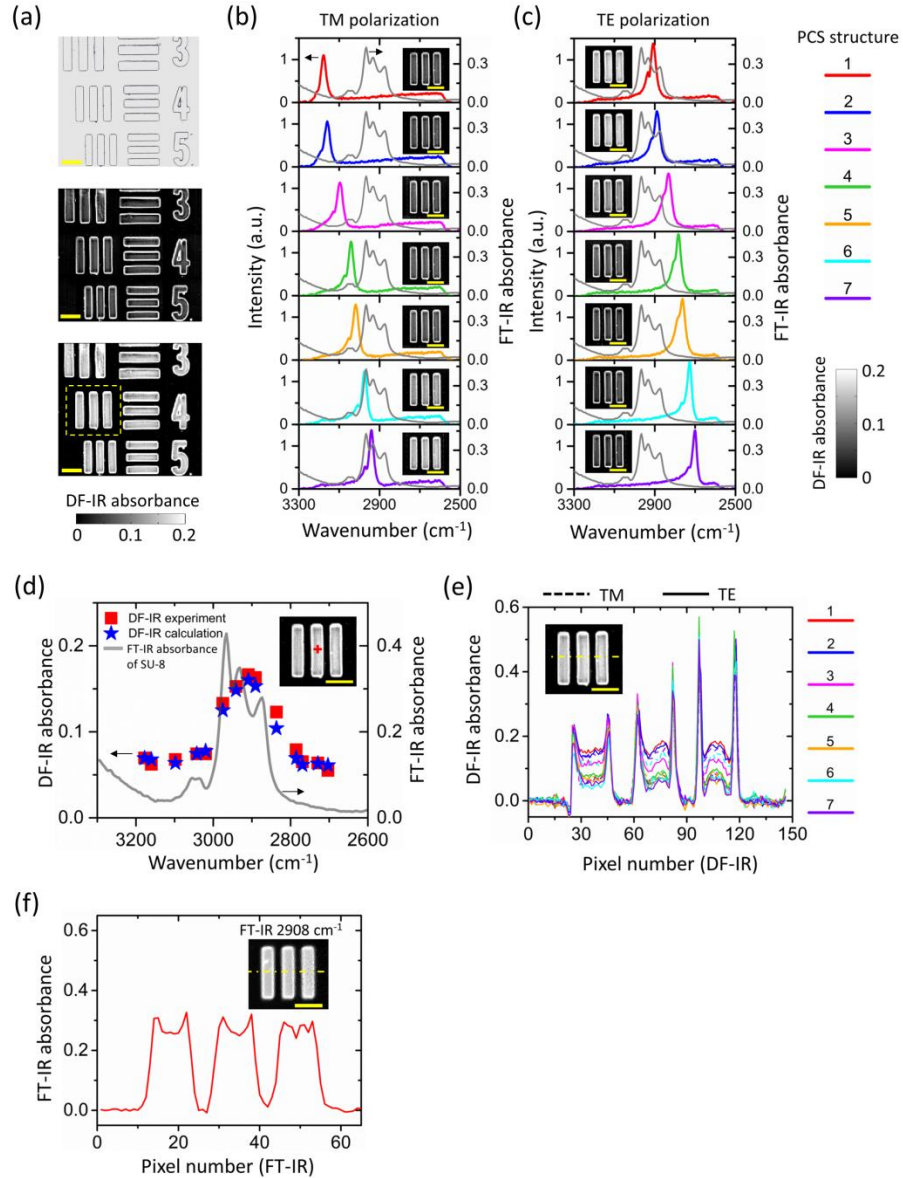


**Figure 5.** DF-IR imaging spectroscopy of the USAF target (group 3) in C-H stretching region (2700-3200 cm<sup>-1</sup>). The USAF targets are made in SU-8 photoresist on BaF<sub>2</sub> substrate. (a) Optical image of the USAF target and DF-IR absorbance imaging when PCS filter resonance is on/off SU-8 absorption peaks. Scale bar: 100 micro meters. DF-IR absorbance images and their corresponding reflected PCS filter spectra (colored) with broadband pass filter and SU-8 absorbance spectra (grey) for TM (b) and TE (c) polarizations. (d) Measured and calculated DF-IR absorbance spectra acquired at the location with red cross, compared with measured FT-IR spectrum of the SU-8 at the same place. The spectral location of each PCS filter is determined by curve fit using analytical model. (e) DF-IR absorbance profile along the yellow dash dot line. The peaks at boundaries of the USAF target are due to absorbance contributed by scattering. (f) Measured FT-IR absorbance profile of the same USAF target.

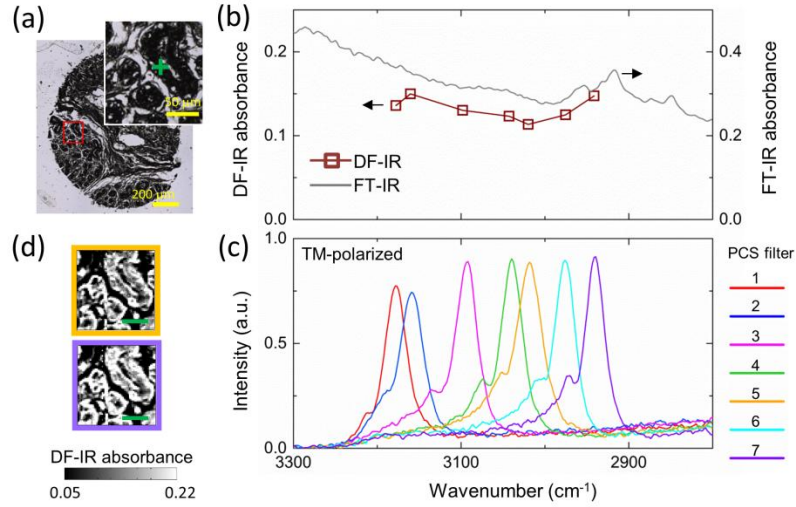


**Figure 6.** DF-IR imaging of the human breast tissue with a set of PCS filters. (a) Optical image of the sample. (b) DF-IR absorbance acquired at the position with green cross in (a) using TM-polarized PCS filters shown in (c). FT-IR absorbance spectrum at the same location is also provided for reference. Although human breast tissue has smaller absorbance contrast in C-H stretching region, the trend of DF-IR absorbance can still match that of the FT-IR absorbance spectrum approximately. (d) The DF-IR absorbance imaging of tissue shows higher absorbance in epithelium region with PCS filter 7 (purple) than with PCS filter 5 (orange).

## **46th Midwest Regional ACS Meeting - Saint Louis MO**

### **Transmission Raman tomography for determining the position and size of targets buried in light scattering media**

Matthew R Kole, Matthew V Schulmerich, Matthew K Gelber, and Rohit Bhargava.

#### **Abstract**

The use of Raman spectroscopy to provide label-free chemical contrast of analytes buried below light scattering media has a wide variety of biomedical related applications ranging from disease diagnosis to monitoring drug delivery. Developing and validating methods for obtaining the size, shape, and position of buried targets is a first step towards realizing this potential. In this research, we present experimental results and theoretical considerations from a series of transmission Raman tomography measurements on targets (Teflon spheres) buried inside of Intralipid-based tissue phantoms along with the resulting two-dimensional image reconstructions. Measurements were collected with a fiber-based Raman instrument using varying source-detector collection angles. We compare two forward-modeling methods, radiative transport calculation (Nirfast, an open-source diffuse optical tomography modeling package)<sup>1</sup> and Monte Carlo simulation (written in-house), for the modeling of light fluence throughout the phantom. Reconstruction of the size and position of buried targets can be employed without the use of spatial priors via an iterative modified-Tikhonov minimization algorithm, and these results are validated against computed tomography (CT) images. We present the differences between the two forward algorithms and highlight the important advantages and disadvantages of each approach.

(1) Dehghani, H.; Eames, M.E.; Yalavarthy, P.K.; Davis, S.C.; Srinivasan, S.; Carpenter, C.M.; Pogue, B.W.; Paulsen, K.D. *Commun. Numer. Meth. Engng.* 2008, 25 (6), 711-732.



**University of Michigan Analytical Chemistry Seminar – Ann Arbor, MI**

**Raman Spectroscopy in the Presence of Light Scattering: polymer model systems and applications toward biomedical and agricultural research**

Speaker: Matthew Schulmerich

**Abstract**

Raman spectroscopy has proven to be a non-destructive approach to obtaining chemically specific information from a wide variety of analytes. Conventional experimental configurations illuminate the sample and collect the backscattered Raman signal from the same points of illumination. However, by strategic illumination and collection of the Raman signal, even in the presence of light scattering, it is possible to tune the sampling depths to obtain signal from localized regions of interest. In this talk, a number of experimental examples will be presented illustrating applications for spatially offset Raman spectroscopy, dark field Raman spectroscopy, and transmission Raman spectroscopy. We illustrate the ability to gain spectral/chemical information with both spatial and depth resolution using polymer models, tissue phantoms as well as murine and human tissue. Considerations toward quantitative measurements will be illustrated using prostate tissue and soybeans.

## **Poster presentation at the University of Illinois Chicago Cancer Center Forum – Chicago, IL**

### **Raman spectroscopy in the presence of light scattering: methods towards non-invasive optical biopsy**

Matthew Schulmerich, Michael Walsh, Matthew Gelber, Krishnarao Tangella, Andre Kajdacsy-Balla, and Rohit Bhargava

#### **Abstract**

Raman spectroscopy has proven to be a nondestructive approach to obtaining label free chemically specific information from a wide variety of analytes. The underlying data consist of both spectral and structural images, which can act as inputs to statistical pattern recognition classifiers to identify different cell types (ie. epithelial and stromal cells), collectively providing recognition of tissue structure and disease. While conventional microscopy based approaches are effective for biopsied tissue, other existing methods are more suitable for analyses in vivo. Conventional microscopy experimental configurations illuminate the sample and collect the backscattered Raman signal from the same points of illumination. However, by strategic illumination and collection of the Raman signal, even in the presence of light scattering, it is possible to tune the sampling depths to obtain signal from localized regions of interest. Raman images acquired from prostate and breast tissue will be used to illustrate chemical contrast achievable by Raman spectroscopy and a number of experimental instrument configurations are presented here illustrating approaches for spatially offset Raman spectroscopy, dark field Raman spectroscopy, and transmission Raman spectroscopy. We illustrate the ability to gain spectral/chemical information with both spatial and depth resolution using polymer models and tissue phantoms.

**Oral Presentation at SciX (Formally called FACSS –Federation of Analytical Chemistry and Spectroscopy Societies) - Kansas City, MO**

**Cell-type discrimination in breast tissue with Raman and FTIR imaging**

Matthew Schulmerich, Michael Walsh, Matthew Kole, Andre Kajdacsy-Balla, Krishna Tangella, and Rohit Bhargava

**Abstract**

Myoepithelial cells makeup the basal layer of normal mammary epithelial tissue. Their identification has particular diagnostic value as they are lost in malignancy but retained in most benign lesions. Raman images were acquired from regions containing epithelial cells, myoepithelial cells, and stroma on normal tissue and tissue with invasive carcinomas. Serial sections were stained with Hematoxylin and Eosin (H&E) as well as the immunohistochemical (IHC) stain P63 to verify the presence of myoepithelial cells in the regions of interest. Several Raman bands can be used to achieve chemical contrast in distinguishing epithelial cells, myoepithelial cells, and stroma. For example, spectra collected over stromal tissue have larger amide III contribution ( $1244\text{ cm}^{-1}$  and  $1274\text{ cm}^{-1}$  correlated with C-N and N-H vibrational modes) than spectra collected over epithelia or myoepithelial cells. Additionally, the Raman signal at  $1045\text{ cm}^{-1}$  (C-C stretch) also has a larger relative contribution in the stroma and myoepithelium than the epithelium. We show that Raman imaging could be used to identify the presence or absence of myoepithelial cells and discuss the prospects of clinical utility.

**Oral Presentation at The American Chemical Society's Central Michigan Regional Meeting - Midland, MI**

**Cellular contrast in breast tissue biopsies with Raman spectroscopy and imaging**

Matthew Schulmerich, Michael Walsh, Matthew Kole, Andre Kajdacsy-Balla, Krishna Tangella, and Rohit Bhargava

**Abstract**

The cellular distribution in tissue is of interest for breast pathology. Raman images were acquired from regions of tissue containing epithelium, myoepithelium, and stroma to explore clinical utility. Serial sections were stained with H&E and P63 to verify the presence of cell types in the regions of interest. Several Raman bands can be used for chemical contrast in detecting myoepithelium which is a cell-type with particular diagnostic value as they are lost in malignancy but retained in most benign lesions.

